

**Study of spin pumping and inverse spin Hall effect on
manganite based thin films**

By

Pushpendra Gupta

Enrolment No. PHYS11201704021

National Institute of Science Education and Research, Bhubaneswar

A thesis submitted to the

Board of Studies in Physical Sciences

In partial fulfillment of requirements

for the Degree of

DOCTOR OF PHILOSOPHY

of

HOMI BHABHA NATIONAL INSTITUTE

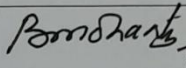
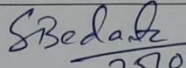
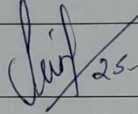
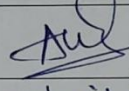
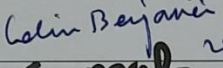
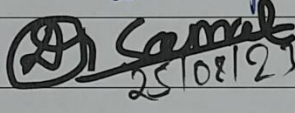


May, 2023

Homi Bhabha National Institute¹

Recommendations of the Viva Voce Committee

As members of the Viva Voce Committee, we certify that we have read the dissertation prepared by **Pushpendra Gupta** entitled “**Study of spin pumping and inverse spin Hall effect on manganite based thin films**” and recommend that it may be accepted as fulfilling the thesis requirement for the award of Degree of Doctor of Philosophy.

Chairman -	Prof. Bedangadas Mohanty	 25/8/2023
Guide / Convener -	Prof. Subhankar Bedanta	 25/08/2023
Co-guide -		
Examiner -	Prof. Sunil Nair	 25-AUG-2023
Member 1 -	Dr. Ajaya Kumar Nayak	 25/08/2023
Member 2 -	Dr. Colin Benjamin	 28.08.2023
Member 3 -	Dr. Debakanta Samal	 25/08/23

Final approval and acceptance of this thesis is contingent upon the candidate's submission of the final copies of the thesis to HBNI.

I/We hereby certify that I/we have read this thesis prepared under my/our direction and recommend that it may be accepted as fulfilling the thesis requirement.

Date: 25/08/2023

Place: Jalni

Signature

Co-guide (if any)

Signature

Guide Prof. S. Bedanta

¹ This page is to be included only for final submission after successful completion of viva voce.

STATEMENT BY AUTHOR

This dissertation has been submitted in partial fulfillment of requirements for an advanced degree at Homi Bhabha National Institute (HBNI) and is deposited in the library to be made available to borrowers under rules of the HBNI.

Brief quotations from this dissertation are allowable without special permission, provided that accurate acknowledgement of source is made. Requests for permission for extended quotation from or reproduction of this manuscript in whole or in part may be granted by the Competent Authority of HBNI when in his or her judgment the proposed use of the material is in the interests of scholarship. In all other instances, however, permission must be obtained from the author.



(Pushpendra Gupta)

DECLARATION

I, hereby declare that the investigation presented in the thesis has been carried out by me. The work is original and has not been submitted earlier as a whole or in part for a degree / diploma at this or any other Institution / University.

A handwritten signature in black ink, appearing to read 'Gupta', with a long horizontal flourish extending to the right.

Pushendra Gupta

List of Publications arising from the thesis

Journal

1. **#P. Gupta**, B. B. Singh, K. Roy, A. Sarkar, M. Waschk, T. Brueckel, and S. Bedanta, *Simultaneous Observation of Anti-Damping and the Inverse Spin Hall Effect in the $La_{0.67}Sr_{0.33}MnO_3/Pt$ Bilayer System*, *Nanoscale* **13**, 2714 (2021).
2. **#P. Gupta**, B. B. Singh, A. Mishra, A. Kumar, A. Sarkar, M. Waschk, T. Brueckel, and S. Bedanta, *Tailoring spin to charge conversion efficiency via microwave frequency in $La_{0.67}Sr_{0.33}MnO_3/Pt$ bilayer system*, *SPIN*, (**in print**).

Manuscript in preparation

1. **#P. Gupta**, S. Bedanta *et al et al.*, *Exchange bias and vertical shift in $La_{0.67}Sr_{0.33}MnO_3/SrRuO_3$ bilayer system* (manuscript under preparation).
2. **#P Gupta**, S. Bedanta *et al et al.*, *Study of inverse spin Hall effect in $La_{0.67}Sr_{0.33}MnO_3 / La_{0.2}Sr_{0.8}MnO_3$ heterostructures* (manuscript under preparation).
3. **#P Gupta**, S. Bedanta *et al et al.*, *Self-induced inverse spin Hall effect in pulsed laser deposition grown $La_{0.67}Sr_{0.33}MnO_3$ films* (manuscript under preparation).

#: Publications related to the thesis

Others

1. B. B. Singh, K. Roy, **P. Gupta**, T. Seki, K. Takanashi, and S. Bedanta, *High Spin Mixing Conductance and Spin Interface Transparency at the Interface of a $Co_2Fe_{0.4}Mn_{0.6}Si$ Heusler Alloy and Pt*, *NPG Asia Mater* **13**, 1 (2021).
2. B. Sahoo, K. Roy, **P. Gupta**, A. Mishra, B. Satpati, B. B. Singh, and S. Bedanta, *Spin Pumping and Inverse Spin Hall Effect in Iridium Oxide*, *Advanced Quantum Technologies* **4**, 2000146 (2021).
3. K. Roy, A. Mishra, **P. Gupta**, S. Mohanty, B. B. Singh, and S. Bedanta, *Spin pumping and Inverse Spin Hall Effect in $CoFeB/IrMn$ Heterostructures*, *J. Phys. D: Appl. Phys.* **54**, 425001 (2021).
4. K. Roy, S. Nayak, **P. Gupta**, and S. Bedanta, *Spin dynamics and inverse spin Hall effect study in $Pt/NiMn/CoFeB$ system*. *Phys. Chem. Chem. Phys.*, **24**, 24323–2432 (2022).

5. S. Goswami, **P. Gupta**, S. Nayak, S. Bedanta, Ò. Iglesias, M. Chakraborty and D. De, *Dependence of Exchange Bias on Interparticle Interactions in Co/CoO Core/Shell Nanostructures*, *Nanomaterials* **12**, 3159 (2022).
6. S. Goswami, **P. Gupta**, S. Bedanta, M. Chakraborty and D. De, *Coexistence of exchange bias and memory effect in nanocrystalline CoCr₂O₄*, *Jour. of All. and Com.* **890**,161916 (2021).
7. K. Roy, A. Mishra, S. Nayak, **P. Gupta**, B. B. Jena and S. Bedanta., *Spin pumping and inverse spin Hall effect in semi-conducting antiferromagnetic Co₃O₄*, *ACS, Applied electronic material*, (2023)
8. B. B. Jena, P. Gupta, S. Nayak, A. Mishra, A. Azevedo, H. Ding. and S. Bedanta, *Optimizing spin pumping and spin mixing conductance via Cu spacer layer in Mn₂Au/Py system*, *Phys. Scr.* 98, 075924 (2023).



Pushendra Gupta

Dedicated to my parents

ACKNOWLEDGEMENTS

I want to express my special gratitude to my supervisor, mentor, friend, philosopher and guide, Prof. Subhankar Bedanta. He has always motivated me in many aspects of life during my stay at NISER. He is a local guardian for me in NISER. He has given his valuable time for the research topic discussion, paper writing, and other scientific discussions, as well as to motivate me whenever I was feeling morally low. He has always supported me whenever I need his support. During my research, I have often faced academic and non-academic difficulties, and I always found him giving me support like a guardian so that I could overcome the difficulties by learning from them. He has immense knowledge of the research field. Hence, we always get some tricks, tips, hints and valuable suggestions from him, which boosted my knowledge and skill towards the research. He always encouraged me to participate in and join different national and international conferences and workshops to improve my skills in presenting my research works. I always enjoyed and learned from his company during my Ph.D. I got a lot of chances to celebrate the different festival functions and occasions with him. I am thankful to him for what I am today, especially in the research field. It would never have been possible to complete my research work without his constant guidance and support.

I would like to thank my doctoral committee members, Prof. Bedangadas Mohanty, Dr. Ajaya Kumar Nayak, Dr. Colin Benjamin from SPS, NISER, Bhubaneswar, for their valuable suggestions and for enriching me with their expertise. I would also thank Dr. Debakanta Samal from IOP Bhubaneswar for his kind evaluation of my work and for giving his valuable suggestion as an external doctoral committee member.

I extend my acknowledgement to my collaborator Dr. Braj Bhushan Singh, Prof. Vivek Amin, Prof. Thomas Brueckel, Dr. Anirban Sarkar, Dr. Markus Waschk, Dr. Piero Torelli, Dr. Patrov, Dr. In Jun Park, Dr. Ashutosh Rath, Dr. Biswaroop Sathpati, Dr. Shwetha G. Bhat, Dr.

Debakanta Samal, Dr. Vivek Malik, Prof. Anil Kumar and Prof. Satadeep Bhattacharjee for their kind help and suggestions in a different part of my research work as well as providing theoretical support.

I extend my acknowledgement to my seniors Dr. Sougata Mallick, Dr. Srijani Mallick, Dr. Thiruvengadam Vijayabaskaran, Dr. Purbasha Sharangi, Dr. Ravi Kumar, Dr. Amar Shrivastava for their support and training me different instruments which I have used in my research. I also thank to Dr. Anupama Swain, Abhisek Mishra, Dr. Sagarika Nayak, Dr. Koustuv Roy and Kshitij Singh Rathore for helping me with the experiments and lot of discussion during the research. I take the opportunity to thank my friends and colleagues Brindaban Ojha, Esita Pandey, Shaktiranjana Mohanty, Dr. Bibhuti Bhushan, Dr. Antarjami Sahoo, Dr. Palash Manna, Azhar, Bhuvneshwari, Swayang, Biswajit, Aditya, Akilan, Santosh, Bijaylaxmi and all my lab members and juniors (from Ph.D. and M.Sc.) for giving their unconditional support during academic and non-academic work.

I also thank Rahul Yadav, Tusharadri Mohapatra, Tapas, Nripesh Kumar, Prashant Khare, Dr. Anupa, Dr. Tanim, Dr. Charanpreet, Rashmi, Sujit, Lipsa, Ranvir, Subhranshu, Priyabrat and other friends for motivating me in my ups and down.

I acknowledge NISER and DAE, Govt. of India, for providing the financial support to carry out the experimental work. I also acknowledge School of Physical Sciences and Centre for Interdisciplinary Sciences, NISER. Further I extend my acknowledgement to UGC for JRF and SRF fellowship during the PhD tenure. I also acknowledge German Academic Exchange Service (DAAD) for providing funds to visit and prepare samples in Germany. I also thank to NFFA Europe facility for providing an opportunity to prepare samples at their end.

Last but not the least, I would like to express my love towards my parents and family for their unconditional love and all type of support toward me and for boosting my confidence for higher

education and research. I am extremely grateful to my brother Mr. Deepak Gupta for his full support, motivation, and his help in all ups and down of my life.

CONTENTS

Content Details	Page No
Summary	i
List of Figures	iii
List of Tables	xi
List of Abbreviations	xii
CHAPTER 1: Introduction and Fundamentals	1-32
1.1 Introduction	1
1.2 Current-induced switching via spin torques	3
1.3 Spin transfer torque	3
1.4 Spin-orbit torque	4
1.5 Magnetization dynamics	7
1.5.1 LLG equation	8
1.6 Ferromagnetic resonance	11
1.6.1 Damping of thin film	14
1.7 Spin current and charge current	15
1.8 Spin-orbit interaction	19
1.8.1 Skew scattering	20
1.8.2 Side-jump scattering	21
1.8.3 Intrinsic Interaction	22
1.9 Spin Hall effect and inverse spin Hall effect	22

1.10 Spin pumping	24
1.11 Exchange bias	26
1.12 LSMO	29
1.12.1 Crystal structure	31
1.12.2 Some potential application of LSMO	32
CHAPTER 2: Experimental Techniques	33-68
2.1 Thin film fabrication techniques	33
2.1.1 Oxygen-assisted molecular beam epitaxy (OMBE)	34
2.1.1.1 Process of OMBE	38
2.1.1.2 Advantages of OMBE	38
2.1.2 Pulsed laser deposition (PLD)	39
2.1.2.1 Pulsed laser deposition setup	41
2.1.2.2 Advantages and disadvantages of PLD	44
2.2 Low energy electron diffraction (LEED)	45
2.3 Reflection high energy electron diffraction (RHEED)	47
2.4 X-ray diffractometer	48
2.4.1 X-ray diffraction (XRD)	49
2.4.2 X-ray reflectivity (XRR)	50
2.4.3 Reciprocal space mapping (RSM)	52
2.5 Transmission electron microscope (TEM))	55
2.5.1 Working of TEM	56
2.5.2 Specimen preparation for TEM	57

2.6 Transport and magnetotransport measurement setup	59
2.7 Superconducting quantum interference device (SQUID)	
magnetometry	60
2.8 Ferromagnetic resonance (FMR) spectrometer	62
2.8.1 Lock-in based FMR	65
2.8.2 Vector network analyser	67
2.8.3 ISHE measurement setup	68
CHAPTER 3: Spin-to-charge conversion study in	70-81
La_{0.67}Sr_{0.33}MnO₃/Pt bilayer samples grown by oxygen-assisted	
molecular beam epitaxy	
CHAPTER 4: Tailoring spin to charge conversion efficiency via	82-94
microwave frequency in La_{0.67}Sr_{0.33}MnO₃/Pt bilayer system	
CHAPTER 5: Spin to charge conversion in	95-109
La_{0.65}Sr_{0.35}MnO₃(FM)/La_{0.2}Sr_{0.8}MnO₃(AFM) bilayer system	
CHAPTER 6: Self-induced inverse spin Hall effect in	110-121
La_{0.67}Sr_{0.33}MnO₃ films	
CHAPTER 7: Exchange bias and vertical shift in	122-145
La_{0.67}Sr_{0.33}MnO₃/SrRuO₃ bilayer system	
CHAPTER 8: Summary and conclusion	146-152
REFERENCES	153-164

Summary

Generation and detection of pure spin current in the Ferromagnetic layer (FM)/ High spin orbit coupling (HS) layer are the key to spintronics devices. Much effort has been made to optimize the FM/HS system for efficient spin-to-charge conversion. There are two essential components in FM/HS systems. First is the choice of the FM layer for various novel magnetic properties, viz. low Gilbert damping constant (α), high saturation magnetization, and large spin polarization. In this context, the popular choice of FM materials is CoFeB, NiFe, and YIG. A low α value is required for its various advantages in spintronics, i.e., faster switching, low power consumption, high frequency operations, etc. The second component consists of the search for alternatives to heavy metals as in the periodic table, HMs are limited. Antiferromagnets (AFM), topological insulators (TI), and 2-dimensional metal dichalcogenides (2DMDs) have shown potential as a suitable replacement for heavy metals. In this thesis work, $\text{La}_{0.67}\text{Sr}_{0.33}\text{MnO}_3$ (LSMO) has been chosen as a FM layer due to its different interesting properties, i.e., high spin polarization, high Curie temperature, robustness in nature, and reasonably low α , etc. For HS material, a different category of the material has been used, i.e., Pt (diamagnetic), SrRuO_3 (SRO)(paramagnetic), and $\text{La}_{0.2}\text{Sr}_{0.8}\text{MnO}_3$ (LSMO(AFM)) (antiferromagnetic).

In the first chapter, the inverse spin Hall effect (ISHE) in oxide-assisted molecular beam epitaxy (OMBE) grown ferromagnetic LSMO/Pt bilayer samples have been investigated. The coexistence of anti-damping (decrease in Gilbert damping constant) and enhanced spin pumping has been observed. In the second chapter, it has been shown that the spin-to-charge conversion efficiency in LSMO/Pt heterostructures can be tailored by varying the microwave frequency. This gives an additional dimension to enhance the spin-to-charge conversion, which is one of the key requirements from the application point of view.

It is desired to explore the alternative of HM, which should have high spin orbit coupling (SOC) and can be grown epitaxially adjacent to epitaxial LSMO films. The third chapter comprises, magnetization dynamics and ISHE in LSMO(FM)/LSMO(AFM) bilayer heterostructures have been investigated. A significant enhancement in spin pumping voltage is observed in bilayer samples in comparison to

LSMO(FM) single layer. Obtained spin Hall angle values for LSMO(AFM) are comparable to Pt values. In the fourth chapter, the self-induced ISHE in PLD-grown epitaxial LSMO films has been explored. When LSMO exhibits FMR, a spin current is generated, which flows in the LSMO itself. The SOC of LSMO films helps convert spin current to charge current. Therefore, a significant self-induced ISHE has been observed in LSMO films.

In the fifth chapter, SRO is used as high SOC material for ISHE studies. LSMO(FM)/SRO bilayer samples have been grown using the pulsed laser deposition (PLD) technique. Structural and magnetic characterization confirms the good quality of grown films. Unfortunately, a significant spin pumping in this bilayer system has not been observed; nevertheless, heterostructures show very interesting interface-dominated magneto transport and exchange bias properties, which have been explored in detail. The magnetotransport of bilayer samples shows the noncollinear chiral spin texture-like behaviour, which may be arising due to the presence of spin glass-like frustration in the LSMO/SRO interface.

List of Figures

1.1: Schematic representation of MRAM (a) '0' and (b) '1' bit depending upon magnetization direction of free and fixed FM layer.

1.2: Schematic of (a) STT and (b) SOT devices. STT provides the same path for the read and write process, while SOT provides a separate path for reading and writing.

1.3: (a) Schematic of the spin-orbital torque system in which a spin current is generated in the high spin-orbit coupling layer HS to apply torque on the magnetization of the ferromagnetic layer (FM). (b) Represent the spin current moments interaction with free layer magnetization.

1.4: Magnetization precession (a) when damping is absent and (b) when damping is present.

1.5: Schematic of (a) pure charge current, (b) spin-polarized current, and (c) pure spin current.

1.6: Schematic of (a) skew scattering, (b) side jump, and (c) intrinsic scattering mechanism.

1.7: Representation of (a) SHE, where charge current gets converted into spin current due to interaction with SOC of HS. (b) Represent the ISHE process where transverse charge current is generated due to spin current due to SOC of HS.

1.8: Spin pumping process in FM/HS bilayer system. The FMR is used to inject spin current in the form of spin angular momentum from FM layer to HS. Due to spin dependent scattering, spin current in HS causes the generation of transverse voltage.

1.9: Schematic of the hysteresis loop of a FM when (a) when there is no EB. After a +ve biasing field H is applied during the cooling, the shift direction of the hysteresis loop will decide the NEB or PEB. (b) NEB: hysteresis shifted towards the -ve field axis, (c) PEB: hysteresis shifted towards the +ve field axis.

1.10: (a) Phase diagram of $\text{La}_{1-x}\text{Sr}_x\text{MnO}_3$. the x-axis is the concentration of Sr. (b) Crystal structure of LSMO.

1.11: Mechanism of SEI and DEI. SEI favours the AFM arrangement, while DEI favours the FM arrangement (this figure is inspired from master thesis of Haifeng Li, Forschungszentrum Juelich).

2.1: (a) Schematic of MBE technique and (b) effusion cell. A set of effusion cells mounted in an MBE system for multilayer or co-deposition. Evaporation materials are kept inside the effusion cells. Heating of effusion cells resulted in evaporation of the material, which gets deposited into the substrate.

2.2: Oxygen-assisted MBE chamber at (a) Forschungszentrum Jülich, Germany, and (b) CNR-IOM Trieste (Italy). These facilities were utilised to prepare LSMO/Pt and LSMO(FM)/LSMO(AFM) bilayer films.

2.3: (a) Schematic of the deposition process in PLD. The pulsed laser falls on the target surface due to this material from the target being ablated and getting deposited on the substrate surface. (b) Schematic diagram of PLD chamber, laser and optics.

2.4: (a) PLD chamber at LNMM, SPS, NISER, Bhubaneswar, and (b) target assembly, where six targets can be mounted simultaneously. The target indexer is mounted to select the particular target during the deposition. This PLD facility has been used to deposit LSMO single layer and LSMO/SRO bilayer films.

2.5: Schematic diagram of the basic experimental arrangement adopted in a low energy electron diffraction (LEED) experiment.

2.6: The simplest RHEED setup includes an electron gun, a sample, and a camera (or fluorescent screen).

2.7: (a) The XRD facility available at SPS, NISER, Bhubaneswar. (b) The schematic of the X-ray diffraction process from the crystal planes.

2.8: Schematic of X-ray reflectivity measurement. If the incident angle θ is less than the θ_c , the total internal reflection occurs.

2.9: A typical XRR spectra for the single-layer film. The period of the oscillations gives information about film thickness, the oscillation amplitude provides information about the density, and from the intensity decay rate, surface or interface roughness can be estimated.

2.10: Reciprocal lattice vector and reciprocal lattice point for a lattice plane.

2.11: Reciprocal space maps of epitaxial bilayer films when (a) there is no strain in the film, (b) when strain is present, and (c) when film planes are tilted at an angle to in reference to substrate planes.

2.12: (a) The TEM facility is available at the Centre for Interdisciplinary Sciences (CIS), NISER, Bhubaneswar. (b) The schematic of ray diagram of the TEM is displayed.

2.13: (a) Thin film specimen, (b) two pieces of sample pasted together using epoxy. (c) A diamond wire saw is used to cut the sample of the required dimension such that it can go inside the brass tube. (d)-(e) Sample was inserted inside the brass tube and the brass tube was filled with epoxy to stick the sample rigidly with the tube. (f)-(g) Using a diamond wire thin disc made from a brass cylinder. (h)-(i) Manual grinding done with the help of polishing paper to thin down the disc. (j) Dimple grinding was done to further reduce the thickness near the centre. (k) Finally, sample is kept inside the PIPS for ion milling.

2.14: (a) Physical properties measurement system (PPMS) and (b) in-house developed room temperature resistivity measurement setup.

2.15: (a) SQUID magnetometry facility (MPMS-3) available at LNMM, SPS, NISER, Bhubaneswar. (b) The schematic of SQUID setup with detection coils.

2.16: (a) Schematic of FMR spectrometer and ISHE measurement setup. (b) Schematic of the Zeeman splitting under the application of the external magnetic field. (c) FMR response with respect to the magnetic field.

2.17: NanOsc Phase FMR set-up available at LNMM, SPS, NISER, Bhubaneswar. The setup has been modified for the ISHE measurements.

2.18: VNA-FMR setup available at LNMM, SPS, NISER, Bhubaneswar.

3.1: (a) LEED (b) RHEED images for sample S1.

3.2: X-ray diffraction pattern measured in θ - 2θ geometry for samples (a) S1 and (b) S3.

3.3: FMR signal for different frequencies for samples (a) S1, (b) S2 and (c) S3.

3.4: (a) f vs H_{res} and (b) ΔH vs f for samples S1, S2 and S3 studied by lock-in based FMR. The solid lines in (a) and (b) are the best fits for equations (3.2) and (3.3), respectively.

3.5: ISHE voltage for samples S2 and S3 are shown in (a) and (b), respectively. Open circles (in blue) are the measured ISHE voltage, and the solid line (in red) represents the best fit of the data fitted by equation (4). Dash (in black) and dot (purple) lines represent the V_{sym} and V_{asym} components, respectively, evaluated by fitting to equation (3.4).

3.6: (a) and (c) Angle dependent V_{sym} for samples S2 and S3, (b) and (d) angle-dependent V_{asym} for samples S2 and S3, Figures (a) and (c) were fitted by using equation (3.5) while Figures (b) and (d) were fitted by using equation (3.6).

3.7: (a) and (b) Power-dependent voltage signal for samples S2 and S3 measured at a $f = 7$ GHz. (c) and (d) show power-dependent V_{sym} and V_{asym} components for samples S2 and S3, respectively.

4.1: X-ray diffraction for sample S2. The XRD measurement has been performed in θ - 2θ geometry.

4.2: TEM image for sample S2, and SAED image for STO/LSMO interface are shown in (a) and (b), respectively.

4.3: FMR spectra for samples (a) S1 and (b) S2. (c) Corresponding measured voltage for sample S2. The numbers shown in the figure are the microwave frequency in GHz. Solid lines in (c) are the best fits to the data using equations (4.1).

4.4: (a)- (i) P_{abs} and their corresponding V_{meas} for different frequencies. The blue circle represents VNA FMR absorption spectra, and the red open square represents the measured voltage. (d) P_{abs} and V_{sym} dependency on f .

4.5: (a) P_{abs} and V_{sym} dependency on f , (b) spin angular momentum to J_s conversion efficiency for sample S2. The solid line represents the fitting to equation (4.2).

4.6: (a)-(f) V_{sym} vs Φ plot for different frequencies. Solid red lines are the best fits to the equation (4.4).

4.7: (a)-(f) V_{asym} vs Φ plot for different frequencies. Solid red lines are the best fits to the equation (4.5).

4.8: V_{sp} and θ_{SHA} vs f for sample S2.

5.1: RHEED pattern taken on the surface of the samples (a) A0 (b) AF20. (c) and (d) shows the RHEED pattern at the interface and on the sample surface for sample A20. (e) The schematic diagram of FMR and ISHE measurement setup.

5.2: (a) X-Ray diffraction data for sample FM-20/AFM-20. XRD has been performed in θ - 2θ geometry.

5.3: (a) The HRTEM image is shown for the sample FM-20AFM-2. The inset shows the zoomed part of interface between FM and AFM layer. (b) The HRTEM images for the sample FM-20/AFM-20. The insets show the zoomed part of the (i) STO substrate, (ii) LSMO (FM) layer and (iii) LSMO(AFM) layer.

5.4: (a) M - T data for (a) A0 and (b) AF20 sample. M - T measurements were performed in zero-field cooling (ZFC) mode. During the measurement, a magnetic field of 100 Oe was applied.

5.5: The presence of exchange bias in the (a) A2, (b) A5 and (c) A20 sample. The exchange bias measurement has been performed at ± 1 T cooling field. These all measurement have been performed at 5 K.

5.6: FMR spectra in the range of 3-16 GHz for samples (a) A0, (b) A2, (c) A5 and (d) A20, respectively.

5.7: FMR spectra with two FMR modes. The higher intensity mode is the uniform ($n=0$) mode, while the mode with lower intensity is the non-uniform mode ($n=0$). The red solid line is the best fit for equation (5.1).

5.8: (a) f vs H_{res} and (b) ΔH vs f for samples A0, A2, A5 and A20. The solid lines in (a) and (b) are the best fits for equations (5.2) and (5.3), respectively.

5.9: Angle-dependent V_{sym} for samples (a) A0, (b) A2 and (c) A5. Solid lines are the best fit the equation (5.5).

6.1: (a) XRD data, (b) zoomed part of (200) peak (c) HRTEM image for SL2 sample.

6.2: XRR measured data and its corresponding best fits of the sample (a) SL1, (b) SL2, and (c) SL3. Open blue circles represent the experimental data and the solid red lines are the best fits to the data.

6.3: M vs T data for SL2 sample. Measurement have been performed in thermoremanent magnetization mode at 100 Oe magnetic field. From the graph T_c value is 320 K.

6.4: FMR signal for different frequencies for samples (a) SL1, (b) SL2, and (c) SL3. Solid lines are the fits using the Lorentzian equation.

6.5: (a) f vs H_{res} plot and (b) ΔH vs f plot for STO/LSMO samples. Solid lines are the best fits for equations (6.1) and (6.2).

6.6: V_{meas} and its different components for SL1. Data is fitted to equation 6.3 to disentangle these symmetric and asymmetric voltage contributions.

6.7: (a) ϕ dependent V_{sym} and (b) V_{asym} for LSMO films. Red and black solid lines are the best fits using equations (4) and (5), respectively.

7.1 (a) Sample structure studied in this chapter. (b) XRD data for the BL2 sample corresponding to (100) and (200) peaks of LSMO and SRO, respectively.

7.2: Asymmetric reciprocal space mapping (RSM) around (103) of STO for BL2 and C1 films.

7.3: HRTEM image for sample BL1. The inset shows the SAED pattern of the STO/LSMO interface.

7.4: M - T data for all the samples under TRM.

7.5: ρ vs T measurement for samples (a) C1, (b) C2, (c) BL1, and (d) BL2, respectively. Measurements were performed in four probe geometry and a 100 μ A DC was supplied during the measurements.

7.6: ρ vs $\ln(T)$ for samples (a) C1, (b) C2, (c) BL1 and (d) BL2, respectively. Data were fitted using equation (7.1). ρ vs T^2 data for sample (e) C1, (f) C2, (g) BL1 and (h) BL2, respectively. The linear fits (red solid lines) indicates that the $\rho(t)$ have linear dependency with T^2 .

7.7: Magnetoresistance curve and their corresponding M-H data at 5 K for samples (a) & (e) C1, (b) & (f) C2, (c) & (g) BL1, and (d) & (h) BL2, respectively. The butterfly shape is arising due to the anisotropy nature of the SRO.

7.8: MR% and their corresponding M-H data at 100 K for samples (a) & (e) C2, (b) & (f) BL1, and (c) & (g) BL2, respectively. The butterfly shape in MR data shrinks due to the loss of anisotropy at the higher temperatures (as T_c of SRO is close to 100 K).

7.9: FMR spectra for samples (a) C1, (b) BL1, and (c) BL2, respectively.

7.10: (a) f vs. H_{res} for C1, BL1, and BL2, Solid line are Kittel fit using equation (2). (b) ΔH vs. f for samples C1, BL1, and BL2, respectively. The solid lines represent the best fit to equation (3). (c) represent the measured voltage for sample BL1 at 0° .

7.11: Introduction to exchange bias. Hysteresis loop 1(a) when there is no EB, (b) when EB is present in the system. FM2 represents hard ferromagnet while FM1 is soft ferromagnet. (c)-(1) at $T > T_{c2}$, FM2 spins will be randomly oriented. in (c)-(2) $T < T_{c2}$ FM2 spins will align in direction of applied H . (c)-(3-7) represent the different orientations of spins during the field sweep.

7.12: Representative cooling field dependent exchange bias at 5 K for (a) sample C2, (b) sample BL1, and (c) sample BL2.

7.13: Dependency of (a) H_{ex} , (b) H_c , and (c) $M_{S_{shift}}$ on H_{CF} for sample BL1 and BL2.

7.14: Temperature-dependent exchange bias measurement for samples (a) BL1 and (b) BL2. All the measurements were performed in presence of a H_{CF} of +1T.

7.15: Temperature dependency of (a) H_{ex} , (b) H_c , and (c) $M_{S_{shift}}$ for sample BL1 and BL2.

7.16: Training effect data for samples (a) C2, (b) BL1, and (c) BL2.

7.17: H_{ex} vs n data obtained from training effect at 5 K for BL1 and BL2 samples.

7.18: Training effect data under 1 T cooling field at 75 K. (a) H_{ex} vs $n^{-1/2}$ experimental data where solid lines are the linear fits. (b) H_{ex} vs n fitted using frozen and rotatable spin relaxation model (c) fitted using modified Binek model and (d) fitted using a model derived from LK theory.

List of Tables

3.1: Sample details studied in this work and their corresponding nomenclature.

3.2: Fitted parameters for samples S2 and S3.

3.3: Comparison of various parameters from the literature for LSMO/Pt bilayers.

4.1: Comparison of various parameters at different frequencies for S2. Here V_{sp} and V_{AHE} have been obtained by fitting equations (4) and (5) to Fig.4.6 (a)-(f) and Fig.4.7 (a)-(f), respectively. Similarly, θ_{SHA} and J_s have been calculated using equations 4.7 and 4.8, respectively.

5.1: Sample structure and their name.

5.2: V_{sp} and V_{AHE} and obtained from fitting of equations (5.5), (5.6). $g_{eff}^{\uparrow\downarrow}$ calculated using equation (5.10).

6.1: XRR fitting parameters obtained from the Fig.6.2 (using GenX software).

6.2: V_{sp} and V_{AHE} values for all samples from the fitting of the data shown in Fig.6.6 (a) and (b) using equations (4) and (5). V_{AMR} values were calculated using equation (6).

7.1: Parameters obtained from H_{ex} vs n data fitting using equation (7.6)

List of Abbreviations

α	Gilbert damping
AFM	Antiferromagnetic materials.
AHE	Anomalous Hall effect
AMR	Anisotropic magneto-resistance
CPW	Coplanar wave-guide
ΔH	Linewidth broadening
ΔH_0	Inhomogeneous broadening
EDX	Energy dispersive x-ray
f	Microwave frequency
FM	Ferromagnet
FMR	Ferromagnetic resonance
g	Lande-factor
γ	Gyromagnetic ratio
GIXRD	Grazing incident angle x-ray diffraction
GMR	Giant magnetoresistance
$g_{eff}^{\uparrow\downarrow}$	Effective spin mixing conductance
$g_r^{\uparrow\downarrow}$	Real part of spin mixing conductance
H_{dc}	DC magnetic field
H_{eff}	Effective magnetic field
H_k	Anisotropic field
H_{res}	Resonance field
HM	Heavy metals
HS	High spin orbit coupling material
h_{rf}	Radio frequency field
HRTEM	High resolution transmission electron microscope
I_{eddy}	Eddy current
I_S	Spin current
ISHE	Inverse spin Hall effect

J_{ex}	Exchange coupling
J_c	Charge current density
j_s	Spin current density
LLG	Landau-Lifshitz-Gilbert
m	Magnetic moment
M	Magnetization
M_{eff}	Effective magnetization
MRAM	Magnetic random access memory
m_s	Magnetic quantum number
M_S	Saturation magnetization
RHEED	Reflection high energy electron diffraction
σ	Conductivity
SHE	Spin Hall effect
SOC	Spin orbit coupling
SOT	Spin orbital torque
SQUID	Superconducting quantum interference device
TEM	Transmission electron microscope
θ_{SHA}	Spin Hall angle
TMS	Two-magnon scattering
V_{AHE}	Voltage due to anomalous Hall effect
V_{AMR}	Voltage due to anisotropic magnetoresistance
V_{ISHE}	ISHE voltage
V_{meas}	Measured voltage
V_{sp}	Spin pumping voltage
V_{sym}	Symmetric component of measured ISHE voltage
V_{asym}	Asymmetric component of measured ISHE voltage
XRD	X-ray diffraction
XRR	X-ray reflectivity

CHAPTER 1: Introduction and Fundamentals

1.1 Introduction:

The integrated circuit (IC) industry has extensively investigated complementary metal oxide semiconductor (CMOS) technology. This CMOS technology has been used to read, write, and transmit information into memory devices. Due to the advancement in technology, now individual IC dimensions have been shrunk down to less than 5 nm. Further reducing the dimension in current CMOS technology is very difficult due to fundamental limits such as heating effects, power consumption, etc. Looking at the expansion of technology, the requirement for high-density, portable, energy-efficient memory devices is increasing day by day. Artificial intelligence, auto transportation, robotics, and bioinformatics are some fields that require lightning-fast, portable, and small-scale devices. Hence to switch to the alternative of CMOS technology seems to be a viable option and is in high demand.

Till this time, a lot of prototypes of the spintronics devices have been developed, though magnetic random access memory (MRAM) is proven to be the most useful technology. MRAM utilizes the magnetic tunnel junction (MTJ) as the main component [1–3]. Two FM layers separated by a thin non-magnetic spacer layer is the key component of MTJ devices. In MTJ, one of the FM layers is the reference layer i.e., the magnetization of this layer is fixed and requires high energy to change its magnetization. While the other FM is a free layer such that the magnetization of this layer can be switched by applying a small amount of energy. This energy can be in the form of electrical or magnetic. Depending on the easy axis direction, MTJ devices can be divided into two sub-categories, one is in-plane MTJ, and the other is out-of-plane or perpendicular MTJ.

When a current passes through the FM layer, the current gets polarized in the direction of magnetization of the fixed layer due to the spin-filtering effect of FM materials. In MTJ devices, the current should tunnel from one FM layer (FM1) to another FM layer (FM2) via an oxide spacer

layer. Once the filtered spin-polarized current enters to FM2 layer, which is a free layer, the spin magnetic moments of electrons apply a torque to the magnetization of FM2. Hence the magnetization of FM1 and FM2 can be aligned in parallel or antiparallel orientations. The tunnelling of an electron from FM1 to FM2 depends on the available state of spins. Hence the probability of electron scattering is less if both the FM are parallelly aligned; this will be a low resistive state. While a scattering of the electron is more probable if both the FM are anti-parallelly aligned, and this will be considered as a high resistive state. The difference in resistance of both states is called tunnelling magnetoresistance (TMR) and can be calculated as

$$TMR = \frac{\Delta R}{R_P} = \frac{R_{AP} - R_P}{R_P} \quad 1.1$$

Where, R_{AP} and R_P are the resistance when the magnetization of both FMs are in the anti-parallel and parallel states, respectively. These states can be achieved by applying an external magnetic field or by applying a sufficient current which causes to switch the magnetization of the free layer. The data is stored in the form of a binary digit (1 and 0) in parallel or anti-parallel states in MRAM devices, as shown in Fig.1.1(a) and (b). In the reading and writing process these different resistive states are used as two different memory states to store the data in binary (0 or 1) form. Therefore, MRAM devices work in a resistance-based mechanism, and the application of a magnetic field or electric current can control the reading and writing in such devices.

Spintronics devices require cost-effective and energy-efficient methods to store and read the data in them. Electric current-based magnetization switching can give a pathway in this regard. Hence this method has attracted a lot of attention from researchers.

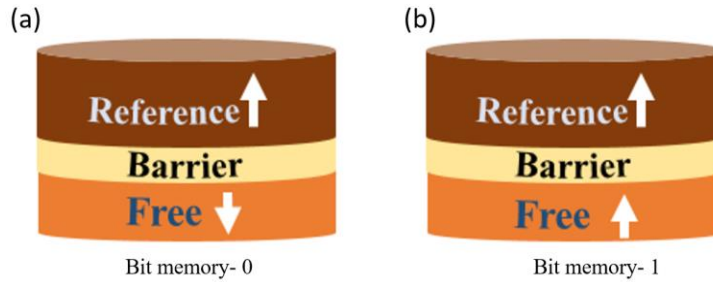


Figure 1.1 Schematic representation of MRAM (a) ‘0’ and (b) ‘1’ bit depending upon magnetization direction of free and fixed FM layers.

1.2 Current-induced switching via spin torques

In MRAM devices, the polarized current is used to switch the magnetization of FM. Spin-polarized currents transfer their spin angular momentum to the magnetization of the FM2. The magnetization of FM2 is reoriented due to the realization of torque from spins. This spin torque can be of two types, the first is spin transfer torque (STT), and the second is spin-orbit torque (SOT). STT happens when current passes through MTJs, while SOT happens from a high SOC material. This SOC of materials provides the channel for the spin Hall effect. STT and SOT are described in detail below.

1.3 Spin transfer torque (STT)

Berger investigated the first current-induced domain wall motion in 1978 [4]. Slonczewski and Berger have also predicted that STT can be investigated in thin film multilayer, where the magnetization of the free layer (FM2) can be switched by the application of current [5,6]. The experimental realization of the above concept has been made first in MTJs devices [7,8] and further led to the development of STT-MRAM devices [9–12]. STT was observed due to the spin-filtering effect of the FM layer. In a MTJ device, when current passes through a fixed layer (FM1),

the current becomes spin-polarized in the direction of magnetization of FM1. This spin-polarized current goes to the free layer (FM2). It transfers its spin angular momentum to FM2 until the magnetization of the free layer switches in the direction of spin polarization direction. Therefore, the magnetization of the free layer reorients parallel to fixed layer magnetization. If the current direction is reversed, then the magnetization direction of the free layer is forced to be anti-parallelly aligned with respect to the fixed layer. Hence, by changing the current polarity, one can achieve parallel or anti-parallel alignments, which correspond to low and high resistive states.

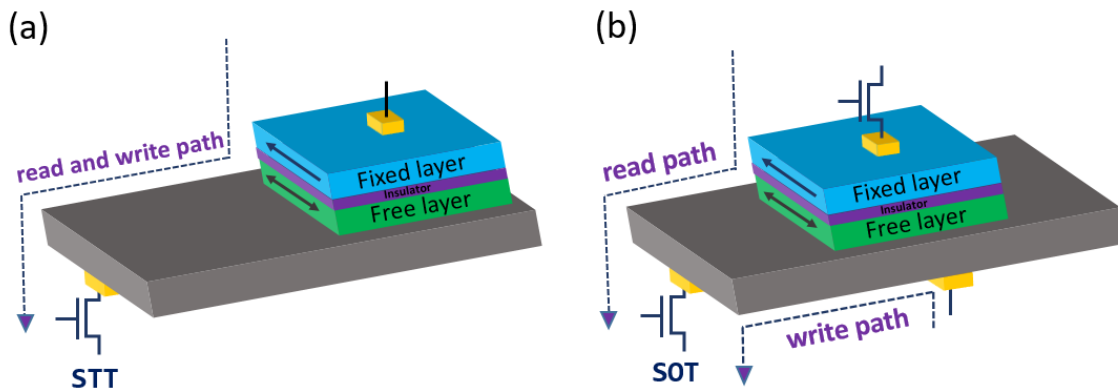


Figure 1.2 Schematic of (a) STT and (b) SOT devices. STT provides the same path for the read and write processes, while SOT provides separate paths for reading and writing.

1.4 Spin-orbit torque (SOT)

STT has shown its tremendous application and advantages over conventional memory devices [13,14]. Still, there are some limitations and challenges for STT-based devices, i.e., they require high current density to switch the magnetization, which is essential for writing the data. The second important limitation comes due to the same read-and-write path as shown in Fig.1.2 (a). Writing requires higher current density, while reading requires comparatively lower current. As both processes are performed by the same path, it can degrade the device's endurance and

reduce reliability. Due to same path for reading and writing it is difficult to maintain the enough margin for data disturbance during reading. The third important drawback of STT devices is that they are slow, as initial switching requires a large incubation time [15]. Therefore, an alternate method is required to overcome the issues realized in STT.

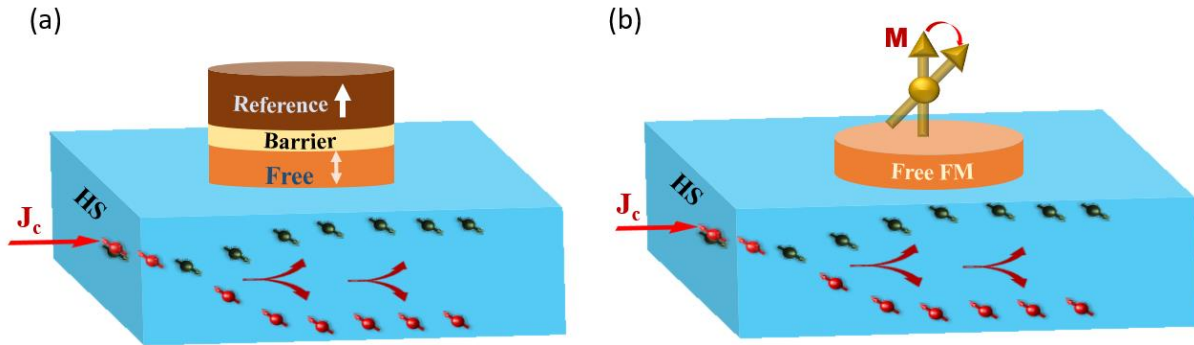


Figure 1.3 (a) Schematic of the spin-orbit torque system in which a spin current is generated in the high spin-orbit coupling layer (HS) to apply torque on the magnetization of the ferromagnetic layer (FM). (b) Schematic of interactions of the spin current with free layer magnetization.

The spin-orbit torque (SOT) gives a way to handle the issues discussed above. SOT is realized in FM/HS bilayer system, where HS is a material with high spin-orbit coupling. When current is passed through HS, the SOC of HS causes the deflection of opposite spins (as shown in Fig.1.3 (a)) in opposite directions due to different spin-dependent scattering mechanisms i.e., skew scattering, side jump, etc. [16,17]. These scattering mechanisms have been described in the later part of this thesis. This process is known as the spin Hall effect (SHE) [18]. The scattering of spins gives non-equilibrium spin accumulation which gives rise to spin current. This spin current gets injected into the adjacent FM layer and applies a torque to the magnetization of FM, as shown in

Fig.1.3 (b). This is SOT and causes to switch the magnetization of the FM layer. If the current direction is reversed, the polarized spin direction also gets reversed. Hence, the magnetization of FM is switched to the opposite direction. Recently, this SOT writing mechanism has been applied in three-terminal MTJs devices. The structure of a three terminal MTJ is shown in Fig.1.3 (a), which is an MTJ placed on top of HS material. The current passed through HS will generate a spin current which will be injected in MTJs, and the magnetization of the free layer will be reoriented parallel or anti-parallel depending on current polarity. In SOT-MRAM, for reading and writing, two separate paths are defined (as shown in Fig.1.2 (b)), and a small current is required for reading. Hence, the endurance of these devices increases. SOT-MRAM also has the potential to write with lower power than STT-MRAM as the writing path independently can be optimized by choosing highly spin-to-charge conversion-efficient materials [19–21]. SOT switching also overcomes incubation delay as SOT switching is much faster than STT switching. In contrast to STT, since SOT is governed by, SHE, the torque produced by SHE results in direct switching since there is no opposing torque. As a result, SOT can alter magnetization faster than STT, enabling MRAM to operate fast and effectively [22–24]. Therefore, it can be said that SOT-based memory devices are probably the future of data storage technology.

Hence, the search for such FMs, which can be used as an efficient spin current generation and materials with high SOC, which can provide an efficient spin Hall channel, has attracted the researcher's attention. The most studied FMs in regard are which show low Gilbert damping constant i.e., $\text{Y}_3\text{Fe}_5\text{O}_{12}$ (YIG), NiFe (called as permalloy), CoFeB, etc. In this thesis, we have explored manganite, particularly $\text{La}_{0.67}\text{Sr}_{0.33}\text{MnO}_3$ (LSMO), as a FM, which is an interesting class of FMs and has advantages due to its advanced properties such as half-metallicity, high spin polarization, high Curie temperature, etc. Looking towards the HS materials, we have investigated spin to charge conversion efficiency in a different class of materials which are supposed to exhibit

high SOC. In this thesis, first, we have used Pt to understand the properties of LSMO, as Pt is well-understood material for such studies. Further, we have explored the other class of oxides, such as antiferromagnets (AFM) and low-temperature ferromagnets, which are paramagnetic at room temperature. We have chosen $\text{La}_{0.2}\text{Sr}_{0.8}\text{MnO}_3$ as AFM and SrRuO_3 as their lattice constants match with the lattice constant of $\text{La}_{0.67}\text{Sr}_{0.33}\text{MnO}_3$. Hence it is possible to grow epitaxial heterostructures and study them.

In this thesis, chapter 1 is dedicated to the introduction and fundamental concepts which are essential to understand the thesis work. Chapter 2, describes all the experimental techniques which have been used throughout the thesis work. Chapter 3 explores the LSMO/Pt bilayer for spin-to-charge conversion. In chapter 4, we have shown that microwave frequency can be used to tune the spin-to-charge conversion efficiency in LSMO/Pt bilayer system. In chapter 5, LSMO(FM)/LSMO(AFM) heterostructures have been explored for spin-to-charge conversion. Chapter 6, shows that the intrinsic SOC of LSMO can also be used for the generation and detection of spin current. In chapter 7, we studied the LSMO/SRO bilayer for spin-to-charge conversion. Though we have not observed significant ISHE in these bilayer samples, a very interesting interface phenomenon of exchange bias has been observed, which has been explored in detail. Finally, we have summarized our results and the future outlook has been discussed.

1.5 Magnetization dynamics:

A fundamental method for investigating the dynamical characteristics of magnetic materials is ferromagnetic resonance (FMR) [25]. Griffiths (1946) developed this ferromagnetic resonance technique, and Charles Kittel (1947) came up with its underlying theory [26]. FMR has been widely used in various projects, i.e., determining the magnetic anisotropy constant, Lande-g-factor, and the interfacial magnetic coupling of films and multilayers [27]. By examining the

linewidth (ΔH) of the absorption spectra, the FMR spectroscopic approach can offer details on the magnetic relaxation process of the spins [28].

1.5.1 LLG equation:

If a magnetic dipole moment μ experiences a torque in a magnetic field, H , the equation of motion can be written as [29,30]

$$\frac{d\mu}{dt} = -\gamma(\mu \times H_0) \quad 1.2$$

$$\frac{dM}{dt} = -\gamma(M \times H_{eff}) \quad 1.3$$

where $\gamma(= \frac{g\mu_b}{\hbar})$ is the gyromagnetic ratio having unit $\text{rad}\cdot\text{sec}^{-1}\text{T}^{-1}$.

In 1935, Landau-Lifshitz (LL) proposed the equation of the ferromagnetic spin chain, also known as the Landau-Lifshitz (LL) equation, while investigating the dispersive theory of magnetization of ferromagnets. This LL equation classically explains the rate of variation of magnetization as a function of time and space when an effective local field, H_{eff} , is applied. At the same time, the effect of the damping term has also been considered [30]. The LL equation is given as

$$\frac{dM}{dt} = -\gamma[M \times \mu_0 H_{eff}] - \frac{\lambda}{M_s^2} [M \times (M \times \mu_0 H_{eff})] \quad 1.4$$

where λ is the phenomenological damping term. The first term in the LL equation describes the torque on the magnetization vector due to the effective field, H_{eff} . The last term refers to the damping torque, which causes the magnetization vector to be reoriented towards the effective field. The schematics of precession spins in a FM in the absence or presence of damping are shown in Fig.1.4 (a) and (b), respectively. The evolution of the magnetic field due to spins of ferromagnets, as well as the precession of the magnetization in an effective field, both are described by the LL

equation [31,32]. Gilbert modified the Landau-Lifshitz (LL) equation in 1954 based on the concept of the Lagrangian, and this equation is now known as the Landau-Lifshitz-Gilbert (LLG) equation [30]. The LLG equation can be written as [33–37]

$$\frac{dM}{dt} = -\gamma[M \times H_{eff}] + \frac{G}{\gamma M_s^2} [M \times \frac{dM}{dt}] \quad 1.5$$

Where $\alpha = \frac{G}{\gamma M_s}$ is the Gilbert damping constant. G is a relaxation rate per second [36]. Hence, the above equation can be modified as

$$\frac{dM}{dt} = -\gamma[M \times H_{eff}] + \frac{\alpha}{M_s} [M \times \frac{dM}{dt}] \quad 1.6$$

The first term in the LLG equation is the precessional torque, while the second is the Gilbert damping torque [28,34,35,38]. In the limit of small damping, $\frac{G}{\gamma M_s} \ll 1$, LLG relaxation torque, and LL relaxation terms are equivalent. It can be seen from Eq. (1.4) and Eq. (1.6) that the precession term in the LL equation, $M \times \mu_0 H_{eff}$ is replaced by time-dependent Magnetization ($\frac{dM}{dt}$) term in the LLG equation.

The incoherent scattering of electron-hole pair excitations by phonons and magnons results in the Gilbert damping coefficient G in metals. Either a spin flip or a spin holds during the electron-hole pair excitations is present. Itinerant electrons and magnons engage in an exchange process that results in spin-flip excitations (s-d exchange interaction [39]). Because of the spin-orbit interaction, which causes a dynamic redistribution of electrons in the electron momentum space, non-spin-flip excitations are produced [40].

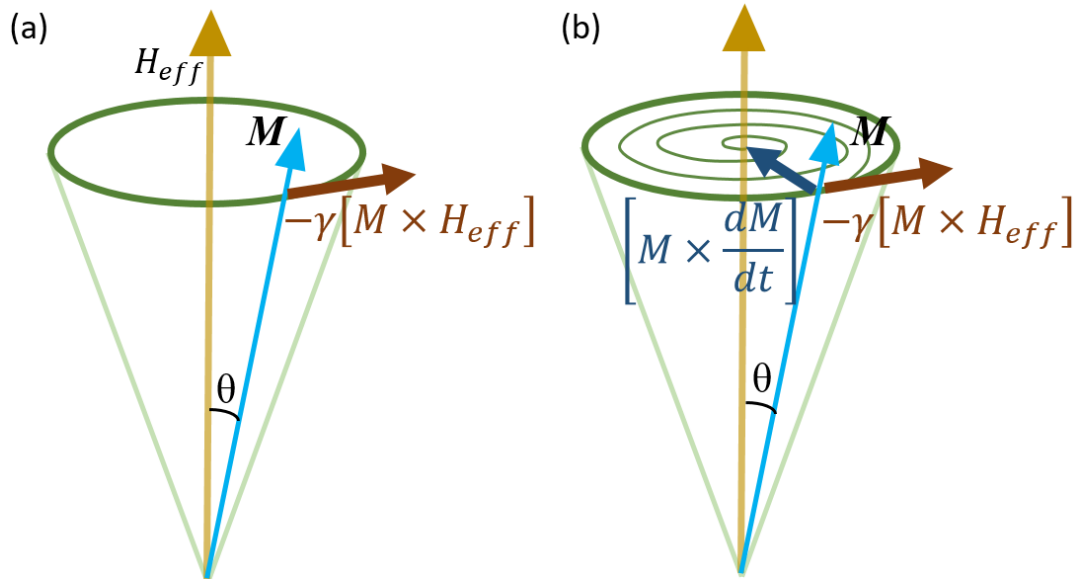


Figure 1.4 Magnetization precession (a) when damping is absent and (b) when damping is present.

A connection between the LLG equation and other physical systems, such as the motion of a vortex filament and the motion of curves and surfaces, has also been demonstrated [30]. Gilbert damping constant and switching speed for bits of information are closely correlated in the field of magnetic devices, including MRAM. A ferromagnetic grain's magnetization direction and the energy requirements for switching are used to encode this information [41]. More research on the Gilbert damping processes, particularly in the metallic ferromagnets, can result in better achievement in creating new materials for various applications [41]. The LLG equation can accurately represent the key aspects of the dynamics of magnetization that take place in condensed matter systems. However, many issues still need to be resolved [37].

1.6 Ferromagnetic resonance (FMR)

FMR is a technique used to investigate the magnetic characteristics of magnetic thin films [33,42]. C. Kittel (1947) [26] developed the theory for ferromagnetic resonance classically. In a typical FMR experiment, a FM material is microwave-irradiated in an applied field, which is swept at a fixed frequency [28,35,43]. To detect precession in FMR, high-frequency (in the GHz range) radiation should interact with the sample, and the resulting wavelength must be longer than the sample size. The resonance phenomena can be characterized by applying a macroscopic equation of motion to the magnetization, M , generated by the magnetic moments μ in the sample [44]. The M can be expressed as [45]

$$M = \frac{\mu}{V_0} \quad 1.7$$

where μ and V_0 are the magnetic moments per atom and atomic volume, respectively. The M is considered homogeneous across the sample for a single-domain magnetic film whose thickness is below the ultrathin film limit [44] which is less than the radio frequency (*rf*) skin depth and exchange length [33]. Skin depth is defined as

$$\delta = \frac{c}{\sqrt{2\pi\mu\omega\sigma}} \quad 1.8$$

and the exchange length can be denoted as the following

$$d_{ex} = \frac{A}{\sqrt{2\pi M_s^2}} \quad 1.9$$

At normal temperature, the typical skin depth and exchange length for bulk bcc Fe (001) are 6×10^{-5} cm and 3×10^{-7} cm, respectively, while the atomic planes of bcc Fe (001) film are separated by

1.425×10^{-8} cm. [56]. This satisfies the ultrathin film limit. The exchange length in most practical FM materials is typically in the 2-5 nm range [46].

In FMR spectrometers, the two important parameters measured are microwave power P_m absorbed by the sample as a function of the applied dc magnetic field, H . In contrast, another quantity is the absorption derivative with respect to the field, H [45]. The P_m is related to the component of the dynamic susceptibility in the direction of the microwave, h_0 [45,47]. The susceptibility can be denoted as [47]

$$\chi = \chi' - i\chi'' \quad 1.10$$

The real part of the susceptibility χ' denotes the dispersive process, while the imaginary part, χ'' , denotes the dissipation process [47,48]. Eddy currents are the main cause of dissipation for conductive samples. Hence, P_m can be written as [33,45,47]

$$P_m = \frac{1}{2} \omega \text{Im}[\chi_y] h_0^2 \quad 1.11$$

This is the energy delivered from the microwave to the sample [47]. The dissipation of this type of energy is typically converted to heat as a result of lattice vibration [47]. The magnetic susceptibility linked to the rf -magnetic field can be written as [26]

$$\chi_{rf} = \frac{M_x}{H_{rf}} = \frac{\chi_H}{1 - \frac{\omega^2}{\omega_0^2}} \quad 1.12$$

where $\chi_H = M_y/H$. At $\omega = \omega_0$, The magnetic susceptibility is maximum, where ω and ω_0 are the frequencies of the rf magnetic field and magnetization precession, respectively [26]. Hence when $\text{Im}[\chi_y]$ is maximum, FMR occurs, which is corresponding to the maximum power absorbed by the sample [33,45].

In an FMR experiment, resonance can be achieved in two ways; the first is keeping the microwave frequency ω fixed and sweeping the external dc field. In a second way, one can fix the dc magnetic field and sweep the microwave frequency. If H_0 is the resonance field, the real part of H_{FMR} can be expressed as the following equation (in parallel configuration) [45]

$$\frac{\omega^2}{\gamma^2} = [H_{FMR} + 4\pi M_{eff} + \frac{K_1^{eff}}{2M_s} (3 + \cos 4\theta) + \frac{i\omega G}{\gamma^2 M_s}] \times [H_{FMR} + \frac{K_1^{eff}}{2M_s} \cos 4\theta + \frac{i\omega G}{\gamma^2 M_s}] \quad 1.13$$

Where θ is the angle between the field and the crystal axis. While in the case of the perpendicular condition, the resonance condition can be written as [45]

$$\frac{\omega}{\gamma} = H_{FMR} - 4\pi M_{eff} + \frac{2K_1^{eff}}{M_s} \quad 1.14$$

The above equations are valid only when the applied magnetic field is high enough to align the moment parallel to the external dc field, H_0 [45]. If a static external field magnetizes a thin magnetic film with in-plane uniaxial anisotropy to saturation along the easy axis, the Kittel equation for FMR can be expressed as

$$\omega = \gamma\mu_0 \sqrt{(H_{ext} + H_K)(H_{ext} + H_K + M_s)} \quad 1.15$$

If the saturation magnetization is ignored in Eq. (1.15), i.e., saturation magnetization, $M_s = 0$, we observe that Eq. (2.1.44) simplifies to

$$\omega = \gamma\mu_0 (H_{ext} + H_K) \quad 1.16$$

This equation (2.1.45) agrees with the experimentally measured frequency for lower modes [49,50]. Simplifying the equation (1.15), assuming saturation magnetization is non-zero, the Kittel FMR resonance expression can be given as

$$\omega = \gamma\mu_0\sqrt{H_{ext}^2 + H_k^2 + 2H_kH_{ext} + M_s(H_K + H_{ext})} \quad 1.17$$

Considering only the second-order terms (quadratic terms of H_{ext} and H_k) in this equation, we can write it as

$$\omega = \gamma\mu_0\sqrt{H_{ext}^2 + H_k^2} \quad 1.18$$

This is also consistent with the fact that resonance at higher modes is quadratically positioned as a function of the applied field [49]. The frequency of the ferromagnetic resonance can change depending on several parameters. Shape anisotropy and magnetocrystalline anisotropy are two of these factors [46]. This is true in the case of shape anisotropy since various geometrical samples have a varied demagnetizing factor [46].

1.6.1 Damping of thin film

In thin films by measuring the peak-to-peak FMR linewidth (ΔH_{pp}), one can experimentally estimate the α [37,51]. Due to the slight mismatch of lattice constant between substrate and material deposited, there will be a strain in the lattice of thin film, which causes larger damping compared to relaxed films. Hence, it has been demonstrated that the α in thin films is larger than its bulk material [37,52].

The LLG equation Phenomenologically describes magnetic relaxation in metallic FM films [53]. The second component on the right hand of the equation describes the damping term (1.6). It is obvious from Eq. (1.6) that damping can arise when the magnetization is time-dependent. FMR linewidth ΔH_{pp} can be predicted using the LLG equation on a FM thin film that is magnetized in the plane or perpendicular to the plane [35]. The ΔH_{pp} is related to the magnetic damping parameter, α , by

$$\Delta H_{pp} = \frac{2}{\sqrt{3}} \alpha \frac{\omega}{\gamma} \quad 1.19$$

The ΔH_{pp} is directly related to the microwave frequency ω and has an inverse relation with M_s . These are the intrinsic contribution to linewidth [28]. However, an extra frequency-independent component to the linewidth, known as the inhomogeneous contribution, has been identified through experimental observation [28]. This extra contribution to the FMR linewidth arises from a disorder in the sample [28]. Both above linewidths contributions arise due to the combined effect of SOC and exchange interaction [37]. This contribution to linewidth can be separated using the following equation [37,53]

$$\Delta H_{pp} = \Delta H_{inhomo} + \Delta H_{homo} = \Delta H_{inhomo} + \frac{2}{\sqrt{3}} \alpha \frac{\omega}{\gamma} \quad 1.20$$

Some mechanisms can contribute to the ΔH_{pp} . These are the intrinsic Gilbert damping ($\alpha_{intrinsic}$), the broadening induced, which occurs due to the magnetic proximity effect, and the extrinsic magnetic relaxation, etc. [37].

1.7 Spin current and charge current:

Electrons have two essential properties; the first is the elementary charge, and the second is spin. The spin of electrons is studied in the form of spin angular momentum (S). Spin angular momentum is a quantum mechanical entity and can be given as [54]

$$S = \frac{\hbar}{2} \sigma \quad 1.21$$

where \hbar is reduced Planck's constant and σ is the Pauli spin matrices vector. Pauli matrices can be written as

$$\sigma_x = \begin{pmatrix} 0 & 1 \\ 1 & 0 \end{pmatrix}, \quad \sigma_y = \begin{pmatrix} 0 & -i \\ i & 0 \end{pmatrix}, \quad \sigma_z = \begin{pmatrix} 1 & 0 \\ 0 & -1 \end{pmatrix} \quad 1.22$$

Considering the two states of spins, “spin up” ($|\uparrow\rangle$) and “spin down” ($|\downarrow\rangle$), the wave function can be given by the following equation [55]

$$|\psi\rangle = a|\uparrow\rangle + b|\downarrow\rangle \equiv \begin{pmatrix} a \\ b \end{pmatrix} \quad 1.23$$

where complex numbers a and b can be normalized as $|a|^2 + |b|^2 = 1$, and $|\uparrow\rangle$ and $|\downarrow\rangle$ are the two eigenstates of S which correspond to the eigenvalues $\pm\hbar/2$, respectively. The magnetic moment of the electron is a direct result of its spin and can be represented as [56]

$$\mu = -g\mu_B \frac{S}{\hbar} \quad 1.24$$

where $\mu_B (= \frac{e\hbar}{2m})$ is Bohr magneton and g is the electron Lande-g-factor. Using the normalization $a^2 + b^2 = n_\uparrow + n_\downarrow = n$ where n_\uparrow and n_\downarrow denote the classic carrier densities for spin-up and spin-down electrons, and n is the total carrier density. Let us consider the charge operator" $Q = -e\mathbb{1}_2$ and the spin operator S for an electron. The charge density (ρ_c) and the spin density ($\rho_{s,\hat{s}}$) for spins with a quantization axis along \hat{s} can be written as [57,58].

$$\rho_c = \langle\psi|Q|\psi\rangle, \quad 1.25$$

$$\rho_{s,\hat{s}} = \hat{s} \cdot \langle\psi|S|\psi\rangle \quad 1.26$$

Now inserting ψ in the above equation while choosing, without loss of generality, $\hat{s} = (0, 0, 1)$ gives

$$\rho_c(x) = -e\langle\psi|\psi\rangle = -e(a^2 + b^2) = -e(n_\uparrow + n_\downarrow) \quad 1.27$$

$$\rho_{s,\hat{s}}(x) = \hat{s} \cdot \langle\psi|S|\psi\rangle = \frac{\hbar}{2}a^2 - \frac{\hbar}{2}b^2 = \frac{\hbar}{2}(n_\uparrow - n_\downarrow) \quad 1.28$$

If carrier velocity is v , then the product of $\rho_{s,\delta}$ with v gives spin current density ($J_s = \rho_{s,\delta}v$). This is similar to charge current density ($J_c = \rho_c v$) [23]. Putting the calculated densities values from the above equation and using the charge current densities for the two different carrier species $J_\uparrow = -en_\uparrow v_\uparrow$ and $J_\downarrow = -en_\downarrow v_\downarrow$ give the J_c and J_s as

$$J_c = J_\uparrow + J_\downarrow \quad 1. 29$$

$$J_s = -\frac{\hbar}{2e}(J_\uparrow - J_\downarrow) \quad 1. 30$$

Thus, J_c is given by adding the current densities of the J_\uparrow and J_\downarrow , whereas J_s is given by their difference. The unit J_s is given as $A/m^2 \cdot \hbar/e$, whereas units for J_c, J_\uparrow and J_\downarrow are given in terms of A/m^2 . It should be noted that a separate treatment of the two spin states ($|\uparrow\rangle$ and $|\downarrow\rangle$) is only considered if the spin-flip time is sufficiently larger than the momentum relaxation time ($\tau_{sf} \gg \tau_t$) [59,60]. From the above equations, three conditions can arise, which are shown in Fig.1.5. Fig.1.5 (a) shows the situation when only charge current flows. This is a case for the normal metal or paramagnetic conductors where the density of both spin states J_\uparrow and J_\downarrow are considered to be equal. While in the case of metallic FM, spin density for one type of spin is large (here $J_\uparrow > J_\downarrow$), then, along with the charge current, a spin current is also transported, which is shown in Fig.1.5 (b). In the third case, which belongs to the material with high SOC, even spin densities for both types of spins are equal; the opposite spin travel opposite to each other (i.e., $J_\uparrow = -J_\downarrow$), and hence net charge current get cancelled, and a pure spin current is transported, which is shown in Fig.1.5 (c). This transportation of pure spin current is known as the flow of spin angular momentum.

Generally, the difference in electrochemical potential between the two points causes the transport of electrons in a diffusive channel. In this condition, a force ($F = -\nabla\mu_{\uparrow(\downarrow)}$) is experienced by an electron, where the spin-dependent electrochemical potential is defined as

$$\mu_{\uparrow(\downarrow)} = \mu_{ch\uparrow(\downarrow)} - e\phi \quad 1.31$$

The above equation consists of spin-dependent chemical potential $\mu_{ch\uparrow(\downarrow)}$ and a spin-independent electric potential ϕ . For a small deviation from equilibrium, $\mu_{ch\uparrow(\downarrow)}$ can be given as

$$\mu_{ch\uparrow(\downarrow)} = n_{\uparrow(\downarrow)}/\mathcal{N}_{\uparrow(\downarrow)} \quad 1.32$$

where $\mathcal{N}_{\uparrow(\downarrow)}$ is the spin-dependent density of states at the Fermi energy. Hence, it can be concluded that electron transportation can be governed by either a spatial variation of spin-dependent chemical potential or due by an electric field ($E = -\nabla\phi$). The former process is a diffusive process and occurs due to a gradient in spin current density. The latter process is known as drift and occurs due to the electro potential of electrons. The resulting current densities are given by [61,62]

$$J_{\uparrow(\downarrow)} = \frac{\sigma_{\uparrow(\downarrow)}}{e} \nabla\mu_{\uparrow(\downarrow)} \quad 1.33$$

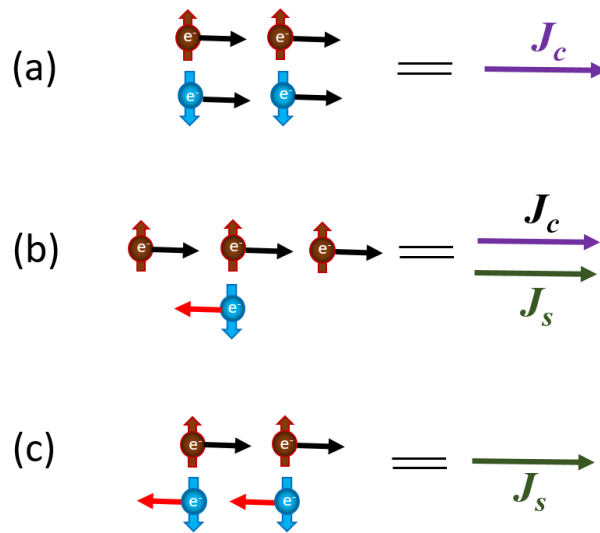


Figure 1.5 Schematic of (a) pure charge current, (b) spin-polarized current, and (c) pure spin current.

The spin accumulation can be defined as the difference between the electrochemical potential of J_{\uparrow} and J_{\downarrow}

$$\mu_s = \mu_{\uparrow} - \mu_{\downarrow} \quad 1.34$$

and the spin current density can be written in terms of electrochemical potential as

$$J_s = -\frac{\hbar}{2e^2} \nabla \mu_s \quad 1.35$$

Therefore, J_s arises from a gradient in the spin accumulation. It's interesting to note that pure spin currents are anticipated to dissipate less, which suggests that they are not always connected to process that generate heat [63,64]. In contrast to conventional currents, spin currents are said to be invariant during time reversal, which is the basis for this prediction. Since it might be possible to decouple energy and information transit from heating, the prediction that spin currents dissipate less has garnered considerable interest. However, whether pure spin currents are dissipation less is a matter of debate and has yet to be experimentally verified.

1.8 Spin-orbit interaction (SOI):

Microscopically, J_s and J_c both are related to each other via spin-orbit interaction (SOI). This SOI is the interaction of an electron's "spin" motion with its "orbital" motion. SOI of metal is the main driving force for spin-to-charge interconversion. Besides this, SOI also plays a main role in spin relaxation. If an electron having a velocity v , moves in an external field E , the magnetic field experienced by the electron can be given as [64]

$$B = \frac{1}{c^2} E \times v \quad 1.36$$

Here c is the speed of light. Since B is perpendicular to E and v , it is parallel to the electron's orbital angular momentum L . Considering this, Hamiltonian for SOI of an electron in a lattice potential can be written as [65]

$$H_{SOI} = -\frac{\hbar}{4m^2c^2} \sigma \cdot (p \times \nabla \tilde{V}) \quad 1.37$$

Here m , p , σ and \tilde{V} are defined as the electron mass, electron momentum, the Pauli matrices vector and Coulomb potential, respectively. The semi-classical method of transport theory identifies three primary causes, which are detailed below. These are the two extrinsic contributions- side jump and skew scattering, which are caused by impurity scattering, and the intrinsic contribution, which originates from the band structure.

1.8.1 Skew scattering:

Skew scattering is also known as Mott scattering. Skew scattering was first introduced by Smit in 1956 to explain anomalous Hall conductivity [66]. The basic mechanism is that the SOC produces an effective magnetic field in the scattering plane. Depending on the direction of electron spins the field gradient applies a resultant force whose direction can be towards or away from the scattering center as shown in Fig.1.6 (a) [64]. Hence skew scattering causes the spin Hall effects. Thus, spin skew scattering produces spin Hall effects even in the presence of spin-orbit interactions, and no further symmetry violation is required. Scattering planes decides the spin polarization direction and result in spin current. Spin Hall conductivity in this case is directly proportional to longitudinal charge conductivity. Hence, the ratio of two is known as the spin Hall angle and it is independent of impurity concentration [67]. However, in this case, magnitude of the spin Hall effect depends on the difference in SOC of the host and impurity material (e.g., Pt in Cu or Cu in Pt). The larger difference can lead to larger spin Hall conductivity [68]. Therefore, by selecting host and impurity

material judiciously, spin Hall conductivity can be tuned. Also, the spin Hall effect at the surface is more pronounced due to spin skew scattering phenomena.

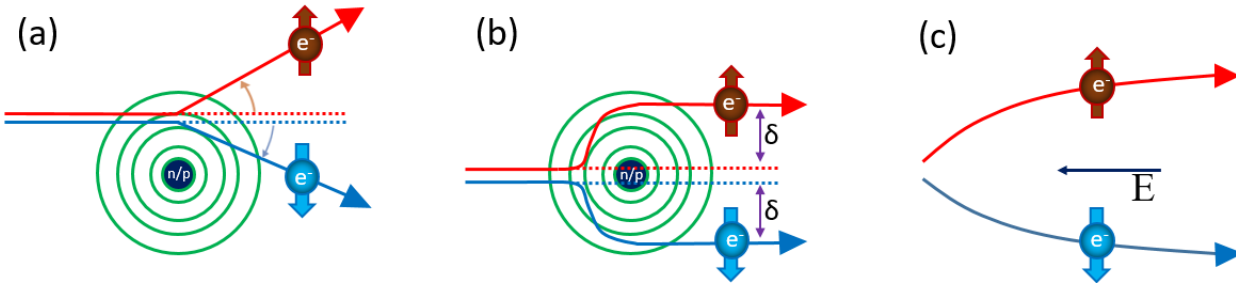


Figure 1.6 Schematic of (a) skew scattering, (b) side jump, and (c) intrinsic scattering mechanism.

1.8.2 Side-jump scattering:

In 1970 Berger proposed an additional mechanism of side-jump scattering to explain the anomalous Hall conductivity [17]. This type of scattering takes place due spin dependent different acceleration and deceleration during scattering. In spin-orbit coupled systems, side-jump scattering is caused by an anomalous form of the velocity operator [69]. This results in a transverse displacement of electrons by multiple scattering. This mechanism results in a higher spin Hall angle at sufficiently high impurity concentrations i.e., spin Hall angle is proportional to impurity concentration due to the side-jump mechanism [70]. Usually, in metals, the intrinsic or skew scattering contributions are larger than the side-jump contribution to the spin Hall conductivity. According to Berger, a discontinuous sideways displacement δ of the center of mass of an electron wave packet following a collision depends on the direction of the spin but is unaffected by the impurity potential sign (shown in Fig.1.6 (b)).

1.8.3 Intrinsic interaction:

It was predicted that there is still another SOI mechanism that exists in perfect crystals. The term "intrinsic" or "Berry phase" mechanism refers to a mechanism that results from the spin dependence of the alleged anomalous velocity [71]. The Intrinsic scattering has been demonstrated in Fig.1.6 (c).

For very clean conductors with low scattering, rates of extrinsic spin skew scattering are expected to be the dominant mechanism. While for moderately dirty conductors, intrinsic or side-jump scattering can be dominant.

1.9 Spin Hall effect (SHE) and inverse spin Hall effect (ISHE):

One can produce a pure spin current in many ways, such as spin pumping with FMR [72–75] and spin Seebeck effect (SSE) by developing a temperature gradient across the edges [76–78]. All these methods generate pure spin currents from the FM. Recently, the spin Hall effect (SHE) has been proven a potential technique since it paves a way to generate pure spin current without any FM. Dyakonov and Perel gave the first prediction for SHE in 1971 [79,80]. The mechanisms of SHE can be divided into two categories: First is intrinsic SHE [81]; the second is extrinsic SHE [17,66]. In 1999, Hirsch revived the concept and named this phenomenon as spin Hall effects [18].

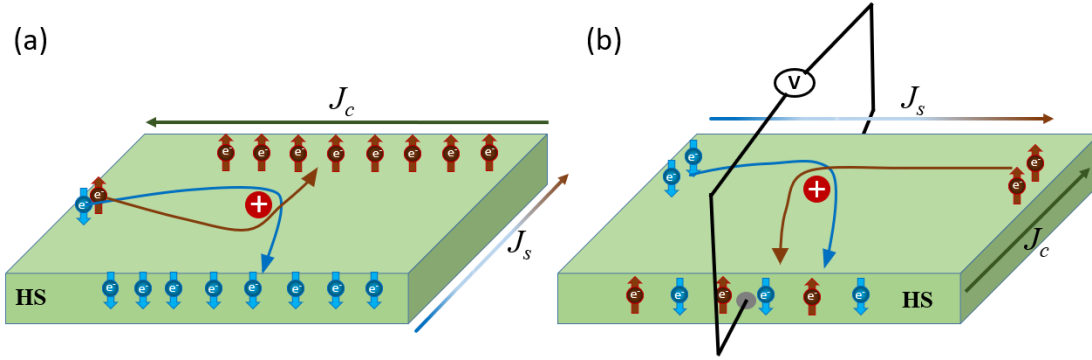


Figure 1.7 Representation of (a) SHE, where charge current gets converted into spin current due to interaction with SOC of HS (b) Represent the ISHE process where transverse charge current is generated due to spin current due to SOC of HS.

From scattering theory, when a charge current flows (electrons move) in the metals, the SOI of the metal deflects spin-up and spin-down electrons to opposite edges. This movement of opposite spins to opposite edges causes spin accumulation on the edges in the transverse direction, resulting in a pure spin current. A schematic of SHE has been shown in Fig. 1.7 (a). The spin current is perpendicular to the charge current direction. And its reciprocal process, where spin current gets converted into charge current is known as the inverse spin Hall effect (ISHE). A schematic of ISHE has been shown in Fig.1.7 (b). The conversion efficiency is described by a spin Hall angle.

$$I_s = \theta_{SHA} \left(-\frac{\hbar}{2e} \right) s \times I_c \quad 1.38$$

where θ_{SHA} is the spin Hall angle, which parameterizes the strength of the SOC of the NM. s is the polarization direction of the spin current. As the number of up spins and down spins are equal on opposite edges, there will be no electric potential across the edges. This makes the detection of SHE a complicated phenomenon. For 30 years of its first prediction, SHE was not detected experimentally. Y. Kato first demonstrated the direct observation of SHE in a semiconductor by

Kerr Microscope [82]. Magneto-optic Kerr effect (MOKE) was good for magnetic systems, but for nonmagnetic metals, it was not useful. The other limitation of MOKE is it can give qualitative pictures only. Later, in 2006, Valenzuela and Tinkham first reported the direct detection of the inverse spin Hall effect (ISHE) via electrical methods [83]. Further different HM with high SOC have been extensively explored for ISHE study. Saitoh et. al., have first demonstrated the room temperature ISHE which is caused by the pure spin current in Ni₈₁Fe₁₉/Pt bilayer films by spin pumping [84]. In addition to this, one big achievement was observed that SHE in some metals was sufficient to switch the magnetization of the neighbour FM layer. This gives the scope of utilization of SHE and ISHE in spintronics devices.

1.10 Spin pumping:

For a spin, its magnetic moment M is associated with its angular momentum as $\gamma L = MV = M_s V$ where V is the volume of FM and M_s is the saturation magnetization. For a given FM, at FMR, the precession of magnetization requires the precession of its angular momentum around the external magnetic field. This effective magnetic field is essential to precess the angular momentum. Due to the magneto-elastic interaction, a lattice of the FM system applies an additional torque which gives rise to magnetic damping [85]. In the case of the FM/NM bilayer system, an extra damping torque can also exert; this extra torque arises due to the absorption of spin current in the NM layer. This process of transfer of spin current from the FM layer to the NM layer in the form of spin angular momentum is called spin pumping. Hence spin pumping also contributes to the enhancement of magnetic damping. Fig.1.8 demonstrates the FMR-based spin pumping. Therefore, for an FM/NM system, Gilbert damping can be written as

$$\alpha = \alpha_0 + \alpha' \quad 1.39$$

Now rewriting equation

$$\alpha' = \alpha - \alpha_0 = \Delta\alpha \quad 1.40$$

Where α is total damping, α_0 is the damping of isolated FM (when there is no adjacent NM), and α' is the damping due to spin pumping. This α' depends on the spin current absorption efficiency of NM. $\Delta\alpha$ is defined as the difference in the Gilbert damping constant from bilayer FM/NM to a single FM layer. This α' depends on the spin current absorption efficiency of NM. This efficiency of absorption is defined as spin mixing conductance ($g^{\uparrow\downarrow}$). The $g^{\uparrow\downarrow}$ is primarily dependent on FM and NM interface quality [86] and can be related to damping parameters as following

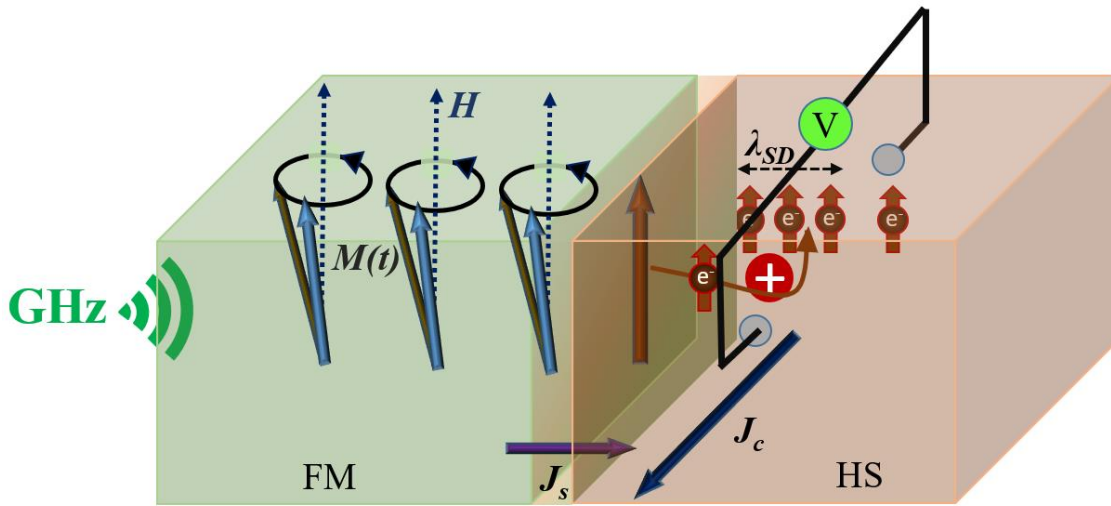


Figure 1.8 Spin pumping process in FM/HS bilayer system. The FMR is used to inject spin current in the form of spin angular momentum from FM layer to HS. Due to spin dependent scattering, spin current in HS causes the generation of transverse voltage.

$$\Delta\alpha = \frac{g^{\uparrow\downarrow}g\mu_b}{4\pi M_s t_{FM}} \quad 1.41$$

Which can be rewritten as

$$g^{\uparrow\downarrow} = \frac{4\pi\Delta\alpha M_s t_{FM}}{g\mu_b} \quad 1.42$$

There are two ways to quantify spin-pumping: the first is to measure the change in $\Delta\alpha$ and the second is measuring electrically via ISHE. The second method measures voltage due to spin pumping across the edges. Due to the ISHE, this spin current in HS is changed into a charge current that can be electrically sensed as a voltage in open circuit situations. The polarity of the recorded dc voltage signal can be determined by the direction of the charge current and, consequently, the polarity of the voltage, depending on the polarization state of the spin current.

1.11 Exchange bias:

In such FM/HS heterostructures, the HS can be an antiferromagnet (AFM) as some AFMs exhibit high SOC. In such FM/AFM heterostructures, another interesting phenomena can be observed which is called as “exchange bias”. The exchange bias (EB) phenomena, was first observed in 1956 in Co-CoO core-shell structure by Meiklejohn and Bean [87,87,88]. In the Co-CoO core-shell structure, Co is FM while CoO is AFM. The CoO layer coexisting with the Co particle causes the shift in the hysteresis of Co. In EB, the hysteresis loop of a system shifted along the horizontal axis (i.e., magnetic field axis). The conventional system for the EB studies is FM with AFM materials. The term EB was coined because exchange interaction between two materials in contact is the main mechanism behind the shifting of the hysteresis loop on the application of biasing field [89,90]. For the realization of EB sample must be heated above the blocking temperature, and then a biasing field is applied. Above the Neel temperature, the spins of AFM are oriented randomly as the material remains in paramagnetic states. Below the Neel temperature, the AFM

ordering started. The shift in hysteresis is quantified as EB field (H_{EB}) and the width of hysteresis is calculated as coercivity (H_c) of the hysteresis loop. From the understanding of EB studies, it has been concluded that EB predominantly arises due to interaction at the interface of FM and AFM. EB can be observed in a given temperature range i.e., till the so-called blocking temperature, the temperature, above which EB is absent. It should be noted that EB has been considered an interface phenomenon. In past few decades a lot of EB studies have been performed in FM/AFM bilayer thin film structures.

The exchange bias has been categorized into two types, the first is conventional exchange bias which is also known as negative exchange bias (NEB) and the other is unconventional exchange bias which is known as positive exchange bias (PEB) [91]. When the sample is heated above the Neel temperature and cooled to a low temperature in absence of any magnetic field, the nature of hysteresis is symmetric about zero value of the magnetic field (shown in Fig.1.9(a)). In case if any field is applied during the cooling of the sample, depending on the shift direction of hysteresis, the exchange bias type can be decided. As shown in Fig. 1.9(b)-(c) if the biasing field is positive, and the shift in hysteresis is towards the -ve magnetic field, the exchange bias is known as NEB. In the case of a positive biasing field, the shift is towards the +ve magnetic field, the exchange bias is known as PEB.

For the exchange bias study, FM/AFM systems have been explored extensively. The pinned magnetic moment of FM spins at the interface causes the EB mechanism. Other unconventional systems such as FM/FM, FM/FIM (Ferrimagnetic), FM/PM, etc., have been also explored for EB study. The difference in anisotropy of the two FM gives rise to EB in FM/FM bilayer system. In chapter 7, we explored LSMO/SRO bilayer system for the exchange bias study. More details about EB can be found in chapter 7.

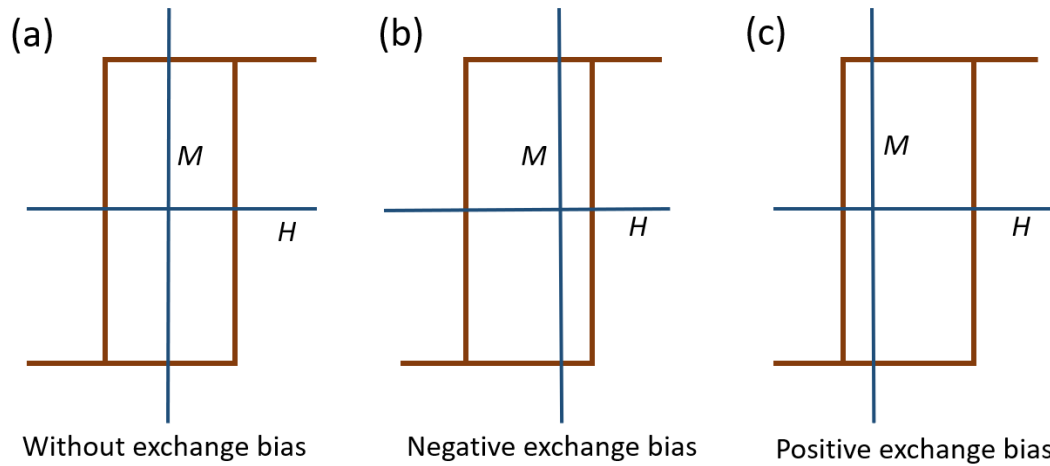


Figure 1.9 Schematic of the hysteresis loop of a FM when (a) when there is no EB. After a +ve biasing field H is applied during the cooling, the shift direction of the hysteresis loop will decide the NEB or PEB. (b) NEB: hysteresis shifted towards the $-ve$ field axis, (c) PEB: hysteresis shifted towards the $+ve$ field axis.

1.12 $\text{La}_{1-x}\text{Sr}_x\text{MnO}_3$ (LSMO):

In this thesis work, we have majorly focused on the very popular manganite, $\text{La}_{1-x}\text{Sr}_x\text{MnO}_3$ (LSMO) which is a perovskite material. The perovskites with structure ABMnO_3 have attracted a lot of attention for spintronics applications due to their various advantages, which are described in the later part of this section. Here A is a lanthanide cation (La, Nd, Pr, etc.) and B is alkaline earth cation (Sr, Ba, Ca, etc.) [92–94]. The physical properties such as structural, electrical, and magnetic properties can be tuned in $\text{A}_{1-x}\text{B}_x\text{MnO}_3$ by changing the concentration of B i.e., by changing the doping level x one can tune several important properties [95]. It is well known that manganite perovskites transform their phases from FM to PM or metal to insulator, or some structural transformation occurs when they experience changes in composition, stress or defects

introduced, or temperature varied [96,97]. These materials possess unique magnetic and electrical properties [98]. These properties depend on different factors such as the doping concentration ratio between Mn^{3+} and Mn^{4+} ions. Interaction between Mn^{4+} and Mn^{3+} with O^{2-} ions decide the magnetic interaction type in the material [99]. The physical properties of manganites strongly depend on their crystal lattice parameters [100]. These mixed valance manganites also show interesting ferroelectricity or superconductivity properties, even at high temperatures [100]. Manganite perovskites have also got huge interest due to the requirement of insulating FM with high magnetization and high-frequency applications [93,94]. Further investigation of colossal magnetoresistance (CMR) in manganite opened a new field for research in these materials [94,101,102]. The CMR effect is known as the change of resistance of the materials under the application of a magnetic field [103]. $\text{La}_{0.67}\text{Sr}_{0.33}\text{MnO}_3$ and $\text{La}_{0.67}\text{Ca}_{0.33}\text{MnO}_3$ (LCMO) are a few examples of the most studied perovskite manganites. There are few reports on LSMO/Pt bilayer, where LSMO have been prepared using pulsed laser deposition technique, which shows that the LSMO can be proven as a good alternate to conventional FM due its high spin polarization [104,105]. Here we attempted to study LSMO/HS systems prepared with oxygen assisted molecular beam epitaxy (OMBE) also by PLD system. First, we have explored LSMO properties in LSMO/Pt bilayer samples as Pt is a HS material whose properties are well understood. We have also attempted to enhance the spin to charge conversion efficiency in this standard LSMO/Pt system. In the next part of this thesis work, we have replaced Pt with other HS materials which are also oxides and have good lattice matching with LSMO. We have taken a different class (AFM, FM) of material in this regard. This study can provide a clear understanding that how epitaxial system can be utilizes for enhancement of spin to charge conversion efficiency. In this thesis work, we have explored LSMO for different spintronic-related studies.

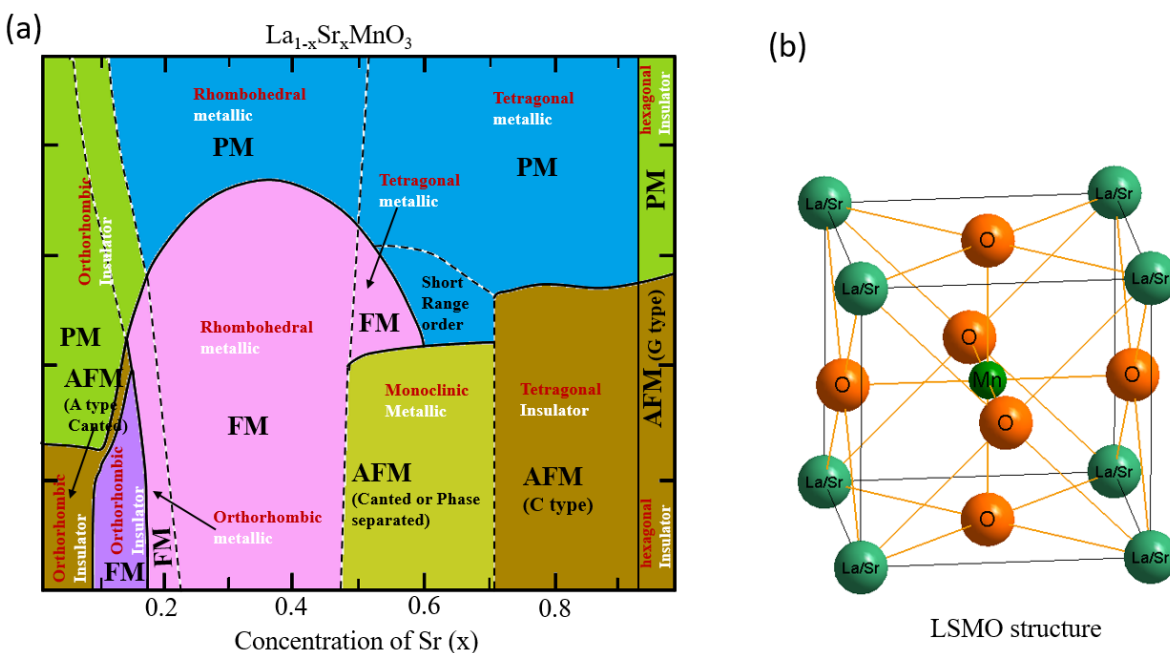


Figure 1.10 (a) Phase diagram of $\text{La}_{1-x}\text{Sr}_x\text{MnO}_3$. the x-axis is the concentration of Sr. (b) Crystal structure of LSMO.

$\text{La}_{0.67}\text{Sr}_{0.33}\text{MnO}_3$ is a well-known FM. The parent compound LaMnO_3 shows AFM with Neel temperature (~ 150 K) and shows insulating behaviour. These properties of LaMnO_3 can be significantly or fully modified by doping Sr in it. Considering $\text{La}_{1-x}\text{Sr}_x\text{MnO}_3$, where x is the concentration of Sr. At $x=1/3$, the compound shows FM and metallic behaviour [93,106]. The Curie temperature for LSMO is the maximum (~ 370 K) among all known manganite-based FMs [107]. It also shows the electrical high conductivity at room temperature, a fully spin-polarized conduction electron band, and a highly stable crystal structure [108–110]. Hence it has attracted a lot of attention from an application point of view. A detailed phase diagram for $\text{La}_{1-x}\text{Sr}_x\text{MnO}_3$ has been shown in Fig 1.10 (a). It can be seen that $x=0.8$ will give a C-type AFM structure, having a Neel temperature around 275 K. We have also explored this composition as a spin sink.

1.12.1 Crystal structure:

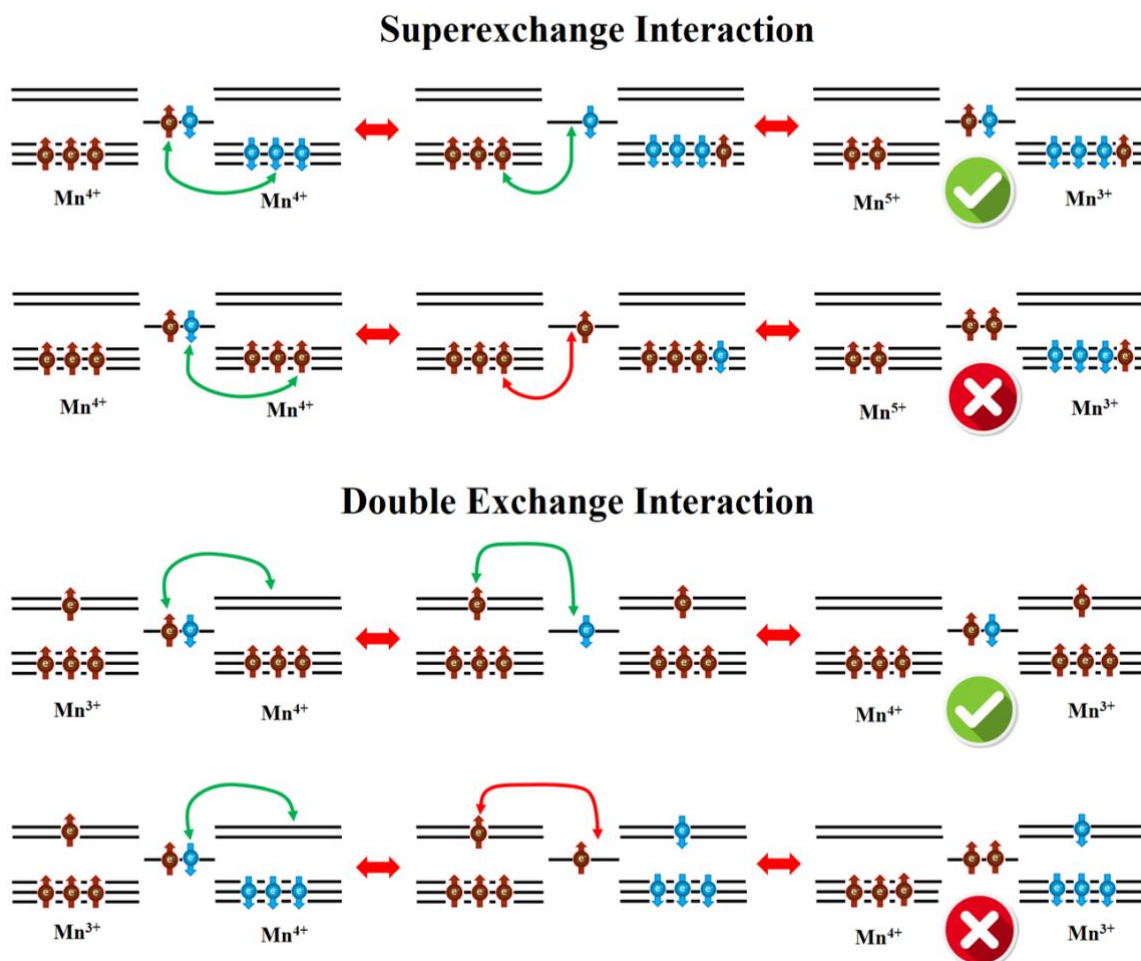


Figure 1.11 Mechanism of SEI and DEI. SEI favours the AFM arrangement, while DEI favours the FM arrangement (this figure is inspired from master thesis of Haifeng Li, Forschungszentrum Jülich).

LSMO has a perovskite structure (as shown in Fig.1.10 (b)), with a pseudo cubic lattice constant of 3.87 Å. The La/Sr occupy the vortices position and share with eight similar cubic cells. Mn atoms occupy the body-centred position, while oxygen atoms sit at face centred position and share with two similar cubic cells shown in Fig1.10 (b). Hence Mn-Mn atoms can interact via oxygen atoms. This interaction can be of two types: the first is superexchange interaction (SEI), and the second is double exchange interaction (DEI). When Mn^{4+} and Mn^{4+} interact via an oxygen atom,

one electron hops to Mn^{4+} , and the vacancy created at oxygen is fulfilled by the electron from other Mn^{4+} . Therefore, finally, Mn^{5+} and Mn^{3+} state form. This is known as SEI and is only possible if the arrangement of spins is in FM order in Mn^{4+} ions. In the case of DEI, Mn^{4+} interacts with Mn^{3+} via oxygen atoms. DEI favours FM configuration, while SEI supports AFM arrangement. An electron from oxygen hop to Mn^{4+} and this vacancy created in oxygen get filled by Mn^{3+} . Therefore, finally, Mn^{4+} and Mn^{3+} state form. This hopping of electrons is only possible if Mn^{4+} and Mn^{3+} spins are arranged in AFM order. The process has been shown in Fig.1.11(a) and (b). A detailed discussion about DEI and SEI can also be found in chapter 7.

1.12.2 Some potential applications of LSMO:

LSMO has been proven a very useful material due to its advanced structural, electronic, and magnetic properties. It is possible to grow LSMO in an epitaxial thin film with special physical vapour deposition methods. Due to its CMR properties, it can be used in high-frequency tuneable microwave filters [111,112]. High CMR also helps to use LSMO in ferroelectric field effect transistors (FeFET), magneto-electronic, some other spin-sensitive devices, and memory devices [96,109,113]. Magnetic states of LSMO like manganite can be controlled easily. Hence, it can be used to study and understand the magnetic interaction in multilayer and at the interface with other materials [114]. Due to its half-metallic nature, it gives high spin polarization. These properties make it a potential candidate for spintronics applications such as TMR, non-volatile magnetic random-access memory (MRAM), etc. [115]. LSMO also shows the magnetocaloric effect, hence, it can be used for magnetic refrigeration [93].

CHAPTER 2: Experimental Techniques

This chapter provides a brief description of various experimental methods employed to prepare thin films and analyse their structural, magnetic, and transport characteristics. We fabricated the perovskite films, i.e., LSMO(FM), LSMO(AFM), SRO, and Pt films, using oxygen-assisted molecular beam epitaxy (OMBE) and pulsed laser deposition (PLD) techniques. Structural characterization of the thin films was performed via low-energy electron diffraction (LEED), reflection high-energy electron diffraction (RHEED), X-ray diffraction (XRD), X-ray reflectivity (XRR), and transmission electron microscopy (TEM). The magnetic measurements were performed by a superconducting quantum interference device (SQUID) magnetometer. Room temperature resistivity has been measured by an in-house developed four-probe technique-based setup. Low temperature transport and magnetotransport measurements have been performed in a quantum design-based physical properties measurement system (PPMS). The Gilbert damping constant evaluation and Inverse spin Hall effect (ISHE) measurements were carried out via ferromagnetic resonance (FMR) spectroscopy.

2.1 Thin film fabrication techniques

Thin films are low-dimensional materials created by sequentially condensing atomic, molecular, and ionic species of matter onto a substrate. Thin films may have different magnetic, mechanical, carrier transportation, superconductivity, ferroelectricity, optical, and other properties from their bulk counterparts because of a decrease in dimensionality and difference in lattice matching between the material and substrate. This lattice mismatch in substrate and film causes strain or stress in the film, which may result in differences in the above properties. The thin film allows us to use them on a very small scale, specifically in today's technological advances in optoelectronic, photonic, and magnetic devices. In light of this, thin films, particularly in a new generation of

integrated circuits, are essential due to the demands of tiny devices with improved capabilities. Various strategies have been used to grow thin films depending on the properties of the materials and cost considerations. These techniques can be broadly classified into two categories-

1. Chemical vapour deposition (CVD)
2. Physical vapour deposition (PVD)

The heated substrate surface and the gaseous reagents supplied in the case of the CVD process undergo a chemical reaction. In contrast, the target material is vaporised, and the target element is deposited onto the substrate in PVD. In this work, PVD has been used to deposit the perovskite films. As LSMO and SRO are metallic oxides, PLD and OMBE techniques are the best-suited techniques for the epitaxial deposition of such thin films. We have used only these techniques for our sample fabrications. The details of OMBE and PLD techniques are as follows.

2.1.1: Oxygen-assisted molecular beam epitaxy (OMBE):

The state of art molecular-beam epitaxy (MBE) is a synthesis method for creating semiconductor heterostructures with high purity, mobility, and precise atomic-layer thickness control. Its application for developing multicomponent oxides had a rocky beginning about 30 years ago. However, throughout the following decades, it has also emerged as one of the best ways to create oxide heterostructures, particularly when investigating their inherent features. In the vacuum deposition technique MBE, an epitaxial film is grown when well-defined thermal beams of atoms or molecules interact with a crystalline surface. GaAs and (Al, Ga)As were the primary targets of its development [116]. Nevertheless, its usage has been extended to other semiconductors, metals, and insulators due to its unparalleled ability to control stacking at the monolayer level and

compatibility with surface-science tools to monitor the growth process during the deposition [117,118]. The typical MBE technique is shown in Fig. 2.1(a).

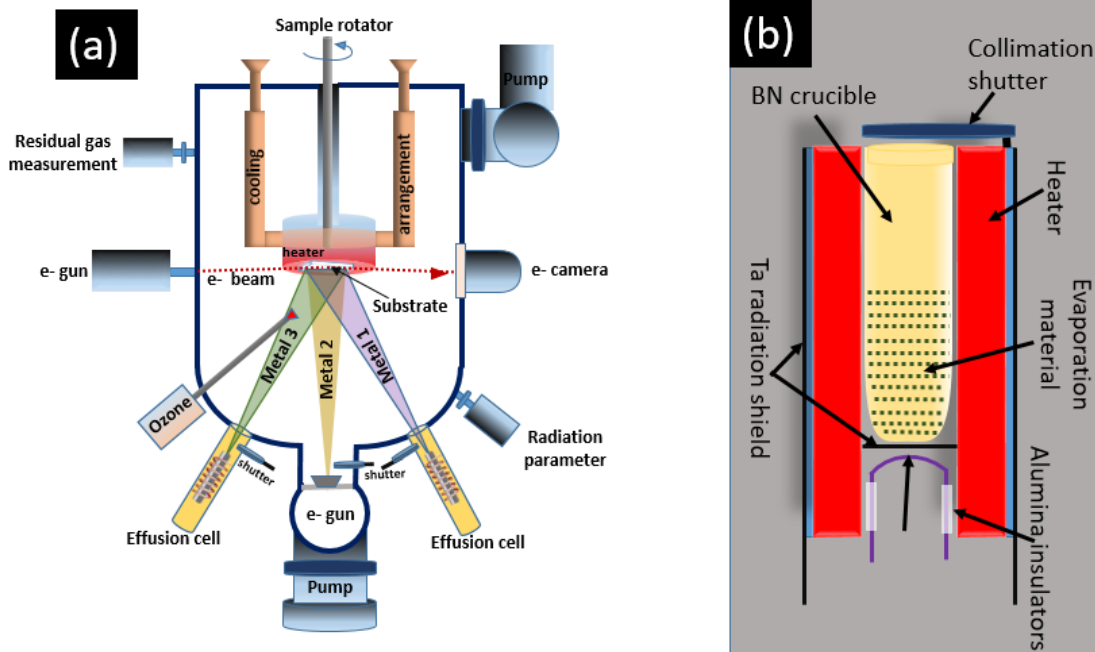


Figure 2.1 (a) Schematic of MBE technique and (b) effusion cell. A set of effusion cells mounted in an MBE system for multilayer or co-deposition. Evaporation materials are kept inside the effusion cells. Heating of effusion cells resulted in evaporation of the material, which gets deposited into the substrate.

MBE differs from previous thin film preparation techniques for epitaxial oxides due to epitaxial growth, a clean ultra-high vacuum deposition environment, in situ characterisation during growth, and the absence of highly energetic species. These capabilities are crucial to modify oxide heterostructures at the atomic layer level. In addition to molecular beams coming from heated crucibles holding distinct elements, molecular beams of gases can also be used, for instance, to

create oxides or nitrides. The design of an MBE system for the growth of multicomponent oxides differs significantly from the more typical MBE systems used today to grow semiconductors in several significant aspects. The main variations are the necessity of an oxidant species, stricter composition control, and increased pumping to accommodate the oxidant gas load. A molecular beam of oxidant is utilised to oxidise the elemental species that reach the substrate and produce the desired composite oxide. The large mean free path required for MBE is protected by limiting the acceptable pressure of this oxidant. The maximum pressure will vary depending on the MBE shape, the element being oxidised, and the oxidant species being utilised; however, MBE normally needs oxidant pressures below roughly 10^{-4} Torr [118]. Molecular oxygen has been used to produce oxides that are easily oxidised. Still, oxidants with higher activity are required to grow ferroelectrics or superconductors that contain species which are more difficult to oxidize, such as oxides containing bismuth, lead, or copper [119,120]. Purified ozone or plasma sources have been used successfully for this purpose [121–123]. Ozone is explosive when distilled, although silica gel distillation can safely confine it. Indeed, all commercial MBE firms employ this method to provide distilled ozone for their oxide MBE systems [123].

Oxide MBE is the preferred approach for attaining the intrinsic properties of sensitive materials since no highly energetic species are present during the deposition. For example, only oxide MBE can produce antiferromagnetic EuTiO_3 [124,125], while other processes can produce ferromagnetic EuTiO_3 [126,127].

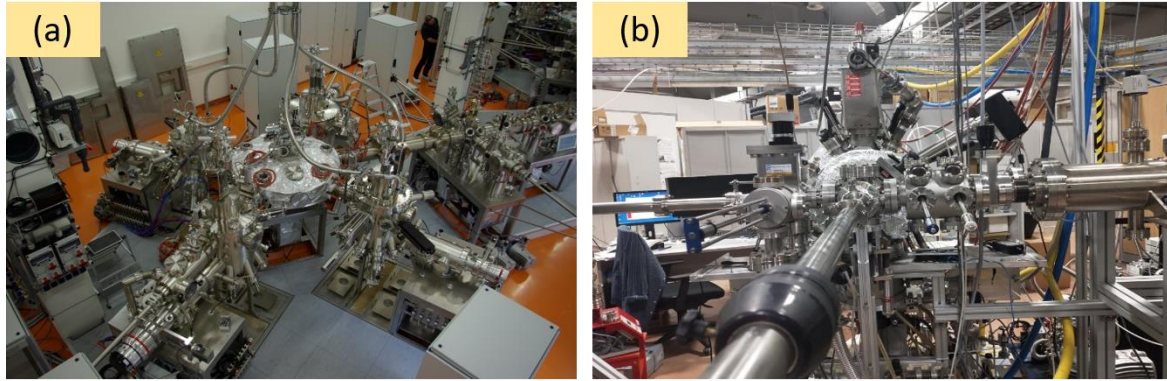


Figure 2.2 Oxygen-assisted MBE chamber at (a) Forschungszentrum Jülich, Germany, and (b) CNR-IOM Trieste (Italy). These facilities were utilised to prepare LSMO/Pt and LSMO(FM)/LSMO(AFM) bilayer films.

MBE uses a molecular beam of low energy from source materials that impinges at the substrate at a high temperature and the UHV. When molecules or atoms have longer mean free pathways than the distance from a source to a substrate, this is referred to as a molecular beam (due to the UHV environment). As a result, before they reach the substrate, there are no inter-atomic or molecule collisions. Single-crystalline films are more likely to develop at high temperatures. In MBE, individual species are either evaporated using an effusion (or Knudsen) cell or an electron beam, combining chemical and physical vapour deposition. Fig.2.1 (a) shows the schematic of the effusion cell used in the MBE technique. These species interactions create a material layer at the substrate's surface. Fig.2.2 (a) shows the OMBE facilities available at Forschungszentrum Jülich, Germany and CNR-IOM Trieste (Italy), respectively. In this thesis work, we have performed the sample preparations at these facilities for the deposition of LSMO/Pt and LSMO(FM)/LSMO(AFM) bilayer heterostructures, respectively.

2.1.1.1 Process of OMBE:

- i. Ultra-pure material was used as a source.
- ii. A molecular beam is created using an effusion cell by heating sources to the melting point.
- iii. Ozone or molecular oxygen is used as the reactant gas.
- iv. The gaseous elements can condense on the wafer, where they may react with each other.
- v. Several sources aimed at the substrate.
- vi. The ultra-high vacuum provides source molecules with a large mean-free path, forming a straight beam.
- vii. The beam impinges on a heated substrate.
- viii. Incident molecules diffuse around the surface to the proper crystal sites and form crystalline layers.
- ix. Characterisation tools (RHEED and/or LEED) allow growth to be monitored in situ.
- x. The mass spectrometer monitors the residual gases and checks source beams for leaking.

2.1.1.2 Advantages of OMBE:

- i. The deposition rate is 1 $\mu\text{m/hr}$ or one monolayer/sec.
- ii. Defect-free, single atomic layer control is only possible by MBE.

Multiple beams can impinge the surface at once to create materials or doping a layer during growth.

2.1.2 Pulsed laser deposition (PLD):

The pulsed laser deposition technique can be utilized to fabricate thin films. Due to its success in producing epitaxial high-temperature superconducting $\text{YBa}_2\text{Cu}_3\text{O}_{7-\delta}$ films in the 1980's, PLD became well-known [128–131]. In general, four phases are involved in depositing thin films by PLD-

- (i) Plasma formation and target material ablation with a laser.
- (ii) Plasma dynamics.
- (iii) Depositing the ablated material from the target onto the substrate.
- (iv) The nucleation and growth of the film on the substrate's surface.

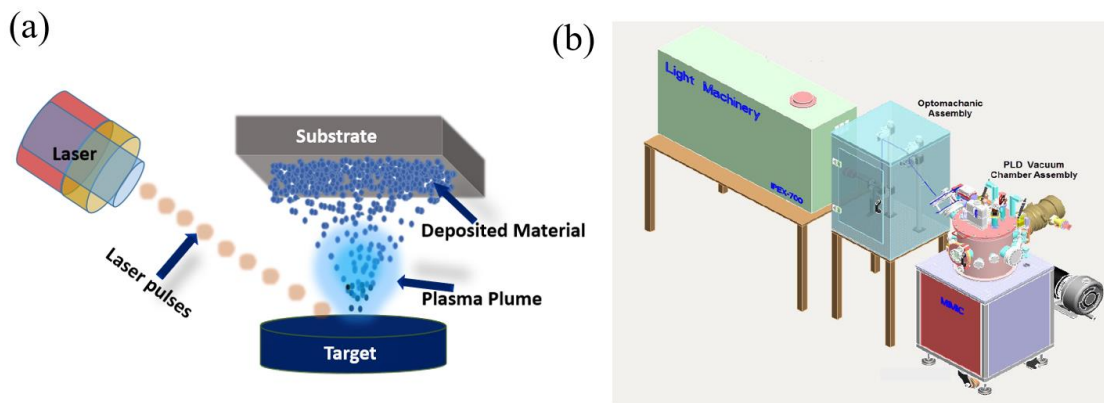


Figure 2.3(a) Schematic of the deposition process in PLD. The pulsed laser falls on the target surface due to this material from the target being ablated and getting deposited on the substrate surface. (b) Schematic diagram of PLD chamber, laser, and optics.

Chapter 2: Experimental Techniques

In this technique, the target's surface is vaporised by a pulsed laser beam, and the vapour then condenses on a substrate. PLD is a vacuum-based physical vapour deposition technology with several features in common with sputter deposition and molecular beam epitaxy. The ablation procedure must be carried out in a vacuum chamber where the released particles can expand for high-quality film formation without restriction. A laser, a few optical components, and a vacuum system are the primary parts of the PLD technique. It differs from conventional evaporation procedures because, unlike other techniques, only a small part of the target is heated by a focused laser beam. The schematic of the PLD deposition process is shown in Fig.2.3 (a).

Each laser pulse ablates a small portion of the material when the energy density is high enough, resulting in a plasma plume. This plasma plume consists of ions, molecules, electrons, and atomic and diatomic species [132,133]. The ablated plume supplies the required material flux for film deposition. For stoichiometric ablation of complex materials, a small thermal diffusion length and a high optical absorption coefficient at the chosen laser wavelength are required. The thermal diffusion length is given as $l = 2(\sqrt{D\tau})$, where τ is the laser pulse duration and D is a diffusion constant. For insulating materials, it is quite small, and the laser heat transfer is primarily limited by the depth of absorption, irrespective of the length of the laser pulse. Conversely, the diffusion constant is large, such as in metals and semiconductors. In PLD, the laser pulse width is 20 ns. Due to the pulse's short duration and high power (~10 MW) delivered to the target even before thermodynamic equilibrium is attained, ablation occurs due to energy absorption. The laser should have an energy density higher than the threshold value for the material to be deposited. In addition to the short pulse width, it should be absorbed by the target material. This will cause the target material to be ablated, also known as congruent evaporation, which will keep the target material's

stoichiometry in the thin film being deposited. On the contrary for metals the higher reflectivity and thermal conductivity make the ablation process less efficient.

The processes used in the current work's thin film deposition by PLD are

- (i) Cutting the substrate to the necessary dimensions.
- (ii) Cleaning it with an ultra-sonicator in acetone and isopropanol.
- (iii) Substrates were dried using compressed dry nitrogen and mounted on the substrate holder using silver paste.
- (iv) Rotary and turbo pumps create the necessary vacuum inside the deposition chamber.
- (v) After the base pressure is reached, the substrate is heated to the required temperature.
- (vi) The required distance between the substrate and target, laser energy, frequency, oxygen/nitrogen partial pressure, etc., are maintained as per the required values.
- (vii) Deposition in the required condition was attempted for thin film preparation.
- (viii) Deposited sample post-annealed (if required) in a particular partial pressure.
- (ix) The sample cooled at a particular cooling rate.

The pulsed laser deposition setup, the excimer laser fundamentals, and its operating principle are briefly described here.

2.1.2.1 Pulsed laser deposition setup:

The main components of pulsed laser deposition are as follows-

- (i) Excimer laser
- (ii) Optical components for manipulating the laser beam,
- (iii) Deposition chamber (which includes rotating target assembly, substrate holder with heater).

(iv) Turbo-molecular and rotary pumps.

The image of the excimer laser and PLD chamber is shown in Fig.2.3(b) It should be mentioned that the laser source is located outside the deposition chamber and is made to an incident on the bulk target material positioned inside the deposition chamber with the aid of optical components.

As most bulk target materials show significant absorption in this range, the wavelength range for pulsed laser deposition is typically 200-400 nm. The absorption coefficient is generally higher for shorter wavelengths. The penetration depth on the target surface thus gets shorter. Although excimer lasers and solid-state lasers can generate laser beams in this wavelength range, excimer laser sources are more efficient. The laser beam is focused at a 45° angle with the target normal to an incident on the material with the desired energy density. Optical components must fall within the range of the transmittance of the laser wavelength. Fused silica lenses with a UV rating are regularly utilised. The target was rotated using a stepper motor to ensure consistent erosion, maximum utilisation, and prevent crater formation. The necessary energy density is achieved by controlling the laser energy and focusing the laser beam on the proper spot size.

Excimer lasers are gas lasers that emit ultraviolet (UV) light pulses with durations of 10 nanoseconds to several nanoseconds. They are the UV lasers with the highest power. The most widely used excimer lasers are made of krypton fluoride (KrF, 248 nm), argon fluoride (ArF, 193 nm), and xenon chloride (XeCl, 308 nm). The word ‘excimer’ stands for “exciting dimers”. Since excited complexes of rare gas mono halides rather than excited dimers provide the active medium in today's powerful excimer lasers, the term excimer laser is only used by convention. Additionally, exciplexes are stable only in the excited state. By combining Ar, Kr, or Xe with F or Cl, exciplexes are created. The most significant ones are KrF, XeCl, ArF, and XeF [134]. In an excimer laser, a pulsed gas discharge produces excited molecules with a non-binding electronic

ground state. Therefore, reabsorption of the radiation is not possible since these molecules dissociate after emitting spontaneously or in response to stimulated emission. However, they can create bonded molecules with one another or with halogens momentarily when stimulated. Since the lifetime of the excited molecule is only a few ns, it quickly decays back into unbound atoms via spontaneous emission.

We have utilised the "Light Machinery" KrF excimer laser available at NISER, Bhubaneswar. The laser has a 248 nm wavelength and a 20–30 ns pulse width. The Laser energy and frequency range are 250–700 mJ and 1–50 Hz, respectively.

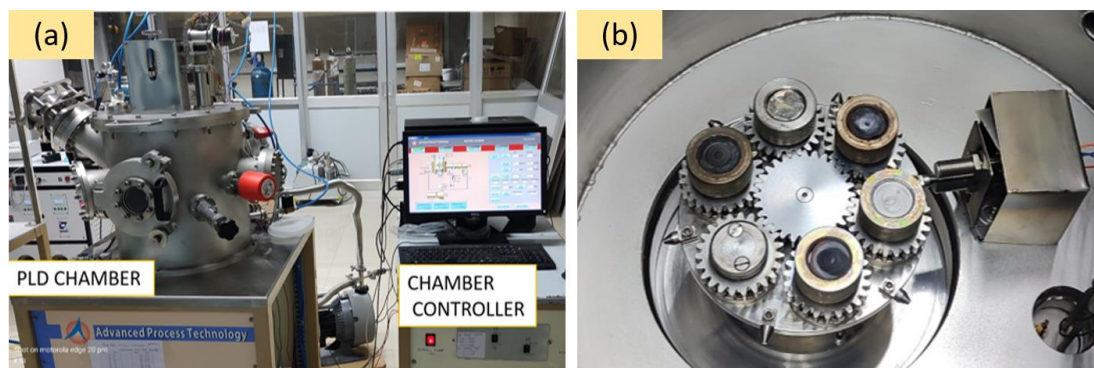


Figure 2.4 (a) PLD chamber at LNMM, SPS, NISER, Bhubaneswar, and (b) target assembly, where six targets can be mounted simultaneously. The target indexer is mounted to select the particular target during the deposition. This PLD facility has been used to deposit LSMO single layer and LSMO/SRO bilayer films.

Substrate Heater: An optical heater consisting of a halogen lamp is used to heat the substrate. It has a radiation shield that helps to keep the heated surface consistent by preventing heat loss in all directions. A heater may raise the substrate's temperature to a maximum of about 850°C (K

thermocouple type is embedded in the heater). One can use the clips provided on either side of the heater to hold the substrate, but often, the substrates are fixed with silver paste on the substrate holder. A shutter attached to the heater prevents deposition on the substrate while the target is being pre-ablated.

Target Assembly: The target assembly consists of a stepper motor, target turret, indexer, and target shield. The six target holders are connected to the target turret. This turret has bearings, gears, and other components that allow for the positioning and rotation of targets as needed. A stepper motor and a target indexer rotate and select the desired target. A thin sheet with a single opening for exposing the intended target to the laser is fixed on two studs in front of the target turret. With the help of this shield, the material that has been ablated from one target cannot be deposited on the other targets. Additionally, this prevents heat from the substrate heater from reaching the targets that are not exposed.

Fig. 2.4 (a) shows the PLD chamber available at LNMM, NISER, Bhubaneswar, used in this thesis work to deposit LSMO single layer and LSMO/SRO bilayer films. Fig. 2.4 (b) shows the target assembly that can accommodate six targets simultaneously.

2.1.2.2 Advantages and disadvantages of PLD:

Due to the laser light source's location outside the deposition chamber provides a significantly greater degree of flexibility for adjusting the deposition settings, which can substantially affect the film's properties.

- (i) Material can be transferred stoichiometrically from the target to the substrate.
- (ii) The growth rate can be precisely controlled using a pulsed laser beam.
- (iii) Power density's adaptability makes it possible to ablate a lot of materials or alloys.

- (iv) Greater control over film growth is possible by easily adjusting the different deposition parameters, such as target-to-substrate distance, substrate temperature, and background gas pressure.
- (v) By mirroring laser beams in many deposition chambers, it is economical to utilize a single laser source for multiple deposition chambers.
- (vi) In comparison to sputtering, smaller targets size is required.

There are also disadvantages to performing PLD:

- (i) Macroscopic particles are produced during the ablation process, and growth defects are carried by bombardment of high kinetic energy particles.
- (ii) In comparison to heavier elements, light elements like the oxygen in lithium have differing expansion velocities and angular distributions in a plume. As a result, a second source is needed to complement these components to produce the required film composition, such as sufficient surrounding gas or a customised target composition.
- (iii) PLD is not suitable for large-area deposition.

2.2 Low energy electron diffraction (LEED):

Low energy electron diffraction (LEED) is a surface-sensitive technique often used in situ to monitor the growth of thin films in the vacuum chamber. In LEED, a very low energy (20 to 200 eV) electron beam is used normally to substrate plane [135]. These low-energy electrons interact with the atoms strongly. As the energy is very low, they can penetrate the sample up to the length of 1 to 2 nm only. The electron, which interacts with the surface atoms only, leaves the surface

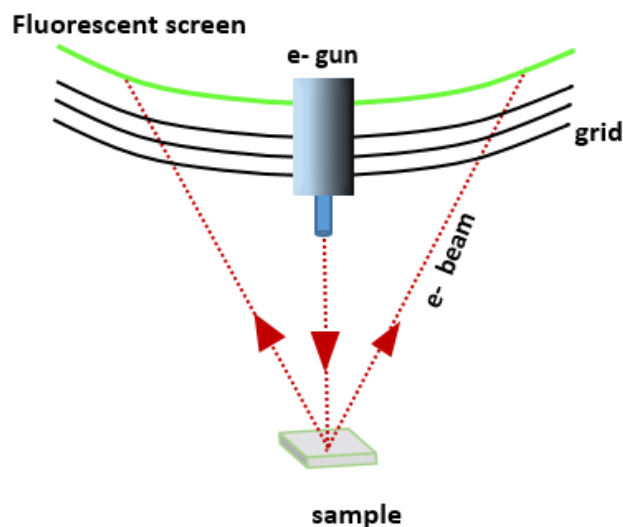


Figure 2.5 Schematic diagram of the basic experimental arrangement adopted in a low energy electron diffraction (LEED) experiment.

and produces a diffraction pattern in the fluorescent screen. For this, the surface of the sample should be well arranged to produce the backscattered diffraction pattern. The elastically scattered electrons take part in the generation of the diffraction pattern. Hence, from LEED, only surface information can be achieved. Very low-energy electron is removed by the energy filtering grid, which is kept before the camera screen (fluorescent screen). The schematic of LEED is shown in Fig. 2.5. The working principle for LEED is the famous Bragg's law (equation 2.1). In Bragg's law, the distance between two diffraction points is inversely proportional to the inter-atomic spacing. The LEED gives the spots as a diffraction pattern which describes the information in reciprocal space [136].

2.3 Reflection high-energy electron diffraction (RHEED):

Reflection high-energy electron diffraction (RHEED) is a low-cost, non-destructive, surface-sensitive technique used to characterize surface structural information and thickness of thin films [137]. Usually, RHEED is used in a high vacuum chamber such as MBE. However, high-pressure RHEED can also be used in the PLD technique. Fig.2.6 shows the schematic of the RHEED experiment. RHEED uses an electron gun to send an electron beam onto the sample, and the diffraction is measured using the camera.

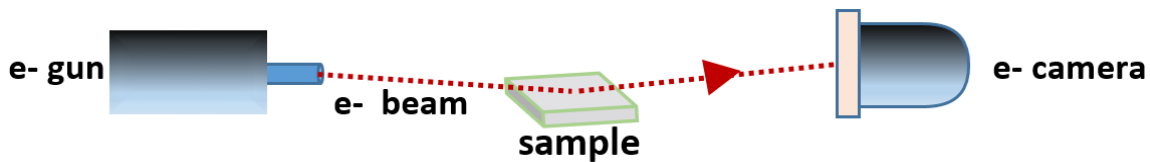


Figure 2.6 The simplest RHEED setup includes an electron gun, a sample, and a camera (or fluorescent screen).

Usually, the energy of the electron beam is in the range of 5 to 100 keV, and the camera used is a phosphor-coated fluorescent screen. In RHEED, the angle of incidence of the electron beam is very low (in the range of 1 to 4°). This low incidence angle allows studying the surface properties of the grown thin film [138]. Fig. 2.6 shows the simplest schematic of the RHEED setup.

In MBE or PLD chamber, sample rotation about its normal axis is possible, which gives freedom to align the sample about some specific crystallographic direction. In RHEED, a large sample to camera length is possible. This gives an advantage of measuring the diffraction pattern during the

growth even at high temperatures, which is not possible in LEED due to the over-saturation of the screen due to high thermal energy.

In ideal conditions, the RHEED pattern should be visible as spots if films are perfectly epitaxial in nature. However, in experiments, the RHEED pattern can show a wide range of features due to different surface imperfections. Commonly streaks lines have been visualised due to imperfection in the surface. This has been usually observed that atomically flat surfaces can have multiple domains. If the width of the domains is smaller than the coherence length of the electron beam, the reciprocal rods broaden. The intersection of reciprocal rods with the Ewald sphere forms the streak line in the diffraction pattern [139].

2.4 X-ray diffractometer:

X-ray diffraction (XRD) is the most powerful, non-destructive cost-effective technique to identify the crystal structure information of a material. In a crystal, the atoms are arranged in a pattern of regular arrays. The X-rays have a wavelength in the order of a few Å, a similar order of lattice spacing of the materials. Therefore, X-rays are capable of giving information about crystal structure very precisely. When a high-energy electron beam bombarded a Cu target, X-rays were generated. A part of this generated X-ray (characteristic X-ray) is used to determine the different structural properties of the samples. Fig. 2.7(a) shows the X-ray diffractometer (Rigaku smartLab) available at SPS, NISER.

2.4.1 X-ray diffraction:

X-ray diffraction (XRD) is used to determine the crystal structure, crystallite size, strain etc. When X-rays beam interact with the crystalline material, where the atoms are well arranged in regular arrays, the X-rays get diffracted from the atomic planes, and the constructive interference forms the diffraction pattern. Fig. 2.7 (b) shows the X-ray diffraction mechanism. The condition for constructive interference is that it should satisfy Bragg's law [140]

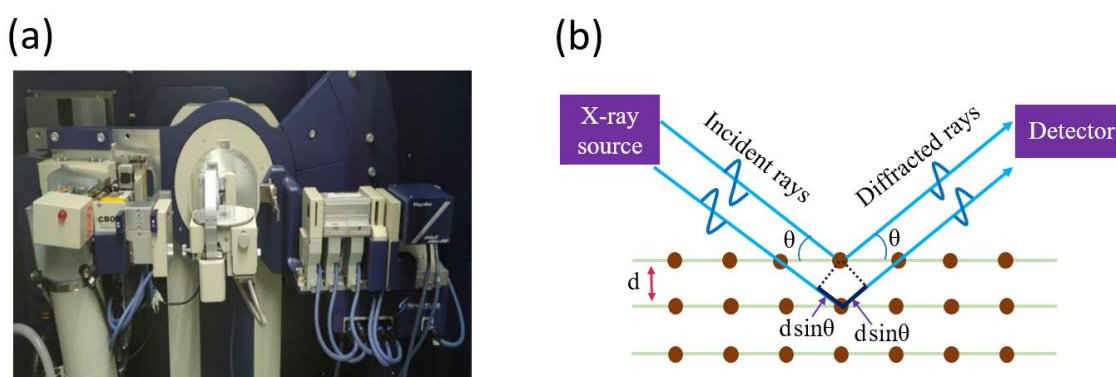


Figure 2.7 (a) The XRD facility available at SPS, NISER, Bhubaneswar. (b) The schematic of the X-ray diffraction process from the crystal planes.

$$2d \sin\theta = n\lambda \quad 2.1$$

where θ , d , and λ are the angle of incidence, d is the spacing between the two atomic planes, and the wavelength of X-ray used, respectively. Here n can take any integer value, i.e., 1, 2, 3 etc. The path difference is given by $2d \sin\theta$. The source and detector angle can be varied to a wide range to get the diffraction spectrum from the material. The diffraction spectrum may contain some peaks, which will appear at a certain angle, having some broadening and intensities. From the analysis of diffracted rays, i.e., peak positions, intensity and broadening of the peak, one can

analyse the crystalline or polycrystalline nature of the specimen. From the diffraction pattern of XRD, one can also identify the specimen composition.

2.4.2 X-ray reflectivity:

X-ray reflectivity (XRR) is an important tool for calculating the multilayer thin films thickness, roughness and density. It is a non-destructive technique and can be used for crystalline, polycrystalline or amorphous materials. From XRR, one can determine the thickness of the film in the range of 0.1 nm to hundreds of nanometres. Fig. 2.8 shows the schematic of the XRR measurement technique. The total internal reflection occurs when the incident angle is close to the critical angle. Due to this, the intensity of the reflected beam is observed. If the angle is above the critical angle, the reflected beam intensity decreases drastically.

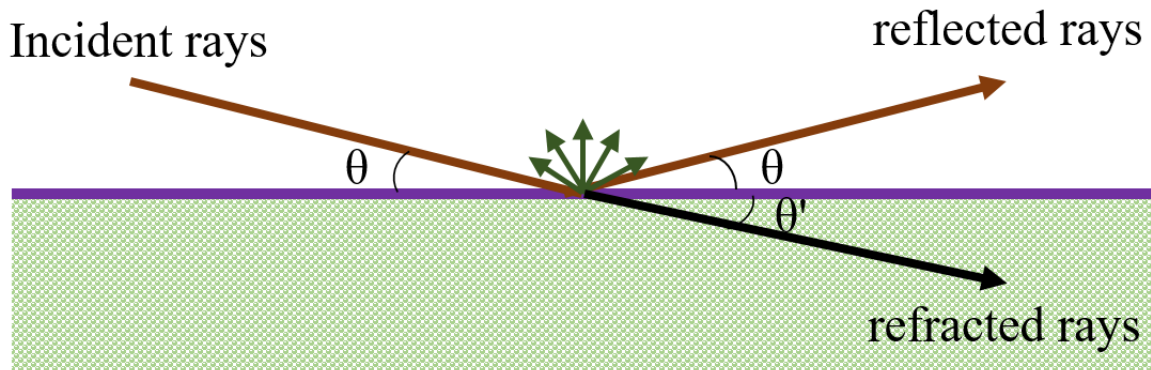


Figure 2.8 Schematic of X-ray reflectivity measurement. If the incident angle θ is less than the θ_c , the total internal reflection occurs.

The typical experimental data obtained from XRR is shown in Fig.2.9 Generally, the observed data is fitted using GenX software. The X-axis is 2θ , and Y-axis denotes the normalized intensity of the X-ray reflectivity curve in the log scale.

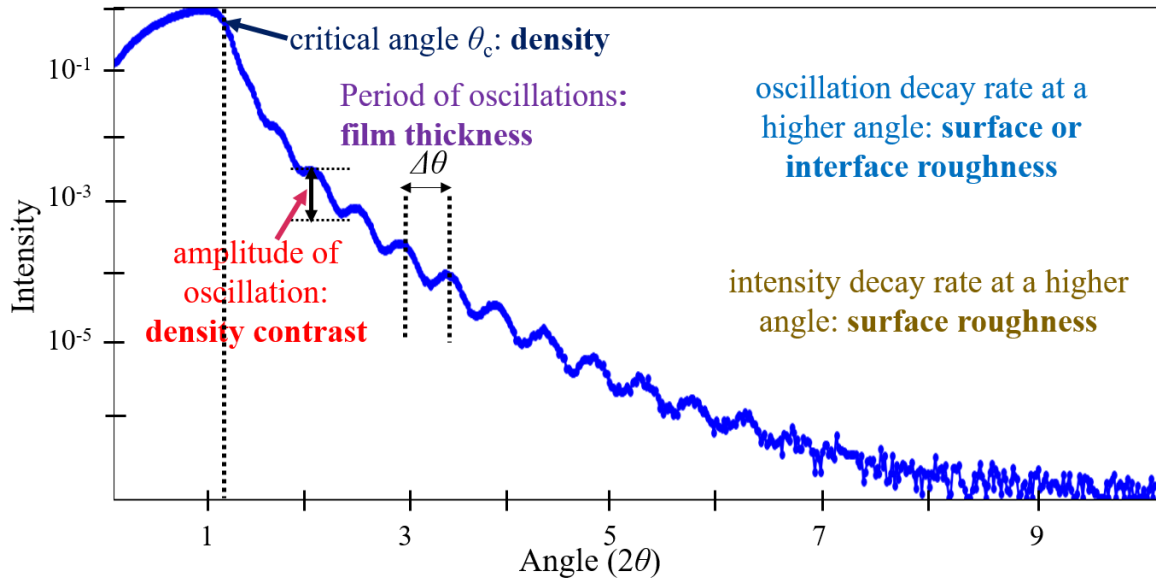


Figure 2.9 A typical XRR spectra for the single-layer film. The period of the oscillations gives information about film thickness, the oscillation amplitude provides information about the density, and from the intensity decay rate, surface or interface roughness can be estimated.

Film thickness:

Observed scattering X-rays are the total of individual electron scattering. The oscillations in the shown graph depend on the film thickness. Higher film thickness will lead to a shorter period of oscillations.

Density:

The density of the film can be extracted from the amplitude of the oscillation and critical angle for total reflection. If the substrate and film have a significant difference in density, the oscillation amplitude will be large.

Interface or surface roughness:

If the surface roughness is large, the intensity of the reflected X-ray decreases sharply. Interface roughness can be understood as an uneven interface, and the interface density changes continuously.

2.4.3 Reciprocal space mapping (RSM):

In thin films, crystal quality and strain analysis are very crucial. In the case of oxide films, where strain or defects such as dislocation, misfits etc., in the film can lead to various effects such as multiferroic, ferroelectricity or change in magnetic ordering etc., the strain analysis and knowing the epitaxial nature of the grown film is very important.

In crystallography, it is very common to represent the crystal lattice plane (hkl) by its reciprocal lattice vector (g_{hkl}). The length of the reciprocal lattice vector is defined as the inverse of the d-spacing of lattice planes (d_{hkl}), and direction is given perpendicular to the lattice planes. Fig.2.10 shows the reciprocal vector of the lattice planes. If there is any change in d_{hkl} or in the direction of lattice planes, the g_{hkl} also changes accordingly. The size of g_{hkl} strongly depends on the crystallinity and anisotropy present in the sample.

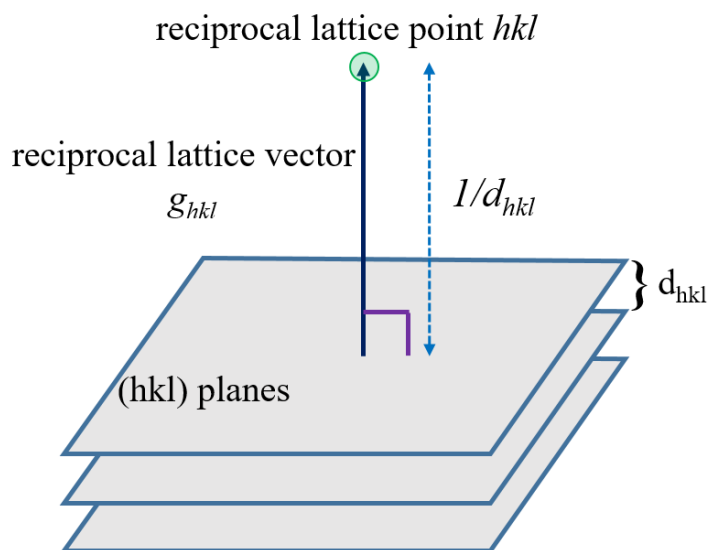


Figure 2.10 Reciprocal lattice vector and reciprocal lattice point for a lattice plane.

Rocking curve measurement, also known as $(2\theta/\omega)$ scan, is performed by rocking a thin film, keeping the detector in a fixed 2θ position. In rocking curve measurement, the tilting axis must be adjusted. The tilt angle should be adjusted for the smallest FWHM and strongest intensity peak position. Further, the χ -axis is adjusted for symmetric reflection, and the Φ -axis (rotation of sample holder around the axis normal to the sample) is adjusted for asymmetric reflection. Now lattice constant can be calculated from the shift of diffraction peaks corresponding to the substrate peak [141].

In reciprocal space mapping measurement, diffraction intensity is recorded by scanning the diffraction angle and sample rotation axis. The obtained data is plotted in the reciprocal space. The analysis of reciprocal space can provide information on crystallinity, crystal structure, crystal orientation relationship, and samples' preferred orientation. In this method, two-dimensional distribution maps are obtained. In RSM distribution of direction and intensity for out-of-plane reciprocal points is measured by in-plane geometry instead of out-of-plane geometry. The basic

required information for measuring RSM is the relation between the direction of substrate orientation and grown film orientation, as well as the diffraction angle information.

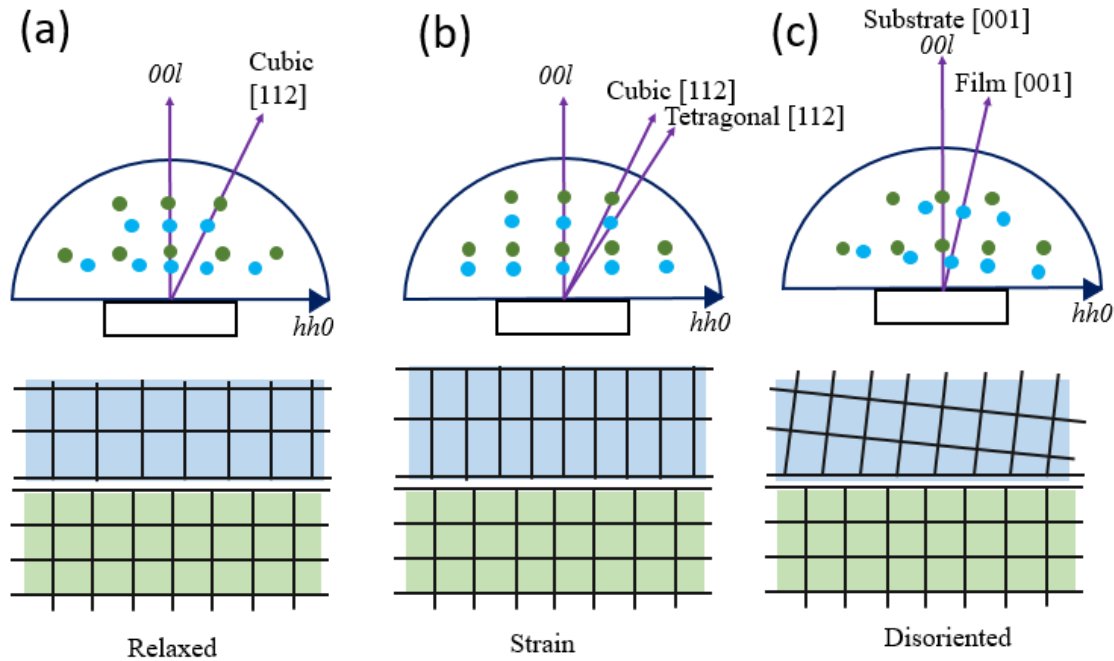


Figure 2.11 Reciprocal space maps of epitaxial bilayer films when (a) there is no strain in the film, (b) when strain is present, and (c) when film planes are tilted at an angle to reference to substrate planes.

Fig.2.11 (a) shows the schematic of reciprocal maps of the relaxed, strained and disoriented films. The relaxed films mean the cubic structure of the film is the same as that of bulk material [141]. In this scenario, the position of the reciprocal point lies in the same line as the substrate reciprocal point connecting the line and origin of the reciprocal lattice.

In the second case, as shown in Fig.2.11 (b), if the grown film has a strain, the sample and substrate lattice constants match. Hence, the reciprocal points of the film will be positioned below the substrate reciprocal lines for both the symmetric and asymmetric diffractions. Fig.2.11 (c) shows the third case, where lattice planes of film and substrate are disoriented, and the reciprocal lattice point of the film is tilted at an angle with respect to the substrate lattice point.

2.5 Transmission electron microscope (TEM):

Transmission electron microscope (TEM) is a very powerful and sophisticated technique for surface and structural analysis. A powerful electron beam is used to visualise the sample of interest. The TEM can generate highly magnified (up to 2M times) images. Due to this, the imaging of small objects at atomic-level is possible with the help of TEM. Fig.2.12 (a) shows the TEM instrument (JEM-F200) available at the Centre for Interdisciplinary Sciences (CIS), NISER. The schematic of the ray diagram of TEM has been shown in Fig.2.12 (b). From Fig (b), it can be concluded that TEM has three essential parts:

1. **Generation and focusing of electron beam:** A V-shaped tungsten filament is used as a cathode, which produces an electron beam. Condenser lenses are used to focus the electron beam on the sample.
2. **Image-producing system:** A set of objective lenses, movable sample stage, objective aperture, and intermediate projective lenses are used to focus the electron beam passing through a sample to form a highly magnified and real image.

3. The image recording system: This system converts the electron images to some perceptible form for the human eye. The image recording system includes a fluorescent screen, digital camera etc.

2.5.1 Working of TEM:

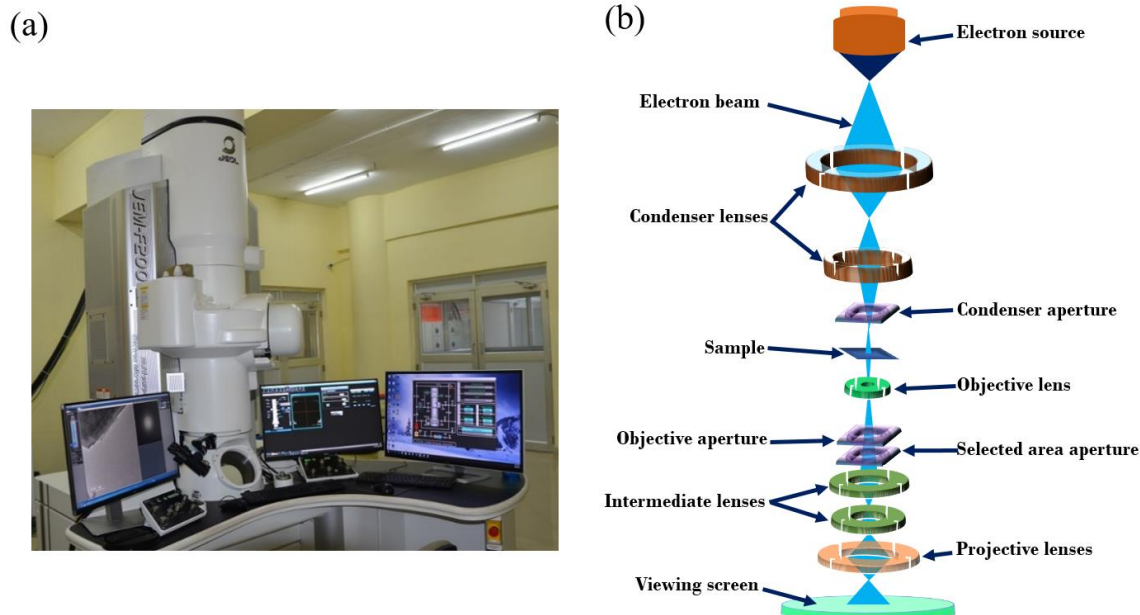


Figure 2.12 (a) The TEM facility is available at the Centre for Interdisciplinary Sciences (CIS), NISER-Bhubaneswar. (b) The schematic of the ray diagram of the TEM is displayed.

TEM uses a very high voltage (200 KV) electron beam to generate the image of a small object. For this, an electron gun is installed at the top, which can produce a high-energy electron beam [142,143]. In TEM, electromagnetic lenses focus the electron beam in a very fine beam. When this beam passes through the sample, having a very small thickness, the transmitted electrons fall on the fluorescent screen, which is installed at the bottom of the microscope. The

exposed part of the sample can be seen on the fluorescent screen. Depending on the density of the atoms from the different parts of the sample, a shaded image appears on the fluorescent screen. The image can be recorded using a digital camera, which can be used directly to study and analysis of the specimen.

2.5.2 Specimen preparation for TEM:

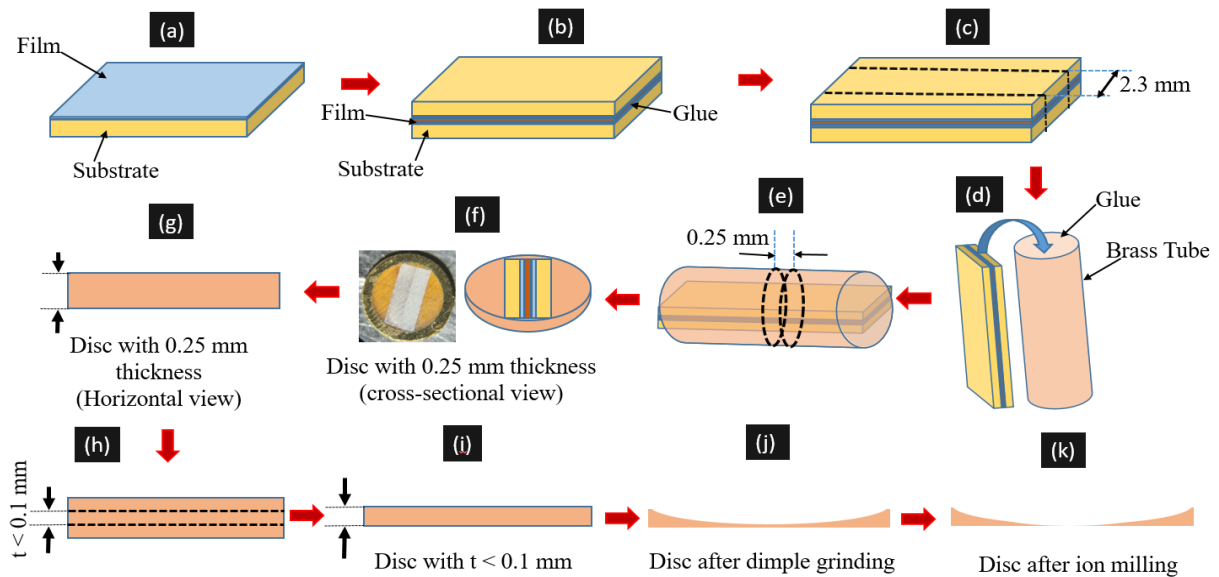


Figure 2.13 (a) Thin film specimen, (b) two pieces of sample pasted together using epoxy. (c) A diamond wire saw is used to cut the sample of the required dimension such that it can go inside the brass tube. (d)-(e) Sample was inserted inside the brass tube and the brass tube was filled with epoxy to stick the sample rigidly with the tube. (f)-(g) Using a diamond wire thin disc made from a brass cylinder. (h)-(i) Manual grinding done with the help of polishing paper to thin down the disc. (j) Dimple grinding was done to further reduce the thickness near the centre. (k) Finally, sample is kept inside the PIPS for ion milling.

For TEM imaging, sample preparation for TEM is very crucial as the thickness should be very small so that electrons can transmit from the specimen to reach the camera. In the case of nanoparticle (bulk) sample preparation for TEM, the nanoparticle mixed solution is poured on top of a carbon-coated grid and then keep it for drying naturally. Nanoparticle samples are ready for imaging. However, in the case of thin film samples, for cross-sectional imaging, the sample preparation process is very sophisticated [144,145]. As shown in Fig.2.13, several steps are followed to make a good quality sample which is described below.

At first we take two sample pieces and then stick these two pieces using epoxy, as shown in Fig.2.13 (b). A heater is used to dry the epoxy between the samples. After this the sample is cut using diamond coated wire cutter in such a way that it can be inserted into the brass pipe (shown in Fig.2.13 (c and d)). Now the rectangular part of the sample is inserted inside the brass pipe and filled with the epoxy so that it can fix properly inside the brass tube (shown in Fig.2.13 (e)); wait for the epoxy to dry. Small discs with a thickness <0.3 mm is cut from the cylinder, as shown in Fig.2.13 (f). Now, the disc's thickness reduces to <0.1 mm by disc grinding using fine grinding papers (40, 15 and 5 microns). Then the disc is taken for the dimple grinding and fine polishing in a “dimple grinder” so it will take shape as shown in the Fig. Finally, ion milling is performed in the disc to reduce the thickness of the film at the centre a few nanometres. Ion milling has been performed by a precise ion polishing system (PIPS) having energy 4-6 keV and 4 to 5° milling angle after this sample is ready for TEM imaging, as shown in Fig.2.13 (k).

2.6 Transport and magnetotransport measurement system:

Electric transport and magnetotransport studies are very useful for understanding a sample's electrical properties, such as resistivity, conductivity, carrier concentration etc., of a sample with varying temperatures and magnetic field. When electrical properties are measured in the presence of a magnetic field, it is known as magnetotransport measurements. The transport and magnetotransport measurements have been performed by Quantum Design physical properties measurement system (PPMS) shown in Fig.2.14 (a), which consists of a cryostat which can be used in the range of 1.8 K to 350 K. A superconducting magnet was used to apply dc magnetic field up to ± 9 T. In PPMS, we can perform DC resistivity and AC resistivity measurements. We can perform the measurement in different protocols, such as

1. Resistivity vs temperature (R-T) measurements.
2. Resistivity vs field (R-H) measurement at a fixed temperature.
3. Resistivity vs temperature (R-T) measurement in the presence of a magnetic field.
4. Hall measurements.

All these measurements can be done in AC or DC modes. PPMS has an inbuilt source meter and a sensitive voltmeter for all these measurements. For the measurement of the thin film, the sample is mounted in the sample holder, and contacts from the sample holder to the samples are made by silver paste or wire bonder. Further, the sample holder is inserted in the cryostat for measurement purposes.

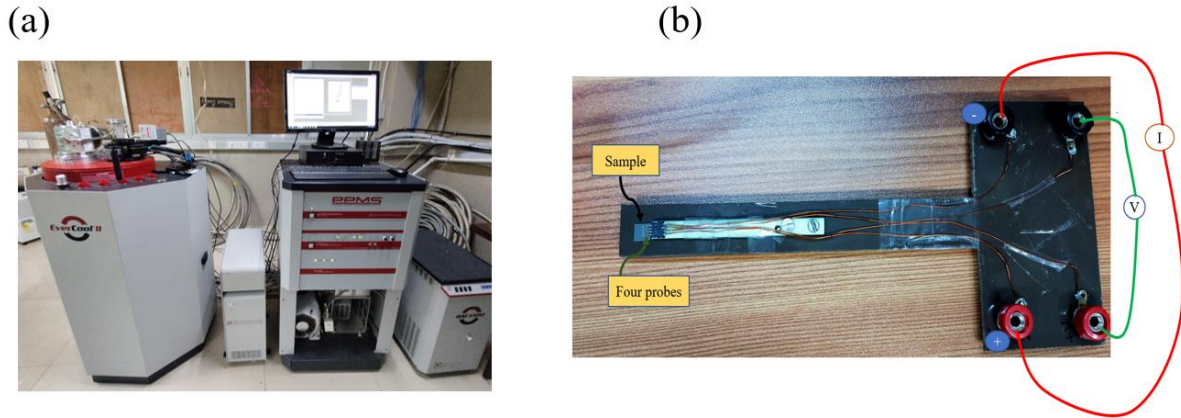


Figure 2.14 (a) Physical properties measurement system (PPMS) and (b) in-house developed room temperature resistivity measurement setup.

For room temperature resistance measurement, we have prepared an easy-to-use setup as shown in Fig.2.14(b) We assembled this setup using gold-coated pins and copper wires on a wooden lamella. This setup is based on four-probe measurement geometry. We can lift the probe, and the sample can be kept below the four probes. The other ends of the probe connected to the source meter and Nano voltmeter, which assured the sensitivity of this setup. The advantage of this setup is that this is non-destructive and easy to use. The sample size of 5 mm x 2 mm is good enough for the measurements.

2.7 Superconducting quantum interference device (SQUID) magnetometry:

A superconducting quantum interference device (SQUID) magnetometer is a very important instrument to quantify the magnetization of a sample. SQUID magnetometers can measure a very small magnetic moment (in the range of 10^{-8} emu) with high accuracy. The SQUID utilises two Josephson junctions, where a thin insulator separates two superconductors [146–148]. The Cooper

pairs present in the superconductors have a similar wave function as that of free electrons. When Cooper pair tunnel the Josephson junction, they have a phase difference proportional to the superconducting current.

$$i_s = i_c \sin \Delta\phi \quad 2.2$$

where i_s , i_c and $\Delta\phi$ are defined as superconducting current, critical current and the phase difference, respectively. Besides this phase difference an additional phase difference arises due to the application of the external magnetic field. The total phase shift can be quantised as

$$\Delta\phi(B) + 2\Delta\phi(i) = 2\pi n \quad 2.3$$

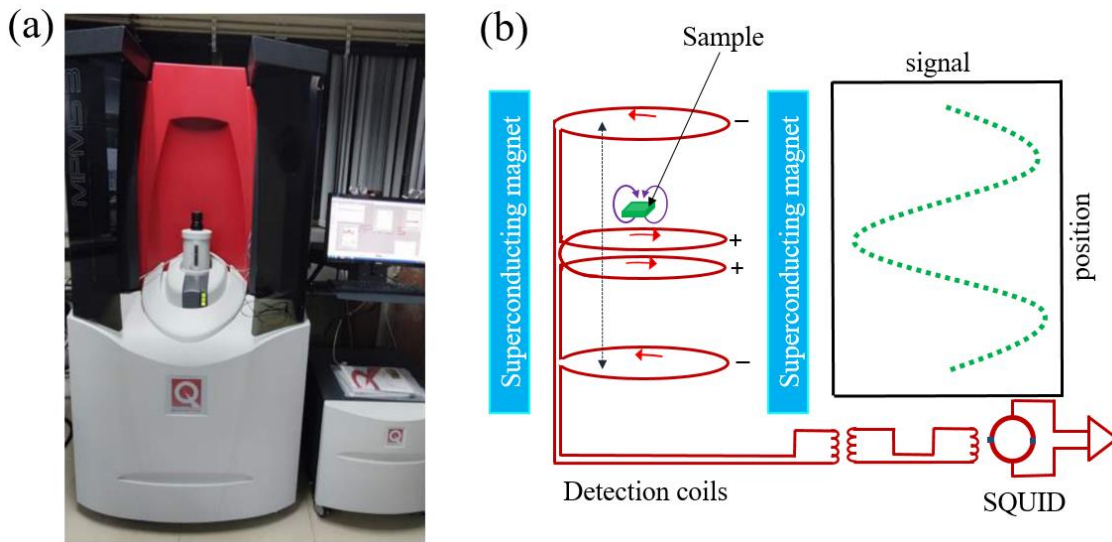


Figure 2.15 (a) SQUID magnetometry facility (MPMS-3) available at LNMM, SPS, NISER-Bhubaneswar. (b) The schematic of the SQUID set-up with detection coils.

Hence, the great sensitivity of SQUID can be attributed to the change in the magnetic field. The change in a magnetic field is directly related to the flux quantisation of the Josephson junction. The Schematic of SQUID working is shown in Fig.2.15 (b). The sample is kept in between the

detection coils, which are superconducting in nature. The coil arrangement is such that the middle coil will have a current flow opposite in the upper and lower coils. These coils are also known as second-order gradiometer coils. This whole assembly is located in between the solenoidal superconducting magnet. The magnetic field distribution inside the superconducting magnet is uniform because of its solenoidal shape. When a magnetic sample is moved inside the detection coils, it produces an alternating magnetic flux in the detection coils. A persistent current is generated in the detection coils due to this induced flux. This magnetic flux is transferred to *rf* SQUID, dipped in liquid He and located away from the sample. This SQUID works as a flux-to-voltage converter with very high sensitivity. Further, this voltage can be converted to the magnetic moment. Finally, the output signal is measured as a function of position, as shown in Fig.2.15 (b). The MPMS3 system, which we have used for measurement purposes, can produce a ± 7 T magnetic field and can be used in the 1.8 K to 400 K temperature range. We have performed magnetic measurements for single-layer LSMO and SRO samples and LSMO/SRO bilayer samples in SQUID magnetometry (MPMS3 manufactured by Quantum Design, USA), shown in Fig.2.15 (a). We have also used SQUID to determine the Curie (T_C) and Neel (T_N) temperatures of the FM and AFM films, respectively.

2.8 Ferromagnetic resonance (FMR) Spectrometer:

A ferromagnetic resonance (FMR) spectrometer is a very useful technique for studying the dynamic properties of a ferromagnetic material. Via this technique, we can evaluate the fundamental properties of a ferromagnetic material, i.e., Gilbert damping constant, gyromagnetic ratio, demagnetisation field etc. In terms of anisotropy study, the FMR setup can determine the

type of anisotropy present in the sample, i.e., uniaxial or cubic anisotropy etc. One can also evaluate the strength of anisotropy with the help of a FMR spectrometer.

FMR works in the principle of resonance. As shown in Fig.2.16 (a), in FMR, a coplanar waveguide (CPW) is used to transmit high-frequency electromagnetic waves (radio frequency signal in the GHz range). At the other end, the transmitted signal is received. If there is no microwave power loss, incident radiation will be equal to the transmitted radiation. However, some dielectric losses are always present due to joints, materials, and other factors. FMR setup is calibrated for these losses. After calibration, the loss is negligible if there is no external microwave-absorbing material. If there is any obstacle in the path of electromagnetic radiation, which can absorb microwave power, the transmitted signal will be less than the incident signal. Whenever any FM material is kept on top of the CPW line, according to the microwave absorption capacity of FM, there will be some finite loss in the microwave signal. Now a DC magnetic field (H) is applied to the FM sample, the spins of the FM will start aligning in the direction of H . Spins will align by precessing about the H axis. The frequency of the precession is known as Larmor frequency. This Larmor frequency for the FM is in the range of GHz and is magnetic field dependent. In FMR measurement frequency of the microwave is kept constant, and H varies over a wide range. Therefore, resonance occurs if Larmor frequency ν matches the microwave frequency. During the resonance, the amplitude of absorption of microwave power by the sample enhances drastically. Due to this, a sharp decrement in the transmitted spectra occurs near resonance shown in Fig 2.16 (c).

Macroscopically this FMR mechanism can be understood in terms of Zeeman splitting. When a magnetic field is applied, the Zeeman energy levels split into two levels having energy $\pm \frac{1}{2}g\mu_B H_{res}$. Hence, the separation between the energy levels is given by

$$\Delta E = g\mu_B H_{res} \quad 2.4$$

Here g is Lande g factor, μ_B is Bohr magneton, and H_{res} is the magnetic field value at which resonance occurs. When electromagnetic radiation (radio frequency field h_{rf}) having frequency ν is applied, the FM material absorbs energy $h\nu$ to reach the excited state. At resonance, the energy of the microwave is equal to the separation of Zeeman energy level, so

$$h\nu = g\mu_B H_{res} \quad 2.5$$

Fig.2.16 (b) shows the splitting of Zeeman levels. In Fig.2.16 (c), the typical transmitted FMR response has been shown. One can extract the value of H_{res} and line width ΔH (FWHM) from this transmitted spectrum using the following Lorentzian function.

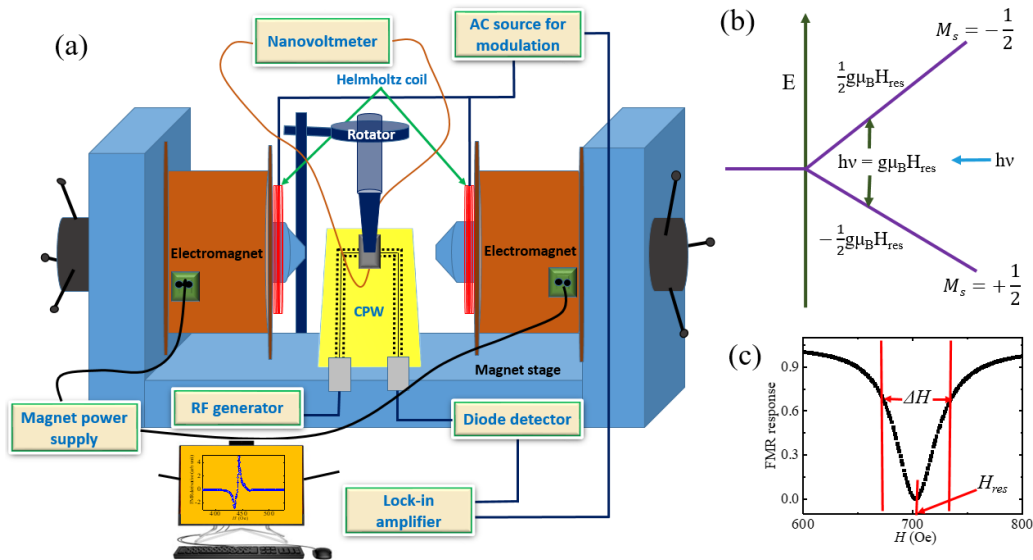


Figure 2.16 (a) Schematic of FMR spectrometer and ISHE measurement setup. (b) Schematic of the Zeeman splitting under the application of the external magnetic field. (c) FMR response with respect to the magnetic field.

$$\frac{dP}{dH} = S \frac{4\Delta H(H - H_r)}{[4(H - H_r)^2 + \Delta H^2]} - A \frac{\Delta H^2 - 4(H - H_r)^2}{[4(H - H_r)^2 + \Delta H^2]} + offset. \quad 2.6$$

Analyzing these extracted values, one can calculate the different magnetic parameters such as Gilbert damping constant, anisotropy, gyromagnetic ratio etc. For the extraction of the damping constant, FMR spectra were measured for a range of microwave frequency values. For each measured FMR spectra, H_{res} and ΔH values were obtained. f vs H_{res} data fitted by using the Kittel equation [26].

$$\omega = \gamma\mu_0\sqrt{(H_{ext} + H_K)(H_{ext} + H_K + M_S)} \quad 2.7$$

The Kittel equation has been explained in detail in the previous chapter in section 1.6. From the fitting of H_{res} vs f data, gyromagnetic ratio (γ) values were obtained. This obtained γ value is used to fit ΔH vs f data as following linear equation.

$$\Delta H = \Delta H_0 + \frac{4\pi\alpha f}{\gamma} \quad 2.8$$

The slope of the plot gives the α of the FM layer.

The FMR setup can be categorised into two sub-categories-

1. Lock-in-based FMR
2. VNA-based FMR

2.8.1 Lock-in-based FMR

As shown, the Fig.2.17 FMR setup consists of the following components-

1. Electromagnets: to produce DC magnetic field
2. RF signal generator: to generate the radio frequency (RF) signal
3. Coplanar waveguide (CPW): to guide the RF signal

4. Helmholtz coil: for the modulation of the signal.
5. Diode Detector: to detect the transmitted signal.
6. Lock-in-Amp: for better SNR and to lock the detecting signal.

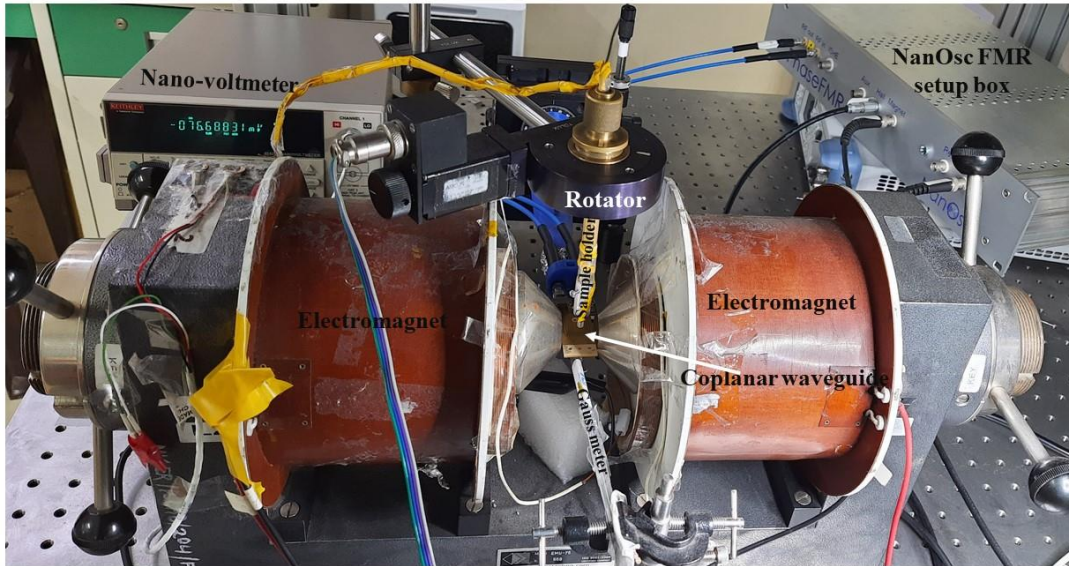


Figure 2.17 NanOsc Phase FMR set-up available at LNMM, SPS, NISER, Bhubaneswar.

The set-up has been modified for the ISHE measurements.

This setup can be operated in two different modes:

1. Constant frequency mode
2. Constant field mode

We fixed our RF frequency in constant frequency mode, and the DC magnetic field swept in a range. While in constant field mode keeping the field fixed, RF frequency sweeping is performed.

In this setup, we can perform our measurement in the 2 to 17 GHz RF frequency range, and the magnetic field can be swept in a range of ± 5 K Oe.

Lock-in-based FMR spectrometer gives a better signal-to-noise ratio; therefore, data obtained from this setup is very clean. However, this setup limitation is that we can detect the absorption signal only qualitatively. This setup does not give information on transmitted or reflected microwave signals quantitatively.

2.8.1 Vector network analyser (VNA)

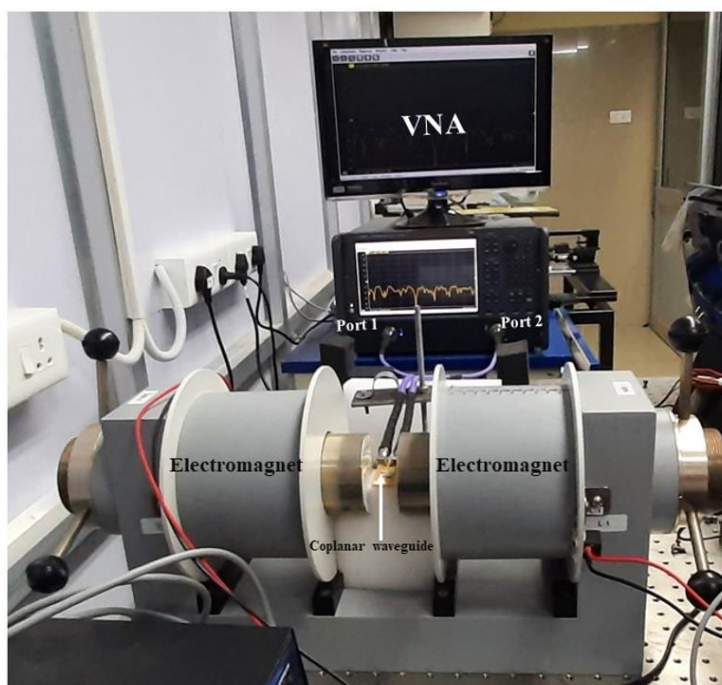


Figure 2.18 VNA-FMR setup available at LNMM, SPS, NISER, Bhubaneswar.

Sometimes it becomes essential to know the amount of power loss and phase change in the samples. A vector network analyser (Keysight PNA network analyzer (model N5222B)) is used to determine the transmitted (S_{21}) or reflected (S_{11}) signal quantitatively. As shown in Fig.2.18, VNA has two ports which can act as sources or detectors. However, one port can work as a source or sink at a time. So S_{21} is the signal where the source is port 1 while the signal is detected by port 2.

The loss in microwave signal due to absorption in a sample can easily determine by taking the difference between the reference and detected signals. We have made a setup for VNA-FMR in our lab. This VNA-FMR setup is also modified to perform angle-dependent ISHE. Different instruments, i.e., Nano-voltmeter, magnet power supply etc., are integrated using Lab-view software. This developed set-up can work in a broad frequency range, i.e., 10 MHz to 26.5 GHz, and the allowed field is in the range of ± 5000 Oe. VNA-FMR can be used in constant frequency as well as in constant field modes.

VNA-FMR has several advantages over FMR as it can give quantitative information. It can also detect transmitted as well as reflected microwave signals. The main drawback of this system is the poor signal-to-noise ratio.

2.8.3 ISHE Measurement setup

The spin pumping study in a bilayer system where one layer is ferromagnetic while the other layer can be any material which can have high spin-orbit coupling, i.e., heavy metals, antiferromagnetic, topological insulators, organic materials etc., is very useful to understand the spin to charge conversion efficiency of the bilayer system. As shown in Fig.2.17, the FMR setup has been modified to measure the ISHE voltage due to spin pumping via FMR. For this, a sample holder has been designed, which is associated with a motor. With the help of a motor, this sample holder can rotate from 0 to 360° in the plane of the magnetic field. A highly sensitive nanovoltmeter is also attached to determine the voltage generated due to spin pumping.

During the resonance, microwave absorption enhances. This absorbs microwave energy and excites the phonons of the FM system. When phonons come to the ground state, they emit their energy in the form of vibration and spin angular momentum. The phonon's vibration can raise the

sample's temperature, while the spin angular momentum gets dissipated into the adjacent NM layer in the form of spin current. The SOC of this NM layer causes the deflection of this spin current and results in transverse voltage. This process is known as ISHE. We record the FMR absorption and measured voltage simultaneously for each FMR spectra. The FMR spectra and measured voltage peak lie in the same magnetic field value, known as resonance field H_{res} . A detailed analysis of the ISHE signal can be found in individual chapters.

CHAPTER 3: Spin-to-charge conversion study in $\text{La}_{0.67}\text{Sr}_{0.33}\text{MnO}_3/\text{Pt}$ bilayer samples grown by oxygen-assisted molecular beam epitaxy

The charge current limits its application due to Joule heating effects. Due to Joule heating a significant amount of energy is lost in the form of heat energy, which also limits the further minimization of devices. Pure spin current (J_s) based devices have shown potential for fulfilling these requirements due to minimal charge current (J_c) involvement. In this context, ferromagnetic (FM)/heavy metal (HS) heterostructures are model systems to investigate various spin-dependent phenomena [14,149–151]. In the ISHE process, J_s is converted to J_c , and the below equation relates these two physical parameters:

$$\vec{J}_c = \theta_{SHA} \vec{J}_s \times \vec{\sigma} \quad 3.1$$

Where θ_{SHA} is the spin Hall angle (SHA), and σ is the polarisation vector transverse to the direction of J_s . The value of SHA, therefore, defines the charge to spin current conversion efficiency. The absorption of spin current (J_s^{abs}) generated by HS into FM creates a spin transfer torque, which can be quantified by spin torque efficiency $\zeta_{SH} = (2e/\hbar) J_s^{abs}/J_c$ [152]. In FM/HS heterostructures, spin pumping increases the value of α due to the absorption of spin angular momentum in the HS layer [153,154]. Further, in such FM/HS bilayers, another type of torque may occur, which is called anti-damping torque [155,156]. This later torque will lead to a decrease in the damping value of the bilayer as compared to the reference single FM layer. It is known that a large value of ζ_{SH} and lower α are important parameters for developing power-efficient devices. Therefore, the anti-damping torque may help to achieve magnetisation switching at a lower current density, which is proportional to α/ζ_{SH} , where α is the damping constant of the FM/HS bilayer [152]. We note that keeping a low α value with spin pumping is a challenge. However, anti-damping-like torque may help to balance the damping-like torque, which is the opposite of that and hence reduces the

value of α in FM/HS heterostructures. Pt has been used widely due to its high spin conductivity and SHA values [157–159]. Studies so far are concentrated mostly on Pt and ferromagnetic metals [158,160–162]. In this context ferromagnetic oxides, in particular, manganites, are worth investigating for spin-to-charge conversion-based applications. $\text{La}_{0.67}\text{Sr}_{0.33}\text{MnO}_3$ (LSMO) is one such ferromagnetic oxide well known for exhibiting high Curie temperature ($T_C \sim 350$ K) and nearly 100% spin polarisation (in bulk) [107]. There are a few reports where spin pumping has been investigated in LSMO/Pt bilayers for which the LSMO is primarily prepared by pulsed laser deposition technique [104,105,163–166]. In this work, we aim to study LSMO/Pt bilayers where the samples have been fabricated by the oxide molecular beam epitaxy (OMBE) technique. In recent years OMBE has been proven to be an excellent technique for growing high-quality complex oxide thin films.

Table 3.1: Sample details studied in this work and their corresponding nomenclature	
Sample Name	Sample Structure
S1	$\text{SrTiO}_3(001)/\text{LSMO}(20 \text{ nm})$
S2	$\text{SrTiO}_3(001)/\text{LSMO}(20 \text{ nm})/\text{Pt}(4 \text{ nm})$
S3	$\text{SrTiO}_3(001)/\text{LSMO}(20 \text{ nm})/\text{Pt}(10 \text{ nm})$

The sample listed in Table 3.1 were prepared on a single crystalline $\text{SrTiO}_3(001)$ substrate using an oxygen plasma-assisted molecular beam epitaxy (MBE) system. Samples were prepared via a collaboration between Prof. S. Bedanta and Prof. Thomas Brückel in Forschungszentrum Jülich, Germany. I sincerely acknowledge Prof. Subhankar Bedanta, and the group members of Prof. Thomas Brückel, Dr. Anirban Sarkar and Dr. Markus Waschk for the sample preparation via collaborative work. The surface and crystalline quality of LSMO films were characterized by in-

situ low energy electron diffraction (LEED) and high energy electron diffraction (RHEED). X-ray diffraction was performed to determine the crystalline phases. Film thicknesses were obtained using X-ray reflectivity at NISER. Magnetization dynamics was studied using co-planer waveguide (CPW) based ferromagnetic resonance (FMR) spectroscopy at NISER. The ISHE measurements were performed using an in-house developed FMR-based ISHE setup. A nanovoltmeter was connected over the two ends of the sample. The measurements were performed on samples of dimension $3 \times 2 \text{ mm}^2$. Angle-dependent ISHE has been performed at $f = 7 \text{ GHz}$ to disentangle spin rectification effects. Microwave power-dependent ISHE measurement has been performed using *rf* signal generator (SMB-100 model from ROHDE & SCHWARZ).

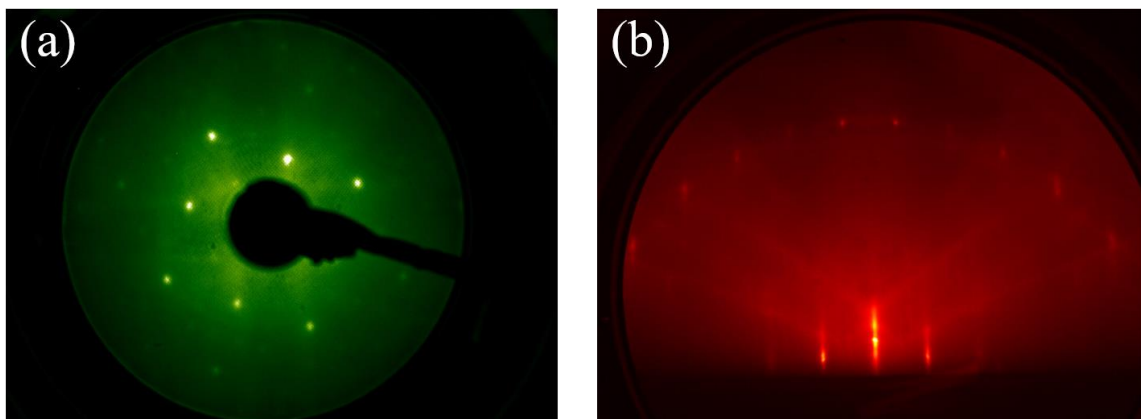


Figure 3.1 (a) LEED (b) RHEED images for sample S1

Fig.3.1 (a) and (b) show the LEED and RHEED images, respectively, for the 20 nm thick LSMO film (sample S1). The presence of sharp spots (Fig.3.1 (a)) and streaks (Fig.3.1 (b)) confirms the epitaxial growth of LSMO films on the $\text{SrTiO}_3(001)$ substrate. The RHEED image also indicates a smooth surface of the LSMO film. The X-ray diffraction shown in Fig.3.2, from the data it is evident that the diffraction peaks are corresponding to 001, 002 and 003 diffractions of STO and LSMO films. Hence the XRD diffraction data also confirms that films are crystalline in nature.

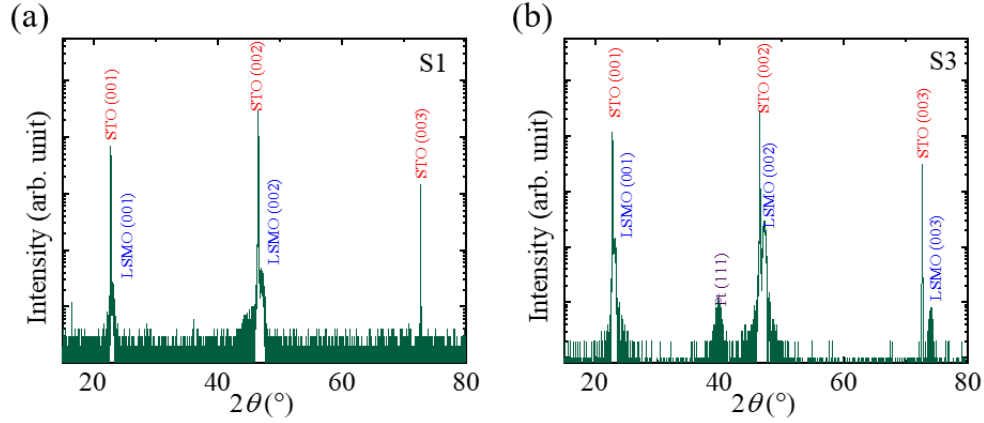


Figure 3.2 X-ray diffraction pattern measured in θ - 2θ geometry for samples (a) S1 and (b) S3.

FMR spectra for a frequency range of 4-16 GHz have been plotted in Fig.3.3(a)-(c) for samples S1, S2 and S3, respectively. Fig.3.4 (a) shows the f vs H_{res} plot for all the samples obtained from the frequency-dependent FMR spectra. The data have been fitted by Kittel equation [26],

$$f = \frac{\gamma}{2\pi} \sqrt{(4\pi M_{eff} + H_{res} + H_K)(H_{res} + H_K)} \quad 3.2$$

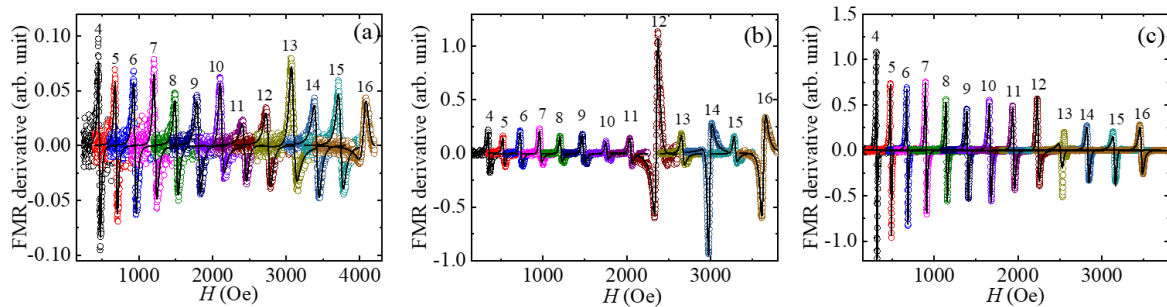


Figure 3.3 FMR signal for different frequencies for samples (a) S1, (b) S2 and (c) S3.

Where $\gamma (=g\mu_B/\hbar)$, g , μ_B and M_{eff} are gyromagnetic ratio, Lande g -factor, Bohr magneton and effective demagnetization, respectively. H_K , K_S and t_{FM} are in-plane anisotropic fields,

perpendicular surface anisotropy constant, and thickness of the LSMO layer, respectively. Further, α was evaluated by fitting data of Fig.3.4 (b) using the relation [167,168].

$$\Delta H = \Delta H_0 + \frac{4\pi\alpha f}{\gamma} \quad 3.3$$

The values of α for samples S1, S2 and S3 are extracted to be 0.0104 ± 0.0003 , 0.0046 ± 0.0004 and 0.0037 ± 0.0004 , respectively. It should be noted that Pt is a well-known metal for exhibiting high SOC, and when coupled to a FM layer, it may lead to an increase in α . However, in our case, it is observed that there is a decrease in α with an increase in t_{Pt} in comparison to the single LSMO layer (S1). The reason for this lowering of α could be an anti-damping-like torque.

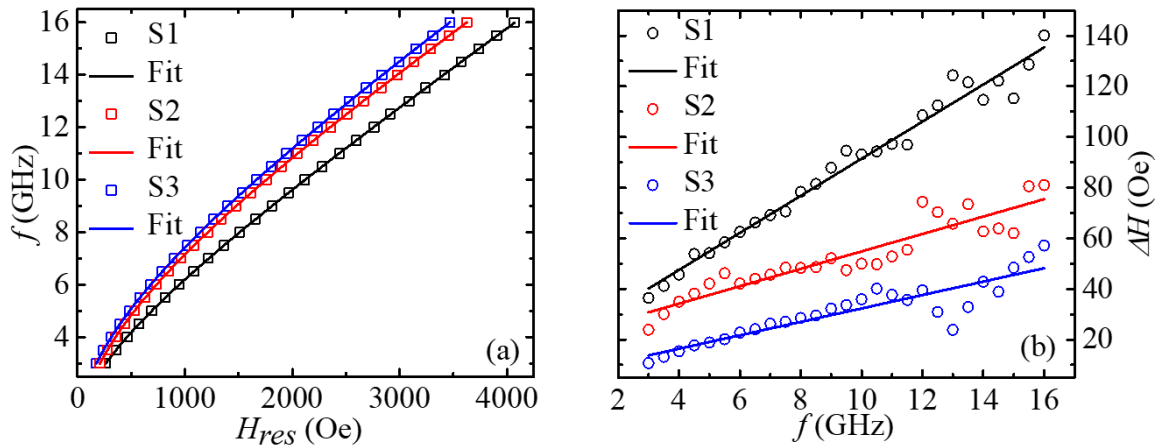


Figure 3.4 (a) f vs H_{res} and (b) ΔH vs f for samples S1, S2 and S3 studied by lock-in based FMR. The solid lines in (a) and (b) are the best fits for equations (3.2) and (3.3), respectively.

Similar anti-damping behaviour has been observed in β -Ta and Py bilayer systems studied by Behera et al. [169]. The anti-damping in an FM/HS heterostructures can be explained in the following manner. In the case of the spin-flip parameter (ϵ) <0.1 , spin angular momentum at the

FM/HS interface creates a non-equilibrium spin density in the Pt layer [29]. This results in a backflow of spin current (J_s^0) into the LSMO layer, which has two components, (i) parallel and (ii) perpendicular to instantaneous magnetisation $m(t)$ of the LSMO layer. The parallel component to $m(t)$ counteracts the spin pumping from the LSMO layer and suppresses the spin pumping in the Pt layer. The transverse component to J_s^0 generates an additional spin-orbit torque (SOT) on this in-plane $m(t)$ of the LSMO layer. This SOT can be effective up to a distance twice the spin diffusion length (λ_{SD}) [170]. Spin accumulation at the interface is very sensitive to λ_{SD} of the Pt layer. For $t_{Pt} < \lambda_{SD}$, spin accumulation dominates over the bulk SOC of Pt. This leads to an increase in J_s^0 and a decrease of α . For $t_{Pt} > 2 \lambda_{SD}$, J_s^0 decreases, which results in a decrease of SOT. This decrease in SOT may lead to an increase in α . We have considered λ_{SD} of 5.9 nm from literature, where the samples studied had a similar structure [104].

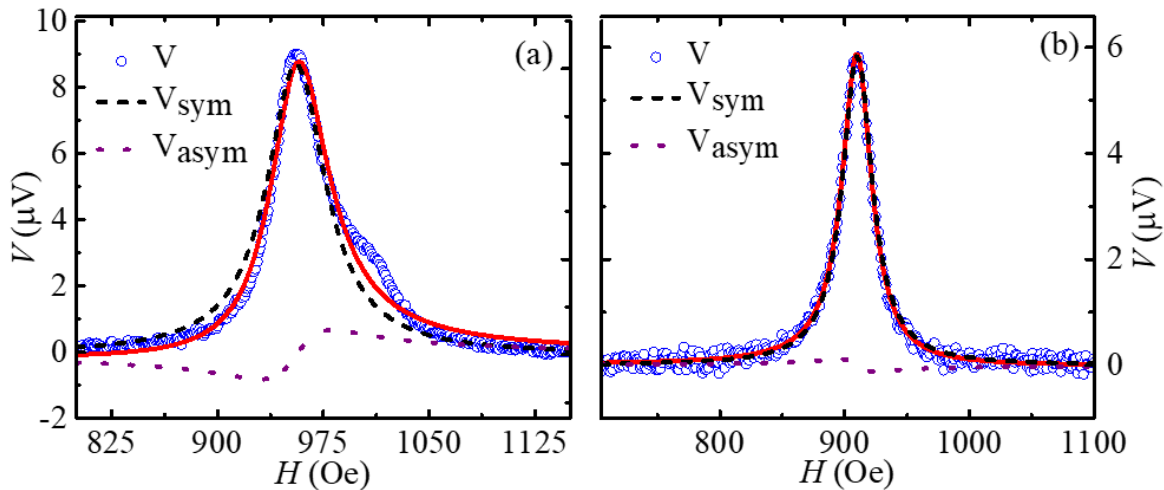


Figure 3.5 ISHE voltage for samples S2 and S3 are shown in (a) and (b), respectively. Open circles (in blue) are the measured ISHE voltage, and the solid line (in red) represents the best fit of the data fitted by equation (3.4). Dash (in black) and dot (purple) lines represent the V_{sym} and V_{asym} components, respectively, evaluated by fitting to equation (3.4).

Therefore, it can be concluded that the anti-damping-like torque is very high and opposite in our samples to overcome damping-like torque, which leads to the reduction of the value of α . To quantify the spin pumping, we have performed ISHE measurements. Fig.3.5 (a) and (b) represent the ISHE voltage (V_{meas}) vs applied field (H) for samples S2 and S3, respectively. It is noted that no ISHE signal has been observed for the reference sample S1. We have separated symmetric (V_{sym}) and anti-symmetric (V_{asym}) voltage signals by using the following equation [171],

$$V_{total} = V_{sym} \frac{(\Delta H)^2}{(H - H_{res})^2 + (\Delta H)^2} + V_{asym} \frac{\Delta H(H - H_{res})}{(H - H_{res})^2 + (\Delta H)^2} \quad 3.4$$

Fig. 3.5 (a) and (b) show that the V_{sym} component is larger than V_{asym} . It is well known that symmetric signal comes predominantly from spin pumping, while asymmetric signal is due to other rectification effects [172]. To separate the effect of anomalous Hall effect (AHE) and anisotropic magnetoresistance (AMR) from spin pumping, we have performed angle (ϕ) dependent ISHE at a step of 2° in the range of 0 to 360° . Here (ϕ) is defined as the angle between the direction of the applied magnetic field (H) and the contacts for voltage measurement. Fig.3.6 (a) and (b) show the angle-dependent V_{sym} and V_{asym} for sample S2, respectively. Similarly, Fig.3.6 (c) and (d) show the evaluated V_{sym} and V_{asym} for sample S3. These plots were fitted using the following relations [173],

$$\begin{aligned} V_{sym} = & V_{sp} \cos^3(\phi + \phi_0) + V_{AHE} \cos \theta \cos(\phi + \phi_0) \\ & + V_{sym}^{AMR \perp} \cos 2(\phi + \phi_0) \cos(\phi + \phi_0) \\ & + V_{sym}^{AMR \parallel} \sin 2(\phi + \phi_0) \cos(\phi + \phi_0) \end{aligned} \quad 3.5$$

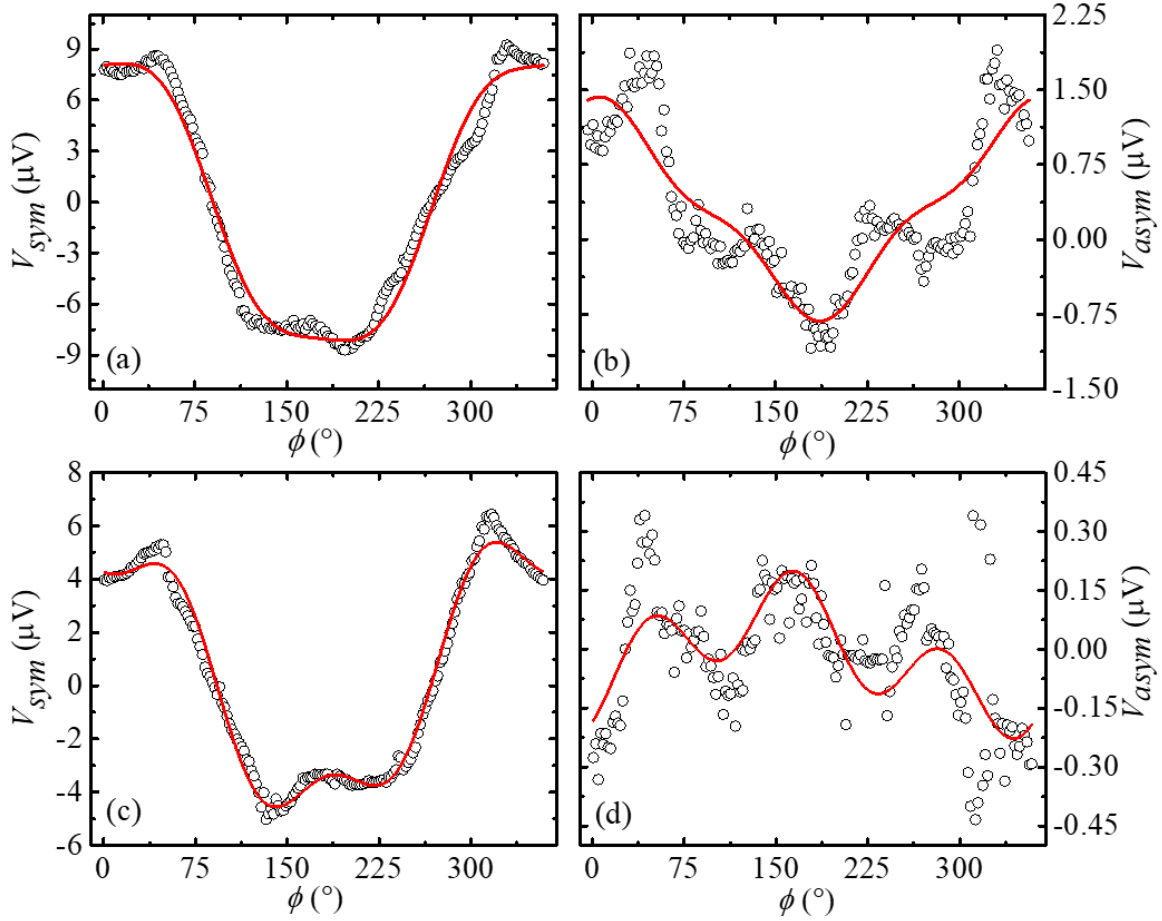


Figure 3.6 (a) and (c) show the angle dependent V_{sym} for samples S2 and S3, respectively. (b) and (d) show the angle-dependent V_{asymp} for samples S2 and S3, respectively. Figures (a) and (c) were fitted by using equation (3.5) while Figures (b) and (d) were fitted by using equation (3.6).

$$\begin{aligned}
 V_{asymp} = & V_{AHE} \sin(\theta) \cos(\phi + \phi_0) \\
 & + V_{asymp}^{AMR \perp} \cos 2(\phi + \phi_0) \cos(\phi + \phi_0) \\
 & + V_{asymp}^{AMR \parallel} \sin 2(\phi + \phi_0) \cos(\phi + \phi_0)
 \end{aligned} \tag{3.6}$$

where V_{sp} and V_{AHE} are voltages due to spin pumping and anomalous Hall effect, further $V_{asym,sym}^{AMR\parallel}$ and $V_{asym,sym}^{AMR\perp}$ are the parallel and perpendicular components of the AMR voltage, respectively. θ

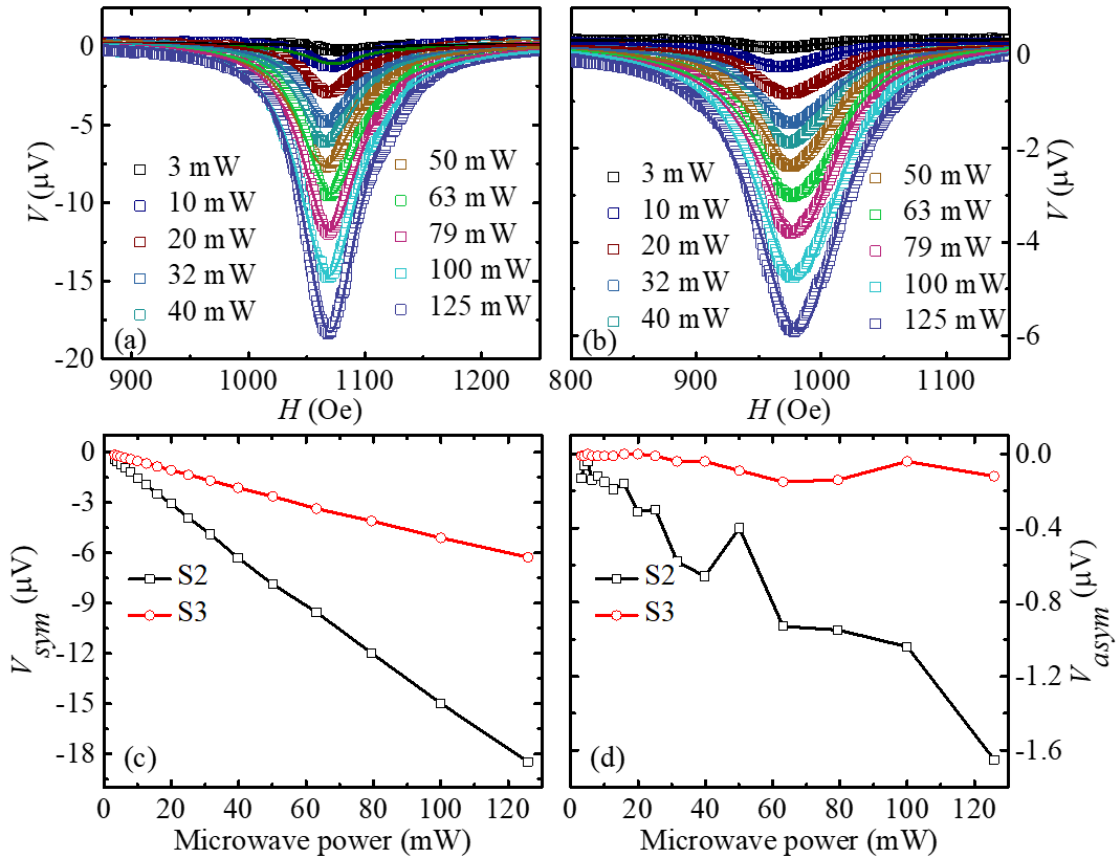


Figure 3.7 (a) and (b) Power-dependent voltage signal for samples S2 and S3 measured at $f=7$ GHz. (c) and (d) show power-dependent V_{sym} and V_{asym} components for samples S2 and S3, respectively.

is the angle between h_{rf} and H , which is 90° in our case, as shown in Figure 1(a). So, equations (3.5) and (3.6) can be written as

$$V_{asym} = V_{AHE} \cos(\phi) \sin \theta + V_{asym}^{AMR \perp} \cos 2(\phi) \sin \theta + V_{asym}^{AMR \parallel} \sin 2(\phi) \cos(\phi) \quad 3.7$$

where $V_{AMR}^{\perp, \parallel}$ can be evaluated by the following equation [173] [38]

$$V_{AMR}^{\perp, \parallel} = \sqrt{(V_{asym}^{AMR \perp, \parallel})^2 + (V_{sym}^{AMR \perp, \parallel})^2} \quad 3.7$$

The values V_{sp} , V_{AHE} , V_{AMR}^{\perp} and V_{AMR}^{\parallel} for samples S2 and S3 were obtained from the best fits and listed in table 3.2.

Sample	V_{sp} (μV)	V_{AHE} (μV)	V_{AMR}^{\perp} (μV)	V_{AMR}^{\parallel} (μV)
S2	20.05 ± 0.28	0.77 ± 0.05	11.98 ± 0.36	0.34 ± 0.22
S3	12.79 ± 0.11	-0.01 ± 0.01	8.49 ± 0.37	0.55 ± 0.07

From Table 3.2, it is observed that V_{sp} decreases for higher Pt thickness. We calculated θ_{SHA} using the below equations [171,174].

$$V_{ISHE} = \left(\frac{w}{t_{LSMO}/\rho_{LSMO} + t_{Pt}/\rho_{Pt}} \right) \times \theta_{SHA} \lambda_{SD} \tanh \left[\frac{t_{Pt}}{2\lambda_{SD}} \right] J_s \quad 3.8$$

where J_s is given by,

$$J_s \approx \left(\frac{g_r^{\uparrow} \hbar}{8\pi} \right) \left(\frac{\mu_0 h_{rf} \gamma}{\alpha} \right)^2 \times \left[\frac{\mu_0 M_S \gamma + \sqrt{(\mu_0 M_S \gamma)^2 + 16(\pi f)^2}}{(\mu_0 M_S \gamma)^2 + 16(\pi f)^2} \right] \left(\frac{2e}{\hbar} \right) \quad 3.9$$

and

$$g_r^{\uparrow} = g_{eff}^{\uparrow} \left[1 + \frac{g_r^{\uparrow} \rho_{Pt} \lambda_{SD} e^2}{2\pi \hbar \tanh \left[\frac{t_{Pt}}{2\lambda_{SD}} \right]} \right]^{-1} \quad 3.10$$

where w , M_S and g_{eff}^{\uparrow} are the width of CPW, saturation magnetisation and spin mixing conductance of the bilayers, respectively. For the evaluation of g_{eff}^{\uparrow} the resistivity (ρ) of the

Chapter 3: Spin-to-charge conversion study in $La_{0.67}Sr_{0.33}MnO_3/Pt$ bilayer samples grown by oxygen-assisted molecular beam epitaxy

samples was calculated by the four-probe method. The (ρ) values are 4.79×10^{-5} , 7.33×10^{-7} and 5.25×10^{-7} Ω -m for the samples S1, S2 and S3, respectively. The value of $g_{eff}^{\uparrow\downarrow}$ can be calculated by the following expression using the damping constant [29]

$$g_{eff}^{\uparrow\downarrow} = \frac{\Delta\alpha 4\pi M_s t_{LSMO}}{g\mu_B} \quad 3.11$$

where $\Delta\alpha$ is the change in the α due to spin pumping.

The values of θ_{SHA} are evaluated to be 0.033 and 0.014 for samples S2 and S3, respectively. These θ_{SHA} values match well to the previously reported values for the Pt [171,175,176] in a similar type of system. For comparison with the LSMO/Pt system we have also prepared one sample S4 with the structure Si/Co₂₀Fe₆₀B₂₀ (5 nm)/Pt (3 nm) by the DC sputtering system. The calculated value of θ_{SHA} for sample S4 is 0.022, which is in the range of θ_{SHA} for Pt in the LSMO/Pt system as mentioned earlier. It is to be noted that V_{sp} for sample S2 is nearly 15 times higher than that for sample S4. However, the enhancement in θ_{SHA} for S2 in comparison to S4 is only 1.1%. To further confirm that the V_{meas} is primarily due to spin pumping, we have performed microwave power-dependent ISHE at 7 GHz. Power-dependent measurement was performed in the microwave power range of 3 to 125 mW. Microwave power-dependent voltage signal is shown in Fig.3.7 (a) and (b) for samples S2 and S3, respectively. Fig.3.7 (c) shows the power-dependent symmetric voltage part for samples S2 and S3. The linear increase in microwave power leads to an increase in V_{sym} signal strength for samples S2 and S3, which confirms that V_{meas} was mainly due to spin pumping. Fig.3.7 (d) shows the V_{asym} dependency over microwave power for samples S2 and S3.

Authors	System	Preparation technique	V_{sp} (μV)	$g_{\text{eff}}^{\text{fl}}$ (m^{-2})	Power (mW)	α (10^{-3})
Atsarkin et al. [164]	LSMO(80 nm)/Pt(10 nm)	PLD	0.56	$10^{16} - 10^{17}$	250	-
Luo et al. [104]	LSMO(20 nm)/Pt(6-30 nm)	PLD	8	1.8×10^{19}	100	4-8
Lee et al. [105]	LSMO(30 nm)/Pt(5-9 nm)	PLD	0.3	2.1×10^{19}	-	1.9-2.9
Luo et al. [165]	LSMO(29 nm)/Pt(10nm)	PLD	~ 1	-	100	-
Luo et al. [166]	LSMO(20 nm)/Pt(5.5 nm)	PLD	~ 5	-	125	~ 5.93
Luo et al. [163]	LSMO(26)/Pt(5.5)	PLD	~ 3.25	-	40	~ 6.50
This work [177]	LSMO(20nm)/Pt(4nm)	OMBE	20.05	1.48×10^{19}	25	4.6

In summary, we have studied spin pumping and ISHE for LSMO/Pt bilayer samples prepared by oxide molecular beam epitaxy. We have observed a decrease in the value of α with an increase in the Pt thickness. This decrease in value may be due to anti-damping-like torque. At the low value of α , we have observed high spin pumping voltage, which makes this system ideal for developing power-efficient spintronics devices. In Table 3.3, we compare various parameters from the literature for LSMO/Pt bilayers. We found a spin Hall angle value of 0.033 for 3 nm Pt thickness which is in the range of previously reported values. It seems that the oxide molecular beam epitaxy is a suitable technique for preparing high-quality complex oxides.

CHAPTER 4: Tailoring spin to charge conversion efficiency via microwave frequency in

$\text{La}_{0.67}\text{Sr}_{0.33}\text{MnO}_3/\text{Pt}$ bilayer system

Higher spin-orbit coupling is desired for better conversion efficiency [84,160]. However, several other parameters, i.e., electrical resistivity (ρ), Gilbert damping constant (α) of ferromagnetic material, spin polarization, interface roughness, thin film quality etc., play a crucial role in improving conversion efficiency. Higher spin angular momentum transfers from ferromagnet (FM) to heavy metal (HS) and large spin pumping voltage in these FM/HS bilayers are the key parameters to operate the spin-based memory and logic devices. In such FM/HS heterostructures, the spin current is generated using spin pumping phenomena, where a magnetic field (H) is applied in FM material, and the system is perturbed using a microwave frequency (h_{rf}) signal [178,179]. Due to the application of H , spins of FM material precess with a frequency known as Larmor precessional frequency. When applied microwave frequency matches Larmor frequency, ferromagnetic resonance (FMR) occurs, and an enhanced absorption peak is observed. This enhanced amplitude causes the transfer of spin angular momentum from the FM layer to the neighbour HS layer. In this phenomenon, the J_s is pumped into the HS layer. Spin-orbit interaction (SOI) of HS causes spin-lattice coupling, i.e., the spin angular momentum of the electron couples with orbital angular momentum in the lattice. This coupling can give rise to damping, which will exert an additional torque to precessing spins in the direction of equilibrium, and the excess angular momentum dissipated into the lattice of this FM subsystem [26].

The spin pumping phenomenon is very interesting and important as it generates pure J_s , and there is no involvement of J_c in this process. This gives a dimension to study the systems with insulating or high resistive FM layers with HS layer. This pumped J_s gets deflected towards the transverse direction and causes the generation of potential difference [153,180]. A combination of FM/HS

bilayer is required for such type of study. Our previous work showed that OMBE prepared LSMO/Pt heterostructures possess very high spin pumping voltage [177]. Due to anti-damping-like torque [169,177], the α significantly decreases in LSMO/Pt bilayer system in comparison to LSMO single layer. In this work, we have explored the microwave frequency dependency of spin pumping. Here we have attempted to co-relate the FMR absorption amplitude to spin pumping voltage amplitude. In the previous chapter, it has been shown that spin pumping voltage first increases up to certain frequencies. Further increase in frequency leads to a reduction in spin pumping voltage [181–183]. The reason can be the heating effect at higher frequencies. Kurebayashi et al. [181] have shown that in YIG/Pt system, spin angular momentum generated from microwave absorption to J_s conversion efficiency is higher at lower frequencies. Hence, with the increase in frequency, the conversion efficiency decreases. The conversion efficiency of J_s to J_c is defined as spin Hall angle (θ_{SHA}), which relates J_c to J_s via equation $J_c = \theta_{SHA} J_s \times \sigma$, where σ is the polarization vector transverse to the J_s [180]. This work also demonstrated that changing the microwave frequency could tune spin-to-charge conversion efficiency.

The samples S1: SrTiO₃(001)/LSMO(20 nm) and S2 : SrTiO₃(001)/LSMO(20 nm)/Pt(4 nm) were prepared using OMBE. The crystalline nature of the samples has been confirmed by in-situ RHEED and LEED for reference sample S1, which can be found in our earlier work [13]. X-ray diffraction (XRD) has been performed using Rigaku SmartLab. Sample preparation has been made for Cross-sectional TEM (details of the preparation process are given in Ref. [145]). Cross-sectional high-resolution transmission electron microscopy (HRTEM) images and selected area electron diffraction (SAED) have been taken by a microscope manufactured by JEOL (model Nr. F-200). To calculate the FMR absorption amplitude, the transmitted coefficient (S_{21}) has been measured in the frequency (f) range of 2 to 15 GHz in steps of 0.2 GHz using Keysight N5222B

vector network analyzer (VNA). Simultaneously frequency dependent voltages have been measured using a Keithley 2182A Nano voltmeter. Further angle-dependent ISHE measurements at different frequencies have been performed to separate out the rectification effects from spin pumping voltage using our home-built ISHE setup [19]. In this study, all the FMR and ISHE measurements were performed at 100 mW microwave power (SMB-100 model from ROHDE & SCHWARZ). For all the measurements, we used a $3 \times 2 \text{ mm}^2$ sample. More details of ISHE measurement can be found in our previous works [168,184–188].

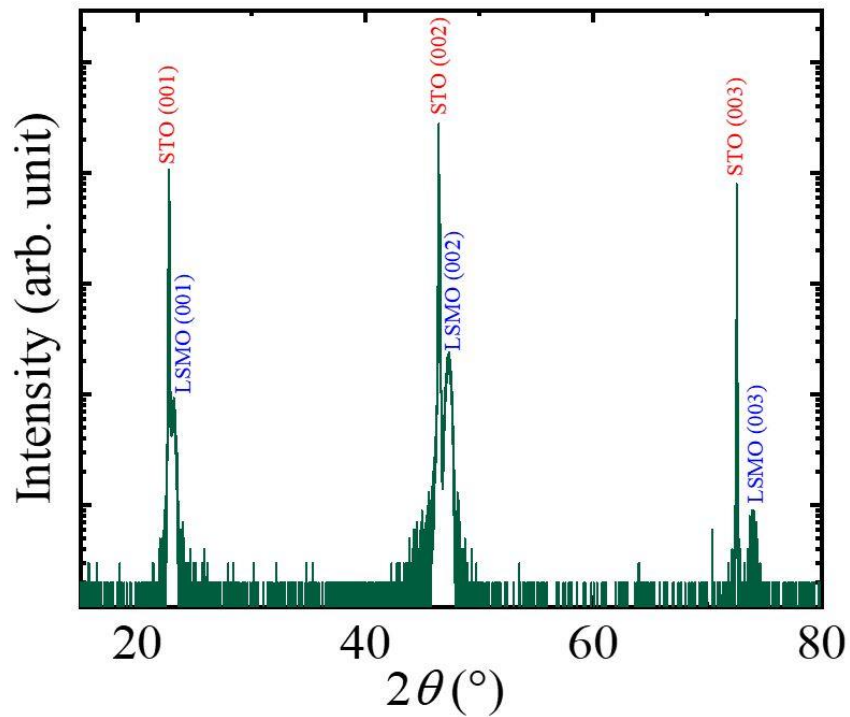


Figure 4.1 X-ray diffraction for sample S2. The XRD measurement has been performed in θ - 2θ geometry.

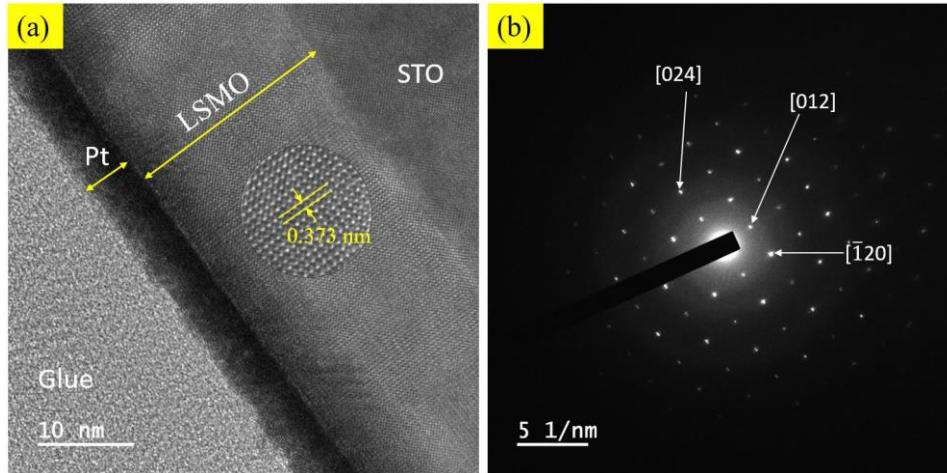


Figure 4.2 TEM image for sample S2, and SAED image for STO/LSMO interface are shown in (a) and (b), respectively.

Fig.4.1 shows the XRD data for sample LSMO/Pt(4 nm). LSMO peaks, which correspond to STO 001 planes, have been observed in the diffraction pattern. This confirms the crystalline nature of LSMO films. From the cross-sectional HRTEM image of sample S2, as shown in Fig.4.2 (a), it can be concluded that the STO/LSMO and LSMO/Pt interfaces are sharp. The zoomed-in image shown in Fig.4.2 (a) confirms the epitaxial nature of LSMO. It is to be noted that this is the same sample which has been studied in our previous work as sample S2[13]. SAED pattern (shown in Fig.4.2 (b)) taken at the interface between STO and LSMO again confirms that LSMO has grown in [012] orientation. In-situ RHEED and LEED patterns for sample S1 have clearly shown the epitaxial nature of LSMO films, as shown in our previous work [177].

FMR and ISHE analysis

The full-range FMR spectra for samples S1 and S2 have been performed in the range of 4 to 17 GHz, as shown in Fig.4.3 (a) and (b). From the FMR spectra shown in Fig.4.3 (a) and (b), it is observed that LSMO shows sign change behaviour in the frequency range of 12 to 16 GHz. In this

frequency range, FMR spectra change their sign. For example, the sign of the FMR signal at 13 GHz is negative, and the sign changes to positive at 14 GHz. Further, by changing the frequency to 15 GHz, the sign of the FMR spectra flips to its initial sign, i.e., negative. We have not observed such sign change in any other metallic FM samples with our FMR setup [168,189]. To avoid any anomaly, we have measured FMR spectra in this range multiple times and observed that the results are reproducible. From the HRTEM image, no apparent structural defects are visible in the LSMO film. We have also observed similar sign change behaviour in PLD-grown STO/LSMO samples (data not shown). Therefore, the FMR signal's sign change as a frequency function is believed to be intrinsic to STO/LSMO. This sign change in FMR absorption may be due to heating effects as during resonance, sample temperature can rise to a few degrees [190] which may lead to a change in the dielectric property of samples. However, a clear understanding of this heating effect on microwave absorption is lacking, which should be addressed theoretically.

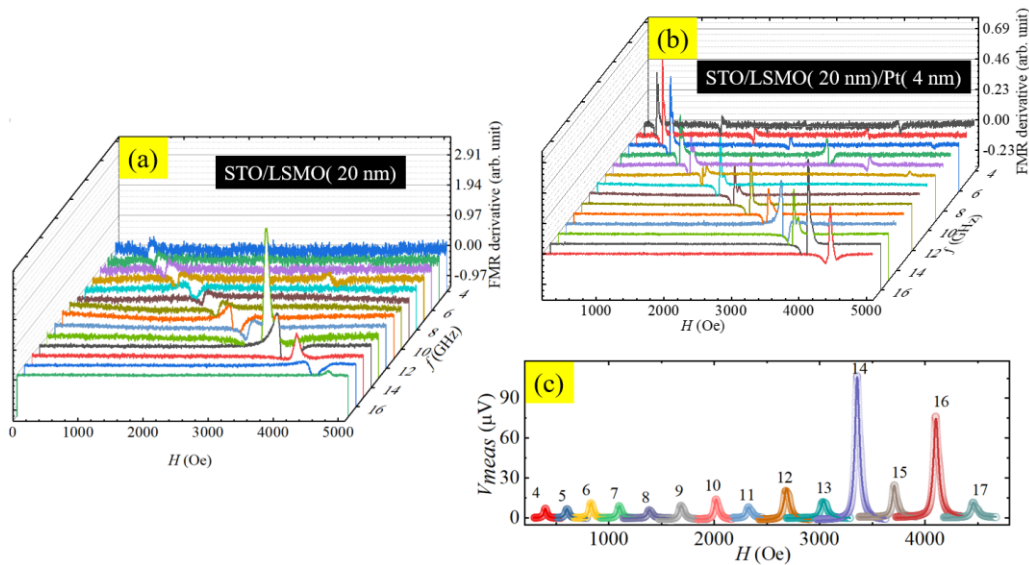


Figure 4.3 FMR spectra for samples (a) S1 and (b) S2. (c) Corresponding measured voltage for sample S2. The numbers shown in the figure are the microwave frequency in GHz. Solid lines in (c) are the best fits to the data using equations (4.1).

Interestingly other FMR modes, in addition to uniform modes, have been observed, as shown in Fig.4.3 (b). Uniform modes have the highest intensity, and they are primarily contributing to ISHE voltage. Hence for simplicity, only uniform modes have been considered for all ISHE measurement and analysis purposes. During the FMR measurement, generated voltage (V_{meas}) corresponding to uniform mode was measured, shown in Fig.4.3 (c).

Microwave absorption analysis

To confirm our observation that V_{meas} is proportional to FMR absorption intensity, we have performed a systematic frequency-dependent spin pumping study. VNA setup has been modified to measure ISHE voltage during FMR measurement. S_{21} parameter from 2 to 15 GHz at a step of 0.2 GHz has been recorded. S_{21} is a transmitted parameter, while the resonance transmitted parameter reduces significantly. Hence a dip is observed. In this work, microwave absorption intensity from the S_{21} parameter has been calculated. As the microwave absorption increases at resonance, we observe a peak in absorption data. It is observed that absorption spectra change their sign around higher frequencies. Data for 13 to 15 GHz, where sign change in FMR absorption spectra takes place, has been shown in Fig.4.4 (a)-(i). During the FMR, the lattice of FM absorbs the microwave energy and gets excited. The lattice of FM releases this energy in the form of heat generated in the sample and the spin angular momentum. This spin angular momentum gets transferred to the neighbour Pt layer.

We have measured the voltage corresponding to FMR absorption simultaneously. The assumption that measured voltage intensity followed the same trend as the absorbed FMR spectra intensity seems valid. Each measured voltage has been fitted to separate symmetric (V_{sym}) and asymmetric voltage contributions (V_{asym}) using the following equation [171]

$$V_{total} = V_{sym} \frac{(\Delta H)^2}{(H - H_{res})^2 + (\Delta H)^2} + V_{asym} \frac{\Delta H(H - H_{res})}{(H - H_{res})^2 + (\Delta H)^2} \quad 4.1$$

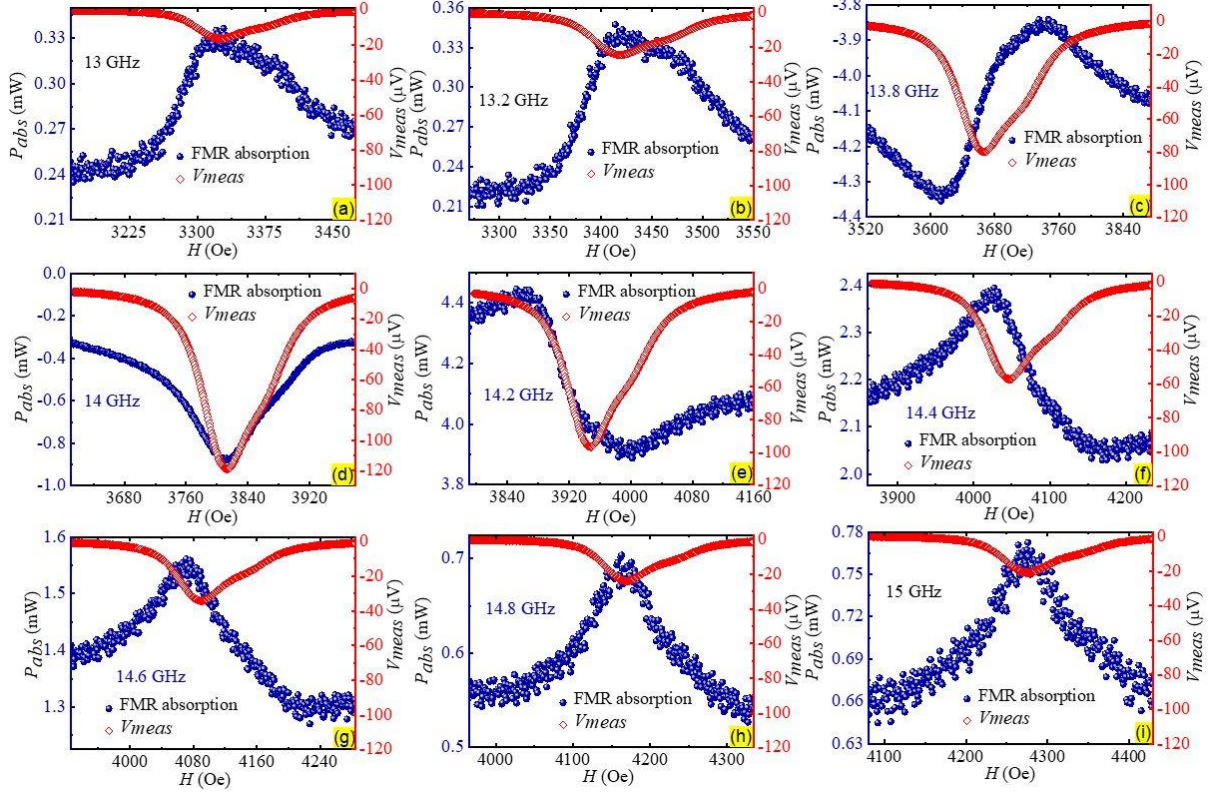


Figure 4.4 (a)- (i) P_{abs} and their corresponding V_{meas} for different frequencies. The blue circle represents VNA FMR absorption spectra, and the red open square represents the measured voltage. (d) P_{abs} and V_{sym} dependency on f .

Further, V_{sym} and P_{abs} have been plotted with frequency, as shown in Fig.4.5 (a). The V_{sym} follows the trends of P_{abs} . Further, in Fig.4.5 (b), we have plotted the microwave absorption-generated spin angular momentum to J_s conversion efficiency with f . This efficiency has been defined by Kurebayashi [181] as the ratio between voltage signals (V_{sym}) to input microwave power (P_{in}). For determining P_{in} , we have calibrated the VNA setup without resonance condition, and the obtained transmitted parameter has been considered as P_{in} . P_{abs} have been taken as the difference between

the P_{in} to a transmitted parameter during resonance. We have fitted the spin angular momentum to J_s conversion efficiency as shown in Fig.4.5 (b) using equation [182]

$$\frac{V_{sym}}{P_{in}} = K \frac{1}{\sqrt{1 + \left(\frac{4\pi f}{\gamma M_s}\right)^2}} \quad 4.2$$

$$K = \frac{e L \theta_{SHA} g_r^{\uparrow} \lambda \tanh\left(\frac{t_{Pt}}{2\lambda}\right)}{\pi \mu_0 \nu t_{Pt} \sigma M_s^2 \alpha} \quad 4.3$$

where e is the charge of the electron, L , θ_{SHA} , g_r^{\uparrow} , t_{Pt} , λ , ν , M_s and σ are defined for the Pt layer as the length between the electrodes, spin Hall angle, the real part of spin mixing conductance, the thickness of the Pt layer, spin diffusion length, the volume of the magnetic layer, saturation magnetization and electrical conductivity, respectively. The value of α has been taken from our previous work [177]. We have fitted the efficiency for different frequencies (shown as the solid red line in Fig.4.5). As shown in Fig.4.5, at lower frequency range, the experimental data shows

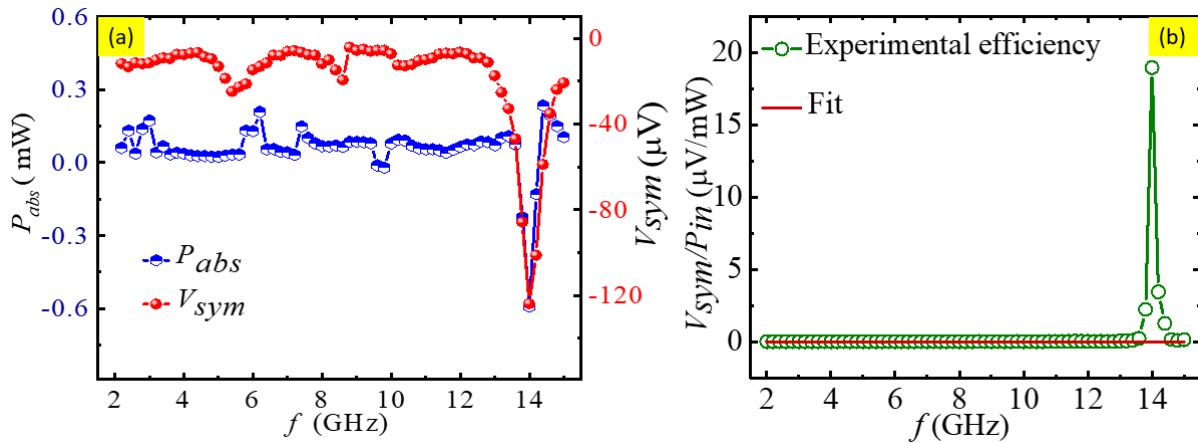


Figure 4.5 (a) P_{abs} and V_{sym} dependency on f ; (b) spin angular momentum to J_s conversion efficiency for sample S2. The solid line represents the fitting to equation (4.2).

agreement with the theoretical model given in ref [15] while at higher frequency region ($f > 13$ GHz), experimental data deviate from fitting values. Particularly near 14 GHz, efficiency shows a huge jump. This deviation is due to the high absorption of microwave power at this frequency range.

Spin-to-charge conversion analysis

As there is a high conversion efficiency of spin angular momentum to J_s at 14 GHz, we should observe higher θ_{SHA} at 14 GHz than at other frequencies. This interesting behaviour draws our attention towards spin-to-charge conversion efficiency. To confirm this, we have performed complete angle-dependent ISHE measurements at different frequencies to separate spin pumping voltage from other rectification effects and to calculate the θ_{SHA} .

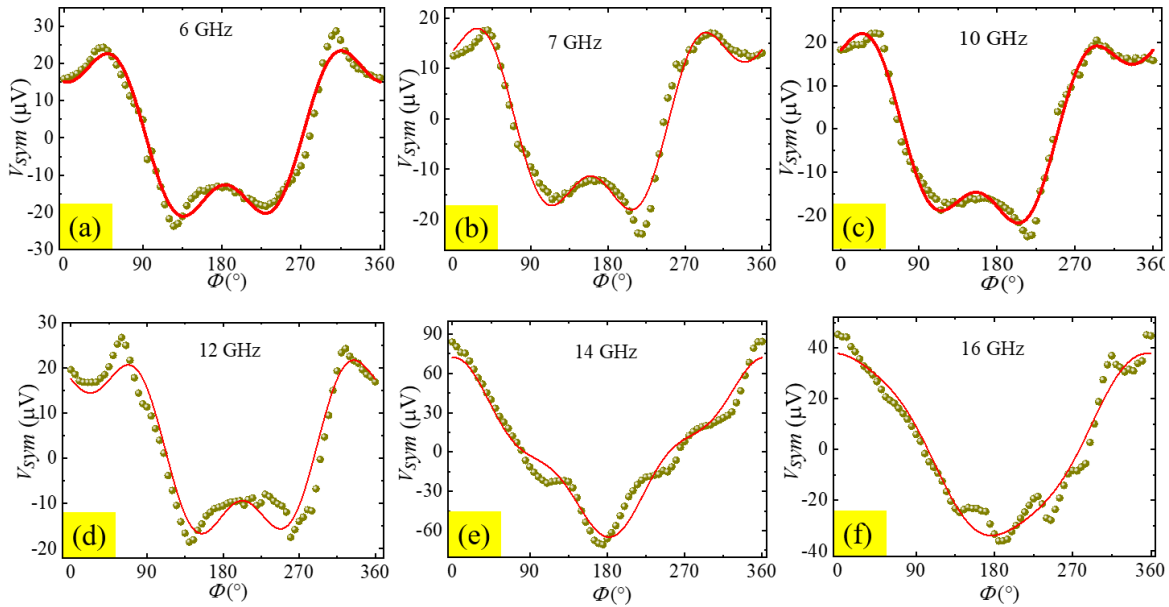


Figure 4.6 (a)-(f) V_{sym} vs Φ plot for different frequencies. Solid red lines are the best fits to the equation (4.4).

Angle-dependent ISHE measurements have been performed for 6, 7, 10, 12, 14 and 16 GHz. From the measured voltage for each angle, we have separated V_{sym} and V_{asym} contributed by fitting the data using equation (4.1). V_{sym} and V_{asym} data are plotted with respect to angle for all frequencies mentioned above. Fig.4.6 (a)-(f) shows the angle-dependent V_{sym} data for sample S2 at different frequencies, as mentioned above. Similarly, Fig.4.7 (a) and (f) represent the V_{asym} data for sample S2 at different frequencies.

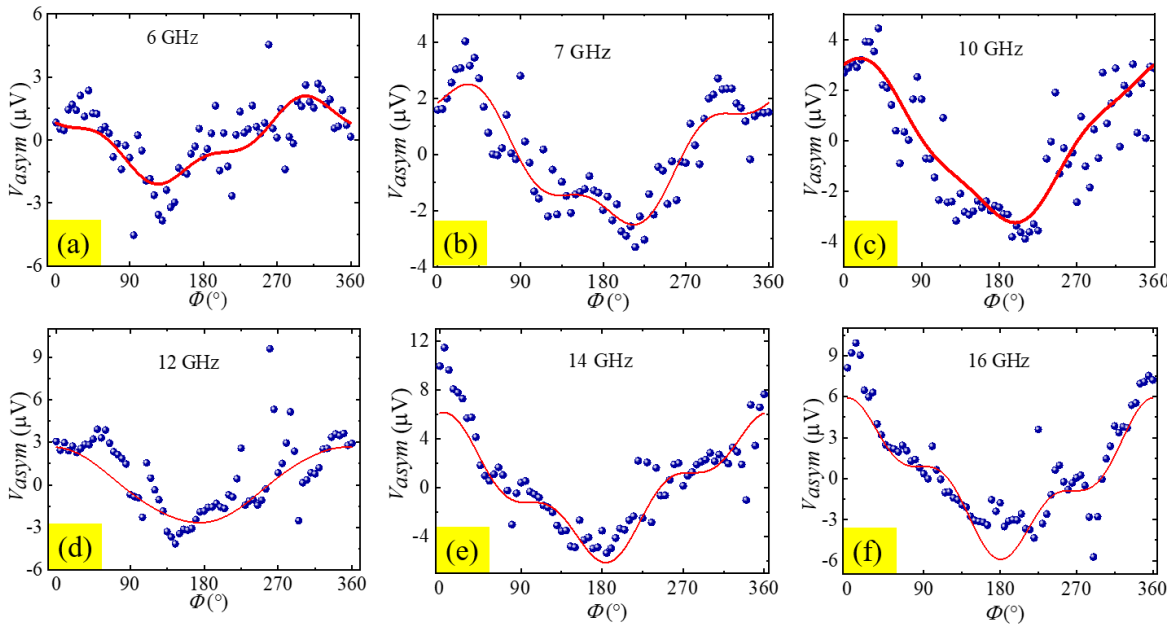


Figure 4.7 (a)-(f) V_{asym} vs Φ plot for different frequencies. Solid red lines are the best fits to the equation (4.5).

The angle-dependent V_{sym} data shown in Fig.4.6 (a) – (f) are fitted using the following equation [173].

$$\begin{aligned}
 V_{sym} = & V_{sp} \cos^3(\phi + \phi_0) + V_{AHE} \cos \theta \cos(\phi + \phi_0) \\
 & + V_{sym}^{AMR \perp} \cos 2(\phi + \phi_0) \cos(\phi + \phi_0) \\
 & + V_{sym}^{AMR \parallel} \sin 2(\phi + \phi_0) \cos(\phi + \phi_0)
 \end{aligned}
 \tag{4.4}$$

Angle-dependent V_{asym} data shown in Fig.4.7 (a) and (f) fitted using the following equation [173].

$$\begin{aligned}
 V_{asym} = & V_{AHE} \sin(\theta) \cos(\phi + \phi_0) \\
 & + V_{asym}^{AMR \perp} \cos 2(\phi + \phi_0) \cos(\phi + \phi_0) \\
 & + V_{asym}^{AMR \parallel} \sin 2(\phi + \phi_0) \cos(\phi + \phi_0)
 \end{aligned}
 \tag{4.5}$$

From the best fits of Fig.4.6, values of V_{sp} , V_{AHE} , $V_{asym, sym}^{AMR \parallel}$ and $V_{asym, sym}^{AMR \perp}$ have been obtained.

From the fitting parameters $V_{AMR}^{\perp, \parallel}$ can be calculated using the following equation-

$$V_{AMR}^{\perp, \parallel} = \sqrt{(V_{asym}^{AMR \perp, \parallel})^2 + (V_{sym}^{AMR \perp, \parallel})^2}
 \tag{4.6}$$

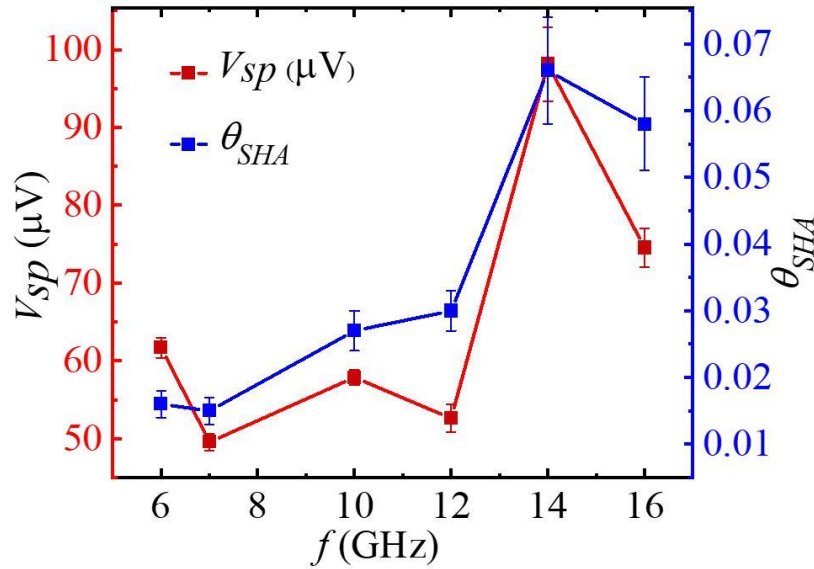


Figure 4.8 V_{sp} and θ_{SHA} vs f for sample S2.

θ_{SHA} can be calculated using the formula [171,174]

$$V_{ISHE} = w R \theta_{SHA} \lambda_{SD} \tanh \left[\frac{t_{Pt}}{2\lambda_{SD}} \right] J_s \quad 4.7$$

Where J_s can be written as

$$J_s \approx \left(\frac{g_{eff}^{\uparrow\downarrow} \hbar}{8\pi} \right) \left(\frac{\mu_0 h_r f \gamma}{\alpha} \right)^2 \times \left[\frac{\mu_0 M_S \gamma + \sqrt{(\mu_0 M_S \gamma)^2 + 16(\pi f)^2}}{(\mu_0 M_S \gamma)^2 + 16(\pi f)^2} \right] \left(\frac{2e}{\hbar} \right) \quad 4.8$$

Further, the spin mixing conductance (real part) can be given as

$$g_{eff}^{\uparrow\downarrow} = g_r^{\uparrow\downarrow} \left[1 + \frac{g_r^{\uparrow\downarrow} \rho_{Pt} \lambda_{SD} e^2}{2 \pi \hbar \tanh \left[\frac{t_{Pt}}{2\lambda_{SD}} \right]} \right]^{-1} \quad 4.9$$

where the value of $g_{eff}^{\uparrow\downarrow}$ can be calculated using the difference in damping constant ($\Delta\alpha$) from sample S1 to sample S2 due to spin pumping using the following formula [179]

$$g_{eff}^{\uparrow\downarrow} = \frac{\Delta\alpha 4\pi M_s t_{LSMO}}{g\mu_B} \quad 4.10$$

Here, R and ρ_{Pt} are defined as the resistance of sample S2 and the resistivity of the Pt layer, respectively. All the spintronic parameters obtained from the calculations are listed in Table-4.1. θ_{SHA} has a clear frequency dependency. Further, we have plotted V_{sp} and θ_{SHA} with respect to frequency, as shown in Fig.4.8. It is observed that V_{sp} and θ_{SHA} can be tuned by varying the frequency.

Table 4.1: Comparison of various parameters at different frequencies for S2. Here V_{sp} and V_{AHE} have been obtained by fitting equations (4) and (5) to Fig.4.6 (a)-(f) and Fig.4.7 (a)-(f), respectively. Similarly, θ_{SHA} and J_s have been calculated using equations 4.7 and 4.8, respectively.

f (GHz)	V_{sp} (μV)	V_{AHE} (μV)	V_{AMR}^\perp (μV)	V_{AMR}^\parallel (μV)	J_s (A/m^2) ($\times 10^6$)	θ_{SHA}
6	62.07	1.72	47.88	1.07	48.97	0.016
7	49.57	2.74	38.27	0.90	41.59	0.015
10	57.58	2.96	42.88	2.12	28.05	0.027
12	52.62	2.68	40.69	0.77	22.85	0.030
14	98.6	2.91	34.88	19.31	19.22	0.066
16	74.54	4.27	39.70	4.90	16.55	0.058

This work explored the effect of microwave frequency on spin-pumping phenomena. We observed that spin pumping does not have any linear relation with frequency. However, at certain frequencies, spin pumping is pronounced. Further, a maximum spin pumping voltage ($\sim 98 \mu\text{V}$) has been obtained from the frequency-dependent spin pumping measurement. To understand microwave absorption behaviour, a relation between P_{abs} and V_{sym} has been established. Measured voltage intensity has a dependency on the amplitude of absorption spectra. A very interesting sign change behaviour in FMR spectra at only a higher frequency range (12 to 15 GHz) has been observed. This sign change should be understood theoretically. We have highlighted that manganite-based FM is among the best-suited materials because of its high spin current injection property. By varying the frequency, one can tune the spin current injection efficiency and the spin Hall angle at a constant microwave power. This additional control over these crucial parameters can help in futuristic spintronic device fabrication.

CHAPTER 5: Spin to charge conversion in $\text{La}_{0.65}\text{Sr}_{0.35}\text{MnO}_3(\text{FM})/\text{La}_{0.2}\text{Sr}_{0.8}\text{MnO}_3(\text{AFM})$ bilayer system

Manganites are exciting materials that show highly promising and application-oriented properties i.e., colossal magnetoresistance [191], exchange bias [192], multiferroic properties [193] and also can be used in magnetic memories and sensors [194]. Hence, manganite have vastly used in spintronics applications [195,196]. Rich magnetic and electronic phase diagram enables tuning of various properties. $\text{La}_{1-x}\text{Sr}_x\text{MnO}_3$ (LSMO) is one of the most studied manganite materials, where by changing the concentration of Sr, one can tune the magnetic and electric properties of LSMO. A Sr-rich ($x\sim 0.8$) phase shows a C-type antiferromagnetic (AFM) nature while reducing the Sr composition ($x\sim 0.35$) leads to a very stable ferromagnetic (FM) phase [95–97]. The parent compound LaMnO_3 shows low-temperature FM behaviour. In general, two types of interaction have been observed in LSMO, (i) the double exchange interaction (DEI), which results in FM nature, and (ii) the other type of interaction is superexchange interaction (SEI), that leads to AFM properties in LSMO. These interactions vary with the Sr concentration. When Sr concentration is low, Mn^{+3} interacts with Mn^{+4} via an intermediate oxygen atom, and this interaction is DEI. In the case of a higher concentration of Sr, Mn^{+4} interacts with Mn^{+4} via an oxygen atom, which is called SEI.

LSMO with $x\sim 0.35$ shows the highest Curie temperature ($T_c \sim 350$ K) among any manganite [107]. LSMO is also well known for high spin polarization due to its half-metallicity nature [107]. Interestingly LSMO ($x \sim 0.35$) has been explored for many applications such as spin valves, exchange bias bases applications, colossal magnetoresistance etc. [96,111,112,114,197] There are a few reports on LSMO/Pt systems on spin-to-charge conversion physics where a high spin pumping voltage has been reported [104,163–165,177]. Low Gilbert damping constant and

observation of anti-damping in the LSMO/Pt system have been demonstrated [177,198]. However, the theoretical understanding of anti-damping-like features still needs to be clarified.

LSMO ($x=0.8$) shows AFM behavior below 280 K, and above 280 K, it shows paramagnetic behavior [199]. AFM materials are suitable for spin-to-charge conversion physics because they can exhibit high SOC and therefore they can replace the heavy metals in SOT based applications [200,201]. The advantages of AFM material are ultrafast magnetization dynamics, absence of stray current and show rigidity as a response to the magnetic field. These properties of AFM make them very useful from the application point of view.

For the study of spin-to-charge conversion physics, i.e. spin pumping and inverse spin Hall effect (ISHE), mostly explored systems are FM with HS, where HS represent the material with high spin-orbit coupling (SOC) [84,153,168,177,202]. The low Gilbert damping FM material is the preferred choice for such studies. For high SOC material Pt, Ta, W etc., have been well exploited. However, there is a search for an alternative to HM. In this regard, AFM, topological insulators, Weyl semimetals etc., have been explored [187,188,203]. AFM has been proven a good choice due to their high SOC, terahertz dynamics, robustness for external magnetic field, etc. However, there are limited studies where FM and AFM are taken from the same mother compound for such studies. It is exciting to study the FM and AFM from the same mother compound as they are compatible in growing epitaxial films adjacent to each other with very high lattice matching.

In this work, we have attempted to explore LSMO (FM)/LSMO(AFM) bilayer samples for spin-to-charge conversion studies. Here, FM and AFM belong to the same manganite family, though their properties are entirely different. We have chosen LSMO ($x=0.8$) composition as a HS material in this work. This composition is AFM (with $T_n = 280$ K) and insulating in nature. The lattice constant for this composition is also similar to LSMO (FM). For this purpose,

LSMO(FM)//LSMO(AFM) bilayer films have been grown on top of the STO (001) substrate by oxygen-assisted molecular beam epitaxy (OMBE). Further, the magnetic phases have been confirmed, and samples have been studied for spin pumping and spin-to-charge conversion efficiency.

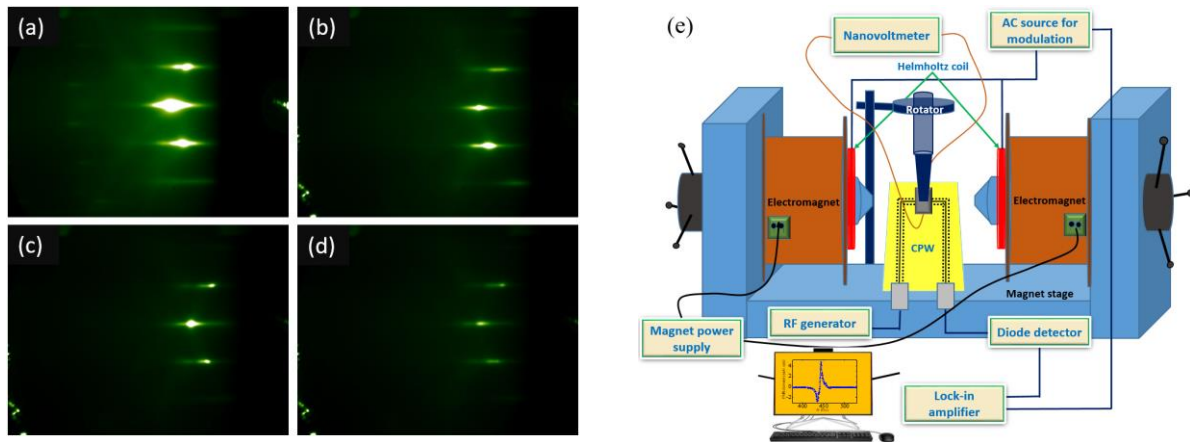


Figure 5.1 RHEED pattern taken on the surface of the samples (a) A0 (b) AF20. (c) and (d) shows the RHEED pattern at the interface and on the sample surface for sample A20. (e) The schematic diagram of FMR and ISHE measurement setup.

The epitaxial $\text{La}_{0.65}\text{Sr}_{0.35}\text{MnO}_3$ (FM)(20 nm)/ $\text{La}_{0.2}\text{Sr}_{0.8}\text{MnO}_3$ (AFM)(t nm) where $t = 0, 2, 5$ and 20 nm bilayer films have been grown on STO(001) substrate, using OMBE. The samples are named as A0, A2, A5 and A20, where the numbers denote thickness of the AFM layer. A reference sample LSMO(AFM) with 20 nm thickness have also been prepared. All the samples and their names are mentioned in Table-1. For the growth of LSMO films, LaSrO and MnO_3 compounds have been used as the base compounds. The substrate temperature was kept at 720 °C. The base pressure was 10^{-9} mbar. The chamber pressure during growth was kept to 10^{-6} mbar, and ozonic

oxygen was supplied during the growth. The sample was in situ characterized via reflective high energy electron diffraction (RHEED). Post-deposition, X-Ray diffraction (XRD) and X-Ray reflectivity (XRR) were used to characterize the samples. The epitaxial nature has been verified by transmission electron microscopy (TEM). The magnetic properties of the films have been studied by a superconducting quantum interference device (SQUID). Studies on magnetization dynamics have been carried out in ferromagnetic resonance (FMR). From frequency-dependent FMR, the Gilbert damping constant (α) has been determined. Further spin pumping studies have been performed by in-house developed inverse spin Hall effect (ISHE) measurement setup.

Table 5.1 : Sample structure and their name.	
Sample Name	Sample structure
A2	$\text{SrTiO}_3(001)/\text{La}_{0.65}\text{Sr}_{0.35}\text{MnO}_3$ (20 nm)/ $\text{La}_{0.2}\text{Sr}_{0.8}\text{MnO}_3$ (2 nm)
A5	$\text{SrTiO}_3(001)/\text{La}_{0.65}\text{Sr}_{0.35}\text{MnO}_3$ (20 nm)/ $\text{La}_{0.2}\text{Sr}_{0.8}\text{MnO}_3$ (5 nm)
A20	$\text{SrTiO}_3(001)/\text{La}_{0.65}\text{Sr}_{0.35}\text{MnO}_3$ (20 nm)/ $\text{La}_{0.2}\text{Sr}_{0.8}\text{MnO}_3$ (20 nm)
A0	$\text{SrTiO}_3(001)/\text{La}_{0.65}\text{Sr}_{0.35}\text{MnO}_3$ (20 nm)
AF20	$\text{SrTiO}_3(001)/\text{La}_{0.2}\text{Sr}_{0.8}\text{MnO}_3$ (20 nm)

A list of samples studied in this work is shown in Table 1. Fig.5.1(a) shows the RHEED pattern for the surface of the A0 sample. Fig.5.1(b) shows the RHEED pattern for the surface of the AF20 sample. The RHEED pattern at the interface between the FM/AFM layer and on the surface for sample A20 has been shown in Fig.5.1(c) and (d), respectively. The RHEED images shown in Fig.5.1(a)–(d) confirm the crystalline nature of the grown films. The streak lines at the interface confirm that the interfaces are sharp, and the streak lines on the surface confirm the smoothness of the surfaces.

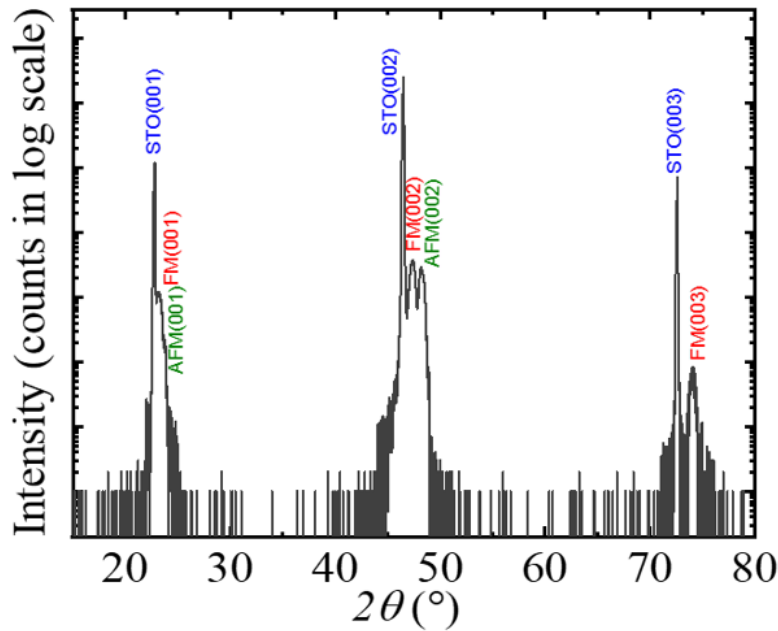


Figure 5.2 X-Ray diffraction data for sample FM-20/AFM-20. XRD has been performed in θ - 2θ geometry.

Fig.5.2 shows the X-ray diffraction peaks for the thicker sample A20. All the observed diffraction peaks correspond to (001) plane of LSMO [204,205]. We have not observed any other diffraction peaks corresponding to different orientations of planes. Further, cross-sectional TEM imaging has been performed for samples A2 and A20. TEM images for samples A2 and A20 have been shown in Fig.5.3 (a) and (b), respectively. The zoomed part is shown in the inset circles, which correspond to different layers. HRTEM images confirm that films are epitaxial in nature. Therefore, we concluded that our thin films are epitaxially grown perpendicular to the 001 plane of the STO substrate. The lattice constants for different layers have been calculated from TEM and the obtained values are 0.390, 0.383 and 0.387 nm for the STO, LSMO(FM) and LSMO(AFM),

respectively. These results corroborate to the XRD analysis. Lattice constants are within ~1% of the reported bulk values of the corresponding materials [206–208]. Therefore, the grown samples are of good quality in terms of crystalline structure. The thicknesses of the grown films have been confirmed from TEM and XRR.

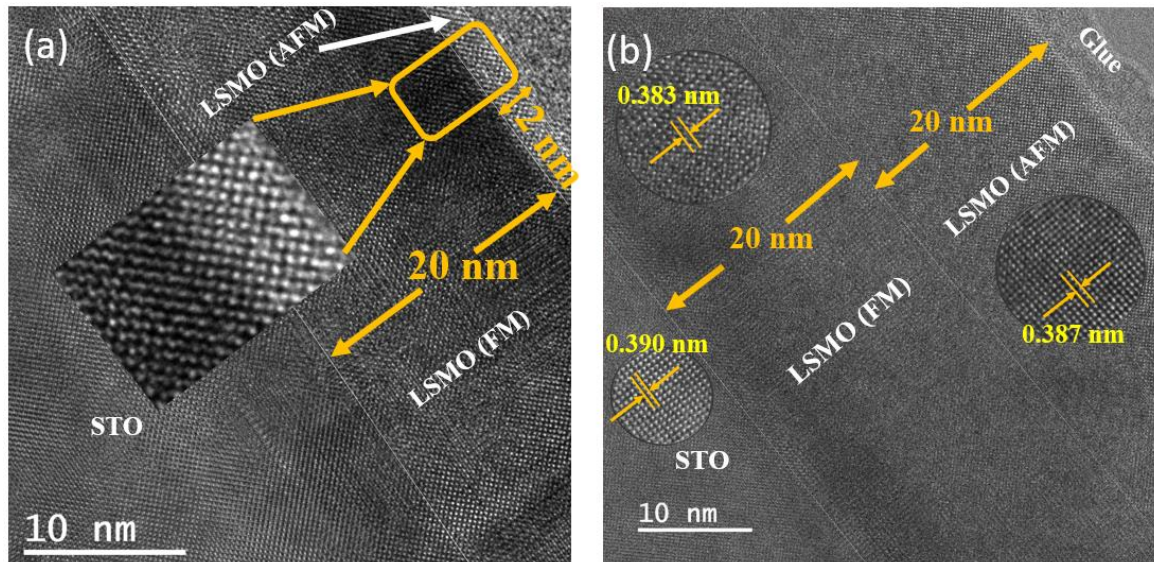


Figure 5.3 (a) The HRTEM image is shown for the sample FM-20/AFM-2. The inset shows the zoomed part of interface between FM and AFM layer. (b) The HRTEM images for the sample FM-20/AFM-20. The insets show the zoomed part of the (i) STO substrate, (ii) LSMO(FM) layer and (iii) LSMO(AFM) layer.

The FM phase of LSMO is well-studied and established. We have also measured the magnetization response of the A0 sample with respect to temperature as shown in Fig.5.4 (a). From M - T measurement of the A0 sample, the Curie temperature (T_c) has been found to be 345 K. From the M - T data of AF20 sample, as shown in Fig.5.4 (b), the Neel temperature is found to be 280 K, which matches well with the bulk value. Further, the AFM nature has been confirmed from

exchange bias measurement in the all the bilayer samples, as shown in Fig.5.5 (a)-(c). We observed ~ 25 Oe negative exchange bias for sample A20 at 5K when cooling field ± 1 T is applied. Exchange bias reduces to ~ 15 Oe and ~ 5 Oe for samples A5 and A2, respectively. It can be clearly seen from EB measurement that AFM thickness plays a crucial role in EB mechanism. With reduction in AFM thickness, EB decreases drastically. From the structural and magnetic characterizations, it has been confirmed that the grown films are in the expected structural and magnetic phases.

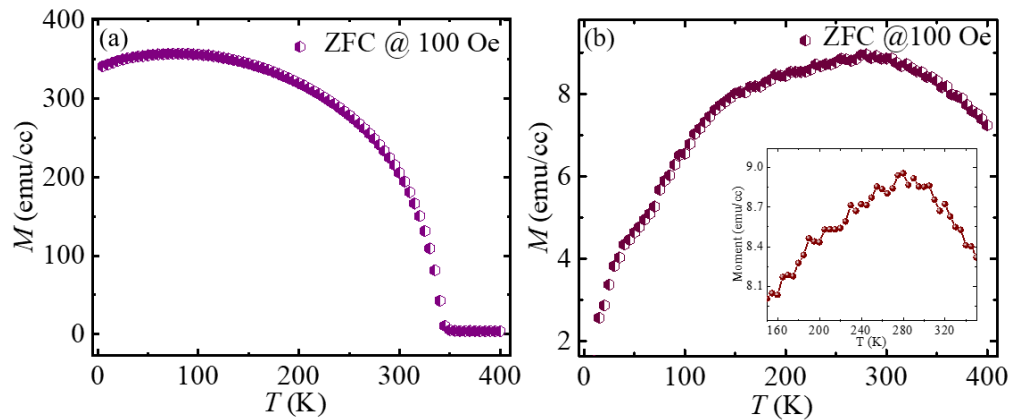


Figure 5.4 M - T data for (a) A0 sample and (b) AF20 sample. M - T measurements were performed in zero-field cooling (ZFC) mode. During the measurement, a magnetic field of 100 Oe was applied.

The FMR measurement for samples A0, A2, A5 and A20 have been performed, and the data is shown in Fig.5.6(a-d). It can be seen from the FMR that in addition to the uniform mode, some other modes are also present, which agrees with our previous FMR data [209]. Hence during the extraction of line width and resonance field, the other modes are considered. For this, we have modified the Lorentzian equation to accommodate the other modes as well. The modified Lorentzian equation is as follows.

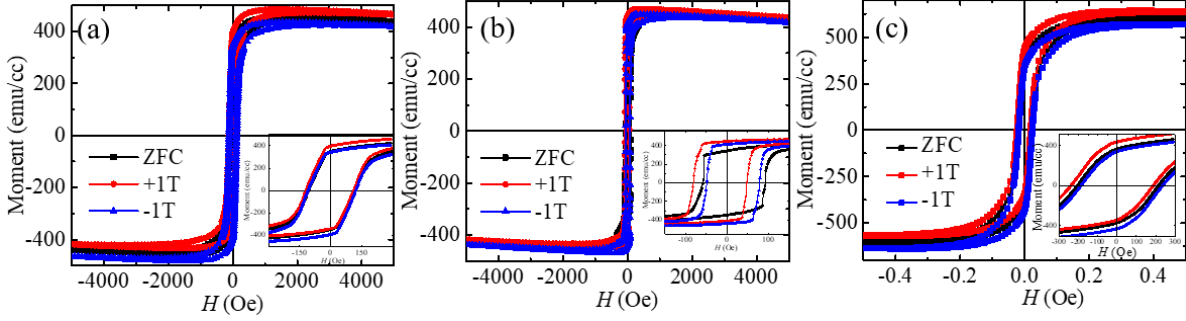


Figure 5.5 The presence of exchange bias in the (a) A2, (b) A5 and (c) A20 sample. The exchange bias measurement has been performed at ± 1 T cooling field. These all measurement have been performed at 5K.

$$\begin{aligned}
 P_{dc}(H) = P_0 + A_{sym1} \frac{(\Delta H_1)^2}{(H - H_{r1})^2 + (\Delta H_1)^2} + A_{Asym1} \frac{\Delta H_1(H - H_{r1})}{(H - H_{r1})^2 + (\Delta H_1)^2} \\
 + A_{sym2} \frac{(\Delta H_2)^2}{(H - H_{r2})^2 + (\Delta H_2)^2} + A_{Asym2} \frac{\Delta H_2(H - H_{r2})}{(H - H_{r2})^2 + (\Delta H_2)^2} \quad 5.1
 \end{aligned}$$

Here H_{r1} , H_{r2} , ΔH_1 and ΔH_2 are the resonance field and linewidth corresponding to first and second peak. This modified Lorentzian will help to extract the accurate value of the ΔH and H_{res} for uniform mode. The fitting of double peak FMR is shown in Fig.5.7. The uniform mode has the highest intensity, and they primarily contribute to ISHE voltage; hence for all analyses, we have considered only the uniform mode. The effect of other modes in ISHE can be understood in future. Further, FMR linewidth (ΔH) and resonance field (H_{res}) for uniform mode have been extracted for each frequency. f vs H_{res} data have been plotted as shown in Fig.5.6 (a) and fitted using the Kittel equation [26]

$$f = \frac{\gamma}{2\pi} \sqrt{(4\pi M_{eff} + H_{res} + H_K)(H_{res} + H_K)} \quad 5.2$$

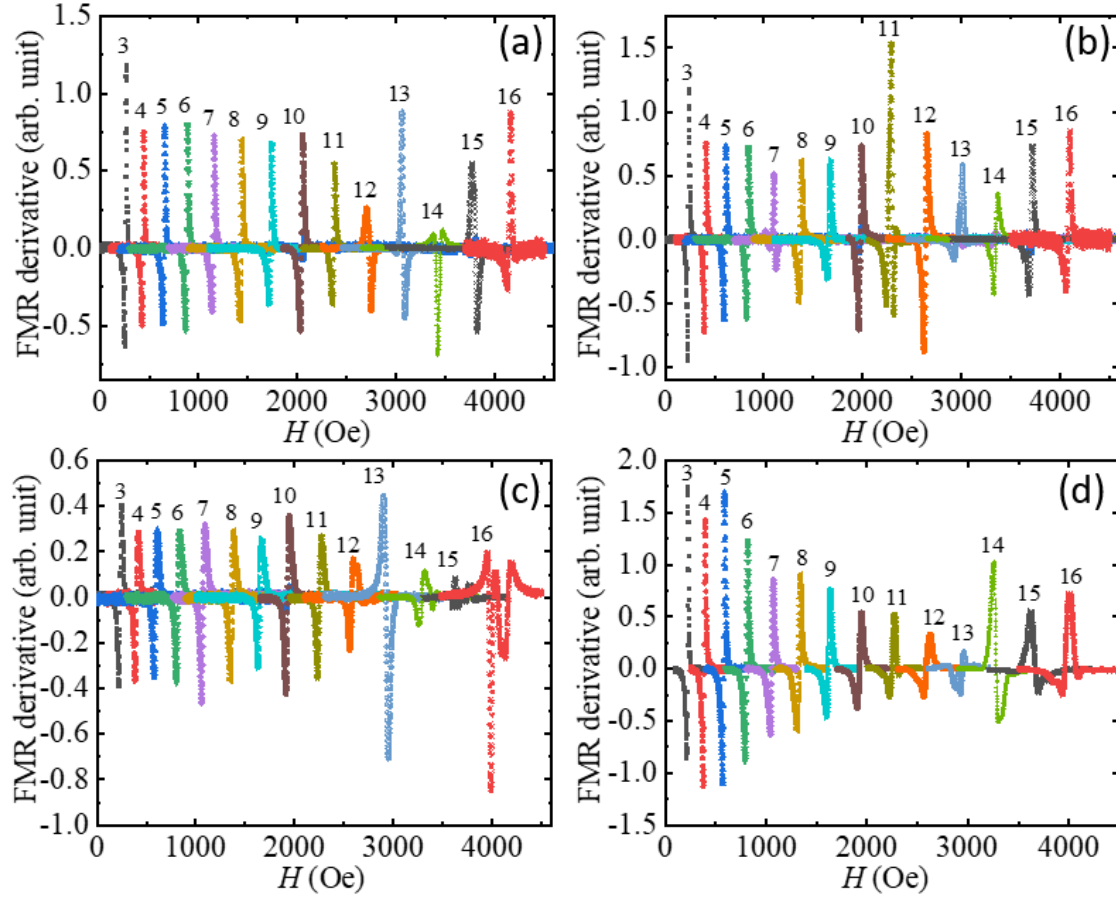


Figure 5.6 FMR spectra in the range of 3-16 GHz are shown for samples (a) A0, (b) A2, (c) A5 and (d) A20, respectively.

where $\gamma(=g\mu_B/\hbar)$, g , μ_B , H_K and M_{eff} are gyromagnetic ratio, Lande g -factor, Bohr magneton, in-plane anisotropic fields and effective demagnetization, respectively, Fig. 5.6 (b) shows the ΔH vs f data for all samples, which have been fitted using the following linear relation [167,168].

$$\Delta H = \Delta H_0 + \frac{4\pi\alpha f}{\gamma} \quad 5.3$$

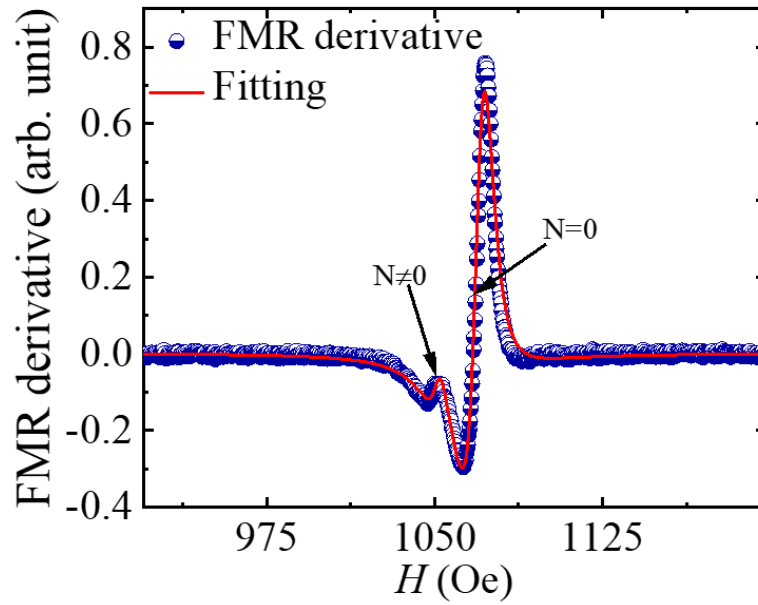


Figure 5.7 FMR spectra with two FMR modes. The higher intensity mode is the uniform ($n=0$) mode, while the mode with lower intensity is the non-uniform mode ($n\neq 0$). The red solid line is the best fit for equation (5.1).

where the slope of the graph (α) is defined as Gilbert's damping parameter. The extracted α values from the fitting of Fig.5.8 (b) are 0.0031 ± 0.0002 , 0.00036 ± 0.0002 , 0.0036 ± 0.0003 and 0.0098 ± 0.0002 for samples A0, A2, A5 and A20, respectively. It can be seen from the damping values that there is an enhancement in the damping constant when LSMO(AF)M is deposited on the top of the LSMO(FM) layer. This enhancement can be attributed to interface roughness, structural defects, or spin pumping in bilayer samples. Further, to confirm the presence of spin pumping in the samples, ISHE measurements have been performed.

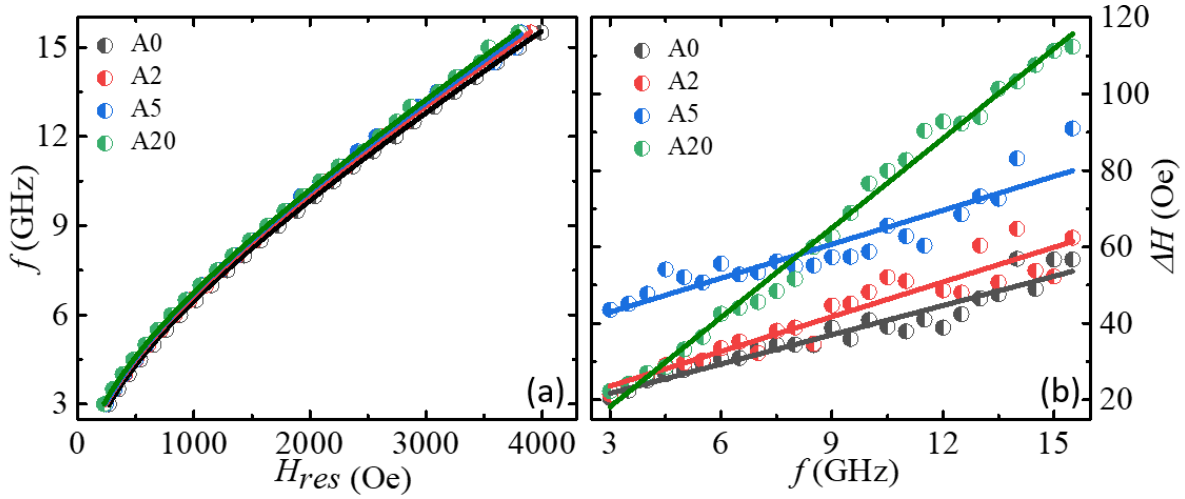


Figure 5.8 (a) f vs H_{res} and (b) ΔH vs f are shown for samples A0, A2, A5 and A20. The solid lines in (a) and (b) are the best fits for equations (5.2) and (5.3), respectively.

The ISHE measurement has been performed for samples A2, A5 and A20. Here FMR is used to inject the spin current into the LSMO(AF) layer from LSMO(FM) layer. The injected spin current in the AFM layer gives rise to the transverse voltage due to the SOC of the AFM. This generated voltage is measured as V_{meas} and consists of symmetric and asymmetric parts. It is well known that voltage due to spin pumping (V_{sp}) is the main contribution to the symmetric part. Further, to separate the symmetric (V_{sym}) and asymmetric (V_{asym}) voltage from the V_{meas} , the data is fitted using the following equation [171].

$$V_{total} = V_{sym} \frac{(\Delta H)^2}{(H - H_{res})^2 + (\Delta H)^2} + V_{asym} \frac{\Delta H(H - H_{res})}{(H - H_{res})^2 + (\Delta H)^2} \quad 5.4$$

Interestingly, we have also observed a finite amount of ISHE voltage in the A0 sample. As no AFM layer is on top of LSMO in the A0 sample, the generated voltage can be attributed to the self-induced ISHE of LSMO(FM) film. This exciting behaviour of self-induced ISHE has been studied in details in chapter 6.

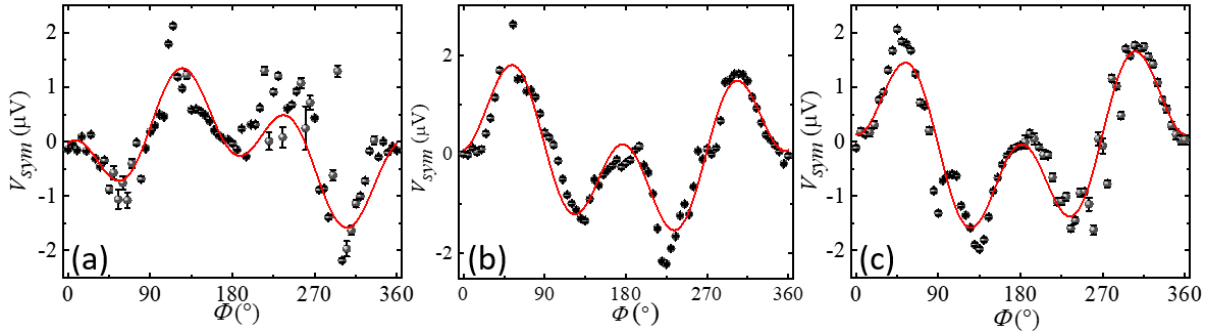


Figure 5.9 Angle-dependent V_{sym} for samples (a) A0, (b) A2 and (c) A5. Solid lines are the best fits to the equation (5.5).

As mentioned previously, the V_{sym} is mainly coming from spin pumping. Further, the asymmetric contribution can arise due to the anomalous Hall effect, anisotropic magnetoresistance, etc. To separate these rectification effects from the V_{sp} , an in-plane angle (Φ) dependent ISHE measurement from 0 to 360 degrees in a step of 5 degrees have been performed. Here Φ is defined as the angle between DC magnetic field and the voltage measurement direction. The measured voltage at each angle has been fitted using equation (5.4) for V_{sym} and V_{asym} . Further, V_{sym} and V_{asym} data have been plotted with respect to Φ . Fig.5.9 (a), (b) and (c) show the angle-dependent V_{sym} data for the samples A0, A2 and A5. The V_{sym} plots were fitted using the following equation [173].

$$\begin{aligned}
 V_{sym} = & V_{sp} \cos^3(\phi + \phi_0) + V_{AHE} \cos \theta \cos(\phi + \phi_0) \\
 & + V_{sym}^{AMR \perp} \cos 2(\phi + \phi_0) \cos(\phi + \phi_0) \\
 & + V_{sym}^{AMR \parallel} \sin 2(\phi + \phi_0) \cos(\phi + \phi_0)
 \end{aligned} \tag{5.5}$$

while V_{asym} plots were fitted using the following equation [173]

$$\begin{aligned}
 V_{sym} = & V_{sp} \cos^3(\phi + \phi_0) + V_{AHE} \cos \theta \cos(\phi + \phi_0) \\
 & + V_{sym}^{AMR \perp} \cos 2(\phi + \phi_0) \cos(\phi + \phi_0) \\
 & + V_{sym}^{AMR \parallel} \sin 2(\phi + \phi_0) \cos(\phi + \phi_0)
 \end{aligned} \tag{5.6}$$

where V_{AHE} is the voltages due to the anomalous Hall effect, further $V_{asym,sym}^{AMR \parallel}$ and $V_{asym,sym}^{AMR \perp}$ are the parallel and perpendicular components of the AMR voltage, respectively. θ is the angle between the microwave magnetic field (h_{rf}) and the electric field in the medium, which is 90° in our case. The values obtained from equations (5.5), (5.6) and (5.7) are listed in Table 5.2.

Table 5.2: V_{sp} and V_{AHE} and obtained from fitting of equations (5.5), (5.6). $g_{eff}^{\uparrow\downarrow}$ calculated using equation (5.10).			
Sample	V_{sp} (μV)	V_{AHE} (μV)	$g_{eff}^{\uparrow\downarrow}$ (m^{-2})
A0	2.54 ± 0.05	0.49 ± 0.12	-
A2	3.87 ± 0.14	-0.08 ± 0.05	2.06×10^{18}
A5	3.98 ± 0.20	-0.03 ± 0.10	1.86×10^{18}

From Table 5.2, it can be seen that V_{sp} is dominating over any other rectification effects. It has also been observed that there is an enhancement of V_{sp} in bilayer samples compared to a single FM sample. We have observed very noisy data for sample A20, and we could not analyse the measured ISHE data for this sample. The LSMO(AFM) is an insulator below $T < T_N$ and metallic above $T > T_N$. ISHE measurement temperature is near the transition temperature, and the sample with a higher thickness of LSMO(AFM) can show its bulk properties, i.e., insulator below the $T < T_N$. The noise in this sample can be due to the higher resistance value. Here, resistivity (ρ) has been measured at room temperature by the four-probe method, and obtained values are 4.4×10^{-6} , 4.1×10^{-6} , 4.7×10^{-6} ,

and $1.7 \times 10^{-5} \Omega$ -meter for samples A0, A2, A5 and A20, respectively. Indeed, the A20 sample's resistivity is much higher than other samples.

This work aimed to calculate the spin-to-charge conversion efficiency (θ_{SHA}). Therefore, we have calculated θ_{SHA} using the following equations [171,174].

$$\frac{V_{ISHE}}{R} = w \times \theta_{SHA} \lambda_{SD} \tanh \left[\frac{t_{AFM}}{2\lambda_{SD}} \right] J_S \quad 5.7$$

Where J_S is the spin current and can be calculated by,

$$J_S \approx \left(\frac{g_r^{\uparrow\downarrow} \hbar}{8\pi} \right) \left(\frac{\mu_0 h_{rf} \gamma}{\alpha} \right)^2 \times \left[\frac{\mu_0 M_S \gamma + \sqrt{(\mu_0 M_S \gamma)^2 + 16(\pi f)^2}}{(\mu_0 M_S \gamma)^2 + 16(\pi f)^2} \right] \left(\frac{2e}{\hbar} \right) \quad 5.8$$

Here $g_r^{\uparrow\downarrow}$ is the real part of the effective spin mixing conductance and can be calculated as

$$g_r^{\uparrow\downarrow} = g_{eff}^{\uparrow\downarrow} \left[1 + \frac{g_r^{\uparrow\downarrow} \rho_{Pt} \lambda_{SD} e^2}{2\pi \hbar \tanh \left[\frac{t_{Pt}}{2\lambda_{SD}} \right]} \right]^{-1} \quad 5.9$$

The $g_{eff}^{\uparrow\downarrow}$ is the effective spin mixing conductance and can be extracted from the change in the damping parameter in bilayer samples in comparison to a single FM sample by equation [29]

$$g_{eff}^{\uparrow\downarrow} = \frac{\Delta\alpha 4\pi M_S t_{FM}}{g\mu_B} \quad 5.10$$

here $\Delta\alpha$ is considered the change in the α due to spin pumping. The other terms used in the above equations, i.e., w , λ_{SD} , t_{AFM} , and R , are defined as the width of CPW, the spin diffusion length of high LSMO(AFM), the thickness of AFM layer in bilayer sample, and the resistance of the sample, respectively. From the above equation (5.10), the obtained $g_{eff}^{\uparrow\downarrow}$ values are 2.06×10^{18} and $1.86 \times 10^{18} \text{ m}^{-2}$ for the samples A2 and A5, respectively. Due to the limited number of samples, we could not evaluate the λ_{SD} of the LSMO(AFM). However, we have considered a large range of

λ_{SD} (1 nm to 20 nm) for θ_{SHA} evaluation. In the given range of λ_{SD} , θ_{SHA} has been evaluated from equation (5.7) as 0.013 to 0.017. This θ_{SHA} value is equivalent to the reported values for the Pt.

In summary we have successfully grown LSMO(FM)/LSMO(AFM) bilayer films by oxygen-assisted molecular beam epitaxy. Here by varying the concentration of Sr, two different materials from the same mother compound have been formed. The bilayer films are highly epitaxial in nature, having sharp interfaces and smooth surfaces, confirmed by the RHEED and the cross-sectional TEM images. The antiferromagnetic phase of LSMO(AFM) film has been confirmed by magnetization vs temperature measurement and preliminary exchange bias measurements. The Gilbert damping constant of the grown films is very low, which is important for spintronic applications. Further, spin pumping and ISHE measurement have been performed. A Self-induced ISHE is reported here in the LSMO film, which can be understood in future. A reasonably high voltage has been observed in bilayer films compared to single-layer FM. We found that spin-to-charge conversion efficiency for LSMO(AFM) film is about 1.5%, which is equivalent to Pt. This study is the first of its kind where two manganites of the same family have been explored in spin-to-charge conversion physics. Further understanding and optimizing this bilayer system can be useful for spintronic applications.

CHAPTER 6: Self-induced inverse spin Hall effect in $\text{La}_{0.67}\text{Sr}_{0.33}\text{MnO}_3$ films

In condensed matter systems, the anomalous Hall effect (AHE) [16,17], spin Hall effect (SHE) [18,63], inverse spin Hall effect (ISHE) [84], and other spin-related phenomena are primarily linked to strong spin-orbit coupling (SOC). For novel energy efficient spintronic devices, spin-orbit torque is an essential phenomenon. Here the spin current generation in the high spin-orbit coupling (HS) material is the key component to apply the torque to switch the magnetization in the ferromagnet (FM). In this context, much focus is being put on optimizing the spin current generation in different types of HS materials via spin pumping. Spin current can be generated in a FM via microwave based ferromagnetic resonance (FMR). Here the spin angular momentum dissipates into the HS to generate transverse voltage via the inverse spin Hall effect (ISHE). FM is typically used as a spin reservoir to inject spin currents into HS [168,177,186–188]. Usually, the SOC of the HS materials is taken into consideration for efficient spin-to-charge conversion. However, SOI can be found in ferromagnetic materials (FMs) [210], which causes anisotropic magnetoresistance (AMR) and AHE. In addition, the presence of the SOC in FMs may also lead to an intrinsic ISHE.

In a recent report by Miao et al., it has been shown that the injection of pure spin current from yttrium iron-garnet (YIG) to NiFe (Py) led to ISHE in Py, in which the flow of pure spin current in Py was shown [211]. This report suggests the presence of significant SOI in the Py layer, which is endorsed by the observation of AMR in Py film. Further, Tsukahara et al. [212] have explored self-induced ISHE experiments in a single layer Py film, i.e. without any adjacent HS material. These results indicate that the spin current generated by Py film interacts with its own SOI, which resulted in significant ISHE voltage. There are a few other studies on intrinsic ISHE in Co and Fe films [213]. All these studies on intrinsic ISHE have been reported in metallic FMs, where

sufficient conduction electrons are present at the Fermi level. Precisely, the angular momentum of 3d electrons is transferred to 4s-conduction electrons during the precession of magnetic moments, resulting in a spin-polarized current in the FM [212,214]. Due to non-uniform magnetization, spins then flow diffusely, and it has been linked to asymmetric spin relaxation at the various interfaces. On a similar note, as we have discussed earlier, manganites such as $\text{La}_{0.67}\text{Sr}_{0.33}\text{MnO}_3$ (LSMO) have attracted the attention in recent years in such spin-to-charge conversion studies due to their robustness, low damping, high Curie temperature ($T_c \sim 350$ K), and high spin polarization, etc. [104,198]. LSMO is an oxide based FM which has been explored only as a spin reservoir in these spin pumping studies [104,105,163,177]. Further, in LSMO/Pt bilayers antidamping has been observed. These recent results show the potential of LSMO for spintronic applications. In this context, it is timely to explore intrinsic ISHE in LSMO single layer films. This study investigates the voltage generated due to ISHE in epitaxial LSMO films under ferromagnetic resonance (FMR).

Samples $\text{STO}(100)/\text{LSMO}(t \text{ nm})$ have been deposited via pulsed laser deposition (PLD) technique having a laser of wavelength 248 nm and a vacuum chamber with base pressure 3×10^{-7} mbar. The samples are called SL1, SL2, and SL3, where $t = 12, 35, \text{ and } 55$ nm, respectively. For the growth of LSMO films, the substrate temperature was kept at 740°C during the deposition. Laser fluence and frequency are kept at 1.4 J/cm^2 and 2 Hz, respectively. The oxygen partial pressure during the growth was maintained at 0.47 mbar. Post-deposition annealing of the sample was performed at the same temperature (740°C) for 30 minutes at 250 mbar oxygen pressure. X-ray reflectivity (XRR) and x-ray diffraction (XRD) have been performed with a diffractometer (model-Rigaku smartLab) with wavelength $\lambda = 0.154$ nm. Cross-sectional high-resolution transmission electron microscopy (HR-TEM) has been performed to check the epitaxy of deposited films by

TEM (JEOL, F-200). The dc magnetometry was performed by a superconducting quantum interference device (SQUID) based magnetometer manufactured by Quantum Design (MPMS3). Co-planar wave-guide (CPW) based ferromagnetic resonance (FMR) spectroscopy (manufactured by NanOsc, Sweden) was carried out to study magnetization dynamics. The sample was kept on

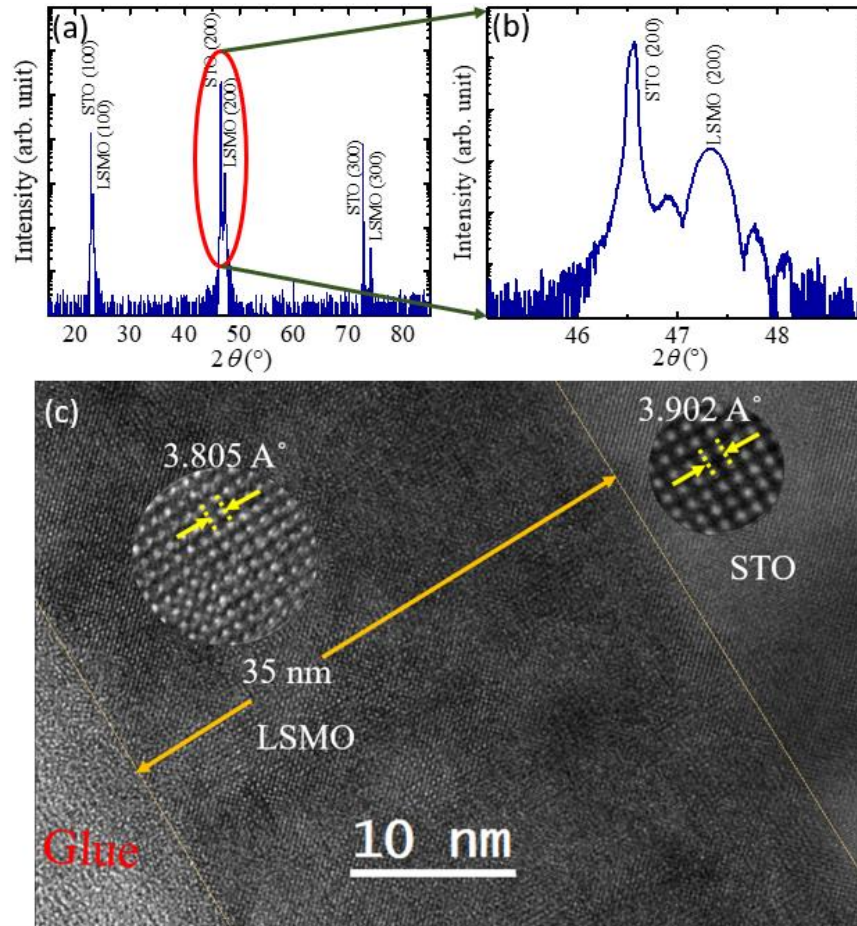


Figure 6.1 (a) XRD data, (b) zoomed part of (200) peak and (c) HRTEM image for SL2 sample.

top of the CPW in a flip-chip manner [177,185]. To prevent shunting, a 25- μm polymer tape was placed between the sample and the CPW. A dc magnetic field (H) was applied perpendicular to the radio frequency field (h_{rf}). By analysing FMR spectra in the frequency (f) range of 3.5-10 GHz

at intervals of 0.5 GHz, the Gilbert damping constant (α) was estimated. ISHE measurement was performed at 7 GHz frequency and 25 mW microwave power. The voltage obtained due to ISHE was measured by a Nanovoltmeter (Keithley 2182A).

The XRD data shown in Fig.6.1 (a) indicate that LSMO films had been grown in (100) orientations which is also the orientation of the STO substrate. This confirms that LSMO films are highly epitaxial in nature. The zoomed-in image corresponding to (200) peak is shown in Fig. 6.1(b). In Fig.6.1 (c) cross-sectional HRTEM image has been shown for sample SL2, which indicates clear and sharp interfaces of STO/LSMO. Film thickness was estimated using X-ray reflectivity (XRR) as shown in Fig.6.2 (a)–(c). From XRR we also estimated the roughness of LSMO films as 0.33, 0.71 and 0.84 nm for samples SL1, SL2 and SL3, respectively. Low values of the roughness indicate the good quality of the grown films. The fitting parameters have been shown in the table 6.1.

Sample	Substrate roughness (nm)	Film roughness (nm)	Film thickness (nm)
SL1	0.3	0.3	11.2
SL2	0.3	0.7	33.9
SL3	0.7	0.8	56.9

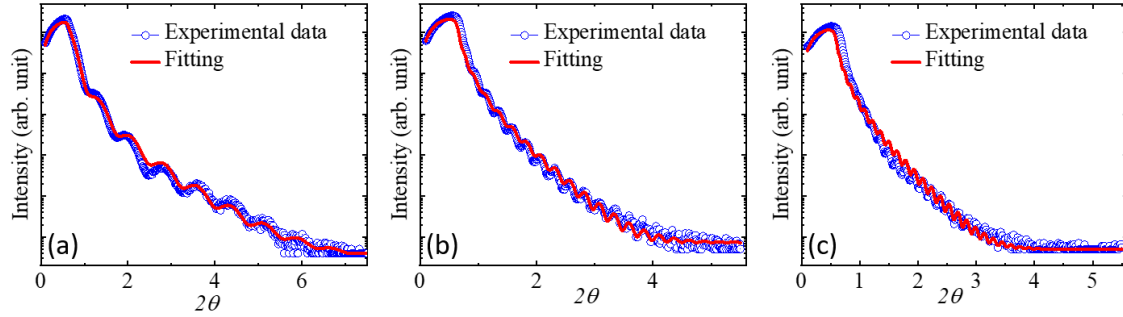


Figure 6.2 XRR measured data and its corresponding best fits of the sample (a) SL1, (b) SL2, and (c) SL3. Open blue circles represent the experimental data and the solid red lines are the best fits to the data.

Further, to confirm the magnetic phase of the grown film magnetization vs. temperature measurement have been performed. Fig.6.3 shows the magnetic moment (m) vs temperature (T) data for LSMO (35 nm) sample. From the data, it can be clearly seen that the Curie temperature (T_c) of the deposited film is 320 K, which confirms the ferromagnetic phase of the sample at room temperature (300 K).

To study the magnetization dynamics, we have performed FMR from 3.5-10 GHz. The FMR spectra for all the samples have been shown in Fig.6.4 (a-c). To calculate the Gilbert damping constant (α), each FMR spectrum was fitted with the derivative of standard Lorentzian equation. From the fitting of FMR data, resonance field (H_{res}) and linewidth (ΔH) have been extracted. F vs. H_{res} plots are shown in Fig.6.5 (a) for all the samples. The data are fitted using the Kittel equation.

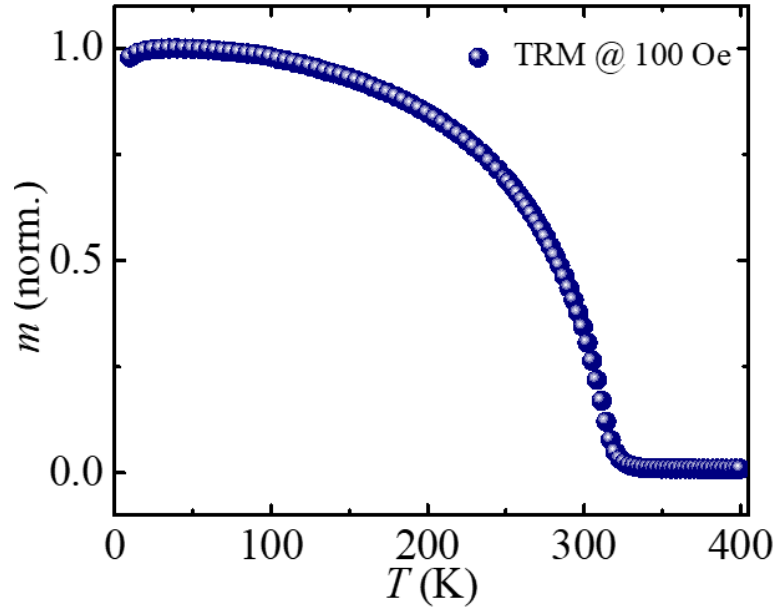


Figure 6.3 M vs T data for SL2 sample. Measurement have been performed in thermoremanent magnetization mode at 100 Oe magnetic field. From the graph T_c value is 320 K.

$$f = \frac{\gamma}{2\pi} \sqrt{(4\pi M_{eff} + H_{res} + H_K)(H_{res} + H_K)} \quad 6.1$$

Where γ ($=g\mu_B/\hbar$), g , μ_B , and M_{eff} are gyromagnetic ratio, Lande g-factor, Bohr magneton, and effective demagnetization, respectively. H_K , K_S , and t_{FM} are in-plane anisotropic fields, surface anisotropy and thickness of the FM layer, respectively. Further, f vs ΔH data shown in Fig.6.5(b) are fitted using the following linear equation.

$$\Delta H = \Delta H_0 + \frac{4\pi\alpha f}{\gamma} \quad 6.2$$

Where ΔH_0 is the inhomogeneous linewidth. The values of α for samples SL1, SL2, and SL3 are evaluated to be 0.0086 ± 0.0002 , 0.0077 ± 0.0008 and 0.0097 ± 0.0009 , respectively. The values of α match well with the previously reported values [165].

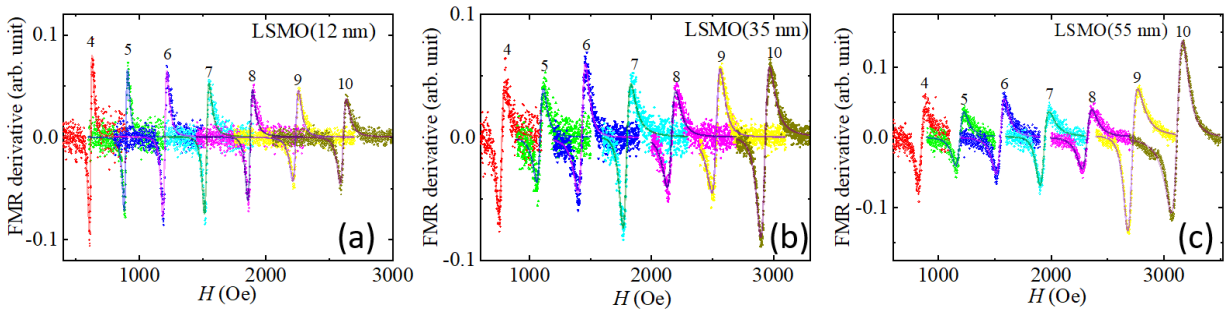


Figure 6.4 FMR signal for different frequencies for samples (a) SL1, (b) SL2, and (c) SL3. Solid lines are the fits using the Lorentzian equation.

Further, we have shown the presence of significant AMR in the LSMO/Pt system, which may arise due to the spin-orbit coupling (SOC) of LSMO film [177]. This SOC can reinforce scattering phenomena, which may lead to spin-to-charge conversion. As LSMO shows metallic ferromagnetic behaviour at room temperature, there is a possibility of intrinsic ISHE in LSMO films due to the presence of conduction electrons at the Fermi level. This intrinsic ISHE causes the measurable voltage across the sample. This voltage is due to ISHE, which is measured via making contacts with Cu wires from the sample to a Nanovoltmeter. Fig.6.6 shows the measured voltage (V_{meas}) data at 0 and 180 degrees for sample SL1. V_{meas} fitted with equation (6.3) to separate the symmetric (V_{sym}) and asymmetric (V_{asym}) contributions to voltage [171].

$$V_{meas} = V_{sym} \frac{(\Delta H)^2}{(H - H_{res})^2 + (\Delta H)^2} + V_{asym} \frac{\Delta H(H - H_{res})}{(H - H_{res})^2 + (\Delta H)^2} \quad 6.3$$

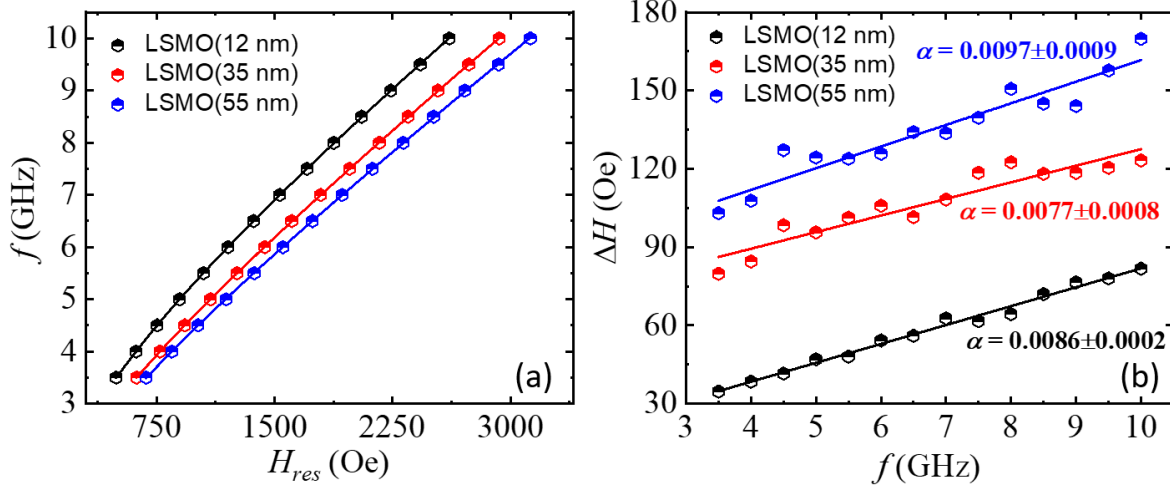


Figure 6.5 (a) f vs H_{res} plot and (b) ΔH vs f plot for STO/LSMO samples. Solid lines are the best fits for equations (6.1) and (6.2).

From Fig.6.6, it can be clearly seen that the V_{sym} is more dominating than the V_{asym} component. Also, it can be noticed that V_{sym} changed its polarity when the sample was rotated to 180 degrees. This is a characteristic property that confirms the ISHE in LSMO films.

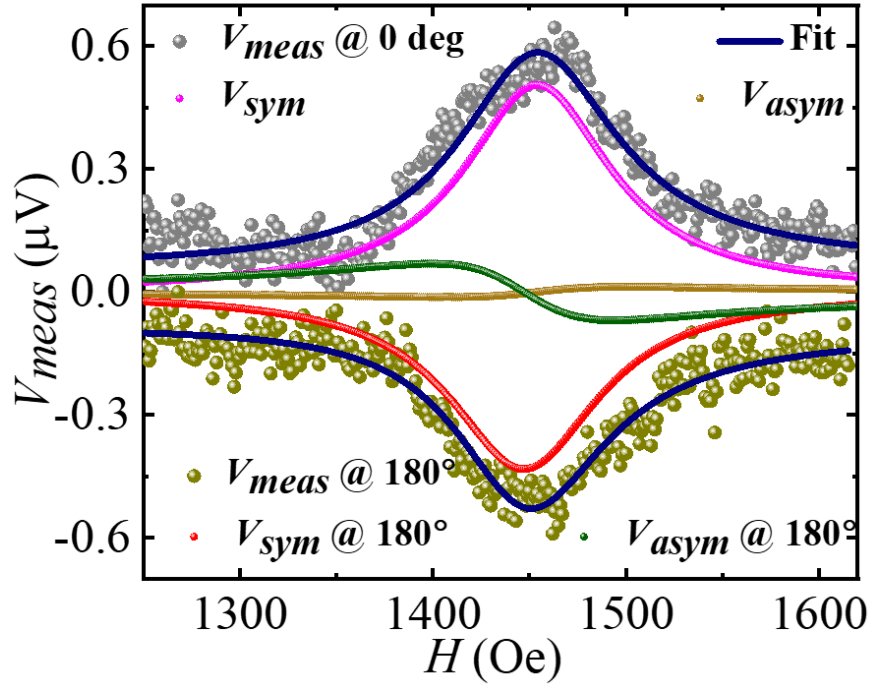


Figure 6.6 V_{meas} and its different components for SL1. Data is fitted to equation 6.3 to disentangle these symmetric and asymmetric voltage contributions.

It is well known that the V_{sym} mainly comes due to spin pumping while the spin rectification effects integrated to AMR, AHE etc., contribute to V_{asym} voltage [172]. To calculate the spin pumping voltage from the measured voltage, a complete angle-dependent ISHE has been performed from 0 to 360° in a step of 5°. Each measured voltage data is fitted to get V_{sym} and V_{asym} values using equation (6.3). Further, V_{sym} and V_{asym} are plotted with their corresponding angles as shown in Fig.6.7 (a) and (b). The V_{sym} data are fitted using the following equation [173]

$$\begin{aligned}
 V_{sym} = & V_{sp} \cos^3(\phi + \phi_0) + V_{AHE} \cos \theta \cos(\phi + \phi_0) \\
 & + V_{sym}^{AMR \perp} \cos 2(\phi + \phi_0) \cos(\phi + \phi_0) \\
 & + V_{sym}^{AMR \parallel} \sin 2(\phi + \phi_0) \cos(\phi + \phi_0)
 \end{aligned} \tag{6.4}$$

while the V_{asym} data are fitted using the following equation [173]

$$\begin{aligned}
 V_{\text{asym}} = & V_{\text{AHE}} \sin(\theta) \cos(\phi + \phi_0) \\
 & + V_{\text{asym}}^{\perp} \cos 2(\phi + \phi_0) \cos(\phi + \phi_0) \\
 & + V_{\text{asym}}^{\parallel} \sin 2(\phi + \phi_0) \cos(\phi + \phi_0)
 \end{aligned}
 \tag{6.5}$$

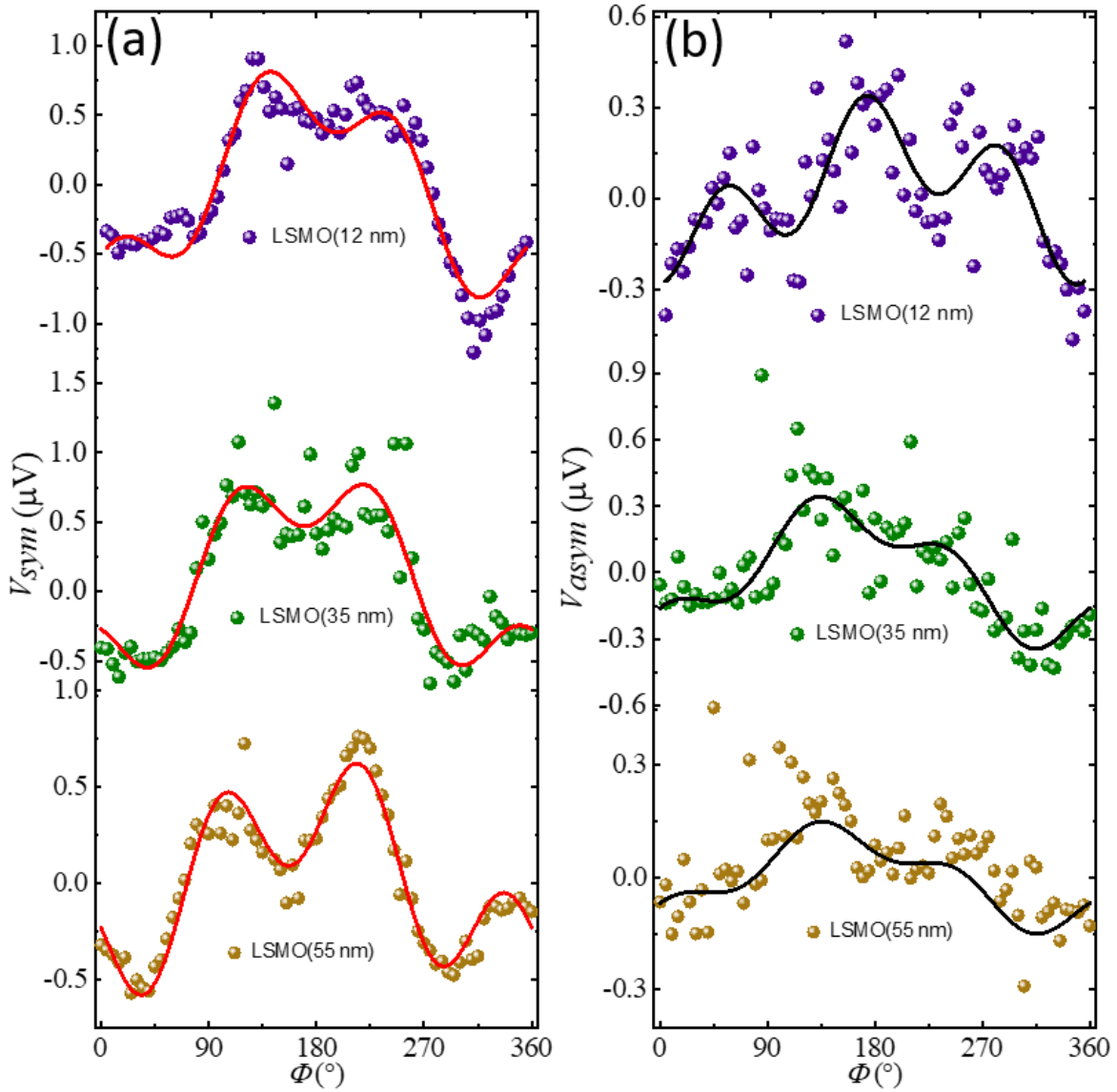


Figure 6.7 (a) ϕ dependent V_{sym} and (b) V_{asym} for LSMO films. Red and black solid lines are the best fits using equations (4) and (5), respectively.

where ϕ is the angle between the electric and magnetic fields of the applied microwave, which is 90° . Angle ϕ is defined as the angle between the voltage measurement direction and perpendicular to the magnetic field direction. V_{AHE} is anomalous Hall voltage, which arises due to the FM nature of the sample. $V_{sym}^{AMR \perp(\parallel)}$ and $V_{Asym}^{AMR \perp(\parallel)}$ are perpendicular (parallel) components of symmetric and asymmetric contributions to V_{AMR} and can be calculated using the following equation [173]

$$V_{AMR} = \sqrt{(V_{Asym}^{AMR \perp, \parallel})^2 + (V_{Sym}^{AMR \perp, \parallel})^2} \quad 6.6$$

From the fitting, a significant spin pumping voltage has been obtained for all the samples, which are listed in table 6.2. The value of V_{sp} is dominating over any other spin rectification effects. As there is no SOC layer adjacent to the LSMO film, V_{sp} can be attributed to the intrinsic ISHE of LSMO films.

In an earlier report, the spin current has been generated in the Py layer itself via FMR due to the high resistivity of the adjacent SiO_2 layer, which prevents the spins from diffusing through it (SiO_2 layer) [212]. A similar self-induced ISHE observation has also been made in Co and Fe films [213]. In our case, the resistivity of STO is comparatively less than SiO_2 [215]. When FMR occurs in the LSMO layer, the spin current is generated, which tends to move towards the LSMO/STO interface. This may cause non-negligible spin diffusion into STO while the major part of the spins is still present in the FM layer itself. At the interface, spins get scattered due to the charged impurities, which might be causing a spin gradient in the LSMO layer. This spin gradient creates spin current, which gets converted into a charge current via ISHE, which leads to the generation of potential difference.

Table-6.2 V_{sp} and V_{AHE} values for all samples from the fitting of the data shown in Fig.6.6 (a) and (b) using equations (4) and (5). V_{AMR} values were calculated using equation (6).				
Sample	V_{sp} (μV)	V_{AHE} (μV)	$V_{sym}^{AMR \perp}$ (μV)	$V_{sym}^{AMR \parallel}$ (μV)
STO(100)/LSMO (12 nm)	1.86 \pm 0.08	0.12 \pm 0.06	1.43 \pm 0.19	0.39 \pm 0.05
STO(100)/LSMO (35 nm)	1.83 \pm 0.10	0.31 \pm 0.04	1.47 \pm 0.12	0.13 \pm 0.06
STO(100)/LSMO (55 nm)	1.39 \pm 0.04	0.12 \pm 0.03	1.31 \pm 0.07	0.15 \pm 0.03

In summary, we have prepared highly epitaxial LSMO films using PLD. These films were characterized by different techniques to confirm the epitaxy nature of the grown films. Further, a detailed magnetization dynamics and inverse spin Hall effect study have been performed to explore the self-induced ISHE in LSMO films. The V_{sp} dominates over any other spin rectification effects in our samples, which indicates the presence of significant SOC in LSMO films. The spin Hall conductivity has been calculated using the first principal model, and the results qualitatively match our experimental findings. This study will help to understand the intrinsic ISHE mechanism in manganite-based films. This process is appealing from the applications point of view as well as providing scope to explore further the underlying physics.

CHAPTER 7: Exchange bias and vertical shift in $\text{La}_{0.67}\text{Sr}_{0.33}\text{MnO}_3/\text{SrRuO}_3$ bilayer system

In our previous work (chapters 3 and 4), we have shown that oxide-based molecular beam epitaxy (OMBE) prepared $\text{La}_{0.67}\text{Sr}_{0.33}\text{MnO}_3/\text{Pt}$ heterostructures possess very high spin pumping voltage [177]. Due to anti-damping torque [169,177], the α significantly decreases in such FM/HS bilayer systems in comparison to FM single layer. In chapter 5, we replaced the heavy metal with an AFM material that belongs to the same family of manganite. We observed that OMBE prepared LSMO(FM)/LSMO(AFM) system also shows spin pumping. We have also shown that the spin-to-charge conversion efficiency of LSMO(AFM) is similar to Pt [216]. Further, in chapter 6, we investigated the intrinsic ISHE in PLD grown LSMO(FM) samples. In this chapter, we attempted to perform the ISHE measurement in LSMO(FM) with a low temperature FM material which is paramagnetic at room temperature and should have high SOC. SrRuO_3 (SRO) is one of our preferred choice due to its low temperature FM nature ($T_c \sim 155\text{K}$) [217,218]. SRO has a lattice constant (0.395 nm) similar to LSMO, and it is easy to grow epitaxially on top of LSMO [219,220]. Therefore, in this study, we have explored LSMO/SRO bilayer samples that are grown epitaxially using pulsed laser deposition technique.

Sample BL1: $\text{SrTiO}_3(100)/\text{LSMO}(12\text{ nm})/\text{SRO}(10\text{ nm})$ and sample BL2: $\text{SrTiO}_3(100)/\text{LSMO}(12\text{ nm})/\text{SRO}(20\text{ nm})$ were prepared using PLD having a laser of wavelength 248 nm. The sample structure has been shown in Fig.7.1 (a). For growing LSMO films, the substrate was heated to 740°C , with laser fluence 1.4 J/cm^2 , oxygen pressure 0.47 mbar, and laser frequency 2 Hz. LSMO films were post-annealed at the same temperature for 30 min at 250 mbar oxygen atmosphere. Further samples were rapidly cooled by switching off the heater. For the growth of SRO films, sample temperature, and oxygen pressure were kept at 650°C and 0.01 mbar while the laser fluence and

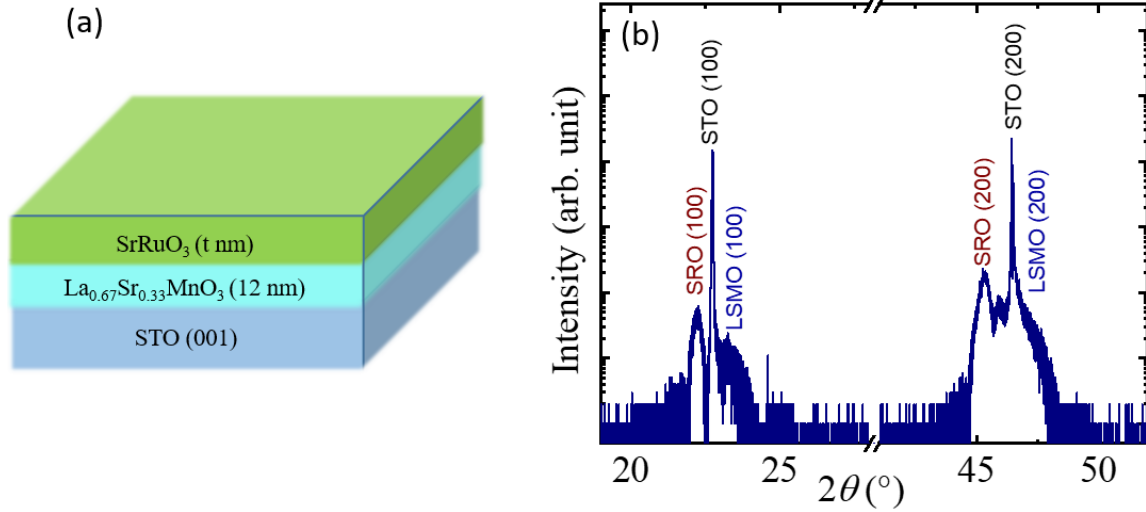


Figure 7.1 (a) Sample structure studied in this chapter. (b) XRD data for the BL2 sample corresponding to (100) and (200) peaks of LSMO and SRO, respectively.

frequency was set to 1.2 J/cm^2 and 2 Hz, respectively. Post-deposition annealing was done for 1 hour at the same temperature. In both the cases, the target rotation and target to substrate distance were 10 rpm and 50 mm, respectively. Further samples were cooled to room temperature at the rate of 10°C/min . Two control samples C1: STO(100)/LSMO(12 nm) and C2: STO(100)/ SRO(20 nm) were also grown in the same condition as described above. Rigaku smartLab X-ray diffractometer (XRD) was used to characterize the structural property of the samples. The thickness of deposited films was obtained using X-ray reflectivity (XRR) measurement. XRR data were fitted using GenX software. We have performed ferromagnetic resonance and spin pumping measurements using coplanar waveguide (CPW) based FMR spectroscopy for different frequencies. All the measurements were performed in this work at 25 mW microwave power. Measurement details can be found in our previous work [185–187]. From Lorentzian fitting of frequency-dependent FMR data, resonance field (H_{res}) and field linewidth (ΔH) have been obtained. Further, f vs H_{res} data fitted using the Kittel equation to obtain Lande-g-factor (g), and

the value of α has been obtained from a linear fit of ΔH vs f data. Further, all the magnetic measurements were performed using a superconducting quantum interference device (SQUID) manufactured by Quantum Design (model: MPMS-3).

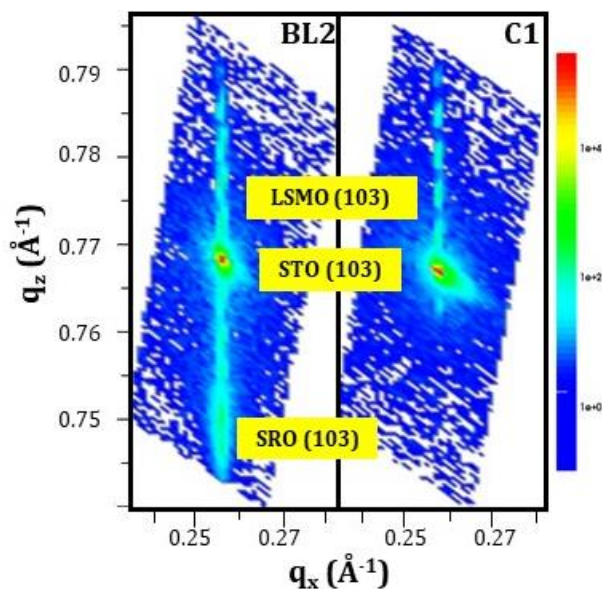


Figure 7.2 Asymmetric reciprocal space mapping (RSM) around (103) of STO for BL2 and C1 films.

High-resolution XRD has been performed to find the growth quality of the deposited sample. XRD data for BL2 is shown in Fig.7.1 (b). Peaks for (100) and (200) planes have been observed for LSMO and SRO layers, which substantiate that samples are crystalline in nature. To understand the epitaxial growth of single and bilayer thin films, we performed asymmetric reciprocal space mapping around (103) of STO. A highly strained growth of films was achieved in both C1 and BL2 samples. Further, the in-plane lattice parameter of LSMO in the case of C1 and SRO/LSMO in BL2 is similar to that of STO (as observed in Fig.7.2). This indicates a tensile (compressive) strain in LSMO (SRO) films. To compensate for the in-plane strained growth, the out-of-plane

lattice parameter of LSMO shrinks to 3.860 \AA and 3.864 \AA in the case of C1 and BL2, respectively. However, SRO's out-of-plane lattice parameter expands to 3.995 \AA in the case of BL2, as found out from out-of-plane geometry measurements. In addition, the narrow distribution of the curve in q_x -space, with a FWHM of $\sim 0.05^\circ$ signifies a superior crystalline quality of the thin films under study. The lattice parameters have also been verified from the cross-sectional TEM image as shown in Fig.7.3. From the TEM image, it can be confirmed that the LSMO/STO and LSMO/SRO interfaces are very sharp and the films are epitaxial in nature.

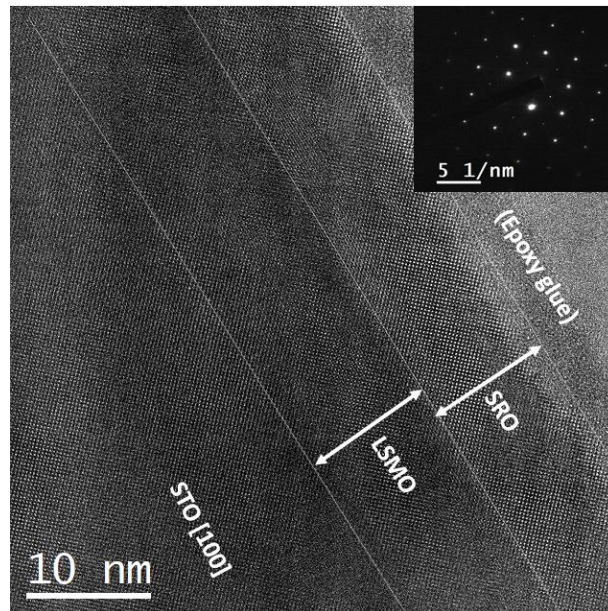


Figure 7.3 HRTEM image for sample BL1. The inset shows the SAED pattern of the STO/LSMO interface.

Further magnetic phases for all the samples have been validated via thermoremanent magnetization (TRM) at a 10 mT magnetic field. In this context, samples were heated to 400 K, which is much above the curie temperature T_C for both LSMO and SRO. A small dc field of 10 mT is applied, which is switched off after cooling the samples to 5 K. Further magnetization (M)

vs temperature (T) data have been recorded. From Fig.7.4, it can be seen that samples C1 and C2 show T_C values of 320 K and 120 K, respectively. These values are slightly less than the bulk values LSMO (350 K) and SRO (155 K), possibly due to the finite size effect and strain in deposited films [221,222]. Samples BL1 and BL2 also show similar behavior. In sample BL2, about 100 K decrement in magnetization is found due to the persistence of antiferromagnetic coupling under TRM [223]. However, in sample BL1, continuous increment in magnetization is found under TRM.

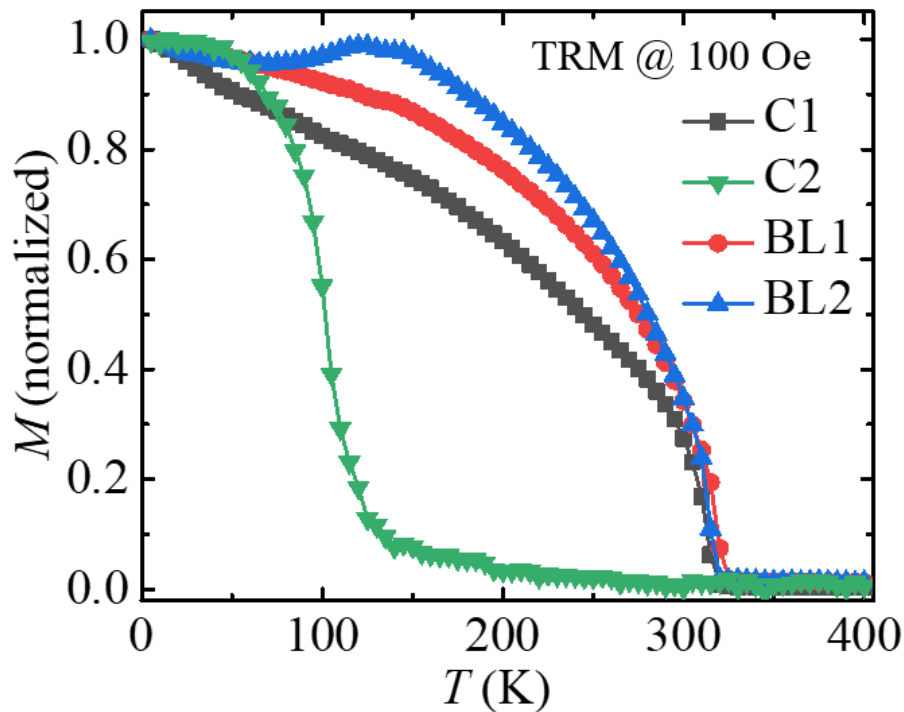


Figure 7.4 M - T data for all the samples under TRM.

Transport and Magnetotransport studies

Further we have tried to understand the transport and magnetotransport properties of the samples.

The magnetotransport study is a very useful technique to examine the microscopic parameters for

example one can investigate the elastic, inelastic, and spin orbit scattering length in metallic thin films [224]. Here we have attempted to understand the weak localization (WL) and weak anti-localization (WAL) in LSMO/SRO bilayer system by analyzing the resistivity vs temperature data. It is to be noted that in this study all the measurements have been performed in four probe geometry, where outer probes are used to give the current while two inner probes are used to measure the voltage. First sheet resistance (R_s) vs temperature (R vs T) measurements have been performed to measure the resistivity (ρ) of the samples. From the R_s , resistivity ($\rho = R_s \times t$) of the thin films, having thickness t , have been calculated and the data have been shown in Fig.7.5 (a), (b), (c), and (d) for samples C1, C2, BL1 and BL2, respectively. The resistivity values match the previous literatures [225,226]. As LSMO is FM in all measured temperature ranges, there is no sharp change in resistivity. In the case of the C2 sample, below 130 K resistivity decreases sharply which is evident of the phase change of SRO from paramagnetic to ferromagnetic. For bulk SRO this behaviour appears around 155K. This temperature difference indicates the presence of strain in our grown films. Similar behaviour has been observed in BL2 samples which is arising due to the SRO.

In the 2-dimensional (2D) limit, the quantum interference effect and electron-electron interaction are more effective at low temperatures as compared to their bulk counterpart [224]. We observed a small upturn in the resistivity at low temperatures in all the samples. The uprise is very small in the C1 sample while it increases with the thickness of SRO. For sample C2 upturn is very prominent. This upturn can be attributed to quantum interference and electron-electron interaction. The kondo-like effect can also contribute to this. In the intermediate temperature region $\rho(t)$ follows the T^2 dependency which is an indication of the presence of electron correlation [224].

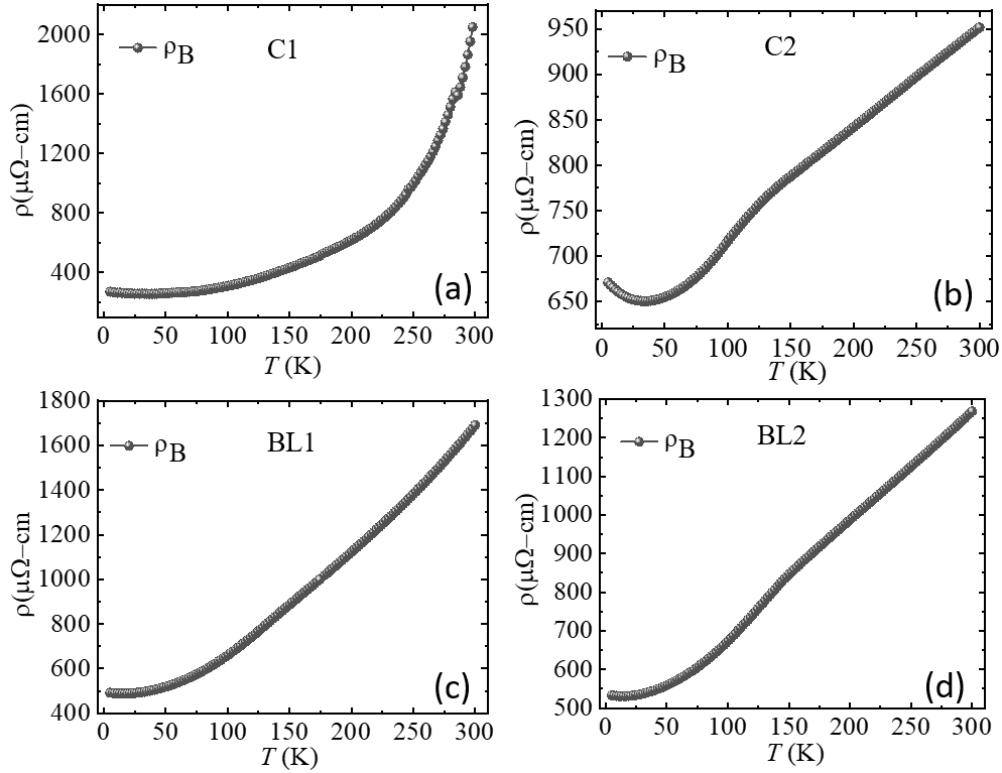


Figure 7.5 ρ vs T measurement for samples (a) C1, (b) C2, (c) BL1, and (d) BL2, respectively. Measurements were performed in four probe geometry and a $100 \mu\text{A}$ DC was supplied during the measurements.

If the crystal has any imperfections, then these imperfections work as the scattering Centre. If there is some randomness in the metallic films then the $\rho(t)$ shows $\ln(T)$ dependency at low temperatures. This phenomenon can arise due to the presence of WL or WAL behaviour, the Kondo effect, and electron-electron interaction in the disordered system [224]. In this case, the $\rho(t)$ can be expressed as

$$\rho(t) = \rho_0 - C_K \ln(T) \quad 7.1$$

Where ρ_0 and C_K are Drude resistivity of a host material and constant, respectively. In Fig.7.6 (a)-(d) we have plotted $\rho(t)$ vs $\ln(T)$ data for the temperature where $T < T_0$, where T_0 is the temperature where films show the minimum $\rho(t)$. Before T_0 the $\rho(t)$ shows upturn behaviour. In Fig.7.6 (a)-(d) we have fitted the $\rho(t)$ vs $\ln(T)$ data for low temperature using the above equation (7.1). From the fitting of equation (7.1), we found the C_K values 7.32, 11.60, 3.11, and 2.10 for samples C1, C2, BL1, and BL2, respectively. This logarithmic temperature dependency confirms the presence of WL and WAL behaviour in our samples. The intermediate temperature range $\rho(t)$ data shows the T^2 behaviour and data have been plotted in Fig.7.6 (e)-(h). The $\rho(t)$ vs T^2 data fitted using linear fits. This $\rho(t)$ linear dependency with T^2 indicates the presence of electron correlation.

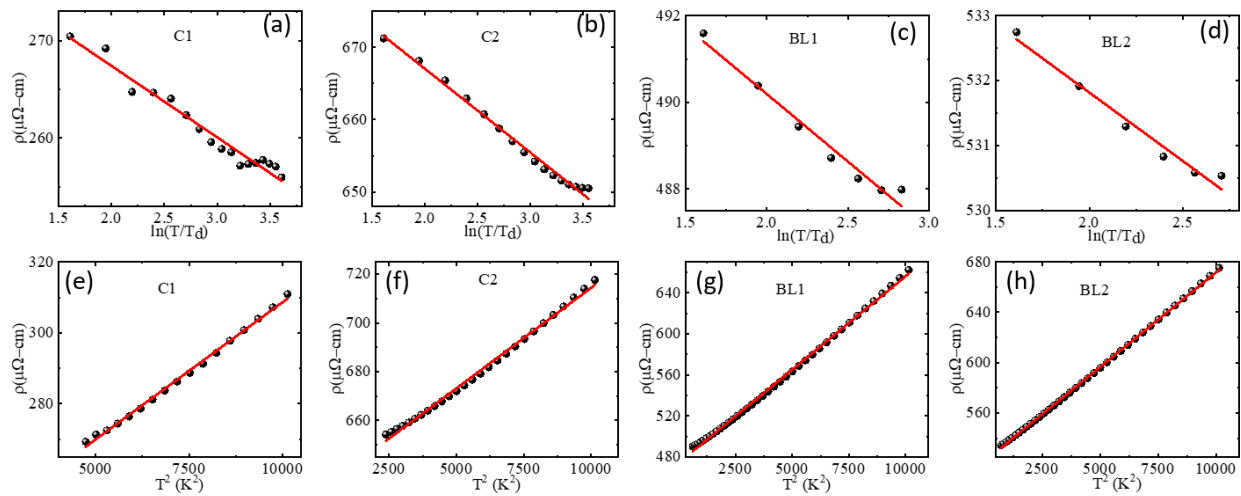


Figure 7.6 ρ vs $\ln(T)$ data for samples (a) C1, (b) C2, (c) BL1 and (d) BL2, respectively. Data were fitted using equation (7.1). ρ vs T^2 data shown for samples (e) C1, (f) C2, (g) BL1 and (h) BL2, respectively. The linear fits (red solid lines) indicates that the $\rho(t)$ have linear dependency with T^2 .

For the magnetotransport studies, resistance vs magnetic field (R-H) measurements at different temperatures have been performed. From the magnetoresistance data, MR% has been calculated using the following equation [227]

$$MR\% = \frac{R_H - R_0}{R_0} \times 100 \quad 7.2$$

where R_H and R_0 are the resistances in presence of a magnetic field and at zero magnetic field, respectively. MR% with the magnetic field have been plotted for all the samples at 5 K which are shown in Fig.7.7 (a)-(d). The C1 sample shows the usual ferromagnetic metallic behaviour and -30% MR% has been observed. For other samples C2, BL1, and BL2, butterfly shape hysteresis have been observed. This butterfly shape can arise due to the presence of SOC and anisotropy in the grown films. We have measured the out of plane M vs H for all samples at 5 K (shown in Fig.7.7 (e)-(h)) and found that indeed the anisotropy is causing the butterfly shape hysteresis in MR data. As anisotropy is absent in M-H for the C1 sample, there is no butterfly shape observed for this sample.

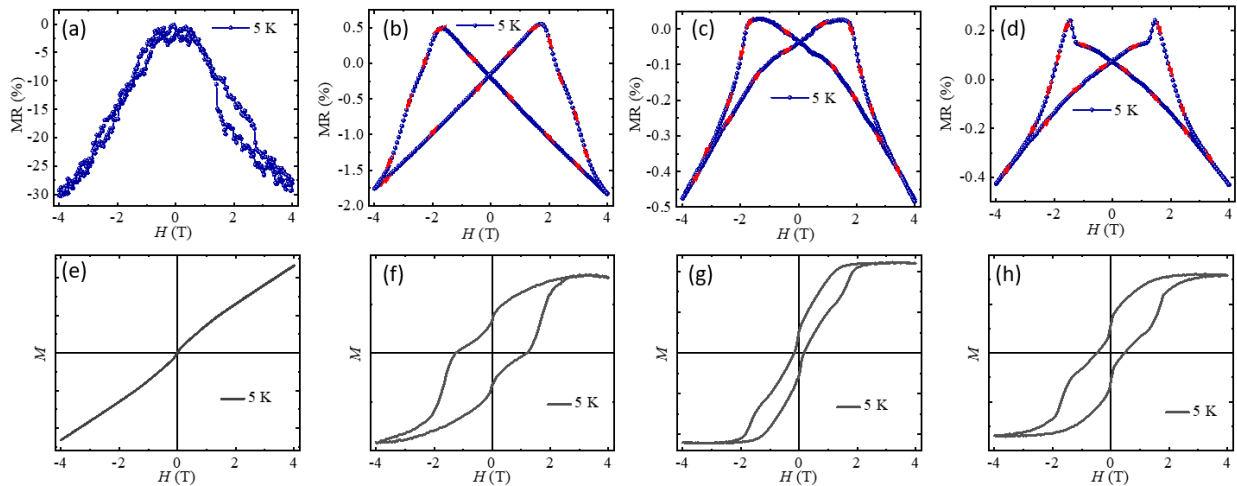


Figure 7.7 Magnetoresistance curve and their corresponding M-H data at 5 K for samples (a) & (e) C1, (b) & (f) C2, (c) & (g) BL1, and (d) & (h) BL2, respectively. The butterfly shape is arising due to the anisotropy nature of the SRO.

Very interestingly for sample BL2, we have observed the spikes in MR data, The unusual spikes might be due to the presence of non-collinear spin texture in SRO. A similar observation have been made in a previous report [228]. We have observed the butterfly shape in C2, BL1, and BL2 samples for the temperature range ($T < T_c$ (SRO)). MR Data at 100 K for samples C2, BL1, and BL2 have been shown in Fig.7.7 (a)-(d), and corresponding M - H data have been plotted in Fig.7.7 (e)-(h). Above this T_c , the butterfly shape disappeared as SRO shows paramagnetic behaviour. SRO is having high SOC which may cause the canting of spins of the LSMO layer at the interface. Further, Fig.7.8 shows the MR data at 100 K for samples C1, BL1 and BL2.

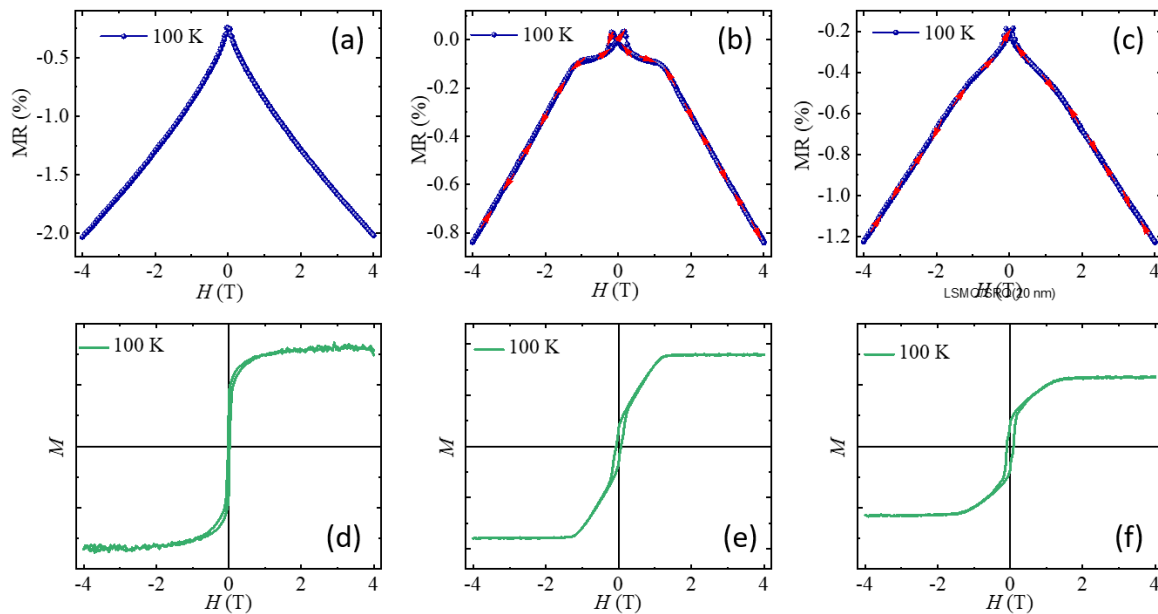


Figure 7.8 Magnetoresistance curve and their corresponding M-H data at 100 K for samples (a) & (d) C2, (b) & (e) BL1, and (c) & (f) BL2, respectively. The butterfly shape in MR data shrinks due to the loss of anisotropy at the higher temperatures (as T_c of SRO is close to 100 K).

From the magnetotransport studies, we conclude that the SRO shows FM transition below 130K which is in agreement with the M-T data. Above 130 K, SRO shows paramagnetic and bad metallic behaviour while LSMO is FM and metallic. At low temperature, SRO possesses high SOC which might be leading to spin canting at the interface of LSMO/SRO, but at room temperature, this behaviour needs to be understood. As the ISHE mainly arise due to the SOC of the material, the spin pumping measurement at room temperature has been investigated in the BL samples in the next section.

Magnetization dynamics and spin pumping studies

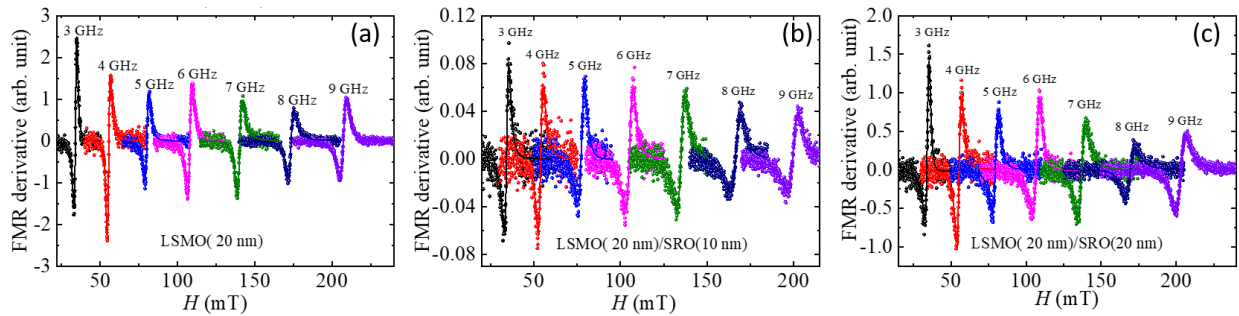


Figure 7.9 FMR spectra for samples (a) C1, (b) BL1, and (c) BL2.

To study the magnetization dynamics, we have performed frequency-dependent ferromagnetic resonance for samples C1, BL1, and BL2, and the corresponding data is shown in Fig.7.9 (a), (b), and (c), respectively. The FMR data were fitted using the Lorentzian equation to extract the H_{res} and ΔH values. Fig.7.10 (a) shows the f vs. H_{res} plot for all the samples obtained from the frequency-dependent spectra. The data have been fitted by the Kittel equation [26],

$$f = \frac{\gamma}{2\pi} \sqrt{(4\pi M_{eff} + H_{res} + H_K)(H_{res} + H_K)} \quad 7.3$$

where $\gamma(=g\mu_B/\hbar)$, g , μ_B , and M_{eff} are gyromagnetic ratio, Lande g-factor, Bohr magneton, and effective demagnetization, respectively. H_K , K_S , and t_{FM} are in-plane anisotropic fields, perpendicular surface anisotropy constant, and thickness of the LSMO layer, respectively. Further, α was evaluated by fitting data of Fig.7.10 (b) using the relation [167,168]

$$\Delta H = \Delta H_0 + \frac{4\pi\alpha f}{\gamma} \quad 7.4$$

The values of α for samples C1, BL1, and BL2 are extracted to be 0.008 ± 0.0003 , 0.012 ± 0.0004 and 0.015 ± 0.0004 , respectively. This enhanced α in BL samples indicates that there might be the possibility of spin pumping in BL samples. Therefore, we have performed inverse spin Hall effect measurement as shown in fig.7.10 (c). Unfortunately, we did not observe any significant ISHE voltage in BL samples. It is to be noted that there is a report on spin pumping study in LSMO/SRO bilayer system as 190 K [229]. However, our study shows that spin pumping vanishes at room temperature.

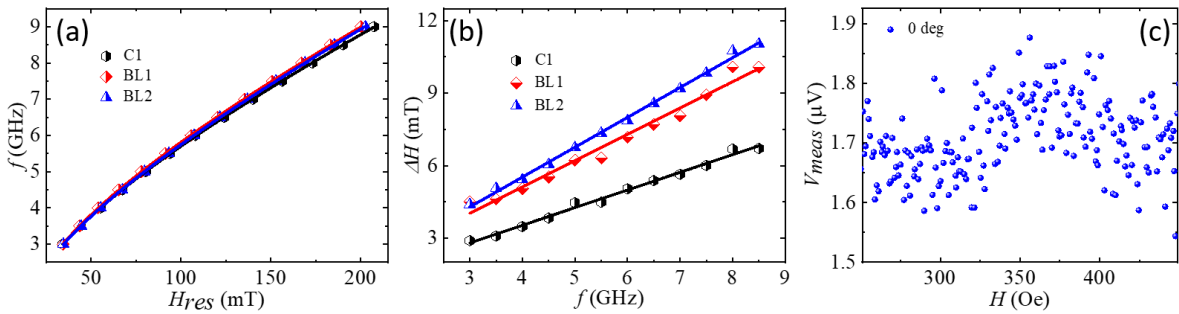


Figure 7.10 (a) f vs. H_{res} for C1, BL1, and BL2, Solid line are Kittel fit using equation (2). (b) ΔH vs. f for samples C1, BL1, and BL2, respectively. The solid lines represent the best fit to equation (3). (c) represent the measured voltage for sample BL1 at 0° .

This may be due to the loss of spin interface transparency in the LSMO/SRO interface, which further indicates that LSMO and SRO spins are showing some coupling that is not favouring the spin pumping mechanism. To find out the type of coupling at LSMO/SRO interface, a detailed exchange bias study has been performed in the next section. Exchange bias is an interface-dominated phenomenon. Therefore, this study can probe some light on our knowledge and will help us to understand the reason for the absence of spin pumping at room temperature.

Exchange bias study

In a FM1/FM2 bilayer system, EB like phenomena can be observed due to the difference in the coercivity of FM1 and FM2 layers [230]. As shown in Fig.7.11 (a), if there is no EB field present, hysteresis will be symmetric about its magnetization axis with $|H_{C1}| = |H_{C2}|$, where H_{C1} and H_{C2} are the coercivity values from +ve to -ve and -ve to +ve magnetization reversal, respectively. Whereas in the presence of EB, loops shift towards left or right (along the field axis) (Fig.7.11 (b)). Let's consider FM2 has higher coercivity than FM1, it means FM2 is a hard ferromagnet and FM1 is a soft ferromagnet. In this case, spins of FM1 will flip easily while spins of FM2 need more Zeeman energy to change their orientation on the application of external magnetic field (H). Let the Curie temperature of FM1 is higher than that of FM2 i.e. $T_{C1} > T_{C2}$. In this case, if we heat the sample more than T_{C2} , the spins of FM2 will be randomly oriented, while FM1 will be in its FM state (Fig.7.11 (c)-1). If a bias field $+H$ is applied and then the sample is cooled below T_{C2} in presence of this bias field, FM1 and FM2 both will be in FM state and spins will orient in direction of the biasing field (Fig.7.11 (c)-2). When the field is swept to $-H$, spins of FM1 will align easily

in the direction of H while FM2 spins will hold their orientation due to their pinning potential. The spins at the interface will be pinned due to the exchange interaction between FM1 and FM2 spins. Further, an increase in the field towards $-H$ aligns the spins of FM2 along the field direction. Due to this rigidity of spins of FM2, hysteresis is shifted towards the $-H$ axis. When the field is swept to $+H$, magnetization reversal occurs before its expected values due to the preferred orientation of spins of FM2.

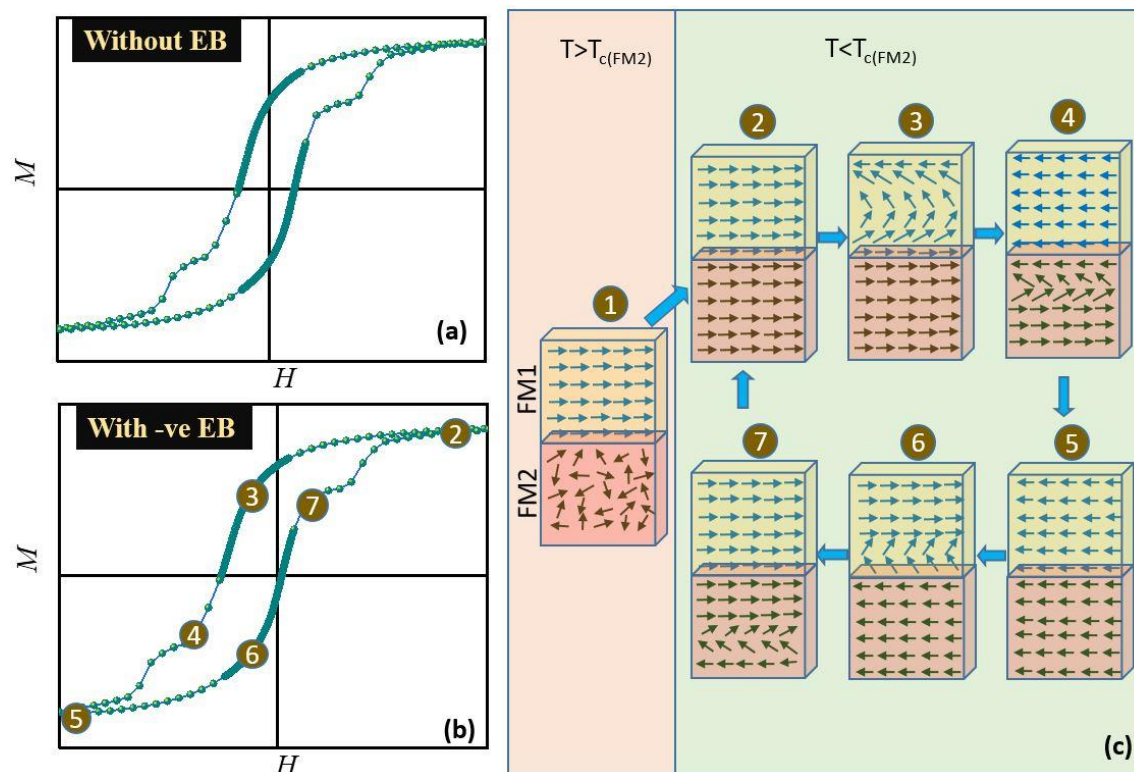


Figure 7.11 Introduction to Exchange bias. Hysteresis loop 1(a) when there is no EB, (b) when EB is present in the system. FM2 represents hard ferromagnet while FM1 is soft ferromagnet. (c)-(1) at $T > T_{c2}$, FM2 spins will be randomly oriented. in (c)-(2) $T < T_{c2}$ FM2 spins will align in direction of applied H . (c)-(3-7) represent the different orientations of spins during the field sweep.

PEB was first observed in FeF_2/Fe bilayers, where antiferromagnetic coupling has been observed at the interface. Recently similar observations have been made in several other systems experimentally [91,231,232]. In such systems, the EB field magnitude and sign depend on the cooling field sign and value (H_{CF}). Presently, perovskites have attracted the attention of researchers for such studies due to their greater tunability to EB. Perovskites give additional dimensions i.e., orbital reconstructions, charge transfer, strain at the interface, etc. Taking the advantage of these properties, one can tune the sign and magnitude of EB. In this work, we have explored LSMO/SRO bilayer system for a detailed EB study. LSMO is well known for its various applications in different fields i.e. TMR sensors, magnetic tunnel junctions (MTJs), biomedical applications, etc. [233–235]. SRO is known for its itinerant FM behaviour. SRO has large anisotropy, while LSMO possesses a small anisotropy. Though there are a few reports of EB on the LSMO/SRO system, a complete detailed EB study is lacking [197,223,236,237]. Therefore, a detailed cooling field-dependent EB, temperature-dependent EB, and training effect study have been performed in LSMO/SRO bilayer systems.

Cooling field dependent EB has been performed for all the samples. For this, samples were heated to a high temperature (400 K) and a biased cooling field was applied. After this samples were cooled to 5 K in presence of the cooling field. We have measured M-H loops with a saturation field of ± 500 mT. It is to be noted that we have not observed any EB in control samples C1 and C2. However, a significant vertical shift in control sample C2 has been observed in presence of a cooling field, as shown in Fig.7.12 (a).

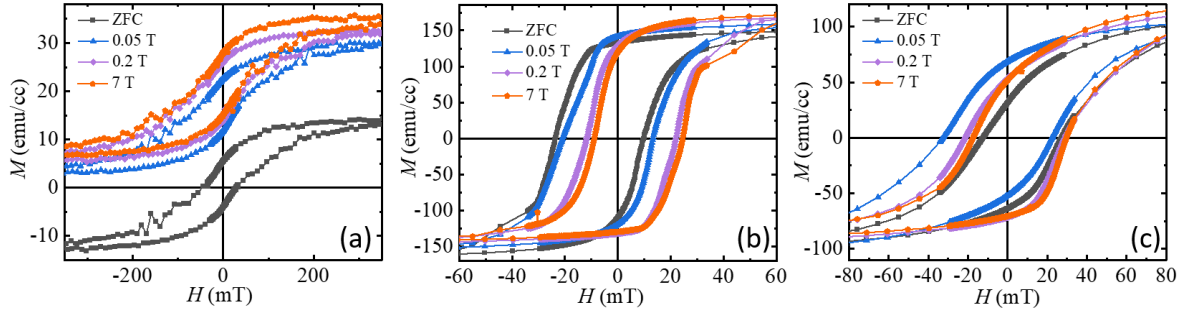


Figure 7.12 Representative cooling field dependent exchange bias at 5 K for (a) sample C2, (b) sample BL1, and (c) sample BL2.

The vertical and horizontal shifts may be associated with the pinned Ru^{4+} moments through the interaction between the FM layers. These interfacial pinned moments are irreversible during the field sweeping whereas unpinned (rotatable) Ru^{4+} moments are reversible. The shift in saturation magnetization along the magnetization axis ($M_{S_{shift}}$) can be calculated using the expression $M_{S_{shift}} = (|+M_{sat}| - |-M_{sat}|)/2$, where $+M_{sat}$ and $-M_{sat}$ are the values of saturation magnetization under positive and negative saturation field values, respectively. It is worth mentioning here that such a large vertical shift ($M_{S_{shift}}$) has been reported in both AFM/FM as well as FM/FM heterostructures [238,239]. In $\text{La}_{0.67}\text{Sr}_{0.33}\text{MnO}_3/\text{SrRuO}_3$ (FM/FM) heterostructures, it is believed that the uniaxial magnetocrystalline anisotropy due to large spin orbit coupling of Ru^{4+} leads to a giant $M_{S_{shift}}$ which drops to zero when the thickness of SRO layer is reduced to 45 nm which may be due to suppression of the uniaxial magnetocrystalline anisotropy in thinner SRO films [239]. The $M_{S_{shift}}$ was also found in pure SRO films in presence of local Ru/O₂ deficiencies [240,241]. The $M_{S_{shift}}$ has been observed to be of the same sign as that of the cooling field which may indicate that the double exchange-dominated ferromagnetic coupling can lead to NEB [91,242]. However,

there are a few reports which show the microscopic AFM coupling which causes PEB can also lead to the vertical shift in M_S [243,244].

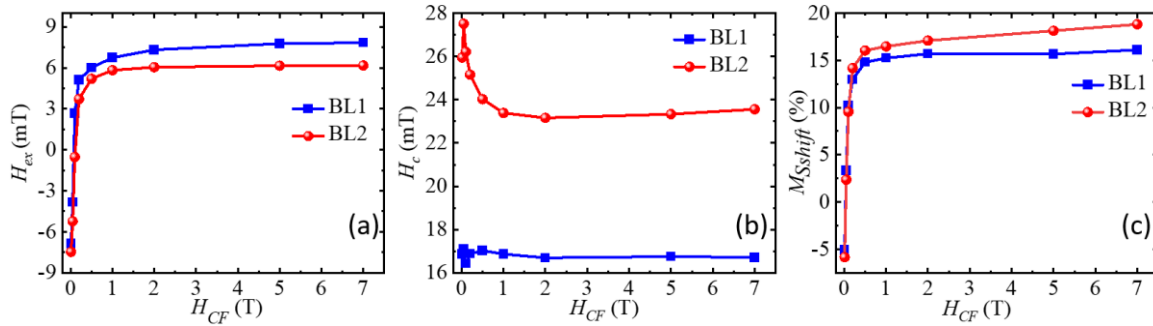


Figure 7.13 Dependency of (a) H_{ex} , (b) H_c , and (c) $M_{S_{shift}}$ on H_{CF} for samples BL1 and BL2.

In the case of bilayer samples, we have observed a clear shift in $M-H$ loops, in the presence of H_{CF} (see Fig.7.12 (b) and (c)), along the magnetic field axis. The shift is towards the positive field side when a large positive H_{CF} is applied. This indicates that the BL1 and BL2 samples exhibit PEB. However, to confirm our observations a detailed H_{CF} dependent EB measurement has been performed. H_{CF} dependent EB has been performed under 0.01, 0.05, 0.1, 0.2, 0.5, 1, 2, 5, and 7 T cooling fields for BL1 and BL2. The exchange bias field ($H_{ex} = (H_{c1}+H_{c2})/2$) and coercive field ($H_c = |H_{c1} - H_{c2}|/2$) have been calculated from the data shown in Fig.7.12 (b) and (c). H_{ex} and H_c values were plotted with respect to the cooling field as shown in Fig.7.13 (a) and (b). It can be seen that there is a crossover from -ve H_{ex} to +ve H_{ex} for both the BL samples when the cooling field increases. Under the low cooling field, FM double exchange interaction dominates over AFM superexchange interaction, which resulted in NEB. At higher cooling fields AFM superexchange interaction at the interface dominates over FM double exchange interaction which causes PEB. A

similar but opposite observation has been reported by Rana et al. in LSFO/SRO bilayer [244]. The H_c values are higher on the lower cooling field due to the ferromagnetic coupling and the interfacial spins take part in magnetization reversal. However, at a higher cooling field side due to antiferromagnetic coupling at the interface, the coercive field decreases as the interface spins do not take part in magnetization reversal. We have also observed $M_{S_{shift}}$ for BL samples due to the role of SRO (see fig.7.13 (c)). This $M_{S_{shift}}$ is absent in the case of control sample C1, where the SRO layer is not present.

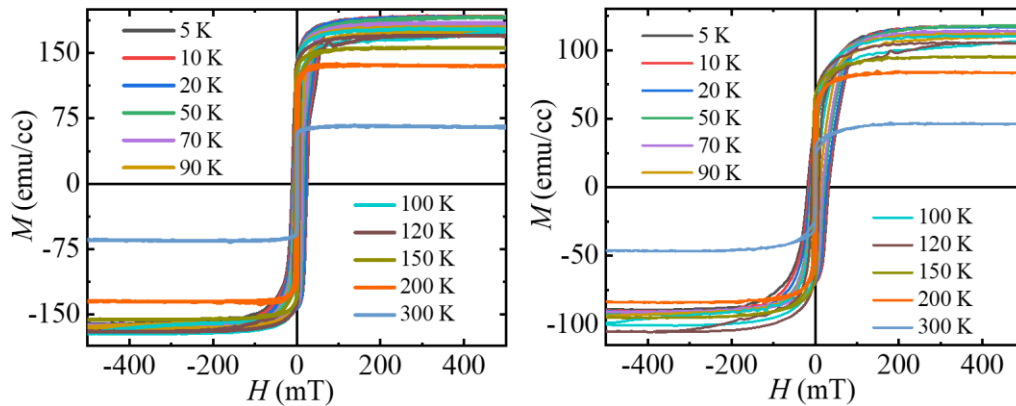


Figure 7.14 Temperature-dependent exchange bias measurement for samples (a) BL1 and (b) BL2. All the measurements were performed in presence of a H_{CF} of +1T.

As a very peculiar NEB to PEB crossover has been observed under various H_{CF} , the similar temperature dependence of EB cannot be ruled out. Therefore, to confirm this a detailed temperature dependent EB study has been performed in BL samples shown in Fig.7.14 (a) and (b). For this, the cooling field was kept at 1 T for recording the M-H loops. H_{ex} and H_c values, calculated from the temperature dependent EB hysteresis loops, have been plotted with respect to

temperature as shown in Fig.7.15 (a) and (b). It is clear that with the increase in temperature H_{ex} and H_c values decrease and vanish near 120 K, which is the T_c of the SRO layer. It can be noted that $M_{S_{shift}}$ is present below the T_c of the SRO (fig.7.15 (c)). Above the T_c of SRO, both exchange bias, as well as vertical shift, disappear. We also found a crossover from positive exchange bias to negative exchange bias about 100 K in both the bilayer samples.

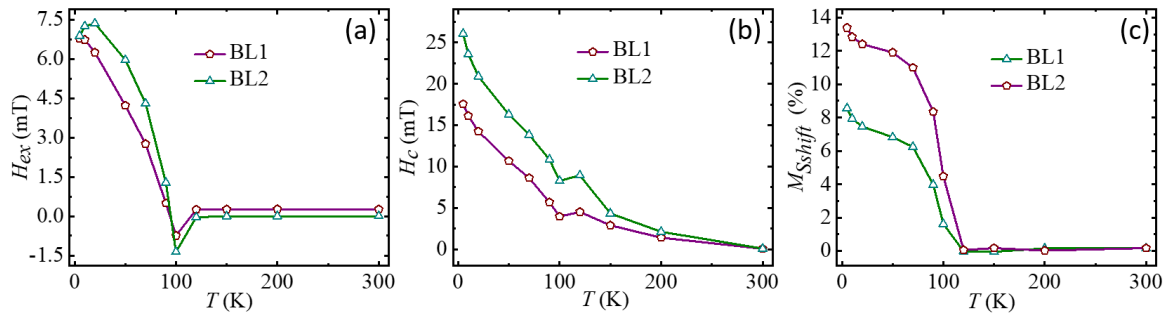


Figure 7.15 Temperature dependence of (a) H_{ex} , (b) H_c , and (c) $M_{S_{shift}}$ for samples BL1 and BL2.

As EB has been observed with various H_{CF} and temperatures, it is very important to understand how the interfacial and bulk spins relax eventually with time. In this context, a training effect experiment is a well known method for such studies. Therefore, to observe the training effect, we first field cooled the samples from 400 K to 5 K in presence of a 1 T cooling field. Then we took 10 consecutive hysteresis loops. Fig7.16 (a)-(c) shows the training effect measurement at 5 K for samples C2, BL1, and BL2, respectively. We observe an anomalous behaviour of the

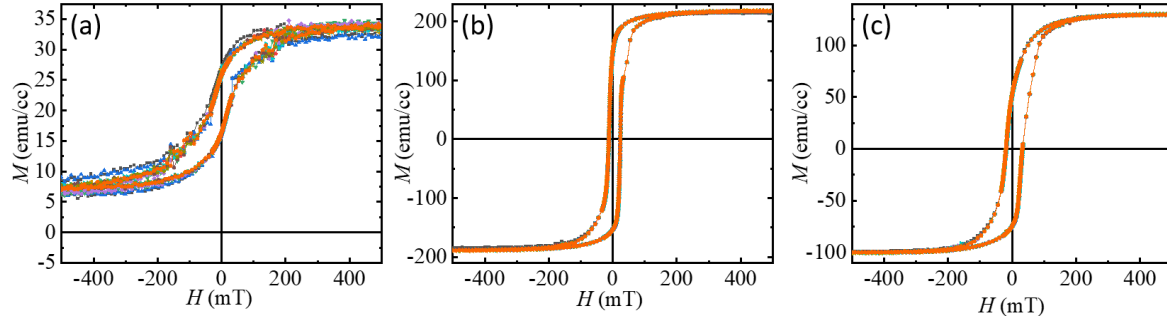


Figure 7.16 Training effect data for samples (a) C2, (b) BL1, and (c) BL2.

H_{ex} vs loop number (n) under training effect at 5 K which is shown in Fig.7.17. H_{ex} fields have been calculated for BL1 and BL2 samples. It is interesting to see that H_{ex} for BL1 first decreases sharply for loop $n=1$ to 2 and further increases gradually with increasing n , whereas for BL2 sample H_{ex} gradually increases with increasing n . In both samples, H_{ex} is saturated around $n=6$. To evaluate the role of temperature on the training effect, we again field cooled the samples from 400 K to 75 K in presence of 1 T cooling field. To evaluate the magnetic nature of the interface, we fitted the training effect data using a thermal relaxation model which is given below [245]:

$$H_{ex} = H_{ex}^{\infty} + \frac{K}{n^{1/2}} \quad 7.5$$

where H_{ex}^{∞} is the exchange bias field when n tends to infinity, H_{ex}^n is the exchange bias field of the n^{th} loop and K is the system dependent constant. This model is relevant for the system with ferromagnetic or antiferromagnetic-like interfaces [245–247]. In ferromagnetic/antiferromagnetic systems, there is a gradual decrease of H_{ex} with n . However, we found a sudden decrease in H_{ex} from $n=1$ to 2. After this, a gradual decrease of H_{ex} is found for $n>2$. This type of behaviour is also found in systems with spin-glass frustration [246]. Then, we fitted the data using

frozen and rotatable spin relaxation models to evaluate the relaxation rate of frustrated interfacial spins [248]:

$$H_{ex} = H_{ex}^{\infty} + A_f e^{-n/P_f} + A_i e^{-n/P_i} \quad 7.6$$

T (K)	Sample	H_{ex}^{∞} (mT)	A_f (mT)	P_f	A_i (mT)	P_i
75	BL1	1.54	5.40 ± 0.72	0.46 ± 0.03	0.35 ± 0.01	12.34 ± 0.88
75	BL2	2.36	3.56 ± 0.57	0.5 ± 0.04	0.26 ± 0.02	13.60 ± 0.17

where, A_f and P_f are parameters related to the interfacial frozen spins, while A_i and P_i are the parameters related to interfacial rotatable spins of the bilayer. The parameters A_f and A_i have the dimension of the magnetic field while P_f and P_i are dimensionless and can be considered equivalents of relaxation time. Parameters obtained from the fit of the H_{ex} vs n data using equation (7.6) are listed in table 7.1.

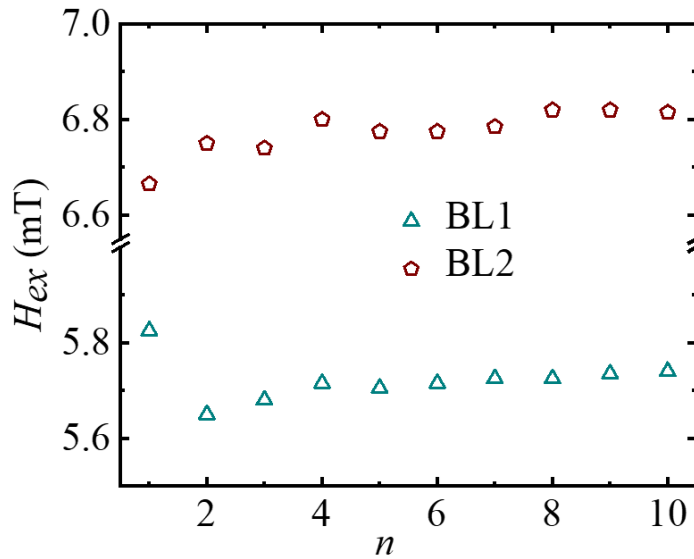


Figure 7.17 H_{ex} vs n data obtained from training effect at 5 K for BL1 and BL2 samples.

Binek proposed a model to evaluate the damping rate of interfacial spins which is given below [249]:

$$H_{C1(2)} = H_{C1(2)}^{\infty} + \frac{k1(2)}{(n + n_0^{1(2)})^{1/2}} \quad 7.7$$

where, $H_{C1(2)}$ is the coercivity at the descending and ascending part of the hysteresis loop, $H_{C1(2)}^{\infty}$ is the coercivity at the descending and ascending part of the hysteresis loop when n tends to ∞ , $k1(2)$ is the damping rate of the interfacial spins at the descending and ascending part of the hysteresis loop, $n_0^{1(2)}$ is the initial state at the descending and ascending part of the hysteresis loop. The damping rate of interfacial spins decreases with the increased thickness of the SRO film.

To know if the bulk spins of SRO relax under the training effect, we fitted the data using the below equation [244,250]. This equation is derived from Landau-Khalatnikov (LK) theory considering pinning layer magnetization is proportional to H_{ex} .

$$H_{ex}(n) = (C + 1)^{(n-1)} \left[H_{ex}(1) - CH_{ex}^e \left[\left(\frac{(C + 1)^{n+1} - 1}{C(C + 1)^{n-1}} \right) - (C + 2) \right] \right] \quad 7.8$$

Where, C is limited to $-1 < C < 0$ for the convergence of LK theory, C is the proportionality constant, $H_{ex}(1)$ is the exchange bias field of the 1st loop, H_{ex}^e is the exchange bias field at the equilibrium condition. The best fit of the training effect data using equation (7.8) indicates that bulk spins of SRO relax under the training effect. Fig.7.18 (a)-(d) show the fitting of the training effect data with various models to evaluate the magnetic nature of the interface and also the relaxation of SRO bulk spins under the training effect.

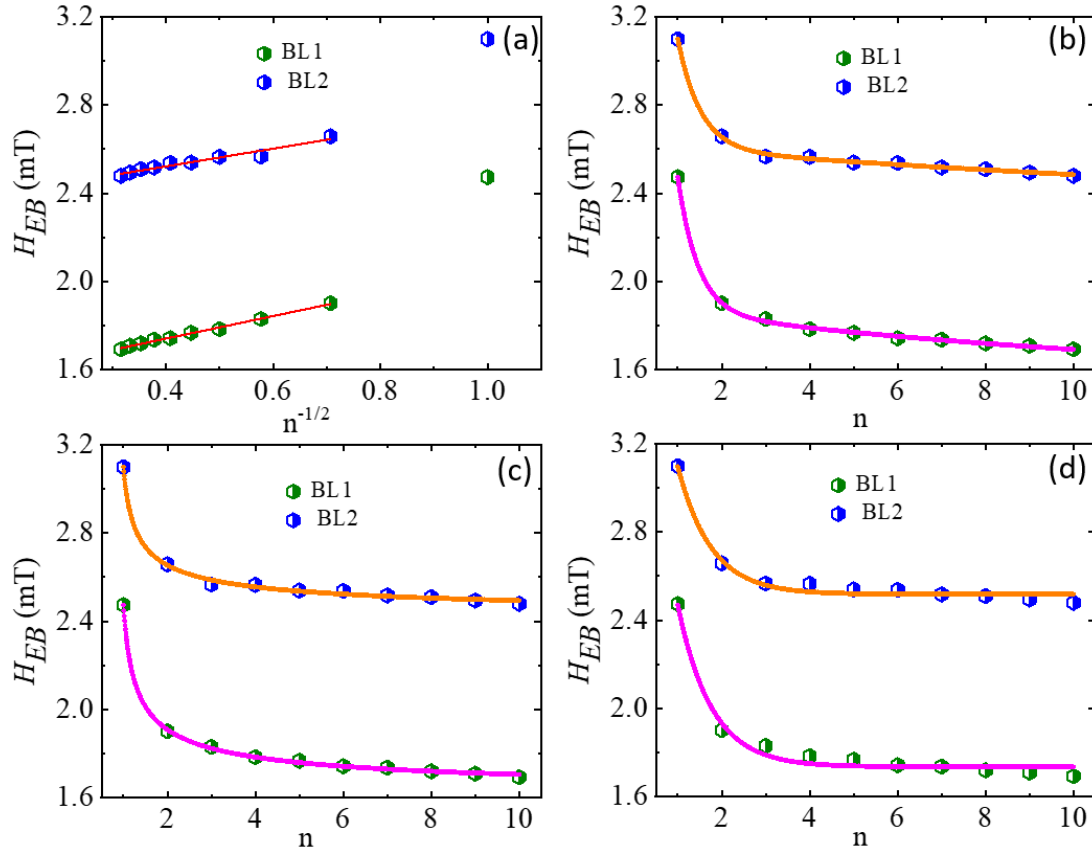


Figure 7.18 Training effect data under 1 T cooling field at 75 K. (a) H_{ex} vs $n^{-1/2}$ experimental data where solid lines are the linear fits. (b) H_{ex} vs n fitted using frozen and rotatable spin relaxation model (c) fitted using modified Binek model and (d) fitted using a model derived from LK theory.

In summary, we have prepared high quality LSMO/SRO bilayer samples by pulsed laser deposition technique. The structural characterization by XRD of the samples confirms the epitaxial nature of the grown samples. TEM images confirm the sharp STO/LSMO and LSMO/SRO interfaces. The indication of strain in the grown films has been observed by reciprocal space mapping. Transport and magnetotransport measurement indicate that weak localization and weak anti-localization may be present in the sample due to SOI, electron correlation, and Kondo-like

effects. From the magneto transport study, MR% for LSMO film has been calculated to -30%, while other samples show very low MR%. The spike in MR data in the BL2 sample at 5 K indicates the presence of chiral spin texture in this sample. The magnetization dynamics study shows the enhancement in damping in BL samples in comparison to the C1 sample. However, significant ISHE has not been observed in these samples. Hence the enhancement in the damping can be attributed to interface roughness, decreased interface spin transparency, and some other defects present in the samples. Further in the EB study, we have shown that LSMO/SRO system shows very interesting exchange bias properties along with the vertical shift in saturation magnetization. A crossover from NEB to PEB has been observed due to a change in interfacial ferromagnetic to antiferromagnetic coupling when the cooling field changes from lower to higher values. This can be attributed to the modification in double exchange interaction (which causes FM coupling) nature to superexchange interaction (which causes AFM coupling) [244,251]. Knowing the strength of the cooling field one can tune NEB to PEB. Further temperature dependent EB has been observed in BL systems, which decreases with increases in temperature. The EB changes sign near 100 K and vanishes after the T_C of SRO. The training effect measurement at 5K suggests that the interfacial spins of BL1 and BL2 have a very large retentivity. Even after taking 10 loops under the training effect, the interfacial spins show no significant relaxation. At 75 K, the retentivity of spins reduces significantly due to the relaxation of SRO bulk spins. Knowing all these properties, one can utilize these special features of LSMO/SRO bilayers to tune NEB to PEB or vice versa to control the reading and writing in magnetic storage media.

CHAPTER 8: Summary and conclusion

In this thesis, we have focused on spin to charge conversion efficiency from ferromagnet (FM) to high spin orbit coupling (HS) layer. We choose LSMO as a FM while in place of HS material a different class of materials (such as HM, AFM and FM) have been explored. Epitaxial films were deposited by state of art oxygen-assisted molecular beam epitaxy (OMBE) and pulsed laser deposition (PLD) techniques. The samples were structurally characterized by XRD, and transmission electron microscopy and magnetic properties were characterized by SQUID magnetometry. Magnetization dynamics were performed at room temperature in a ferromagnetic resonance spectrometer. Spin pumping measurements were performed in an in-house developed ISHE measurement setup. From angle dependent, ISHE measurement spin to charge conversion efficiency has been calculated for the HS materials.

In the 3rd chapter of the work, we focused on the search for an efficient ferromagnet with standard heavy metal. Therefore, we have taken $\text{La}_{0.67}\text{Sr}_{0.33}\text{MnO}_3$ (LSMO) as a ferromagnet due to its high spin polarization and high Curie temperature (~ 350 K). High spin-polarized materials are expected to be an efficient spin current source, i.e., these materials can be good candidates for spin pumping studies. Further, we have taken Pt as standard heavy metal due to its high spin orbit coupling properties⁸. High quality LSMO single layer and LSMO/Pt bilayer samples were prepared by OMBE technique. The growth quality and thickness were monitored in-situ using low-energy electron diffraction (LEED) and reflection high-energy electron diffraction (RHEED) techniques. Magnetization dynamics study has been performed by a ferromagnetic resonance (FMR) spectrometer. We have performed frequency-dependent FMR for all the samples, and from the fitting of this data, α values have been extracted. The obtained α values significantly decreases in LSMO/Pt bilayer samples ($\alpha = 0.004$) in comparison to the single layer LSMO sample ($\alpha =$

0.0104). Interestingly α value significantly decreases with an increase in Pt thickness. In the usual case, it is expected that due to spin pumping, the alpha enhances in the bilayer system compared to a single layer FM. This decrease in the alpha of the bilayer compared to a single layer is known as anti-damping. The reason behind this anti-damping can be given as anti-damping like torque. A detailed explanation of anti-damping can be found in our published work¹³. Further spin pumping measurements have been performed for all the samples. From angle-dependent ISHE measurements, very high spin pumping voltages ($\sim 20 \mu\text{V}$) have been obtained. For single layer LSMO, a negligible ISHE voltage has been observed. We have very high spin pumping voltage and decreased α in our bilayers. These two observed phenomena are usually mutually exclusive. This coexistence of these two properties makes this system very interesting from the spintronics application point of view as we observe high spin pumping voltage and at the same time, α is lesser. Spin Hall angle has been calculated to 0.03. This value matches well with the previous reports [175,176,252].

Further, it has been observed that FMR spectra of LSMO films showed very interesting sign change when we varied the microwave frequency [209]. We have observed that at higher frequencies (12 to 15 GHz) range, FMR spectra change their sign. This is a unique feature of LSMO films. Therefore, to explore the origin of phase change in FMR spectra and its effect on ISHE signal, a systematic frequency-dependent ISHE study has been performed. To confirm the sample quality, we have performed cross-sectional TEM imaging for sample S2. The HRTEM images show that the LSMO film is grown epitaxial. We have not observed any defect in LSMO films. FMR measurements have been performed using a VNA-FMR setup, while ISHE measurements have been performed using in-house modified NanOsc Phase FMR. We have observed that FMR spectra change their sign at 14 GHz in comparison to other frequencies. Further

increasing the frequency to 15 GHz, FMR spectra return to their initial phase. We have observed that the maximum voltage is measured at 14 GHz. Further, we have calculated the microwave power absorption P_{abs} for all frequencies, and then microwave absorption induced angular momentum to spin current conversion efficiency has been calculated. It can be seen that unlike to YIG/Pt system, LSMO/Pt system follows the simulation data for lower frequencies (2 to 12 GHz), while at higher frequencies, efficiency enhances drastically. To explore the origin of sign change, we have performed angle-dependent FMR and ISHE at different frequencies. From the angle-dependent ISHE measurements, spin pumping voltage has been obtained. Observed spin pumping voltage shows non-linear relation with frequency. Further spin Hall angle has been calculated, and spin Hall angle values follow the trends of spin pumping voltage with the frequency. Therefore, we successfully demonstrated that efficiency could be tuned by varying the microwave frequency.

In the 5th chapter of this work, we have studied LSMO(FM)/LSMO(AFM) heterostructures. LSMO shows very interesting properties due to its rich magnetic and electronic phase diagram. When one changes the concentration Sr in LSMO, it changes its phase from ferromagnetic to antiferromagnetic and paramagnetic phases. In this study, we have explored AFM oxide as a spin sink material. In LSMO(FM) and LSMO(AFM), lattice constants are nearly similar (~0.386 nm), which can promote epitaxial growth on top of the SrTiO₃ substrate. It is to be noted that AFM materials are very useful material due to their robustness against magnetic fields and can be utilized for faster spintronics devices as they show terahertz dynamics. We have prepared a series of LSMO(FM)/LSMO(AFM) samples with varying LSMO(AFM) thicknesses. Growth quality has been monitored in situ using RHEED. We have performed XRD and cross-sectional TEM imaging to confirm the epitaxial growth of grown films. The damping for these samples was obtained to be very low (in the range of 0.003) indicating that the samples are of excellent quality and can be

used for spintronics applications. Further, we have measured the ISHE for all samples. Interestingly LSMO(FM) samples show some finite amount of spin pumping voltage. We observed that with the increase in LSMO(AFM) layer thickness, spin pumping voltage also increases. The spin Hall angle values for LSMO(AFM) are comparable to Pt values. Hence it can be concluded that LSMO(AFM) films are a good alternative to HMs.

In the 6th chapter of this thesis, we have explored the intrinsic spin pumping in LSMO(FM) films. For this, we have deposited our LSMO films by pulsed laser deposition. The optimum growth conditions have been taken for the lower damping constant. To study intrinsic ISHE, we have prepared a series of LSMO (t nm) ($t = 12, 35, \text{ and } 55$ nm) films. Further, we have performed X-ray diffraction and TEM for structural characterization. From Magnetization (M) vs. temperature (T) measurements, we have obtained the Curie temperature (T_c). We have performed frequency-dependent FMR in the frequency range of 3.5 to 10 GHz. From the FMR spectra, we have obtained linewidth (ΔH) and H_{res} values. Further, α values were extracted from FMR data, as explained earlier. α values match with previously reported values. To measure spin pumping voltage and separate rectification effects from spin pumping voltage, we have performed angle-dependent ISHE measurements at 7 GHz. Each angle-dependent measured voltage fitted for V_{sym} and V_{asym} values. V_{sym} and V_{asym} were plotted with angle and fitted to obtain different voltage contributions. From the fitting, we observed a significant spin pumping voltage ($\sim 1.8 \mu\text{V}$). As there is no HS layer adjacent to the LSMO layer, it confirms that this is due to the intrinsic ISHE in LSMO films. LSMO is a metallic oxide which may have some finite SOC. This spin current, due to the SOC of the film, gives the finite transverse voltage, which is detected as ISHE voltage, and this phenomenon is called self-induced ISHE.

Chapter 8: Summary and conclusion

In the 7th chapter of the work, we studied LSMO/SrRuO₃ (SRO) bilayer system. SRO is an oxide FM with $T_c \sim 150$ K. There are a few reports which show the spin pumping studies at LSMO/SRO bilayer. However, these studies are at low temperatures. Therefore, it will be interesting to study LSMO/SRO heterostructures for spin pumping at room temperature. Here LSMO is FM, while SRO is paramagnetic. The LSMO/SRO bilayer samples were prepared by PLD. Samples were characterized by XRD, TEM and SQUID. We also measured the magnetotransport properties of the deposited samples and for single layer LSMO, about -30% MR has been obtained. From the damping measurement, we observed an enhancement in damping in bilayer samples in comparison to LSMO single layer. This is an indication that spin pumping may be present in our system. To confirm the spin pumping ISHE measurement was performed, however, we have not observed significant ISHE in bilayer samples. This may be due to some interfacial effects, such as loss of spin transparency etc. To check the coupling at LSMO/SRO interface a detailed exchange bias study has been performed. From cooling field dependent exchange bias, we have observed significant unconventional EB. Cooling field-dependent EB also shows the vertical shift in the hysteresis loop which might be due to the frozen spins. Further temperature-dependent EB studies have been performed. The EB effect decreases with an increase in temperature.

In summary, our results show that spin current propagation efficiency in FM/HS can exhibit novel physics, which are stated in the following:

1. We have observed very high spin pumping voltage and a decrease in Gilbert damping. These two properties are usually mutually exclusive; therefore, the co-existence of these makes LSMO/Pt system very promising from a spintronics application point of view.
2. We have performed frequency-dependent ISHE measurements in LSMO/Pt bilayer samples. The study shows that one can tune the spin-to-charge conversion efficiency by

varying the microwave frequency.

3. We have performed for the first time a spin pumping study in OMBE prepared LSMO(FM)/LSMO(AFM) bilayer system. LSMO(AFM) films are an alternative to HM (e.g., Pt) with a comparable spin Hall angle.
4. We have explored intrinsic spin pumping in PLD-prepared LSMO thin films. At FMR conditions, the finite SOC of LSMO films causes the generation of transverse voltage across the edges of LSMO films.
5. We have performed a magnetization dynamic study in LSMO/SRO bilayer system. From magnetotransport measurement, we have obtained -30% MR in LSMO single layer. We have further explored this system for EB and magnetotransport studies. An unconventional vertical shift in cooling field-dependent EB has been observed.

Future outlook

In this thesis work, we have observed that Pt and LSMO(AFM) material exhibits high SOC. The anti-damping in LSMO/Pt bilayer system is very interesting and it should be understood theoretically. The high SOC of LSMO(AFM) can be used to generate the spin current. Spin current is essential for switching the magnetization of the FM layer in SOT-based MRAM devices. Hence these materials can be utilized in SOT devices.

1. Anti-damping in LSMO/Pt bilayer systems should be understood theoretically.
2. The FMR is a very important tool to understand the dynamic properties of a FM. The FMR spectra of LSMO show various non-uniform modes, sign change properties etc. A thorough understanding of this can give a way to enhance the usability of LSMO in spintronics applications.

Chapter 8: Summary and conclusion

3. LSMO(AFM) material can be explored to generate spin current in SOT-based devices.
4. LSMO(AFM) can be explored in terahertz dynamics due to its AFM nature.
5. LSMO(FM)/LSMO(AFM) material shows significant exchange bias, therefore a detailed EB study can be performed to understand the coupling between LSMO(FM)/LSMO(AFM) bilayer system.
6. Further study of the manganite-based system can give a way to control the spin to charge conversion efficiency for future applications.
7. SRO can be explored with other FM materials to observe the spin pumping at room temperature.

References

- [1] S. Ikeda, K. Miura, H. Yamamoto, K. Mizunuma, H. D. Gan, M. Endo, S. Kanai, J. Hayakawa, F. Matsukura, and H. Ohno, *A Perpendicular-Anisotropy CoFeB–MgO Magnetic Tunnel Junction*, *Nature Mater* **9**, 721 (2010).
- [2] S. Yuasa, T. Nagahama, A. Fukushima, Y. Suzuki, and K. Ando, *Giant Room-Temperature Magnetoresistance in Single-Crystal Fe/MgO/Fe Magnetic Tunnel Junctions*, *Nature Mater* **3**, 868 (2004).
- [3] S. S. P. Parkin, C. Kaiser, A. Panchula, P. M. Rice, B. Hughes, M. Samant, and S.-H. Yang, *Giant Tunneling Magnetoresistance at Room Temperature with MgO (100) Tunnel Barriers*, *Nature Mater* **3**, 862 (2004).
- [4] L. Berger, *Low-field Magnetoresistance and Domain Drag in Ferromagnets*, *Journal of Applied Physics* **49**, 2156 (1978).
- [5] J. C. Slonczewski, *Current-Driven Excitation of Magnetic Multilayers*, *Journal of Magnetism and Magnetic Materials* **159**, L1 (1996).
- [6] L. Berger, *Emission of Spin Waves by a Magnetic Multilayer Traversed by a Current*, *Phys. Rev. B* **54**, 9353 (1996).
- [7] J. A. Katine, F. J. Albert, R. A. Buhrman, E. B. Myers, and D. C. Ralph, *Current-Driven Magnetization Reversal and Spin-Wave Excitations in Co / Cu / Co Pillars*, *Phys. Rev. Lett.* **84**, 3149 (2000).
- [8] J. Z. Sun, *Current-Driven Magnetic Switching in Manganite Trilayer Junctions*, *Journal of Magnetism and Magnetic Materials* **202**, 157 (1999).
- [9] T. Kawahara et al., *2 Mb SPRAM (SPin-Transfer Torque RAM) With Bit-by-Bit Bi-Directional Current Write and Parallelizing-Direction Current Read*, *IEEE J. Solid-State Circuits* **43**, 109 (2008).
- [10] T. Kishi et al., *Lower-Current and Fast Switching of a Perpendicular TMR for High Speed and High Density Spin-Transfer-Torque MRAM*, in *2008 IEEE International Electron Devices Meeting (IEEE, San Francisco, CA, USA, 2008)*, pp. 1–4.
- [11] D. C. Ralph and M. D. Stiles, *Spin Transfer Torques*, *Journal of Magnetism and Magnetic Materials* **320**, 1190 (2008).
- [12] A. Brataas, A. D. Kent, and H. Ohno, *Current-Induced Torques in Magnetic Materials*, *Nature Mater* **11**, 372 (2012).
- [13] S. Bhatti, R. Sbiaa, A. Hirohata, H. Ohno, S. Fukami, and S. N. Piramanayagam, *Spintronics Based Random Access Memory: A Review*, *Materials Today* **20**, 530 (2017).
- [14] S. A. Wolf, D. D. Awschalom, R. A. Buhrman, J. M. Daughton, S. von Molnár, M. L. Roukes, A. Y. Chtchelkanova, and D. M. Treger, *Spintronics: A Spin-Based Electronics Vision for the Future*, *Science* **294**, 5546 (2001).
- [15] M. Baumgartner et al., *Spatially and Time-Resolved Magnetization Dynamics Driven by Spin–Orbit Torques*, *Nature Nanotech* **12**, 10 (2017).
- [16] J. Smit, *The Spontaneous Hall Effect in Ferromagnetics I*, *Physica* **21**, 877 (1955).
- [17] L. Berger, *Side-Jump Mechanism for the Hall Effect of Ferromagnets*, *Phys. Rev. B* **2**, 4559 (1970).
- [18] J. E. Hirsch, *Spin Hall Effect*, *Phys. Rev. Lett.* **83**, 9 (1999).
- [19] A. R. Mellnik et al., *Spin-Transfer Torque Generated by a Topological Insulator*, *Nature* **511**, 449 (2014).
- [20] M. Jamali, J. S. Lee, J. S. Jeong, F. Mahfouzi, Y. Lv, Z. Zhao, B. K. Nikolić, K. A. Mkhoyan, N. Samarth, and J.-P. Wang, *Giant Spin Pumping and Inverse Spin Hall Effect in the Presence of Surface and Bulk Spin–Orbit Coupling of Topological Insulator Bi₂Se₃*, *Nano Lett.* **15**, 7126 (2015).
- [21] Y. Fan et al., *Magnetization Switching through Giant Spin–Orbit Torque in a Magnetically Doped Topological Insulator Heterostructure*, *Nature Mater* **13**, 699 (2014).

- [22] S. Pathak, C. Youm, and J. Hong, *Impact of Spin-Orbit Torque on Spin-Transfer Torque Switching in Magnetic Tunnel Junctions*, Sci Rep **10**, 1 (2020).
- [23] R. L. de Orio, J. Ender, S. Fiorentini, W. Goes, S. Selberherr, and V. Sverdlov, *Optimization of a Spin-Orbit Torque Switching Scheme Based on Micromagnetic Simulations and Reinforcement Learning*, Micromachines **12**, 4 (2021).
- [24] E. Grimaldi, V. Krizakova, G. Sala, F. Yasin, S. Couet, G. Sankar Kar, K. Garello, and P. Gambardella, *Single-Shot Dynamics of Spin–Orbit Torque and Spin Transfer Torque Switching in Three-Terminal Magnetic Tunnel Junctions*, Nat. Nanotechnol. **15**, 2 (2020).
- [25] J. C. Sankey, P. M. Braganca, A. G. F. Garcia, I. N. Krivorotov, R. A. Buhrman, and D. C. Ralph, *Spin-Transfer-Driven Ferromagnetic Resonance of Individual Nanomagnets*, Phys. Rev. Lett. **96**, 227601 (2006).
- [26] C. Kittel, *On the Theory of Ferromagnetic Resonance Absorption*, Phys. Rev. **73**, 155 (1948).
- [27] M. Oogane, T. Wakitani, S. Yakata, R. Yilgin, Y. Ando, A. Sakuma, and T. Miyazaki, *Magnetic Damping in Ferromagnetic Thin Films*, Jpn. J. Appl. Phys. **45**, 3889 (2006).
- [28] J.-M. Beaujour, D. Ravelosona, I. Tudosa, E. E. Fullerton, and A. D. Kent, *Ferromagnetic Resonance Linewidth in Ultrathin Films with Perpendicular Magnetic Anisotropy*, Phys. Rev. B **80**, 180415 (2009).
- [29] Y. Tserkovnyak, A. Brataas, G. E. W. Bauer, and B. I. Halperin, *Nonlocal Magnetization Dynamics in Ferromagnetic Heterostructures*, Rev. Mod. Phys. **77**, (2005).
- [30] M. Lakshmanan, *The Fascinating World of the Landau–Lifshitz–Gilbert Equation: An Overview*, Phil. Trans. R. Soc. A. **369**, 1280 (2011).
- [31] M. Lakshmanan and K. Nakamura, *Landau-Lifshitz Equation of Ferromagnetism: Exact Treatment of the Gilbert Damping*, Phys. Rev. Lett. **53**, 2497 (1984).
- [32] T. Bose and S. Trimper, *Correlation Effects in the Stochastic Landau-Lifshitz-Gilbert Equation*, Phys. Rev. B **81**, 104413 (2010).
- [33] M. Farle, *Ferromagnetic Resonance of Ultrathin Metallic Layers*, Rep. Prog. Phys. **61**, 755 (1998).
- [34] R. Urban, G. Woltersdorf, and B. Heinrich, *Gilbert Damping in Single and Multilayer Ultrathin Films: Role of Interfaces in Nonlocal Spin Dynamics*, Phys. Rev. Lett. **87**, 217204 (2001).
- [35] D. L. Mills and S. M. Rezende, *Spin Damping in Ultrathin Magnetic Films*, in *Spin Dynamics in Confined Magnetic Structures II*, edited by B. Hillebrands and K. Ounadjela, Vol. 87 (Springer Berlin Heidelberg, Berlin, Heidelberg, 2003), pp. 27–59.
- [36] K. Lenz, H. Wende, W. Kuch, K. Baberschke, K. Nagy, and A. Jánossy, *Two-Magnon Scattering and Viscous Gilbert Damping in Ultrathin Ferromagnets*, Phys. Rev. B **73**, 144424 (2006).
- [37] J. B. Youssef and C. Brosseau, *Magnetization Damping in Two-Component Metal Oxide Micropowder and Nanopowder Compacts by Broadband Ferromagnetic Resonance Measurements*, Phys. Rev. B **74**, 214413 (2006).
- [38] C. Liu, C. K. A. Mewes, M. Chshiev, T. Mewes, and W. H. Butler, *Origin of Low Gilbert Damping in Half Metals*, Appl. Phys. Lett. **95**, 022509 (2009).
- [39] J. Stöhr and H. C. Siegmann, *Magnetism: From Fundamentals to Nanoscale Dynamics* (Springer, Berlin ; New York, 2006).
- [40] D. C. Mattis, *Theory Of Magnetism Made Simple, The: An Introduction To Physical Concepts And To Some Useful Mathematical Methods* (World Scientific Publishing Company, 2006).
- [41] N. Umetsu, D. Miura, and A. Sakuma, *Microscopic Theory on the Gilbert Damping Due to Spin Pumping Effects in the Magnetic Multi-Layer System*, J. Phys.: Conf. Ser. **266**, 012084 (2011).
- [42] N. Vukadinovic, M. Labrune, J. B. Youssef, A. Marty, J. C. Toussaint, and H. Le Gall, *Ferromagnetic Resonance Spectra in a Weak Stripe Domain Structure*, Phys. Rev. B **65**, 054403 (2001).
- [43] G. Alejandro, L. B. Steren, H. Pastoriza, D. Vega, M. Granada, J. C. Rojas Sánchez, M. Sirena, and B. Alascio, *Magnetoresistance Effect in (La, Sr)MnO₃ Bicrystalline Films*, J. Phys.: Condens. Matter **22**, 346007 (2010).

- [44] J. Lindner and K. Baberschke, *Ferromagnetic Resonance in Coupled Ultrathin Films*, J. Phys.: Condens. Matter **15**, S465 (2003).
- [45] Z. Celinski, K. B. Urquhart, and B. Heinrich, *Using Ferromagnetic Resonance to Measure Magnetic Moments of Ultrathin Films (Abstract)*, Journal of Applied Physics **81**, 4475 (1997).
- [46] J. M. D. Coey, *Magnetism and Magnetic Materials* (Cambridge University Press, 2010).
- [47] A. Layadi, *Ferromagnetic Resonance Modes in Single and Coupled Layers with Oblique Anisotropy Axis*, Phys. Rev. B **63**, 174410 (2001).
- [48] D. Martien, *Introduction to AC Susceptibility*, (n.d.).
- [49] J. T. Davies, *Effect of Nonuniform Magnetization on the Spin-Wave Spectrum in Thin Ferromagnetic Films*, Journal of Applied Physics **35**, 804 (1964).
- [50] P. C. Fannin, I. Malaescu, and C. N. Marin, *Determination of the Landau–Lifshitz Damping Parameter of Composite Magnetic Fluids*, Physica B: Condensed Matter **388**, 93 (2007).
- [51] M. C. Hickey and J. S. Moodera, *Origin of Intrinsic Gilbert Damping*, Phys. Rev. Lett. **102**, 137601 (2009).
- [52] R. Meckenstock, D. Spoddig, Z. Frait, V. Kambersky, and J. Pelzl, *Anisotropic Gilbert Damping in Epitaxial Fe Films on InAs(0 0 1)*, Journal of Magnetism and Magnetic Materials **272–276**, 1203 (2004).
- [53] J. Lindner, I. Barsukov, C. Raeder, C. Hassel, O. Posth, R. Meckenstock, P. Landeros, and D. L. Mills, *Two-Magnon Damping in Thin Films in Case of Canted Magnetization: Theory versus Experiment*, Phys. Rev. B **80**, 224421 (2009).
- [54] J. Singh, *Quantum Mechanics: Fundamentals and Applications to Technology* (John Wiley & Sons, 2008).
- [55] N. Zettili, *Quantum Mechanics: Concepts and Applications* (John Wiley & Sons, 2009).
- [56] T. Miyazaki and H. Jin, *The Physics of Ferromagnetism* (Springer Science & Business Media, 2012).
- [57] W. (Physiker) Pauli, *Wave Mechanics: Volume 5 of Pauli Lectures on Physics* (Courier Corporation, 2000).
- [58] X. Zhou, Z. Zhang, and C.-Z. Hu, *Spin Continuity Equation and Definition of Spin Current*, arXiv:0904.3796.
- [59] N. F. Mott and R. H. Fowler, *The Electrical Conductivity of Transition Metals*, Proceedings of the Royal Society of London. Series A - Mathematical and Physical Sciences **153**, 699 (1997).
- [60] *Ferromagnetic Materials: A Handbook on the Properties of Magnetically Ordered Substances, Vol. 3 (Volume 3)* (North Holland, 1982).
- [61] S. Datta, *Electronic Transport in Mesoscopic Systems* (Cambridge University Press, Cambridge, 1995).
- [62] F. J. Jedema, M. S. Nijboer, Filip A. T., and B. J. van Wees, *Spin Injection and Spin Accumulation in All-Metal Mesoscopic Spin Valves*, Phys. Rev. B **67**, 085319 (2003).
- [63] S. Murakami, N. Nagaosa, and S.-C. Zhang, *Dissipationless Quantum Spin Current at Room Temperature*, Science **301**, 5638 (2003).
- [64] M. I. Dyakonov, editor, *Spin Physics in Semiconductors*, Vol. 157 (Springer, Berlin, Heidelberg, 2008).
- [65] N. A. Sinitsyn, *Semiclassical Theories of the Anomalous Hall Effect*, J. Phys.: Condens. Matter **20**, 023201 (2007).
- [66] J. Smit, *The Spontaneous Hall Effect in Ferromagnetics II*, Physica **24**, 1 (1958).
- [67] A. Hoffmann, *Spin Hall Effects in Metals*, IEEE Transactions on Magnetics **49**, 5172 (2013).
- [68] M. Gradhand, D. V. Fedorov, P. Zahn, and I. Mertig, *Extrinsic Spin Hall Effect from First Principles*, Phys. Rev. Lett. **104**, 186403 (2010).
- [69] T. Dietl, D. D. Awschalom, M. Kamińska, and H. Ohno, editors, *Spintronics* (Elsevier Academic Press, Amsterdam Heidelberg, 2008).
- [70] A. Fert and P. M. Levy, *Spin Hall Effect Induced by Resonant Scattering on Impurities in Metals*, Phys. Rev. Lett. **106**, 157208 (2011).
- [71] R. Karplus and J. M. Luttinger, *Hall Effect in Ferromagnetics*, Phys. Rev. **95**, 1154 (1954).

- [72] Y. Tserkovnyak, A. Brataas, and G. E. W. Bauer, *Enhanced Gilbert Damping in Thin Ferromagnetic Films*, Phys. Rev. Lett. **88**, 11 (2002).
- [73] E. Shikoh, K. Ando, K. Kubo, E. Saitoh, T. Shinjo, and M. Shiraishi, *Spin-Pump-Induced Spin Transport in p-Type Si at Room Temperature*, Phys. Rev. Lett. **110**, 127201 (2013).
- [74] Y. Ando, K. Ichiba, S. Yamada, E. Shikoh, T. Shinjo, K. Hamaya, and M. Shiraishi, *Giant Enhancement of Spin Pumping Efficiency Using Fe₃Si Ferromagnet*, Phys. Rev. B **88**, 140406 (2013).
- [75] S. Mizukami, Y. Ando, and T. Miyazaki, *Effect of Spin Diffusion on Gilbert Damping for a Very Thin Permalloy Layer in Cu/Permalloy/Cu/Pt Films*, Phys. Rev. B **66**, 104413 (2002).
- [76] K. Uchida, S. Takahashi, K. Harii, J. Ieda, W. Koshibae, K. Ando, S. Maekawa, and E. Saitoh, *Observation of the Spin Seebeck Effect*, Nature **455**, 778 (2008).
- [77] S. Bosu, Y. Sakuraba, K. Uchida, K. Saito, T. Ota, E. Saitoh, and K. Takanashi, *Spin Seebeck Effect in Thin Films of the Heusler Compound Co₂MnSi*, Phys. Rev. B **83**, 224401 (2011).
- [78] K. Uchida, T. Nonaka, T. Ota, and E. Saitoh, *Longitudinal Spin-Seebeck Effect in Sintered Polycrystalline (Mn,Zn)Fe₂O₄*, Appl. Phys. Lett. **97**, 262504 (2010).
- [79] M. I. Dyakonov and V. I. Perel, *Current-Induced Spin Orientation of Electrons in Semiconductors*, Physics Letters A **35**, 459 (1971).
- [80] M. I. D'Yakonov and V. I. Perel', *Possibility of Orienting Electron Spins with Current*, ZhETF Pisma Redaktsiiu **13**, 657 (1971).
- [81] J. Sinova, D. Culcer, Q. Niu, N. A. Sinitsyn, T. Jungwirth, and A. H. MacDonald, *Universal Intrinsic Spin Hall Effect*, Phys. Rev. Lett. **92**, 12 (2004).
- [82] Y. K. Kato, R. C. Myers, A. C. Gossard, and D. D. Awschalom, *Observation of the Spin Hall Effect in Semiconductors*, Science **306**, 1910 (2004).
- [83] S. O. Valenzuela and M. Tinkham, *Direct Electronic Measurement of the Spin Hall Effect*, Nature **442**, 7099 (2006).
- [84] E. Saitoh, M. Ueda, H. Miyajima, and G. Tatara, *Conversion of Spin Current into Charge Current at Room Temperature: Inverse Spin-Hall Effect*, Appl. Phys. Lett. **88**, 18 (2006).
- [85] S. Chikazumi and C. D. Graham, *Physics of Ferromagnetism. (2nd Ed.)*. (Oxford University Press, 1997).
- [86] F. D. Czeschka et al., *Scaling Behavior of the Spin Pumping Effect in Ferromagnet-Platinum Bilayers*, Phys. Rev. Lett. **107**, 046601 (2011).
- [87] W. H. Meiklejohn and C. P. Bean, *New Magnetic Anisotropy*, Phys. Rev. **105**, 3 (1957).
- [88] W. H. Meiklejohn, *Exchange Anisotropy—A Review*, (n.d.).
- [89] J. Nogués, J. Sort, V. Langlais, V. Skumryev, S. Suriñach, J. S. Muñoz, and M. D. Baró, *Exchange Bias in Nanostructures*, Physics Reports **422**, 65 (2005).
- [90] J. Nogués and I. K. Schuller, *Exchange Bias*, Journal of Magnetism and Magnetic Materials **192**, 203 (1999).
- [91] J. Nogués, D. Lederman, T. J. Moran, and I. K. Schuller, *Positive Exchange Bias in Fe F₂-Fe Bilayers*, Phys. Rev. Lett. **76**, 4624 (1996).
- [92] A. P. Ramirez, *Colossal Magnetoresistance*, Journal of Physics: Condensed Matter **9**, 8171 (1997).
- [93] J. M. D. Coey, M. Viret, and S. von Molnár, *Mixed-Valence Manganites*, Advances in Physics **48**, 167 (1999).
- [94] A.-M. Haghiri-Gosnet and J.-P. Renard, *CMR Manganites: Physics, Thin Films and Devices*, J. Phys. D: Appl. Phys. **36**, R127 (2003).
- [95] M. Izumi, Y. Ogimoto, Y. Konishi, T. Manako, M. Kawasaki, and Y. Tokura, *Perovskite Superlattices as Tailored Materials of Correlated Electrons*, Materials Science and Engineering: B **84**, 53 (2001).
- [96] R. Bah, D. Bitok, R. R. Rakhimov, M. M. Noginov, A. K. Pradhan, and N. Noginova, *Ferromagnetic Resonance Studies on Colossal Magnetoresistance Films: Effects of Homogeneity and Light Illumination*, Journal of Applied Physics **99**, 08Q312 (2006).

- [97] M. T. Causa et al., *High-Temperature Spin Dynamics in CMR Manganites: ESR and Magnetization*, Phys. Rev. B **58**, 3233 (1998).
- [98] V. A. Atsarkin, V. V. Demidov, and A. M. Balbashov, *Anomalous Slowing down of the Longitudinal Spin Relaxation near the Antiferromagnetic Phase Transition in LaMnO₃ Manganite*, Jetp Lett. **80**, 593 (2004).
- [99] S. H. Seo, H. C. Kang, H. W. Jang, and D. Y. Noh, *Effects of Oxygen Incorporation in Tensile La_{0.84}Sr_{0.16}MnO_{3-d} Thin Films during Ex Situ Annealing*, Phys. Rev. B **71**, 012412 (2005).
- [100] C. Kwon, S. E. Lofland, S. M. Bhagat, M. Rajeswari, T. Venkatesan, R. Ramesh, A. R. Kratz, and R. D. Gomez, *Stress-Induced Surface Magnetization of (La_{0.67}Sr_{0.33})MnO₃ Thin Films*, IEEE Transactions on Magnetics **33**, 3964 (1997).
- [101] A. K. Pradhan et al., *Magnetic Properties of La_{0.6}Sr_{0.4}MnO₃ Thin Films on SrTiO₃ and Buffered Si Substrates with Varying Thickness*, Journal of Applied Physics **103**, 023914 (2008).
- [102] C. Rettori, D. Rao, J. Singley, D. Kidwell, S. B. Oseroff, M. T. Causa, J. J. Neumeier, K. J. McClellan, S.-W. Cheong, and S. Schultz, *Temperature Dependence of the ESR Linewidth in the Paramagnetic Phase ($T > T_C$) of $R_{1-x}B_xMnO_{3+\delta}$ ($R=La, Pr$; $B=Ca, Sr$)*, Phys. Rev. B **55**, 3083 (1997).
- [103] C. S. Nelson, V. Kiryukhin, J. P. Hill, and D. Gibbs, *Structural Correlations and the Colossal Magnetoresistance Effect*, (2001).
- [104] G. Y. Luo, J. G. Lin, W.-C. Chiang, and C.-R. Chang, *Spin Pump and Probe in Lanthanum Strontium Manganite/Platinum Bilayers*, Sci Rep **7**, 1 (2017).
- [105] H. K. Lee, I. Barsukov, A. G. Swartz, B. Kim, L. Yang, H. Y. Hwang, and I. N. Krivorotov, *Magnetic Anisotropy, Damping, and Interfacial Spin Transport in Pt/LSMO Bilayers*, AIP Advances **6**, 5 (2016).
- [106] Y. Chen, B. G. Ueland, J. W. Lynn, G. L. Bychkov, S. N. Barilo, and Y. M. Mukovskii, *Polaron Formation in the Optimally Doped Ferromagnetic Manganites La_{0.7}Sr_{0.3}MnO₃ and La_{0.7}Ba_{0.3}MnO₃*, Phys. Rev. B **78**, 212301 (2008).
- [107] J.-H. Park, E. Vescovo, H.-J. Kim, C. Kwon, R. Ramesh, and T. Venkatesan, *Direct Evidence for a Half-Metallic Ferromagnet*, Nature **392**, 6678 (1998).
- [108] A. Ray, D. Panda, T. Rakshit, S. K. Mandal, I. Manna, and S. K. Ray, *Growth and Optical Properties of La_{0.7}Sr_{0.3}MnO₃/ZnO Heterojunctions*, in *2009 2nd International Workshop on Electron Devices and Semiconductor Technology* (2009), pp. 1–4.
- [109] B. Kim, D. Kwon, J. H. Song, Y. Hikita, B. G. Kim, and H. Y. Hwang, *Finite Size Effect and Phase Diagram of Ultra-Thin La_{0.7}Sr_{0.3}MnO₃*, Solid State Communications **150**, 598 (2010).
- [110] B. Jugdersuren, S. Kang, R. S. DiPietro, D. Heiman, D. McKeown, Ian. L. Pegg, and J. Philip, *Large Low Field Magnetoresistance in La_{0.67}Sr_{0.33}MnO₃ Nanowire Devices*, Journal of Applied Physics **109**, 016109 (2011).
- [111] S. Iwasaki, M. Tada, J. Yamada, Y. Inamori, J. Nogués, and T. Endo, *Temperature Dependence of FMR of La–Ba–Mn–O Thin Films*, Physica B: Condensed Matter **329–333**, 794 (2003).
- [112] M. Al Ahmad, E.-J. Yun, C. I. Cheon, and R. Plana, *Tunability of Ferromagnetic (La,Sr) MnO₃ (LSMO) Thin Films for Microwave Applications*, in *2008 38th European Microwave Conference* (2008), pp. 1296–1299.
- [113] R. V. Demin, L. I. Koroleva, and Y. M. Mukovskii, *Giant Volume Magnetostriction and Colossal Magnetoresistance at Room Temperature in La_{0.7}Ba_{0.3}MnO₃*, J. Phys.: Condens. Matter **17**, 221 (2004).
- [114] D.-W. Kim, T. W. Noh, H. Tanaka, and T. Kawai, *Influence of Microstructures on Exchange Bias Behaviors of La_{0.7}Sr_{0.3}MnO₃/La_{0.33}Ca_{0.67}MnO₃ Bilayers*, Solid State Communications **125**, 305 (2003).
- [115] M. Bibes et al., *Tunnel Magnetoresistance in Nanojunctions Based on Sr₂FeMoO₆*, Appl. Phys. Lett. **83**, 2629 (2003).
- [116] A. Y. Cho and J. R. Arthur, *Molecular Beam Epitaxy*, Progress in Solid State Chemistry **10**, 157 (1975).

- [117] M. A. Herman and H. Sitter, *Molecular Beam Epitaxy: Fundamentals and Current Status* (Springer Science & Business Media, 2012).
- [118] R. F. C. Farrow, *Molecular Beam Epitaxy: Applications to Key Materials* (Elsevier, 1995).
- [119] R. A. McKee, F. J. Walker, J. R. Conner, E. D. Specht, and D. E. Zelmon, *Molecular Beam Epitaxy Growth of Epitaxial Barium Silicide, Barium Oxide, and Barium Titanate on Silicon*, Appl. Phys. Lett. **59**, 782 (1991).
- [120] R. A. McKee, F. J. Walker, E. D. Specht, G. E. Jellison, L. A. Boatner, and J. H. Harding, *Interface Stability and the Growth of Optical Quality Perovskites on MgO*, Phys. Rev. Lett. **72**, 2741 (1994).
- [121] B. R. Johnson, K. M. Beauchamp, T. Wang, J. Liu, K. A. McGreer, J. Wan, M. Tuominen, Y. Zhang, M. L. Mecartney, and A. M. Goldman, *In Situ Growth of DyBa₂Cu₃O_{7-x} Thin Films by Molecular Beam Epitaxy*, Appl. Phys. Lett. **56**, 1911 (1990).
- [122] D. D. Berkley et al., *In Situ Formation of Superconducting YBa₂Cu₃O_{7-x} Thin Films Using Pure Ozone Vapor Oxidation*, Appl. Phys. Lett. **53**, 1973 (1988).
- [123] D. G. Schlom, A. F. Marshall, J. T. Sizemore, Z. J. Chen, J. N. Eckstein, I. Bozovic, K. E. Von Dessionneck, J. S. Harris, and J. C. Bravman, *Molecular Beam Epitaxial Growth of Layered Bi-Sr-Ca-Cu-O Compounds*, Journal of Crystal Growth **102**, 361 (1990).
- [124] J. H. Lee et al., *Optical Band Gap and Magnetic Properties of Unstrained EuTiO₃ Films*, Appl. Phys. Lett. **94**, 212509 (2009).
- [125] J. H. Lee et al., *A Strong Ferroelectric Ferromagnet Created by Means of Spin-Lattice Coupling*, Nature **466**, 7309 (2010).
- [126] K. Kugimiya, K. Fujita, K. Tanaka, and K. Hirao, *Preparation and Magnetic Properties of Oxygen Deficient EuTiO_{3-δ} Thin Films*, Journal of Magnetism and Magnetic Materials **310**, 2268 (2007).
- [127] S. C. Chae, Y. J. Chang, D.-W. Kim, B. W. Lee, I. Choi, and C. U. Jung, *Magnetic Properties of Insulating RTiO₃ Thin Films*, J Electroceram **22**, 216 (2009).
- [128] A. Inam, M. S. Hegde, X. D. Wu, T. Venkatesan, P. England, P. F. Miceli, E. W. Chase, C. C. Chang, J. M. Tarascon, and J. B. Wachtman, *As-deposited High T_c and J_c Superconducting Thin Films Made at Low Temperatures*, Appl. Phys. Lett. **53**, 908 (1988).
- [129] T. Venkatesan et al., *Substrate Effects on the Properties of Y-Ba-Cu-O Superconducting Films Prepared by Laser Deposition*, Journal of Applied Physics **63**, 4591 (1988).
- [130] H. M. Christen and G. Eres, *Recent Advances in Pulsed-Laser Deposition of Complex Oxides*, J. Phys.: Condens. Matter **20**, 264005 (2008).
- [131] R. Eason, *Pulsed Laser Deposition of Thin Films: Applications-Led Growth of Functional Materials* (John Wiley & Sons, 2007).
- [132] M. J. Aziz, *Film Growth Mechanisms in Pulsed Laser Deposition*, Appl. Phys. A **93**, 579 (2008).
- [133] G. K. Hubler, *Pulsed Laser Deposition*, MRS Bulletin **17**, 26 (1992).
- [134] M. Rao, *Applications of Nd: YAG Lasers in Material Processing: Fundamental Approach*, **2**, (2013).
- [135] A. (Alan M.) Gibbons, *Theory of Low Energy Electron Diffraction*, phd, University of Warwick, 1969.
- [136] F. Jonat and J. A. S. Jr, *Low-Energy Electron Diffraction for Surface Structure Analysis*, (n.d.).
- [137] A. Ichimiya, S. Kohmoto, H. Nakahara, and Y. Horio, *Theory of RHEED and Application to Surface Structure Studies*, Ultramicroscopy **48**, 425 (1993).
- [138] A. Ichimiya, P. I. Cohen, and P. I. Cohen, *Reflection High-Energy Electron Diffraction* (Cambridge University Press, 2004).
- [139] J. M. Van Hove, P. Pukite, P. I. Cohen, and C. S. Lent, *RHEED Streaks and Instrument Response*, Journal of Vacuum Science & Technology A **1**, 609 (1983).
- [140] W. H. Bragg and W. L. Bragg, *The Reflection of X-Rays by Crystals*, Proceedings of the Royal Society of London. Series A, Containing Papers of a Mathematical and Physical Character **88**, 428 (1997).
- [141] M. Yasaka, *X-Ray Thin-Film Measurement Techniques*, (2010).
- [142] B. Fultz and J. M. Howe, *Transmission Electron Microscopy and Diffractometry of Materials* (Springer Science & Business Media, 2012).

- [143] M. Hayat, *Basic Techniques For Transmission Electron Microscopy* (Elsevier, 2012).
- [144] J. C. Bravman and R. Sinclair, *The Preparation of Cross-Section Specimens for Transmission Electron Microscopy*, *J. Elec. Microsc. Tech.* **1**, 53 (1984).
- [145] S. Mohanty, M. Sharma, A. Moharana, B. Ojha, E. Pandey, and S. Bedanta, *Magnetization Reversal and Domain Structures in Perpendicular Synthetic Antiferromagnets Prepared on Rigid and Flexible Substrates*, *JOM* **74**, 1 (2022).
- [146] B. D. Josephson, *Coupled Superconductors*, *Rev. Mod. Phys.* **36**, 216 (1964).
- [147] P. W. Anderson and J. M. Rowell, *Probable Observation of the Josephson Superconducting Tunneling Effect*, *Phys. Rev. Lett.* **10**, 230 (1963).
- [148] B. D. Josephson, *Possible New Effects in Superconductive Tunnelling*, *Physics Letters* **1**, 251 (1962).
- [149] C. Chappert, A. Fert, and F. N. Van Dau, *The Emergence of Spin Electronics in Data Storage*, *Nature Mater* **6**, 11 (2007).
- [150] I. Žutić, J. Fabian, and S. Das Sarma, *Spintronics: Fundamentals and Applications*, *Rev. Mod. Phys.* **76**, 323 (2004).
- [151] V. T. Pham, L. Vila, G. Zahnd, A. Marty, W. Savero-Torres, M. Jamet, and J.-P. Attané, *Ferromagnetic/Nonmagnetic Nanostructures for the Electrical Measurement of the Spin Hall Effect*, *Nano Lett.* **16**, 6755 (2016).
- [152] M.-H. Nguyen, C.-F. (白奇峰) Pai, K. X. Nguyen, D. A. Muller, D. C. Ralph, and R. A. Buhrman, *Enhancement of the Anti-Damping Spin Torque Efficacy of Platinum by Interface Modification*, *Appl. Phys. Lett.* **106**, 222402 (2015).
- [153] K. Ando, S. Takahashi, K. Harii, K. Sasage, J. Ieda, S. Maekawa, and E. Saitoh, *Electric Manipulation of Spin Relaxation Using the Spin Hall Effect*, *Phys. Rev. Lett.* **101**, 036601 (2008).
- [154] S. Mizukami, Y. Ando, and T. Miyazaki, *Ferromagnetic Resonance Linewidth for NM/80NiFe/NM Films (NM=Cu, Ta, Pd and Pt)*, *Journal of Magnetism and Magnetic Materials* **226–230**, 1640 (2001).
- [155] S. Emori, T. Nan, T. M. Oxholm, C. T. Boone, J. G. Jones, B. M. Howe, G. J. Brown, D. E. Budil, and N. X. Sun, *Quantification of the Spin-Hall Anti-Damping Torque with a Resonance Spectrometer*, *Appl. Phys. Lett.* **106**, 2 (2015).
- [156] N. Behera, A. Kumar, S. Chaudhary, and D. K. Pandya, *Two Magnon Scattering and Anti-Damping Behavior in a Two-Dimensional Epitaxial TiN/Py(t_{Py})/ β -Ta(t_{Ta}) System*, *RSC Adv.* **7**, 14 (2017).
- [157] S. Keller et al., *Determination of the Spin Hall Angle in Single-Crystalline Pt Films from Spin Pumping Experiments*, *New J. Phys.* **20**, 053002 (2018).
- [158] J.-C. Rojas-Sánchez, N. Reyren, P. Laczkowski, W. Savero, J.-P. Attané, C. Deranlot, M. Jamet, J.-M. George, L. Vila, and H. Jaffrès, *Spin Pumping and Inverse Spin Hall Effect in Platinum: The Essential Role of Spin-Memory Loss at Metallic Interfaces*, *Phys. Rev. Lett.* **112**, 10 (2014).
- [159] T. Kimura, Y. Otani, T. Sato, S. Takahashi, and S. Maekawa, *Room-Temperature Reversible Spin Hall Effect*, *Phys. Rev. Lett.* **98**, 15 (2007).
- [160] T. Kimura, Y. Otani, T. Sato, S. Takahashi, and S. Maekawa, *Room-Temperature Reversible Spin Hall Effect*, *Phys. Rev. Lett.* **98**, 15 (2007).
- [161] Y. Huo, F. L. Zeng, C. Zhou, and Y. Z. Wu, *Spin Pumping and the Inverse Spin Hall Effect in Single Crystalline Fe/Pt Heterostructure*, *AIP Advances* **7**, 5 (2017).
- [162] X. L. Zheng, L. K. Zou, Y. Zhang, and J. W. Cai, *Large Inverse Spin Hall Effect in Co-Pt Spin-Valve Heterostructures*, *Phys. Rev. Applied* **7**, 4 (2017).
- [163] G. Y. Luo, C. R. Chang, and J. G. Lin, *Influence of Damping Constant on Inverse Spin Hall Voltage of $La_{0.7}Sr_{0.3}MnO_3(x)$ /Platinum Bilayers*, *Journal of Applied Physics* **115**, 17 (2014).
- [164] V. A. Atsarkin, B. V. Sorokin, I. V. Borisenko, V. V. Demidov, and G. A. Ovsyannikov, *Resonance Spin-Charge Phenomena and Mechanism of Magnetoresistance Anisotropy in Manganite/Metal Bilayer Structures*, *J. Phys. D: Appl. Phys.* **49**, 125003 (2016).
- [165] G. Y. Luo, C. R. Chang, and J. G. Lin, *Thickness Dependent Spin Pumping Effects in $La_{0.67}Sr_{0.33}MnO_3$ /Platinum Bilayer Film*, *IEEE Trans. Magn.* **49**, 7 (2013).

- [166] G. Y. Luo, M. Belmeguenai, Y. Roussigné, C. R. Chang, J. G. Lin, and S. M. Chérif, *Enhanced Magnetic Damping in $La_{0.7}Sr_{0.3}MnO_3$ Capped by Normal Metal Layer*, AIP Advances **5**, 9 (2015).
- [167] B. Heinrich, J. F. Cochran, and R. Hasegawa, *FMR Linebroadening in Metals Due to Two-magnon Scattering*, Journal of Applied Physics **57**, 3690 (1985).
- [168] B. B. Singh, K. Roy, P. Gupta, T. Seki, K. Takanashi, and S. Bedanta, *High Spin Mixing Conductance and Spin Interface Transparency at the Interface of a $Co_2Fe_{0.4}Mn_{0.6}Si$ Heusler Alloy and Pt*, NPG Asia Mater **13**, 1 (2021).
- [169] N. Behera, S. Chaudhary, and D. K. Pandya, *Anomalous Anti-Damping in Sputtered β -Ta/Py Bilayer System*, Sci Rep **6**, 1 (2016).
- [170] H. Jiao and G. E. W. Bauer, *Spin Backflow and Ac Voltage Generation by Spin Pumping and the Inverse Spin Hall Effect*, Phys. Rev. Lett. **110**, 21 (2013).
- [171] K.-R. Jeon, C. Ciccarelli, H. Kurebayashi, J. Wunderlich, L. F. Cohen, S. Komori, J. W. A. Robinson, and M. G. Blamire, *Spin-Pumping-Induced Inverse Spin Hall Effect in Nb/Ni₈₀Fe₂₀ Bilayers and Its Strong Decay Across the Superconducting Transition Temperature*, Phys. Rev. Applied **10**, 1 (2018).
- [172] R. Iguchi and E. Saitoh, *Measurement of Spin Pumping Voltage Separated from Extrinsic Microwave Effects*, J. Phys. Soc. Jpn. **86**, 1 (2017).
- [173] A. Conca, B. Heinz, M. R. Schweizer, S. Keller, E. Th. Papaioannou, and B. Hillebrands, *Lack of Correlation between the Spin-Mixing Conductance and the Inverse Spin Hall Effect Generated Voltages in CoFeB/Pt and CoFeB/Ta Bilayers*, Phys. Rev. B **95**, 17 (2017).
- [174] K. Rogdakis et al., *Spin Transport Parameters of NbN Thin Films Characterized by Spin Pumping Experiments*, Phys. Rev. Materials **3**, 1 (2019).
- [175] Y. Wang, P. Deorani, X. Qiu, J. H. Kwon, and H. Yang, *Determination of Intrinsic Spin Hall Angle in Pt*, Appl. Phys. Lett. **105**, 15 (2014).
- [176] X. Tao et al., *Self-Consistent Determination of Spin Hall Angle and Spin Diffusion Length in Pt and Pd: The Role of the Interface Spin Loss*, Sci. Adv. **4**, 6 (2018).
- [177] P. Gupta, B. B. Singh, K. Roy, A. Sarkar, M. Waschk, T. Brueckel, and S. Bedanta, *Simultaneous Observation of Anti-Damping and the Inverse Spin Hall Effect in the $La_{0.67}Sr_{0.33}MnO_3$ /Pt Bilayer System*, Nanoscale **13**, 4 (2021).
- [178] O. Mosendz, J. E. Pearson, F. Y. Fradin, G. E. W. Bauer, S. D. Bader, and A. Hoffmann, *Quantifying Spin Hall Angles from Spin Pumping: Experiments and Theory*, Phys. Rev. Lett. **104**, 4 (2010).
- [179] Y. Tserkovnyak, A. Brataas, and G. E. W. Bauer, *Spin Pumping and Magnetization Dynamics in Metallic Multilayers*, Phys. Rev. B **66**, 22 (2002).
- [180] K. Ando et al., *Inverse Spin-Hall Effect Induced by Spin Pumping in Metallic System*, Journal of Applied Physics **109**, 103913 (2011).
- [181] H. Kurebayashi, O. Dzyapko, V. E. Demidov, D. Fang, A. J. Ferguson, and S. O. Demokritov, *Controlled Enhancement of Spin-Current Emission by Three-Magnon Splitting*, Nature Mater **10**, 9 (2011).
- [182] V. Castel, N. Vlietstra, B. J. van Wees, and J. B. Youssef, *Frequency and Power Dependence of Spin-Current Emission by Spin Pumping in a Thin-Film YIG/Pt System*, Phys. Rev. B **86**, 13 (2012).
- [183] V. Castel, N. Vlietstra, B. J. van Wees, and J. Ben Youssef, *Yttrium Iron Garnet Thickness and Frequency Dependence of the Spin-Charge Current Conversion in YIG/Pt Systems*, Phys. Rev. B **90**, 21 (2014).
- [184] B. B. Singh, S. K. Jena, and S. Bedanta, *Study of Spin Pumping in Co Thin Film Vis-à-Vis Seed and Capping Layers Using Ferromagnetic Resonance Spectroscopy*, J. Phys. D: Appl. Phys. **50**, 34 (2017).
- [185] B. B. Singh, S. K. Jena, M. Samanta, K. Biswas, B. Satpati, and S. Bedanta, *Inverse Spin Hall Effect in Electron Beam Evaporated Topological Insulator Bi_2Se_3 Thin Film*, Phys. Status Solidi RRL **13**, 3 (2019).
- [186] B. Sahoo, K. Roy, P. Gupta, A. Mishra, B. Satpati, B. B. Singh, and S. Bedanta, *Spin Pumping and Inverse Spin Hall Effect in Iridium Oxide*, Adv Quantum Tech **4**, 9 (2021).

- [187] K. Roy, A. Mishra, P. Gupta, S. Mohanty, B. B. Singh, and S. Bedanta, *Spin Pumping and Inverse Spin Hall Effect in CoFeB/IrMn Heterostructures*, J. Phys. D: Appl. Phys. **54**, 42 (2021).
- [188] K. Roy, S. Nayak, P. Gupta, and S. Bedanta, *Spin Dynamics and Inverse Spin Hall Effect Study in the Metallic Pt/NiMn/CoFeB System*, Phys. Chem. Chem. Phys. **24**, 39 (2022).
- [189] B. B. Singh, K. Roy, J. A. Chelvane, and S. Bedanta, *Inverse Spin Hall Effect and Spin Pumping in the Polycrystalline Noncollinear Antiferromagnetic Mn₃Ga*, Phys. Rev. B **102**, 174444 (2020).
- [190] K. Yamanoi, Y. Yokotani, and T. Kimura, *Heat Dissipation Due to Ferromagnetic Resonance in a Ferromagnetic Metal Monitored by Electrical Resistance Measurement*, Appl. Phys. Lett. **107**, 182410 (2015).
- [191] A.-M. Haghiri-Gosnet and J.-P. Renard, *CMR Manganites: Physics, Thin Films and Devices*, J. Phys. D: Appl. Phys. **36**, 8 (2003).
- [192] X. Zhao, H. F. Wong, Y. K. Liu, S. M. Ng, W. F. Cheng, C. L. Mak, and C. W. Leung, *Exchange Bias Effect in Epitaxial La_{0.35}Sr_{0.65}MnO₃/La_{0.7}Sr_{0.3}MnO₃ Bilayers: Impact of Antiferromagnet Growth Conditions*, Vacuum **175**, 109280 (2020).
- [193] M. Staruch, D. Violette, and M. Jain, *Structural and Magnetic Properties of Multiferroic Bulk TbMnO₃*, Materials Chemistry and Physics **139**, 897 (2013).
- [194] I. A. A.-Latif, A. S. Khramov, V. A. Trounov, O. P. Smirnov, Sh. Sh. Bashkirov, V. V. Parfenov, E. A. Tserkovnaya, G. G. Gumarov, and Sh. Z. Ibragimov, *Electrical and Magnetic Properties - Structure Correlation on Nd_{0.65}Sr_{0.35}Mn_{1-x}Fe_xO₃*, Egyptian Journal of Solids **29**, 341 (2006).
- [195] M. Fiebig, T. Lottermoser, D. Fröhlich, A. V. Goltsev, and R. V. Pisarev, *Observation of Coupled Magnetic and Electric Domains*, Nature **419**, 6909 (2002).
- [196] N. A. Hill and K. M. Rabe, *First-Principles Investigation of Ferromagnetism and Ferroelectricity in Bismuth Manganite*, Phys. Rev. B **59**, 8759 (1999).
- [197] X. Ke, M. S. Rzchowski, L. J. Belenky, and C. B. Eom, *Positive Exchange Bias in Ferromagnetic La_{0.67}Sr_{0.33}MnO₃/SrRuO₃ Bilayers*, Appl. Phys. Lett. **84**, 26 (2004).
- [198] Q. Qin, S. He, W. Song, P. Yang, Q. Wu, Y. P. Feng, and J. Chen, *Ultra-Low Magnetic Damping of Perovskite La_{0.7}Sr_{0.3}MnO₃ Thin Films*, Appl. Phys. Lett. **110**, 11 (2017).
- [199] J. Hemberger, A. Krimmel, T. Kurz, H.-A. Krug von Nidda, V. Yu. Ivanov, A. A. Mukhin, A. M. Balbashov, and A. Loidl, *Structural, Magnetic, and Electrical Properties of Single-Crystalline La_{1-x}Sr_xMnO₃ (0.4 < x < 0.85)*, Phys. Rev. B **66**, 094410 (2002).
- [200] C. Song, X. Zhou, X. Chen, P. Zhang, G. Shi, and F. Pan, *Spin-Orbit Torque in Antiferromagnets*, in *2018 IEEE International Magnetism Conference (INTERMAG)* (2018), pp. 1–1.
- [201] R. Ramazashvili, *Zeeman Spin-Orbit Coupling in Antiferromagnetic Conductors*, Journal of Physics and Chemistry of Solids **128**, 65 (2019).
- [202] A. J. Berger, E. R. J. Edwards, H. T. Nembach, O. Karis, M. Weiler, and T. J. Silva, *Determination of the Spin Hall Effect and the Spin Diffusion Length of Pt from Self-Consistent Fitting of Damping Enhancement and Inverse Spin-Orbit Torque Measurements*, Phys. Rev. B **98**, 2 (2018).
- [203] B. B. Singh and S. Bedanta, *Large Spin Hall Angle and Spin-Mixing Conductance in the Highly Resistive Antiferromagnet Mn₂Au*, Phys. Rev. Applied **13**, 4 (2020).
- [204] I. Benguetat-EL Mokhtari, Y. Roussigné, T. Petrisor Jr., F. Zighem, F. Kail, L. Chahed, V. Pierron, L. Méchin, M. Gabor, and M. Belméguenai, *Spin Pumping and Magnetic Anisotropy in La_{2/3}Sr_{1/3}MnO₃/Pt Systems*, Physica Status Solidi (b) **257**, 2000265 (2020).
- [205] R. Bindu, G. Adhikary, S. K. Pandey, and K. Maiti, *Spectral Evolution in an Insulator Exhibiting Linear Specific Heat*, New J. Phys. **12**, 033003 (2010).
- [206] N. Singh, M. Maniraj, J. Nayak, S. K. Pandey, and R. Bindu, *Inverse Photoemission Spectroscopic Studies on Phase Separated La_{0.2}Sr_{0.8}MnO₃*, Solid State Communications **217**, 70 (2015).
- [207] A. Janotti, B. Jalan, S. Stemmer, and C. G. Van de Walle, *Effects of Doping on the Lattice Parameter of SrTiO₃*, Appl. Phys. Lett. **100**, 262104 (2012).
- [208] U. K. Sinha, B. Das, and P. Padhan, *Interfacial Reconstruction in La_{0.7}Sr_{0.3}MnO₃ Thin Films: Giant Low-Field Magnetoresistance*, Nanoscale Adv. **2**, 2792 (2020).

- [209] P. Gupta, B. B. Singh, A. Mishra, A. Kumar, A. Sarkar, M. Waschk, and S. Bedanta, *Tailoring Spin to Charge Conversion Efficiency via Microwave Frequency In*, Unpublished (n.d.).
- [210] J. Bünnemann, F. Gebhard, T. Ohm, S. Weiser, and W. Weber, *Spin-Orbit Coupling in Ferromagnetic Nickel*, Phys. Rev. Lett. **101**, 236404 (2008).
- [211] B. F. Miao, S. Y. Huang, D. Qu, and C. L. Chien, *Inverse Spin Hall Effect in a Ferromagnetic Metal*, Phys. Rev. Lett. **111**, 066602 (2013).
- [212] A. Tsukahara, Y. Ando, Y. Kitamura, H. Emoto, E. Shikoh, M. P. Delmo, T. Shinjo, and M. Shiraishi, *Self-Induced Inverse Spin Hall Effect in Permalloy at Room Temperature*, Phys. Rev. B **89**, 235317 (2014).
- [213] K. Kanagawa, Y. Teki, and E. Shikoh, *Self-Induced Inverse Spin-Hall Effect in an Iron and a Cobalt Single-Layer Films Themselves under the Ferromagnetic Resonance*, AIP Advances **8**, 055910 (2018).
- [214] O. Gladii et al., *Self-Induced Inverse Spin Hall Effect in Ferromagnets: Demonstration through Nonmonotonic Temperature Dependence in Permalloy*, Phys. Rev. B **100**, 174409 (2019).
- [215] P. Saadatkia, P. Stepanov, and F. A. Selim, *Photoconductivity of Bulk SrTiO₃ Single Crystals at Room Temperature*, Mater. Res. Express **5**, 016202 (2018).
- [216] P. Gupta, K. Rothore, A. Mishra, A. Swain, and S. Bedanta, *Study of Spin Pumping in La_{0.67}Sr_{0.33}MnO₃/La_{0.2}Sr_{0.8}MnO₃ Heterostructure.Docx*, (unpublished).
- [217] X. Zhang, A. N. Penn, L. Wysocki, Z. Zhang, P. H. M. van Loosdrecht, L. Kornblum, J. M. LeBeau, I. Lindfors-Vrejoiu, and D. P. Kumah, *Thickness and Temperature Dependence of the Atomic-Scale Structure of SrRuO₃ Thin Films*, APL Materials **10**, 051107 (2022).
- [218] L. Klein, J. S. Dodge, C. H. Ahn, J. W. Reiner, L. Mieville, T. H. Geballe, M. R. Beasley, and A. Kapitulnik, *Transport and Magnetization in the Badly Metallic Itinerant Ferromagnet*, J. Phys.: Condens. Matter **8**, 48 (1996).
- [219] H. Schraknepper, C. Bäumer, F. Gunkel, R. Dittmann, and R. A. De Souza, *Pulsed Laser Deposition of SrRuO₃ Thin-Films: The Role of the Pulse Repetition Rate*, APL Materials **4**, 126109 (2016).
- [220] Y.-J. Chang, J.-I. Kim, and C. U. Jung, *Electrical Properties of SrRuO₃ Thin Films with Varying c-Axis Lattice Constant*, Journal of Magnetism **13**, 61 (2008).
- [221] D. Samal, D. Venkateswarlu, and P. S. Anil Kumar, *Influence of Finite Size Effect on Magnetic and Magnetotransport Properties of Thin Films*, Solid State Communications **150**, 13–14 (2010).
- [222] A. de Andrés, J. Rubio, G. Castro, S. Taboada, J. L. Martínez, and J. M. Colino, *Structural and Magnetic Properties of Ultrathin Epitaxial La_{0.7}Ca_{0.3}MnO₃ Manganite Films: Strain versus Finite Size Effects*, Appl. Phys. Lett. **83**, 713 (2003).
- [223] M. Ziese, E. Pippel, E. Nikulina, M. Arredondo, and I. Vrejoiu, *Exchange Coupling and Exchange Bias in La_{0.7}Sr_{0.3}MnO₃–SrRuO₃ Superlattices*, Nanotechnology **22**, 25 (2011).
- [224] S. Jana, T. Senapati, and D. Samal, *Evidence for Spin-Orbit and e-e Coulomb Interaction from a Magnetotransport Study on CaCu₃Ru₄O₁₂ Thin Films*, Phys. Rev. B **103**, 245109 (2021).
- [225] L. Méchin, S. Wu, B. Guillet, P. Perna, C. Fur, S. Lebargy, C. Adamo, D. G. Schlom, and J. M. Routoure, *Experimental Evidence of Correlation between 1/f Noise Level and Metal-to-Insulator Transition Temperature in Epitaxial La_{0.7}Sr_{0.3}MnO₃ Thin Films*, J. Phys. D: Appl. Phys. **46**, 202001 (2013).
- [226] S. A. Lee et al., *Tuning Electromagnetic Properties of SrRuO₃ Epitaxial Thin Films via Atomic Control of Cation Vacancies*, Sci Rep **7**, 1 (2017).
- [227] Y. He et al., *Large Linear Non-Saturating Magnetoresistance and High Mobility in Ferromagnetic MnBi*, Nat Commun **12**, 1 (2021).
- [228] B. Pang, L. Zhang, Y. B. Chen, J. Zhou, S. Yao, S. Zhang, and Y. Chen, *Spin-Glass-Like Behavior and Topological Hall Effect in SrRuO₃/SrIrO₃ Superlattices for Oxide Spintronics Applications*, ACS Appl. Mater. Interfaces **9**, 3201 (2017).
- [229] M. Wahler, N. Homonnay, T. Richter, A. Müller, C. Eisenschmidt, B. Fuhrmann, and G. Schmidt, *Inverse Spin Hall Effect in a Complex Ferromagnetic Oxide Heterostructure*, Sci Rep **6**, 1 (2016).

- [230] X. Ke, L. J. Belenky, C. B. Eom, and M. S. Rzchowski, *Antiferromagnetic Exchange-Bias in Epitaxial Ferromagnetic $La_{0.67}Sr_{0.33}MnO_3/SrRuO_3$ Bilayers*, Journal of Applied Physics **97**, 10 (2005).
- [231] H. Ohldag, H. Shi, E. Arenholz, J. Stöhr, and D. Lederman, *Parallel versus Antiparallel Interfacial Coupling in Exchange Biased Co/FeF_2* , Phys. Rev. Lett. **96**, 027203 (2006).
- [232] S. Roy et al., *Depth Profile of Uncompensated Spins in an Exchange Bias System*, Phys. Rev. Lett. **95**, 047201 (2005).
- [233] S. Majumdar and S. van Dijken, *Pulsed Laser Deposition of $La_{1-x}Sr_xMnO_3$: Thin-Film Properties and Spintronic Applications*, J. Phys. D: Appl. Phys. **47**, 034010 (2013).
- [234] J. M. De Teresa, A. Barthélémy, A. Fert, J. P. Contour, F. Montaigne, and P. Seneor, *Role of Metal-Oxide Interface in Determining the Spin Polarization of Magnetic Tunnel Junctions*, Science **286**, 5439 (1999).
- [235] W. Hou, Y. Yao, Y. Li, B. Peng, K. Shi, Z. Zhou, J. Pan, M. Liu, and J. Hu, *Linearly Shifting Ferromagnetic Resonance Response of $La_{0.7}Sr_{0.3}MnO_3$ Thin Film for Body Temperature Sensors*, Front. Mater. Sci. **16**, 220589 (2022).
- [236] X. Ke, L. J. Belenky, C. B. Eom, and M. S. Rzchowski, *Antiferromagnetic Exchange-Bias in Epitaxial Ferromagnetic $La_{0.67}Sr_{0.33}MnO_3/SrRuO_3$ Bilayers*, Journal of Applied Physics **97**, 10 (2005).
- [237] Y. Lee, B. Caes, and B. N. Harmon, *Role of Oxygen 2p States for Anti-Ferromagnetic Interfacial Coupling and Positive Exchange Bias of Ferromagnetic LSMO/SRO Bilayers*, Journal of Alloys and Compounds **450**, 1–2 (2008).
- [238] R. Rana, P. Pandey, and D. S. Rana, *Controlling the Coexisting Vertical Magnetization Shift and Exchange Bias in $La_{0.3}Sr_{0.7}FeO_3/SrRuO_3$ Bilayers*, Appl. Phys. Lett. **104**, 9 (2014).
- [239] S. R. Singamaneni, W. Fan, J. T. Prater, and J. Narayan, *Complete Vertical M-H Loop Shift in $La_{0.7}Sr_{0.3}MnO_3/SrRuO_3$ Thin Film Heterostructures*, Journal of Applied Physics **117**, 17 (2015).
- [240] A. Singh and J. Chen, *Large Vertical Hysteretic Shift and Signature of Exchange Bias in $BiFeO_3/SrRuO_3$ Heterostructure*, Ceramics International **45**, 16 (2019).
- [241] M. Zheng, X. Li, W. Xiao, W. Wang, and H. Ni, *Oxygen Deficiency and Cooling Field Driven Vertical Hysteretic Shift in Epitaxial $SrRuO_3/SrTiO_3$ Heterostructures*, Appl. Phys. Lett. **111**, 15 (2017).
- [242] J. Nogués, L. Morellon, C. Leighton, M. R. Ibarra, and I. K. Schuller, *Antiferromagnetic Spin Flop and Exchange Bias*, Phys. Rev. B **61**, R6455 (2000).
- [243] M. R. Fitzsimmons, B. J. Kirby, S. Roy, Z.-P. Li, I. V. Roshchin, S. K. Sinha, and I. K. Schuller, *Pinned Magnetization in the Antiferromagnet and Ferromagnet of an Exchange Bias System*, Phys. Rev. B **75**, 214412 (2007).
- [244] R. Rana, P. Pandey, R. P. Singh, and D. S. Rana, *Positive Exchange-Bias and Giant Vertical Hysteretic Shift in $La_{0.3}Sr_{0.7}FeO_3/SrRuO_{0.3}$ Bilayers*, Sci Rep **4**, 1 (2015).
- [245] D. Paccard, C. Schlenker, O. Massenet, R. Montmory, and A. Yelon, *A New Property of Ferromagnetic-Antiferromagnetic Coupling*, Phys. Stat. Sol. (b) **16**, 1 (1966).
- [246] P. V. Muhammed Shameem and M. Senthil Kumar, *Training Effect of the Exchange Bias in Sputter Deposited Fe_3O_4 Thin Films with Varying Thickness*, Journal of Magnetism and Magnetic Materials **458**, 241 (2018).
- [247] J. Barman, T. Bora, and S. Ravi, *Study of Exchange Bias and Training Effect in $NiCr_2O_4$* , Journal of Magnetism and Magnetic Materials **385**, 93 (2015).
- [248] S. K. Mishra, F. Radu, H. A. Dürr, and W. Eberhardt, *Training-Induced Positive Exchange Bias in $NiFe/IrMn$ Bilayers*, Phys. Rev. Lett. **102**, 17 (2009).
- [249] W.-B. Rui, M.-C. He, B. You, Z. Shi, S.-M. Zhou, M.-W. Xiao, Y. Gao, W. Zhang, L. Sun, and J. Du, *Asymmetric Exchange Bias Training Effect in Spin Glass ($FeAu$)/ $FeNi$ Bilayers*, Chinese Phys. B **23**, 10 (2014).
- [250] Ch. Binek, S. Polisetty, X. He, and A. Berger, *Exchange Bias Training Effect in Coupled All Ferromagnetic Bilayer Structures*, Phys. Rev. Lett. **96**, 6 (2006).

- [251] Q. Qin et al., *Interfacial Antiferromagnetic Coupling between SrRuO₃ and La_{0.7}Sr_{0.3}MnO₃ with Orthogonal Easy Axis*, Phys. Rev. Materials **2**, 10 (2018).
- [252] L. Wang, R. J. H. Wesselink, Y. Liu, Z. Yuan, K. Xia, and P. J. Kelly, *Giant Room Temperature Interface Spin Hall and Inverse Spin Hall Effects*, Phys. Rev. Lett. **116**, 19 (2016).